An investigation on the collisional behaviour of granular flows

Devis Gollin

A thesis submitted in partial fulfilment of the requirements for the degree of

Doctor of Philosophy

The University of Sheffield

Department of Civil and Structural Engineering

July 2017

Declaration

I, Devis Gollin, confirm that the work presented in this thesis is my own. Where information has been derived from other sources, I confirm that this has been indicated in the thesis.

Signed,

July 2017

Abstract

Granular materials are encountered in a diverse range of geophysical contexts such as landslides and debris flows. This research aims to improve our knowledge of debris flows by means of experimental, numerical and theoretical work with a specific focus on the recently developed extended kinetic theory (EKT) for dry granular flows over bumpy bases.

Debris flows undergo rapid rates of deformation in which momentum transfer is mainly carried by frictional and collisional stresses. The random components that generate particle stresses through collisions can be related to the concept of granular temperature. This entity represents the basic concept underpinning the kinetic theory of granular flows. Fundamental characteristics of mobile granular flows are reproduced in laboratory experiments and numerical simulations. The results obtained are used in this thesis to test the predictions and validate the predictions of velocity, granular temperature and solid concentration obtained from the application of extended kinetic theory (EKT).

In the first part of this thesis, dry granular flows are studied. Two imaging techniques proposed for the measurement of velocity and granular temperature, namely Particle Image Velocimetry (PIV) and Particle Tracking Velocimetry (PTV) are critically assessed. Due to lack of guidelines for the correct investigation of granular flows using PTV, an error framework for this technique is presented. The influences of errors generated during the PIV and PTV procedures are examined in experiments on dry monodisperse granular flows made of angular and nearly spherical particles down an inclined chute geometry. For the spherical particles, profiles of velocity, granular temperature, solid concentration and stresses are obtained. In terms of granular temperature, the accuracy of the results is still unclear for flows of angular particles while, for the nearly spherical particles, it is shown how the choice of image resolution and the sampling interval affects both the magnitude and the profile shape of granular temperature.

Based on the experimental investigations, discrete element simulations of steady, fully-developed, inclined flows of identical spheres over bumpy bases, in the presence and absence of flat, frictional sidewalls are conducted. The main features of these flows are described and new insights in the behaviour of numerically simulated flows over a bumpy base is

given. A method to include the influence of rolling resistance in the numerical simulations is examined by comparing to the results of one selected experiment. A good agreement between the two approaches is found. The simulations in the absence of sidewalls are also used to generate synthetic images upon which PIV and PTV are assessed. It is found that PTV is a better technique to measure granular temperature when the appropriate sampling interval is used, at least for dry monodisperse granular flow of identical spheres, while PIV tends to to damp the magnitude of this quantity in some parts of the flow.

The predictions of extended kinetic theory in terms of dimensionless pressure are compared with those obtained from experiments and numerical simulations. In the first case, the results obtained considering the error framework for PTV and the validation via synthetic images find good agreement in the limit of validity of solid concentration measurement. In the second case, a good agreement is also found but it is shown that the constitutive relation for the pressure of EKT must be modified in the proximity of the boundary, because of the influence of currently available radial distribution functions at the bottom boundary. It is also noticed that currently available boundary conditions for flows over bumpy planes underestimate the energy dissipation. These two observations generate a the lack of agreement of EKT with the simulations, in terms of the maximum angles of inclination for which steady flows are possible. However, whenever a solution is possible, the predicted measurements of EKT satisfactorily match the numerical measurements. In addition, for granular flows between sidewalls, it is confirmed that the sidewalls exert, on average, a Coulomb-like resistance to the flow. However, when EKT is tested against the experimental results, a strong disagreement is shown. It is thought that the cause may be connected to the introduction of rolling resistance in the numerical simulations, which in EKT has not yet been accounted for.

In second part of the research, solid-fluid mixtures made of transparent materials are investigated. Monodisperse and polydisperse granular flows are studied. In simple monodisperse granular flows, spherical particles are used to improve the quality of the flow visualization and allow particle tracking. The information obtained from these flows is used to test the prediction of EKT in terms of dimensionless pressure. A qualitative agreement with kinetic theory is found, although the theory underestimates the experimental results. Improvements in the accuracy of the measured flow properties may lead to better agreement. Polydisperse granular flows are performed to match the characteristics of real debris flows. However, the selected particle size distributions, made of spherical particles or a combination of spherical and angular particles, produced unexpected depositional profiles. This may have to do with the boundary conditions imposed at flow release, which were designed to enable steady flows to develop. While these flows are part of preliminary testing used to increase a step further the complexity of the monodisperse granular flows,

better consideration should be made in future to find a balance between flow visualization, experimental apparatus and boundary conditions, and the generation of appropriate mechanics that are characteristic of real debris flows.

Acknowledgements

Many people have made this work possible. First, many thanks go to my main supervisor, Elisabeth Bowman, for her patience, knowledge, and encouragement thorough my postgraduate research. I would also like to thanks my second supervisor Paul Shepley, his advice and feedback over the last three years has been exceptional.

Also thanks to Wernher Brevis and Diego Berzi for their expertise, initial instructions and help in the works which led to the scientific publication of my work.

I would like to acknowledge the technical and support staff in the Department of Civil and Structural Engineering. In particular, I thank Paul Osborne, Mark Foster, David Callaghan and Alex Cargill. I also thank the remaining staff and students of the Geotechnical Engineering Group.

Finally and foremost, thanks to my friends and family. Without their support I would not have been able to survive over these last few years away from home.

Devis Gollin, Sheffield, United Kingdom

Contents

List of Figures

List of Tables

List of publications

A list of the publications submitted in peer-reviewed journals, or published in conferences proceedings and complementary to the material presented in this thesis is given below.

Conference proceedings:

1. Gollin, D., Bowman, E.T., Shepley, P, *Granular temperature measurements of uniform granular flows.* The 6th International Symposium on Deformation Characteristics of Geomaterials, 6, 647 - 654, 2015.

2. Gollin, D., Bowman, E.T., Shepley, P, *Methods for the physical measurement of collisional particle flows*, IOP Conference Series: Earth and Environmental Science, 26(1), 012017, 2015.

3. Gollin, D., Bowman, E.T., *Capturing of the internal mechanics of liquid-granular flows comprised of polydisperse spherical particles.* 8th International Conference on Micromechanics of Granular Media, EPJ Web Conf., 140, 14006, 2017

Journal papers:

1. Gollin, D., Brevis, W., Bowman, E.T., Shepley, P. (2017). *Performance of PIV and PTV for granular flow measurements.* Granular Matter, 19(3):42.

   Contribution: Dr. Wernher Brevis shared his PTV algorithm and gave valuable advice in the development of the error framework for PTV.

2. Gollin, D., Berzi, D., Bowman, E.T. (2017). *Extended kinetic theory applied to inclined granular flows: role of boundaries.* Granular Matter, 19(3):56.

   Contribution: Dr. Berzi Diego made available his formulation of extended kinetic theory and shared his knowledge for the theoretical interpretation of the findings.

List of Abbreviations

Acronyms

I Inertial number

CG Coarse-Graining

DEM Discrete Element Method

EFL Effective Focal Length

EKT Extend Kinetic Theory

KE Kinetic Energy

PIV Particle Image Velocimetry

PLIF Planar Laser-Induced Fluorescence

PSD Particle Size Distribution

PTV Particle Tracking Velocimetry

RET Revised Enskog Theory

SET Standard Enskog Theory

Greek Symbols

β =0.35 (see [36])

$\boldsymbol{\omega}$ angular velocity vector

$\boldsymbol{\sigma}$ macroscopic stresses

$\boldsymbol{\sigma}^c$ macroscopic contact stresses

$\boldsymbol{\sigma}^k$ macroscopic kinetic stresses

$\boldsymbol{\sigma}^{k\prime}$ corrected macroscopic kinetic stresses

δ particle overlap

$\dot{\gamma}$ shear rate

ϵ effective coefficient of restitution

η_f fluid viscosity

η_m molecular viscosity

Γ rate of collisional dissipation

γ_n normal viscous damping

γ_r rolling viscous damping

γ_t tangential viscous damping

κ refactor for tangential stiffness and damping calculation

λ conductivity

λ_{Bag} Bagnold's [1954] linear concentration of solid

$\mathcal{E}$ pseudo-thermal energy

μ particle friction angle

μ^d dynamic particle friction

μ^r rolling particle friction

μ^s static particle friction

μ_w particle wall friction

ν solid concentration

ν_{rcp}^{2D} solid concentration at random close packing in 2D

ν_{rcp} solid concentration at random close packing in 3D

ν_s solid concentration at shear rigidity in 3D

ν_s^{2D} solid concentration at shear rigidity in 2D

ϕ particle friction coefficient

ϕ_{ls} laser fan angle

Ψ coarse-graining function

ψ bumpiness of the rough base

ρ bulk density

ρ^{mic} microscopic (point) mass density

ρ_f fluid density

ρ_p particle density

Θ Dirac delta function

θ slope angle

Υ maximum image intensity in pixels

φ porosity

ϱ rotational factor in $\boldsymbol{\theta}$

ξ ceramic bead circularity

ξ_{min} =0.72 (see [123])

ξ_{rcp} =0.84 (see [36])

d_{50} characteristic mean diameter

n_{sf} scale factor for granular temperature calculation in PIV

Roman Symbols

Δt sampling interval

$\mathcal{A}_{\mathcal{R}}$ ceramic bead aspect ratio

$\mathcal{I}$ particle image intensity profile

$\mathcal{M}$ mass hold-up

b particle to fixed-particle branch vector

C velocity fluctuation

D strain rate tensor

$\mathbf{F}$ total force

$\mathbf{F}^c$ contact force

$\mathbf{F}^n$ force normal component

$\mathbf{F}^t$ force tangential component

$\mathbf{g}$ vector of gravitational acceleration

$\mathbf{I}$ identity matrix

$\mathbf{j}$ torque

$\mathbf{l}$ lever arm for torque calculation

$\mathbf{M}$ momentum density vector

$\mathbf{n}$ normal branch vector

$\mathbf{Q}$ energy flux

$\mathbf{q}^r$ rolling resistance

$\mathbf{r}$ point position vector in coarse-graining

$\mathbf{T}$ stress tensor

$\mathbf{u}$ steam-wise velocity vector

$\mathbf{V}$ macroscopic velocity

$\mathbf{v}$ particle velocity

$\mathbf{v}^n$ relative particle normal velocity vector

$\mathbf{v}^r$ relative particle rolling velocity vector

$\mathbf{v}^t$ relative particle tangential velocity vector

$\mathbf{x}$ particle position vector

A particle image area

C_u coefficient of uniformity

d characteristic particle diameter

d_τ particle image diameter

d_b laser beam diameter

E fluctuating energy crossing a reference surface

e_n normal coefficient of restitution

e_t tangential coefficient of restitution

e_w wall coefficient of restitution

f focal length

f_0 function appearing in the chain length, see Eq. 2.43

f_1, f_2, f_3, f_4, f_5 auxiliary coefficients in the constitutive relations of kinetic theory, see Tab. 2.2

f_p pair-particle distribution function

f_s single-particle distribution function

G, F, J, M, N, H, B auxiliary coefficients in the constitutive relations of kinetic theory, see Tab 2.2

g_0 radial distribution function

h flow height

h_{stop} stopping flow thickness based on slope angle

I_i particle inertia

j span-wise velocity component

k_n normal spring constant

k_r rolling spring constant

k_t tangential spring constant

L chain length

l_x simulation domain size in x-direction

l_y simulation domain size in y-direction

l_z simulation domain size in z-direction

L_{ls} laser working distance

m particle mass

N number of particles

n number of particles per unit volume

N_i particle image density

N_p pore pressure number

N_R quasi-Reynolds number

N_{Bag} Bagnold number

P particle image perimeter

p normal stress

P_* non-hydrostatic fluid pressure

P_h hydrostatic fluid pressure

P_t total fluid pressure

r particle radius

S side surface of a reference volume

s shear stress

T granular temperature

t time

t_γ macroscopic time scale of deformation

t_c collisional time between two particles

t_{fall} microscopic time scale of rearrangement

u steam-wise velocity component

V particle volume

v slope-normal velocity component

W reference volume

w coarse-graining width

X stream-wise direction in the image domain

x stream-wise direction

x_{ls} laser sheet width

Y span-wise direction in the image domain

y span-wise direction

Y_i yield parameter for PTV

Z slope-normal direction in the image domain

z slope-normal direction

m partial mass hold-up

V_{slip} slip velocity

Superscripts and Subscripts

$(\cdot)'$ dimensional form

$(\cdot)^c$ contact

$(\cdot)_n, (\cdot)^n$ normal component

$(\cdot)_p, (\cdot)^p$ particle

$(\cdot)_r, (\cdot)^r$ rolling

$(\cdot)_t, (\cdot)^t$ tangential component

$(\cdot)_w, (\cdot)^w$ wall

$(\cdot)_{corr}$ corrected value

1. Introduction

1.1 Background

Natural phenomena such as landslides play a key role in shaping our environment, strongly interacting with human activity. Their destructive power has become increasingly hazardous with significant socio-economic implications. With the combination of increased population pressure in areas of high risk and ongoing climate change, which may increase the likelihood of debris flow and landslide occurrence, effective defences must be developed. Understanding the physics of formation and basic dynamics of debris flow motion will enable better prediction of this hazard and appropriate defences to be put in place.

The present thesis addresses the investigation of debris flows in the context of dry and saturated granular materials moving down slope under the influence of gravity. A great deal of effort has been devoted to the study such flows in the last few decades. However, understanding and modelling of natural fast flowing mass movements are problematic tasks and a full understanding of the multiple mechanisms involved in debris flow behaviour has not yet been reached. The reasons for this are related to their complex nature. At first approximation, they can be classified as suspensions, i.e. mixtures of fluid and grains. However, these mixtures are highly heterogeneous and are characterised by surge formation, solid particles of different size, particle entrainment and segregation, and very high travelling speeds. This means that debris flow rheology cannot be described with a single, simple constitutive model. Indeed debris flows are, in effect, the perfect example of a multi-scale and multi-behavioural phenomenon. This affects every aspect of interest, from the understanding of their internal mechanics to the prediction of their runouts.

Laboratory experiments, numerical simulations and theoretical models are useful tools to elucidate at least part of the mechanics and to provide the basis for development of prediction tools. However, the complex interplay of fluid and the wide range of grain sizes make the replication of such phenomena difficult in experimental and numerical simulations. As it is often the case, complexities are reduced by means of constitutive simplifying approximations. This enables the isolation and study of appropriate mechanics and facilitates the comparison between the results of experiments, numerical simulations

and theoretical predictions. It is also reasonable to believe that, before extending the analyses to more complex natural phenomena, all these approaches should be capable of fully describing first simpler situations and finding agreement.
Experimental investigations still represent the main and fundamental approach to study granular flows. The information obtained can be used to develop and improve existing constitutive models, such as those based on depth-averaged equations for shallow water. They can be used to investigate dry granular flow as well as solid-fluid mixtures through the use of a two-phase system of equations that describe two constituent phases. These models have been used extensively due to their simplicity and still are the basis for models commonly used in the engineering practice for the creation of hazard maps and evaluation of the risk in vulnerable areas. However, this numerical technique is not able to address the complex internal mechanics involved in debris flows. In fact, the heterogeneity in the flow dynamics is one of the main challenges when simple constitutive laws are adopted, sometimes leading to biased predictions.
More recently, numerical techniques based on discrete element methods have become increasingly popular for the study of debris flows. The abstraction of treating the material as a continuum is no longer necessary and the movement of single grains, even in the interior, can be tracked. These methods are still limited to small scale investigation, as the simulation of different particle shapes and the coupling with fluid solvers are still computationally challenging and problematic. However, as progress advances these features are becoming increasingly popular and easier to implement. Despite these current limitations, the application of such methods has produced new and useful insights into the behaviour of debris flows. These have been also supported by recent theoretical works, e.g., those based on the kinetic theory for granular flows, which mostly relies on the results of numerical simulations. This latter approach has been proven useful to account for the collisional mechanics in granular flows. Kinetic theory aims to incorporate microscale particle interactions into a constitutive modelling framework at the macroscale in order to recreate the best possible dynamics involved in both simple granular flows and more complex geophysical flows. However, due to its relatively recent development compared to other theoretical models, this specific theory requires a more exhaustive comparison and assessment against physical and numerical investigations.
Ultimately, understanding the nature of granular flows involves the interaction of the scientific community as a whole. Laboratory modelling, numerical analyses and theoretical works may benefit from a unified approach. A more fundamental and advanced understanding of the many phenomena may be obtained in a clearer and more comprehensive way through the development of a common framework.

1.2 Aim of the research

The research undertaken aims to clarify the behaviour of granular flows, with a particular view to understanding the role of particle interaction in debris flows reproduced in small scale chute geometries. Specific attention is given to the collisional state that develops within the bulk motion and the implications related to the modelling of debris flows. This particular aspect is investigated in dry and saturated conditions, respectively. The analyses of these flows are achieved by means of experimental investigations and, specifically for the dry condition, also with numerical simulations and theoretical modelling. The aims are summarized as follows:

1. Dry conditions:

    - The aim of the experimental work is to reproduce simple dry granular flows in small-scale controlled environments. This is done with the goal of extracting information at the particle level and then determining whether the current non-intrusive measuring techniques commonly used in such investigations are suitable to reliably measure the kinematic properties of granular systems. The main goal is to provide accurate experimental data against which the numerical and theoretical models can later be tested.
    - The aim of the numerical work is to probe an area of the flows that is difficult to study experimentally. Firstly, numerical simulations via discrete element methods are undertaken to study the rheology of dry granular flows in a general element volume only controlled by gravity and the bottom boundary conditions. The information obtained is used to generate synthetic images to test the reliability of the non-intrusive measuring techniques employed in the experiments. Secondly, flows are numerically studied in an inclined chute configuration in order to make possible a direct comparison with the experimental work. The combination of experiments and numerical simulations should be able to provide a complete basis for the comparison with the theoretical approach. The overall goals are to generate simulations that are able to reproduce the mechanics observed in the experiments, provide data that can be tested against the theoretical predictions and draw further conclusions on the mechanisms that govern the granular motions.
    - The aim of the theoretical work is to test the prediction of extended kinetic theory (EKT) for chute flows over a bumpy base. In particular, the objective is to recreate and possibly match the results of experiments and simulations in a chute flow configuration that involves realistic boundary conditions obtained

from the small-scale experiments. The overall goal is to verify the applicability of the theory in different flow configurations, highlight limitations and possible areas of improvement in the dry condition case and provide a framework that can be extended for future works aiming to understand more complex solid-fluid interactions.

2. Saturated conditions:

   - The experimental work performed with solid-fluid mixtures and investigated internally via planar-laser induced fluorescence (PLIF) has three main objectives. The first consists of improving the visualization of monodisperse saturated granular flows made of spherical particles to enable particle tracking. The second objective is to investigate whether the kinematic properties of these flows can be reliably measured and verify if kinetic theory is suitable to describe such flows. The third objective is to increase a step further the complexity involved in the study of granular flows and investigate polydisperse granular flows made of a few but distinctive particle diameters in the attempt to match the typical characteristics found in real debris flows, while keeping a specific attention to the internal visualization of the flows.

1.3 Outline of the thesis

The material in this thesis is presented as follows: Chap. 2 summarizes the main characteristics of debris flows, the fundamental works, the constitutive modelling and experimental investigations devoted to the study of granular flows. Particular attention is given to studies in the framework of kinetic theory. Chap. 3 covers the work done in this thesis to improve the performance of non-intrusive measurement techniques for the measurements of granular flows. Chap. 4 describes the experimental setup, methodology and the analyses relative to the first part of the research conducted experimentally with dry granular flows. In Chap. 5, descriptions and results of dry granular flows investigated via numerical simulations in two different configurations are discussed. Chap. 6 contains a validation exercise conducted with the use of synthetic images to test the validity of the experimental measurements obtained with the imaging techniques used in this thesis. In Chap. 7, the predictions of extended kinetic theory for dry granular flows over a bumpy base are tested against numerical and experimental results. Chap. 8 describes the apparatus, methodology, and the outcomes of the second part of the research conducted with solid-fluid mixtures and an optical technique used to visualize the flow away from later boundaries. Finally, in Chap. 9 conclusions are drawn, and suggestions for future research are given.

2. Literature review

2.1 Introduction

In the framework of this thesis, simple granular flows are studied in order to shed some light into the behaviour of more complex natural debris flows that also contain fluid. Sec. 2.2.1 is devoted to a detailed description of the complex mechanics involved in geophysical flows with particular focus on debris flows. In Sec. 2.2.2), steady shear flows, a simplistic classification of this phenomenon are briefly described together with the principal flow regimes. Such description will allow a better understanding of the applications and limitations of the current constitutive models and theories for granular flows that are later summarized in Sec. 2.3.

Sec. 2.3 outlines the fundamental works and theories devoted to the study of dry granular flows which are most relevant to this thesis. Since they represent the basics for the understanding of these phenomena, an overview is given below and references to these works are given throughout this manuscript. This review starts from one of the earliest works on granular flows by Bagnold [15](Sec. 2.3.1) and progressively builds in complexity, considering models based on shallow-water equations (Sec. 2.3.2) and the μ(I) rheology (Sec. 2.3.3), concluding with the more recent kinetic theory of granular flows (Sec. 2.3.4).

Sec. 2.4 introduces the constitutive models that have developed for the study of simple granular flows and their more complex manifestations such as debris flows. Models that treat the materials as a continuum are described first in Sec. 2.4.1 while the most recent modelling based on a discontinuum approach is described later in Sec. 2.4.2.

Sec. 2.5 surveys several works that have been undertaken to study the physics of granular flows with a specific focus on debris flows. Investigations performed at different scales are presented first (Sec. 2.5.1). This is followed by an introduction to the recent optical investigation technique used in small-scale experiments (Sec. 2.5.2). Finally, a brief summary of several works performed with the scope of obtaining measurements of granular flows in the framework of kinetic theory is presented in Sec. 2.5.3.

2.2 Granular Flows

2.2.1 Geophysical granular flows

Geophysical granular flows generally involve gravity-driven mass movements which occur spontaneously on slopes that exceed a certain angle, when triggered by applied finite perturbations. The descending movement can propagate without an interstitial fluid, as is often the case in rock avalanches, or when the flow is partially or totally saturated. Classical examples are mud and debris flows.
As defined by Sassa [147] the term *landslide* represents the gravitational mass motion of rock, debris or earth down a slope. By this definition, the term contains an ample collection of phenomena which can be mechanically different and need to be investigated by distinct methods. Debris flows are the main focus of this thesis. To understand better these phenomenological events, their classification and a description of their major characteristics is given below.

2.2.1.1 Debris flows

Debris flows are a common type of fast-moving landslide. They are made of materials ranging from very fine silts to large boulders mixed with watery mud. Their consistency can be dense enough to transport rocky boulders and trees. Difficulties in their temporal predictability together with their high velocity, destructive impact forces, and long depositional spread, cause debris flows to be one of the more hazardous landslide types [158]. Worldwide, these mass movements claim hundreds of lives and are very costly in terms of property lost each year.
Most debris flows originate on steep hillsides from an initially unstable mass of sediment as soil slumps or slides. The most common requirements to initiate the motion are rapid saturation of material, failure of the mass and sufficient energy conversion to change the style of motion from sliding to more widespread deformation that can be recognized as flow [78]. During motion, the material liquefies and accelerates to reach a very high velocity. Debris flows flow down slopes, become frequently channelized and are able to deposit their transported solid and organic material onto more gently sloping surfaces. Characteristic of debris flows is the formation of a succession of surges with varied longitudinal flow depths [182]. Each surge can anatomically be described as having a front (or snout) and a tail. Depending on mixture composition, stones and boulders are preferentially transported to the front which is characterized by a reduced water content. Hence the high pore fluid diffusivity results in the bouldery front having a greater frictional resistance to motion than the mixture behind it. This behaviour causes the generation of instability in which large boulders can be pushed aside to form stationary lateral structures, called levees, that

channel the flow allowing the debris flow to gain longer runout distances. Towards the tail, large amounts of suspended fines tend to accumulate. The rear surge interior provides a mobile core which advects some of its downstream momentum into the resistive, coarse-grained snouts, thereby providing the force to drive the snout forward. This interplay is responsible in determining the unsteady, non-uniform character of debris flow motion and plays a key role in the extension of debris flow runout. Debris flows may also erode material when flowing downstream. In some cases the erosion can be very significant and lead to a multiplication of the initial volume. However, the degree of erosion depends strongly on the composition of the debris flow mixture and the presence of erodible material.

2.2.1.2 Pore pressure and grain agitations in debris flows

Field [117] and experimental evidence [115, 116] suggests that pore fluid pressures that are nearly sufficient to cause liquefaction develop and maintain during flow mobilization and acceleration, persist in debris-flow interior during flow deceleration and deposition, and dissipate by sediment consolidation only after deposition. An increase of fluid pressure occurs because the water that fills the pore space is incompressible and it resists particle rearrangement. After rapid loading, the pressure in a column of water extending from the deposit surface to a certain depth is greater than hydrostatic, and can be written as [115]:

$$P_t = P_h + P_* \tag{2.1}$$

where P_t is the total fluid pressure, P_h and P_* are the hydrostatic and the excess, or non-equilibrium, fluid pressures, respectively. Measurements [115, 116] show that a front surge has little or no excess pore fluid pressure, whereas regions behind it have high excess pore pressures. The tail of the surge is normally characterized by an elevated fines content. The portion of fine grains in the moving mass can affect the dissipation of pore fluid pressure in the shear zone and consequently influence the debris motion. In the rapidly descending mass, intergranular contacts are disrupted and poorly established. There, pore fluid can sustain the entire weight of solid particles, thus the mass reaches a liquefied state.

Another important aspect of debris flow mobility is the degree of agitation that persists between the solid grains. This becomes important when the soil deformation rate exceeds the quasi-static limit during which the grains make continuous contacts with one another. This agitation can be quantified by a quantity known as granular temperature. More details are given later in Sec. 2.3.4. For the moment, it suffices to say that the granular temperature represents the ensemble average of grain velocity fluctuations about their mean. The production of granular temperature arises from the grain interactions that can dilate and disperse the mixture as envisioned by the pioneering work of Bagnold [15] [81].

The combined influence of granular temperature and pore pressure on flow resistance appears to control debris mobility [78]. Debris flows are generally triggered by slope failure caused by soil saturation that results from infiltration of precipitation or other sources such as snowmelt. This increases the soil weight and pore pressure to the point that shear strength is unable to maintain equilibrium and the mass begins sliding downslope. After failure, the sliding mass generates both granular temperature and non-hydrostatic fluid pressures. Intergranular friction is reduced by sustained high fluid pressures which in turn influences grain collisions related to the fluctuating grain motions. Granular temperature needs continuous energy exchange to be maintained as energy is dissipated thorough velocity fluctuations generated by the grain interactions and pore fluid flow. Energy is supplied by bulk deformation which derives from interactions with boundary and external forces (Fig. 2.1). Granular temperature may significantly reduce bulk density, enhancing the fluidity of a debris flow and therefore enhancing the ability of the mass to flow. Fluctuating grain motions and pore fluid pressure help keep the sediment dilated in such a way that, in moving debris flows, consolidation does not occur. An increase of solid volumetric requires an attendant reduction of granular temperature and when all kinetic energy degrades to irrecoverable forms, deposition takes place. According to Iverson [78] complete energy degradation occurs first when granular temperature falls to zero in the coarse-grained debris that collects at debris flow fronts and lateral margins. Debris-flow deposition results from grain-contact friction and bed friction concentrated along the flow perimeter, where leading edges of flows exhibit negligible positive pore pressure [116]. The exact role of these mechanisms remains still unclear - further research is needed to understand the relationship between both pore pressure and granular temperature and how these both influence debris flow behaviour.

2.2.1.3 Debris flow classification

Classifications of the main types of debris flow have been proposed based on different concepts: the dominant mechanism in the flow process [15, 78]; the level of saturation or solid concentration [163]. Based on the work of Coussot and Meunier [44], which is drawn by combining measurable parameters such as solid concentration and ratio of silt to clay to total solid concentration, Schatzmann [152] suggests the classification of different flow types and shown in Fig 2.2. In particular, he distinguishes between the following types of debris flows:

Granular debris flows are composed of a large amount of coarse material and a small amount of fine material. The coarse material constitutes the solid phase while the fluid phase is composed of water and very fine grains. That is, in the fluid phase, if the solely viscous resistance of water is able to keep the grains in suspension for a period of time

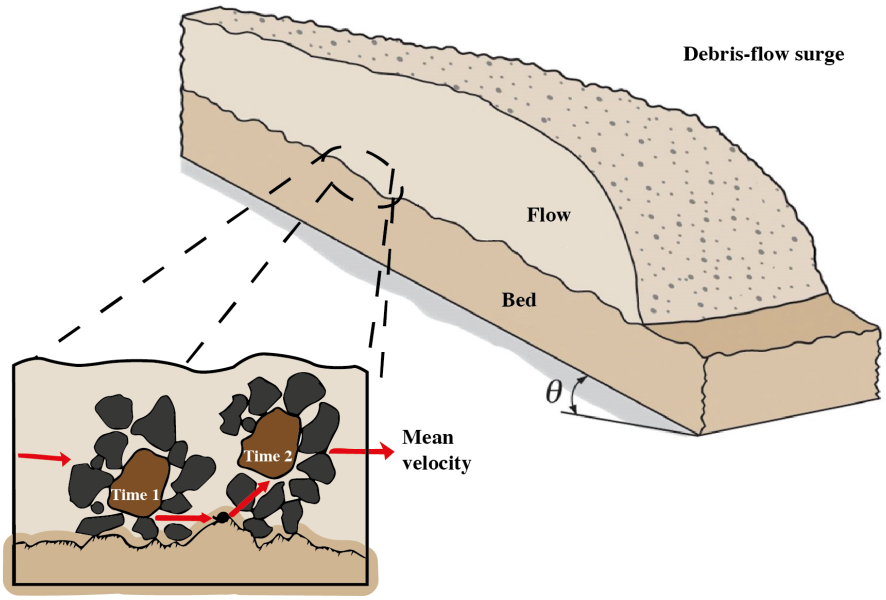

Figure 2.1: Schematic description of the generation of granular temperature by the boundary conditions during the descent of a debris flow at a slope of θ. Adapted from Iverson et al. [81].

comparable or longer than the debris flow duration, these grains may be considered as part of the fluid phase. This typically occurs for grains in the silt-clay size range whereas grains larger than silt size are considered to compose the debris flow solids [78]. Inter-particle collision and inter-granular friction are dominant features within the flow process. Migration of coarse particles toward the front is often observed in this kind of flow.

A *viscous debris flow* is characterized by a high sediment concentration and a content of fine material generally larger than 10%. The material is poorly sorted so that the fine particles can fill the voids between the coarser particles. Collisions between the coarse particles are dampened, making the debris flow appear as one undiversified viscous phase.

Conversely, in a *mudflow* the amount of fine material is predominant, with a small amount of coarse particle in the total mass. Usually the mud phase is indistinguishable to the naked eye. Yet a solid phase can still be distinguished from a fluid phase, which is composed of water and fine sediments. Due to the large amount of fine material, inter-particle friction and especially collisions of the coarse particles play a minor role in the dynamics of the flow.

Viscous-granular debris flows are debris flows exhibiting features common to both the granular and the viscous flows.

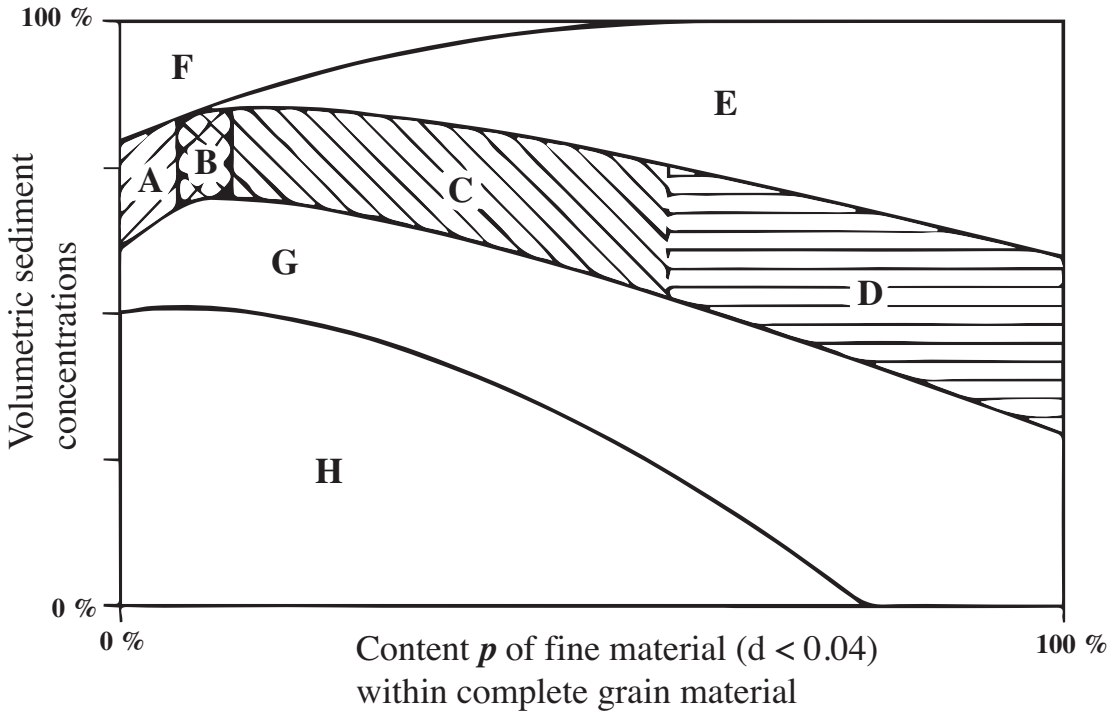

Figure 2.2: Proposed classification by Schatzmann [152]. (A) Granular debris flows; (B) Viscous-granular debris flow; (C) Viscous debris flow; (D) Mud flows; (E) Block type landslide; (F) Rock fall/avalanche; (G) Hyperconcentrated flow; (H) Bed load transport. (E-H) after Coussot and Meunier [44].

2.2.2 Steady, uniform granular flows

The complexity related to the study of natural granular flows is often overcome by simplifying the system under investigation. Typical granular flow experimental configurations are, for example, plane shear [169], rotating drum [74], heap flow [159] and inclined plane [129] where rheological properties of simple shearing flows and can be measured within well-defined boundary conditions. Dry or saturated flows are generally allowed to shear until uniform and steady conditions are reached. In addition, to further simplify the development of models and theories, just one or few particle sizes may be considered. Notably, this means neglecting very important phenomenological behaviours such as particle size segregation. However, the description of a dry, cohesionless flowing granular material still presents a challenge. For example, in a granular flow down an inclined plane, there will be a transition to different states (or regimes), dependent on the stresses, shear rate (the rate of change of velocity across the shear flow) and size of the system. The mechanisms of regime transition have not been fully explored, instead studies have generally focussed

only on one of these regimes. Based on the configuration which is most relevant to this thesis, the inclined chute, these regimes are explained next.

2.2.2.1 Flow regimes

Depending on the mode of deformation, a conglomerate of grains can exhibit different states of matter, i.e., solid, liquid or a gas states. Indeed, these regimes can also develop simultaneously in a single structure. Grains can maintain prolonged stresses and create a stationary heap, flow like a fluid or can produce collisional systems. Figure 2.3 depicts a flow of ball bearings and serves well to represent these three flow regimes. When the shear rate is zero, the dry granular material is in the pseudo-static regime. At some point the material will start to move very slowly and the dynamics will be governed primarily by inter-particle friction. This is known as quasi-static regime; it can be analysed as a series of static states. Momentum is not important to the dynamics of the system. As the shear rate increases, the granular material gradually accelerates, becoming more agitated until it reaches a collisional-dominated rapid flow regime, when momentum transfer occurs between instantaneous particle-particle binary collisions. This may be described by kinetic theory of granular flows (Sec. 2.3.4) following analogies with molecular gases. The regime between the pseudo-static and collisional regime is the dense flow regime, where the solid volume fraction is close to the maximum value attainable. Grain interactions are still partially endured by collisions but a predominant network of contacts evolves through the particles [47].

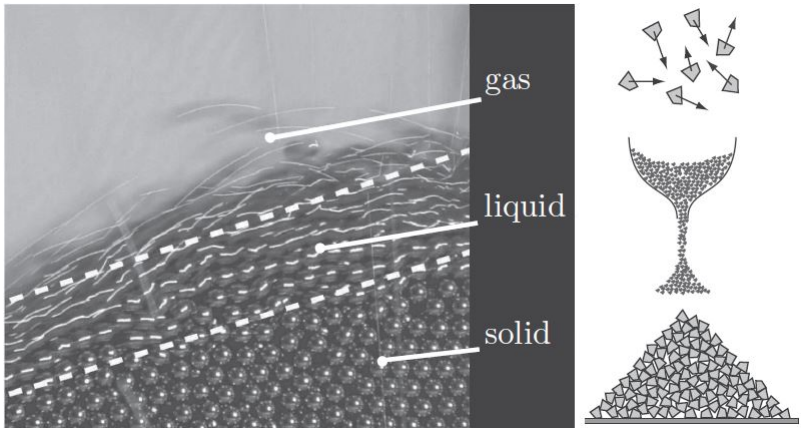

Figure 2.3: Granular flow regimes developing in a flow of ball bearing down an inclined geometry. Adapted from Andreotti et al. [8].

2.3 Mechanics of Granular flows

2.3.1 The work of Bagnold

One the first attempts to formulate a mechanical approach to flowing granular material was the pioneering work carried out by Bagnold [15]. He tried to model a granular material from an individual particles prospective. He performed experiments in a shear cell using a variety of dispersions of wax spheres immersed in an interstitial fluid of water or glycerin-water-alcohol mixture at different solid concentration. To eliminate the gravitationally induced Coulomb friction, he used a buoyant grain-fluid, thus equalizing the density of the fluid to that of the solids. Considering particles having a diameter d and density ρ_p, at a solid concentration ν, in a shear flow of viscosity η_f with shear rate $\dot{\gamma}$, he found that shear stress s and normal stress p vary as a function of these parameters and obey the following scalings:

$$s = f(\nu)\rho_p d^2\dot{\gamma}^2 \tag{2.2}$$

$$p = f(\nu)\rho_p d^2\dot{\gamma}^2 \tag{2.3}$$

Eqs. 2.2 and 2.3 indicate that the stresses should vary according to the velocity gradient or shear rate $\dot{\gamma}$. The simple model was justified by Bagnold in such a way that the first $\dot{\gamma}$ controls the degree at which momentum is exchanged between particles and the second power of $\dot{\gamma}$ represents internal exchange of momentum due to the interparticle collisions [35]. Bagnold also derived a dimensionless number, now known as the *Bagnold number*, which expresses the ratio between inertial stresses induced by particle collisions and viscous stresses induced by the viscosity of the fluid:

$$N_{Bag} = \frac{\lambda_{Bag}^{0.5}\rho_p d^2}{\eta_f}\dot{\gamma}, \tag{2.4}$$

$$\lambda_{Bag}(\nu) = \frac{1}{(\nu_{rcp}/\nu)^{1/3} - 1}. \tag{2.5}$$

In Eq. 2.5, the linear concentration λ_{Bag} reflects the influence of grain concentration on the shear regime. Based on the experimental results, two main regimes were distinguished depending on the value of N_{Bag}. In the *macroviscous regime* ($N_{Bag} \leq 40$), independently of the particle size, the mixture is dominated by fluid viscosity effects. For $N_{Bag} \geq 450$ the flow is dominated by grain inertia and particle-particle interactions whereas the interstitial fluid does not play an important role. This regime is commonly called the *inertial regime*. Velocity profiles for these two regimes are depicted (solid and densely dotted lines, respectively) in Fig. 2.4.

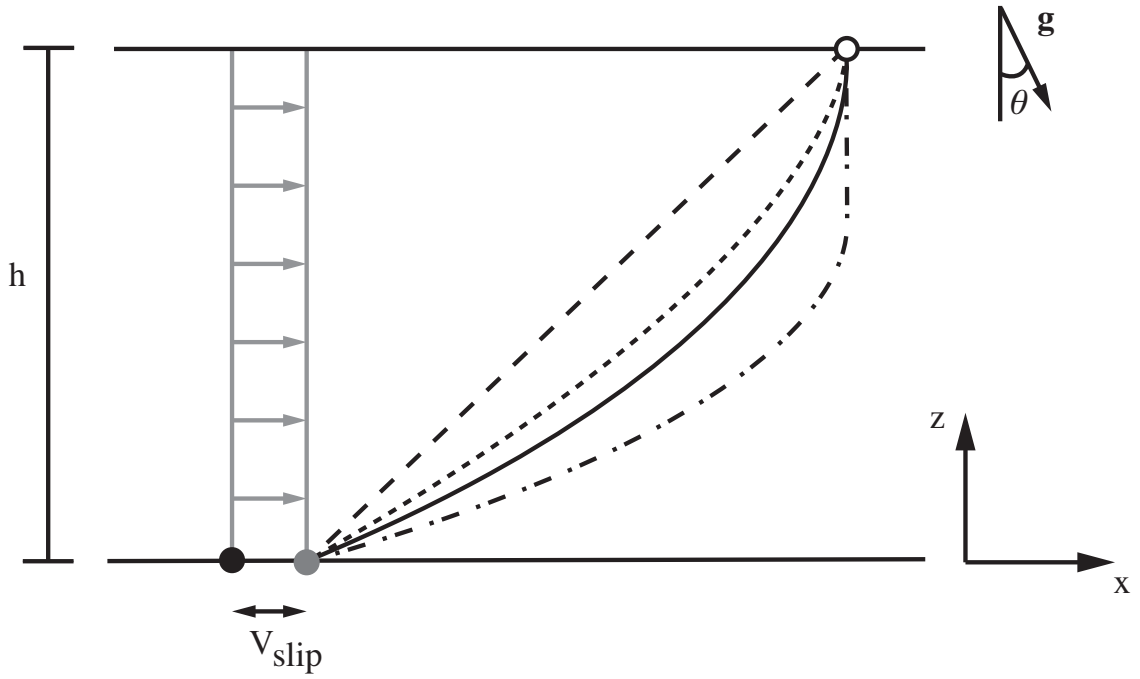

Figure 2.4: Different shapes of velocity profiles: linear approximation (- - -), Bagnold's macro-viscous regime (——), Bagnold's inertial regime (·····) and plug-flow profile (-·-·-). A slip velocity (V_{slip}) may develop when basal sliding occurs. Adapted from Kaitna et al. [96]

2.3.2 The work of Savage et al.

In the context of dry granular material, Savage and Hutter [149] investigated the idealized problem of a finite mass of granular material released from rest and descending a rough inclined plane. The model uses a continuum mechanical theory to describe the flow and does not rely on micro-mechanical parameters. Thanks to its simplicity and physical foundation it has since become popular and is widely used in the study of geophysical granular flows (see also Sec. 2.4). The authors derived depth-averaged equations, similar to the shallow-water equations used in fluid mechanics, which consider horizontal variations (slope parallel) much smaller than the vertical ones (slope normal). By assuming that a typical geophysical flow is much longer than it is deep, the authors were able to develop a model for granular flows down inclines. The shallow-water equations involve integrating the momentum and mass balance equations (similar to eqs. (2.9) and (2.10)) over the flow depth. These provided a set of equations that led to the evolution of transport and geometry profiles, although suitable constitutive assumptions were required. The basal zone was considered the active zone, where the majority of the sliding takes place. Hence, they deemed it sufficient to consider the concentration and velocity profiles to be quite close (or constant) everywhere except at the bed. A basal Coulomb friction law (i.e. the friction force is proportional to the normal pressure, and the frictional coefficient is constant [53]) was then imposed in the model and was assumed that the velocity profile could be resembled to a plug flow (dash-dotted line in Fig. 2.4). With such assumptions, they were only concerned with stresses at the bed rather than the distribution of stress throughout the depth, thus avoiding the need to consider the detailed character of the flow [149]. Indeed, the problems of defining a stress tensor along with a flow rheology were overcome by ignoring the internal stress of the material except at the base. The use of such observations allowed the development of a model able to characterize simple granular flows down inclined geometries.

Many implementations have been developed on the basis of this model, for instance, the recent contribution by Pudasaini et al. [133] to two-dimensional curved and twisted topographies. Its extensions as well as comparison with laboratory experiments have proved it to be largely successful. Indeed, the model is simple to understand, and most importantly, based on physical reasoning and rigorous mathematical foundations.

It is well suited for most granular avalanches but limitations exist. Due to its simplicity, granular avalanches developing along complex geometrical boundaries cannot be well simulated. Furthermore, the presence of various particle sizes and resultant segregation has an important role in the dynamics of natural avalanches. These still remain open problems in implementing the Savage-Hutter model and an adequate answer has not yet been found [53].

Perhaps the weakest assumption of the model was that the moving mass obeys the Mohr-Coulomb yield criterion. Several studies [56, 93, 94] found that the velocity profiles do not always possess a velocity profile resembling a plug flow, indicating that the Coulomb friction model was not always correct. An attempt to incorporate a velocity-dependent friction into the Savege-Hutter model was made by Pouliquen and Forterre [130], whose results agreed well with their experimental observations. This study along with others (with references in the next section) has been the basis for the development of the Inertial number, explained next.

2.3.3 The μ(I) rheology

In Sec. 2.2.2.1 granular flow has been represented in the quasi-static state, subjected to very low deformation, or collisional systems as in the rapid flow regime. In between lies an intermediate granular "liquid" regime where particles remain closely packed and interact by both long-lived contacts and short-lived collisions. A network of contacts and unevenly distributed quasi-linear structures continuously evolve throughout the medium and support the bulk internal stresses. Observations suggest that the stress is shear rate dependent as in a viscous fluid [8], which gives them a viscous-like behaviour. In addition, free surface dense flows can exhibit surface waves similar to those observed in liquids.
The description of this *dense granular flow* regime has given rise to a large amount of work in the past decades. The GDR MiDi [61] gathered experimental results for the most common granular flow configurations. The purpose was to extract the behaviour of the material and identify mutual features such as the effective friction and any flow thresholds. They were able to identify different scales that influence the flow: a macroscopic scale that represents the whole system, a mesoscopic scale (of the order of the particle) which governs the local rearrangement of the grains, and a microscopic scale which involves the deformation of the particles. They pointed out that, on a local scale, the flow is not controlled by the deformation and energy dissipation associated with the inelasticity of the particles. Therefore, the microscopic friction and boundary conditions (especially at the base) have very marginal influence on the larger scale kinematics and only modify the effective frictional coefficient. They proposed a dimensionless parameter, called the *Inertial number*, to describe the importance of particle inertia and confining stresses

$$I = \frac{\dot{\gamma} d}{\sqrt{p/\rho_p}}, \tag{2.6}$$

where $\dot{\gamma}$ is the shear rate, d the particle diameter, p the particle normal pressure and ρ_p the density of the particles. This parameter derives conceptually from the simplest geometry, i.e., plane shear as shown in figure 2.5.
The inertial number can be interpreted as the ratio between two time scales:

- Macroscopic time scale ($1/\dot{\gamma}$): that is, the time taken for a layer of flowing particles to move a distance equal to the grain diameter (Fig. 2.6(a));
- Microscopic time scale ($d/\sqrt{p/\rho_p}$): gives the typical confinement or rearrangement time scale. It can be interpreted as the time required for a particle to fall into a gap of size comparable to the particle diameter under the pressure p (Fig. 2.6(b));

Furthermore, it has been shown through numerical simulations [47], that the shear stress

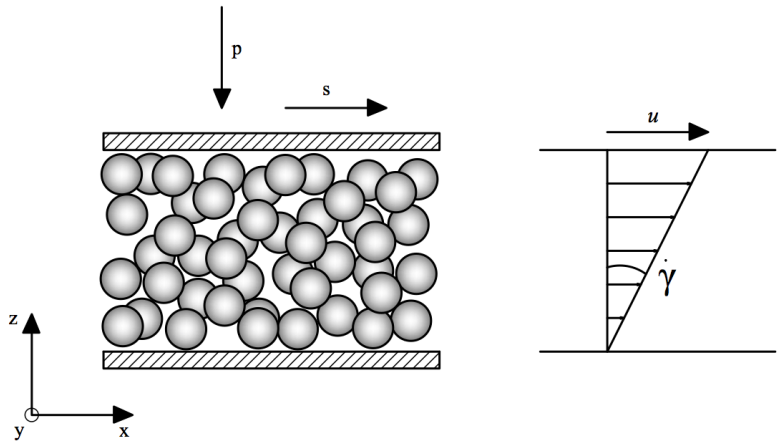

Figure 2.5: Plane shear flow configuration

s and the volumetric particle fraction ν obey the following laws:

$$\frac{s}{p} = \mu(I), \tag{2.7}$$

$$\nu = \nu(I). \tag{2.8}$$

From these two equations it can be argued that the particle friction angle μ and the volume fraction ν should depend on I. Notably, the variation of ν is only applicable within a range of I. For small values of I ($I \leqslant 10^{-2}$) grain inertia is negligible. Here particles are largely in contact with each other. At the other end, a large value of I ($I \geqslant 0.3$) corresponds to a collision-dominated regime. This suggests that, as I increases, the flow will in fact

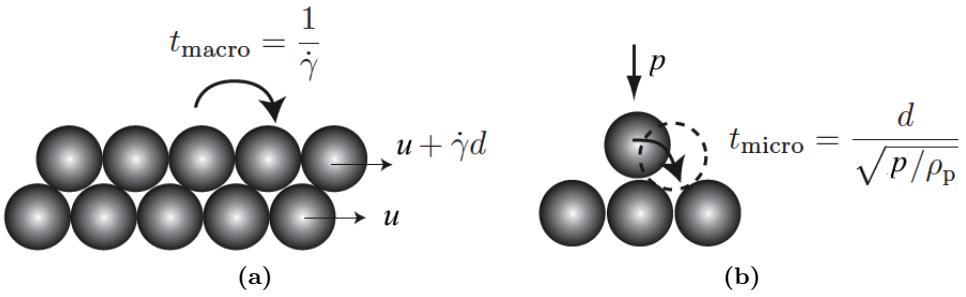

Figure 2.6: Deformation time scales. P is the particle normal pressure. Adapted from Andreotti et al. [8]

become dilute and the reasoning of a constant volume fraction ν will break down.

Under the aforementioned assumptions it is appealing to consider the frictional and dilatancy laws (Eqs. 2.7-2.8) as a constitutive rheology for all dense granular flows. Indeed, the I rheology shows some of its best agreement also with steady, fully developed flows down an inclined plane, but this is respected because the parameters used to fit the friction laws are taken from such experiments. However, stresses developing in inhomogeneous systems may behave differently from the simple plane shear from which the model was derived. It turns out that this rheology is true only locally, where shear stress solely depends on shear rate and pressure. This can be understood by considering the predictions of the local rheology for flows down inclined plane configurations. Firstly, for inclinations where $\tan\theta < \mu$ (θ being the slope angle) no flow is possible. Secondly, for $\tan\theta > \mu$, the fact that the stress ratio s/p is constant implies that the inertial number I and the volume fraction (ν) are constant across the layer. Thirdly, with I being constant, a Bagnold velocity profile (Fig. 2.4) is observed since the shear rate has to vary as the square root of the pressure [56]. Good agreement is found when the predictions of the model are compared with experimental and numerical simulation results. However, this occurs only locally, i.e., away from the flow thresholds (quasi-static and collisional regimes) and within certain angles of inclination. When the slope becomes shallow enough, the whole layer senses the presence of the boundary. In this case, the threshold is also a function of the thickness of the layer. It was shown by Pouliquen [129] that there exists a critical thickness h_{stop} below which no flow is possible. This has repercussions also on the shape of the velocity profile. When $h \sim h_{stop}$ the profile is linear and cannot be predicted by the rheology. This indicates the presence of the quasi-static threshold where there may be non-local effects such as force chains (i.e. quasi-linear structures that support the bulk of the internal stress within the material [35]) and particle correlations. Thus, the local rheology gives poor agreement when approaching thin and slow flows.

For very steep inclinations there is a transition to the collisional regime. Performing experiments on a steep inclined surface Holyoake and McElwaine [73] shed some light on the applicability of the $\mu(I)$ rheology in high-speed granular flows on steep slope (ranging from 30° to 50°). They showed the rheology is inaccurate for large inclinations and for high I ($I \geqslant 0.5$). While flat bottom boundary flows were well-modelled, a bumpy boundary surface generated a number of different regimes previously not observed, along with a central plug region produced away from the sidewalls. It was clear from their study that, down steep slopes and rough beds, the flow became agitated and the mechanics were not only controlled by a friction law, but collisions between particles should also be taken into account. The major drawback of the $\mu(I)$ rheology may concern the assumption of constant volume fraction. Previous studies on flows over inclined planes have shown that ν

is roughly constant [109] which is in agreement with numerical simulation [154]. However, if I increases ($I \geqslant 0.3$), the flow will become diluted and the constant volume fraction assumption will break down. Moreover, the $\mu(I)$ rheology, assuming an homogeneous simple shear flow in a large system (where boundaries have negligible influence), renders the shear rate, normal and shear stresses the only parameters that govern the flow. In making this assumption, one implicitly assumes that the granular temperature does not influence the dynamics, and therefore the local generation of the kinetic agitations balances the dissipation.

2.3.4 Kinetic theory of granular flows

As discussed in Sec. 2.2.2.1, there exists a regime characterized by a collisional medium where grains are far from one another and uncorrelated collisions characterize the flow. Theoretical understanding of these dilute granular flows began in the late 1970's [124] based upon analogies with the kinetic theory of gases. Assuming that a gas is in a continuous state of relentlessness, molecules are small, hard, elastic spheres acting on each other during collisions. It is assumed that molecules oscillate about their mean value in a very chaotic and isotropic manner. On the other hand, if we consider rapidly deforming, relatively dense granular materials, the transfer of momentum is chiefly carried by forces in collisions between pairs of neighbouring particles. Interparticle contacts are momentary, and it is usual to consider interactions as instantaneous collisions. Analogous to molecular kinetic energy, the granular temperature is introduced, a variable of the system reminiscent of the thermodynamic temperature of a gas. This quantity measures the strength of particle velocity fluctuations and represents the degree of agitation of the system [169].
Despite the parallel, dissimilarities between the kinetic theory of gases and of granular flows lie behind the fact that grain collisions are typically inelastic. The inelasticity implies loss of energy on contacts in the form of heat to the grains, plastic deformation, attrition, and particle break up. Hence, in order to maintain the flow as fluidized, energy must be added into the random components of velocity to balance the losses caused by the dissipative collisions.
Following a statistical approach, kinetic theory deals with the probability distribution functions describing the state of a granular gas [9]. The reason for this is that a complete description of the random motion of many particles in a granular gas is actually problematic. A fully deterministic approach based on classic Newtonian mechanics is, in principle, applicable. Unfortunately, the large number of degrees of freedom associated with the particle motion and uncertainty in the knowledge of the exact initial velocity and position of each particle prevents that approach from being adopted. Hence, a statistical approach is preferred. One of the main approaches for statistical mechanics was established by Boltzmann [28] when trying to describe the random motion of molecules in a gas. Similar Boltzmann equations can be derived for a dilute gas of inelastic particles where collisions are dominant. However, they are restrictive and several assumptions are introduced in order to reduce the level of complexity and close a series of balance equations. These assumptions are the following:

(I) particles are spherical;

(II) particles are identical, i.e., the system is monodisperse;

(III) particles are frictionless;

(IV) coefficient of restitution is constant;

(V) collisions are nearly instantaneous (i.e., the time spent during the encounter is much shorter than the mean interval between two successive collisions);

(VI) collisions are binary, i.e., only pairs of particles are involved;

(VII) the system is dilute;

(VIII) velocities of the colliding particles are uncorrelated, i.e. use the molecular chaos assumption;

From the kinetic theory derived from the Boltzmann equations, macroscopic state parameters of the continuum medium, density ρ, velocity $\mathbf{u}$ and granular temperature T, are defined as functions of the moments of the single-particle distribution functions f_s (i.e., the probability of finding particles with velocity $\mathbf{v}$ at point $\mathbf{x}$ at a specific moment in time t). Then, by appropriate manipulation of the time evolution equation of this distribution, the macroscopic hydrodynamic balance equations of motion can be derived. The closure of these balance equations requires additional constitutive equations for the stress tensor ($\mathbf{T}$), energy flux ($\mathbf{Q}$) and rate of energy dissipation (Γ). The rigorous solution for $\mathbf{T}$, $\mathbf{Q}$ and Γ has been proposed independently by Chapman (Chapman [39, 40]) and Enskog ([51]) in 1916-1917 and is known as Chapman-Enskog (CE) expansion. The entire procedure is a lengthy mathematical process which is not described here (a rigorous and formally correct description can be found in [41]) . Instead, a simplified derivation of the balance equations and the other additional constitutive equations for the closure are given here first, based on a very dilute granular gas [22]. The intent is only to provide a simple, albeit somewhat crude way to understand the physics behind their derivations.

2.3.4.1 Hydrodynamic equations of motion

Macroscopic fields for granular gases, such as the velocity $\mathbf{u}$, the mass density ρ and the granular temperature T can be defined as for the case of molecular gases. First of all, using fluid mechanics principles, the motion of a fluid (and a granular flow can be considered as such) can be described in terms of balance of mass and momentum:

$$\frac{\partial \rho}{\partial t} + \nabla \cdot (\rho \mathbf{u}) = 0 \tag{2.9}$$

$$\frac{\partial (\rho \mathbf{u})}{\partial t} + \nabla \cdot (\rho \mathbf{u} \otimes \mathbf{u}) = \rho \mathbf{g} - \nabla \mathbf{T} \tag{2.10}$$

where $\mathbf{g}$ is the external force due to gravity per unit volume and $\mathbf{T}$ is the stress tensor. The bulk density ρ (i.e. $\rho = \rho_p \cdot \nu$) and velocity $\mathbf{u}$ represent the hydrodynamic fields (functions

of time and spatial position), i.e., the unknowns of our problem. These two quantities can be solved for specific initial and boundary conditions once the external force (generally the gravitational force $\mathbf{g}$) and the stress tensor, in terms of the hydrodynamic fields, are defined. For a Newtonian fluid, the stress tensor reads:

$$\mathbf{T} = \left(p + \frac{2}{3}\eta_m \nabla \cdot \mathbf{u}\right)\mathbf{I} - 2\eta_m \mathbf{D} \tag{2.11}$$

where p is the pressure, η_m the (molecular) viscosity, $\mathbf{I}$ the identity matrix and $\mathbf{D}$ the strain rate tensor. Both p and η_m can be simply derived from kinetic theory for a very dilute gas as demonstrated next.

2.3.4.2 Granular pressure

The concept and the importance of granular pressure can be understood by considering an assembly of identical spheres of mass m and diameter d (and particle density $\rho_p = 6m/(\pi d^3)$) moving randomly with velocity $\mathbf{v}$ in a 3D domain in absence of external forces with no preferential direction. Therefore, the velocity of the particles is expected to be zero on average. In other words, the mean hydrodynamic velocity field $\mathbf{u} = \langle \mathbf{v} \rangle = 0$ everywhere, where $\langle \cdot \rangle$ represents the averaging of a generic quantity. In this particular case, the fluctuation velocity $\mathbf{C} = \mathbf{v} - \mathbf{u}$ coincides with the particle velocity $\mathbf{v}$.

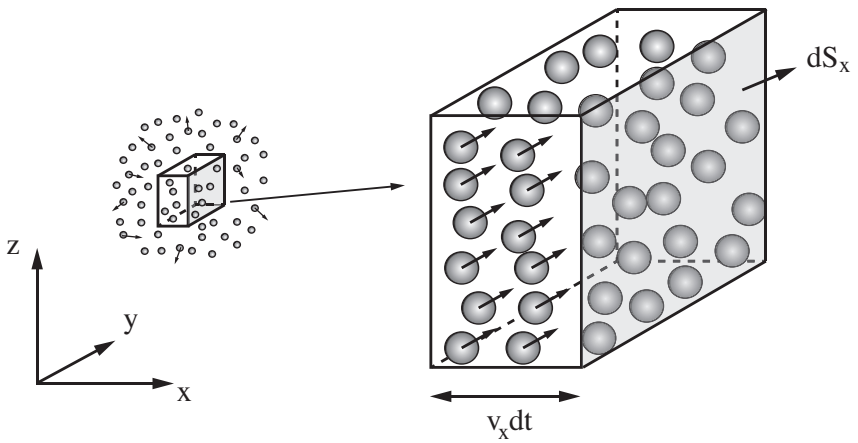

Figure 2.7: Physical origin of granular pressure.

Now, if a small reference surface dS_x perpendicular to the x-direction in a generic rectangular frame of reference (Fig. 2.7) is considered, the average amount of x-momentum that the number N of particles crossing the surface (dS_x) in the time interval dt carry

with them can be calculated as $\langle Nmv_x \rangle$. The particles that can cross the surface dS_x in the time interval dt are only those present in the cylinder of volume $dS_x v_x dt$. Introducing the number density n, i.e., the number of particles per unit volume, one obtains:

$$\langle NmV_x \rangle = \langle mnv_x dS_x v_x dt \rangle = mn\langle v_x^2 \rangle dS_x dt = \rho \langle v_x^2 \rangle dS_x dt \tag{2.12}$$

The flux of x-momentum across dS_x per unit time is the normal force exerted by the particles on the surface. Dividing Eq. 2.12 by $dS_x dt$ allows the normal stress along x, i.e., the element p_{xx} of the stress tensor to be obtained:

$$p_{xx} = \rho \langle v_x^2 \rangle, \tag{2.13}$$

Analogously:

$$p_{yy} = \rho \langle v_y^2 \rangle \quad \text{and} \quad p_{zz} = \rho \langle v_z^2 \rangle. \tag{2.14}$$

Now, the granular pressure p can be defined as the isotropic component of the normal stresses, i.e., one third of the trace of the stress tensor, so that:

$$p = \frac{1}{3}(p_{xx} + p_{yy} + p_{zz}) = \rho \frac{1}{3} \langle v_x^2 + v_y^2 + v_z^2 \rangle. \tag{2.15}$$

The granular temperature T is now introduced:

$$T = \frac{1}{3} \langle v_x^2 + v_y^2 + v_z^2 \rangle, \tag{2.16}$$

which is a measure of the strength of the particle velocity fluctuations (the analogue of the thermodynamic temperature which is a measure of the strength of the velocity fluctuations of the molecules). With this, Eq. 2.15 becomes:

$$p = \rho T \tag{2.17}$$

which represents the equation of state of a granular gas. Effectively, Eq. 2.17 represents only the contribution to the pressure due to the transport of momentum by the particles that cross a surface (streaming contribution), ignoring the possibility that momentum can be exchanged across the surface through collisions (collisional contribution). The latter becomes important when the number density increases beyond a certain value. Eq. 2.17 is therefore the actual equation of state of a dilute granular gas, i.e., in the limit $\nu \longrightarrow 0$.

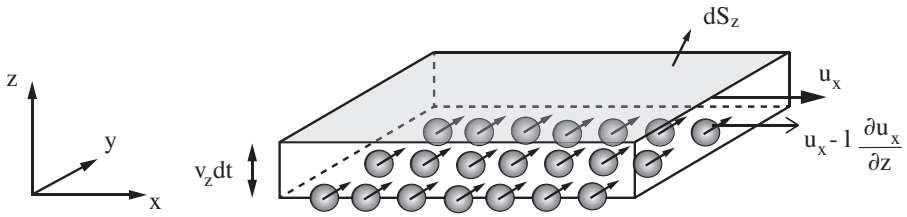

Figure 2.8: Definition sketch of granular viscosity.

2.3.4.3 Granular viscosity

The case in which the mean velocity field **u** has a non-zero component only in one direction, for instance the x-direction (Fig. 2.8), is now considered. Again, taking a small surface dS_z parallel to the x-direction, the average amount of x-momentum that the particles crossing the surface in the time interval dt carry with them can be calculated. This is done by imagining that the number N of such particles are, on average, at a small distance l from the surface dS_z, with an x-component of mean velocity equal to $u_x l \partial u_x/\partial z$ (u_x is the x-component of the mean velocity at the surface dS_z). The particles coming from below are those present in the volume $dS_z v_z dt$ (along the z-direction the particle velocity is just the fluctuation velocity), so that $N = n v_z dS_z dt$. Hence, the average net amount of x-momentum carried by the particles crossing the surface dS_z in the time interval dt from below is:

$$\left\langle Nm\left(u_x - l\frac{\partial u_x}{\partial z} - u_x\right)\right\rangle = -mn\langle l v_z\rangle \frac{\partial u_x}{\partial z} dS_z dt \tag{2.18}$$

The quantity $m(u_x - l\partial u_x/\partial z)$ provides the momentum of the particles at $u_x - l\partial u_x/\partial z$ when they meet particles with u_x and thus with different momentum. Dividing it by $dS_z dt$ the shear stress p_{zx} is obtained. Using $\rho = mn$ and assuming that l is of order of one diameter and v_z is of order $T^{1/2}$ (from the definition of the granular temperature, Eq. 2.15), one gets:

$$p_{zx} \propto -p d T^{1/2} \frac{\partial u_x}{\partial z}. \tag{2.19}$$

The quantity $\partial u_x/\partial z$ represents the shear rate. The coefficient of proportionality of the shear stress with the shear rate is the viscosity η_m. For a dilute granular gas (again neglecting the collisional contribution to the stresses also in this case) the granular viscosity is therefore:

$$\eta_m \propto -p d T^{1/2}. \tag{2.20}$$

The granular viscosity (Eq. 2.20), which is the transport coefficient of momentum diffusion, and the granular pressure (Eq. 2.15), can be inserted into Eq. 2.11 to obtain the constitutive expression of the stress tensor for a dilute granular gas. Note that, for a granular gas, the granular temperature T represents an additional hydrodynamic field that needs to be determined in addition to ρ and $\mathbf{u}$.

2.3.4.4 Balance of fluctuating energy

In order to close the problem, an additional balance for the granular temperature is needed. From the first principle of thermodynamics for a molecular fluid, which states that the internal energy is equal to the difference of heat transfer into a system and the work done by the system:

$$\frac{\partial \mathcal{E}}{\partial t} + \nabla \cdot (\mathcal{E}\mathbf{u}) = -\mathbf{T} : \mathbf{D} - \nabla \cdot \mathbf{Q}, \tag{2.21}$$

where $\mathcal{E}$ is the internal true thermal energy (i.e., the kinetic energy associated with the fluctuating velocities of the molecules) per unit volume and $\mathbf{Q}$ is the energy flux per unit time and unit area. The double dot product of the stress tensor $\mathbf{T}$ with the strain rate tensor $\mathbf{D}$ represents the energy production due to the internal stresses. In the case of a granular gas, the first principle of thermodynamics must be modified:

$$\frac{\partial \mathcal{E}}{\partial t} + \nabla \cdot (\mathcal{E}\mathbf{u}) = -\mathbf{T} : \mathbf{D} - \nabla \cdot \mathbf{Q} - \Gamma, \tag{2.22}$$

because $\mathcal{E}$, now called pseudo-thermal energy per unit volume, is not conserved due to the inelasticity of collisions. In Eq. 2.22, Γ is a sink term that represents the rate of collisional dissipation of $\mathcal{E}$. This term represents the kinetic energy per unit volume associated with the particle velocity fluctuations. It can be calculated given the definition of the granular temperature (Eq. 2.16) as:

$$\mathcal{E} = n\frac{1}{2}m\langle v_x^2 + v_y^2 + v_z^2 \rangle = \frac{3}{2}\rho T. \tag{2.23}$$

Then, inserting Eq. 2.23 into Eq. 2.22 gives:

$$\frac{3}{2}\frac{\partial(\rho T)}{\partial t} + \frac{3}{2}\nabla \cdot (\rho T \mathbf{u}) = -\mathbf{T} : \mathbf{D} - \nabla \cdot \mathbf{Q} - \Gamma \tag{2.24}$$

The constitutive relations for the energy flux $\mathbf{Q}$ and the dissipation Γ in terms of the hydrodynamic fields ρ, $\mathbf{u}$ and T (constitutive relations) can be simply derived again considering a dilute granular gas as explained next.

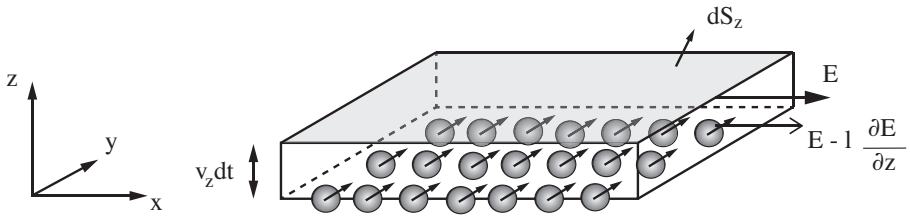

Figure 2.9: Definition of granular conductivity.

2.3.4.5 Conductivity

In Fig. 2.9, the case in which the mean velocity field **u** has a non-zero component only in one direction, for instance the x-direction, is considered. If a small surface dS_z parallel to the x-direction is taken, the average amount of fluctuating energy that the particles carry when crossing the surface in the time interval dt can be calculated. The number N of particles coming from below are, on average, at a small distance l from the surface dS_z with a fluctuating energy equal to $E - l\partial E/\partial z$, where $E = \frac{3}{2}mT$ is the fluctuating energy at the surface dS_z. The particles coming from below are those present in the volume $dS_z V_z dt$ (along the z-direction the particle velocity is just the fluctuation velocity), so that $N = nv_z dS_z dt$. Hence, the average net amount of fluctuating energy carried by the particles crossing the surface dS_z in the time interval dt is:

$$\left\langle N\left(E - l\frac{\partial E}{\partial z} - E\right)\right\rangle = -n\langle l v_z\rangle \frac{\partial E}{\partial z} dS_z dt \tag{2.25}$$

By dividing Eq. 2.25 by $dS_z dt$ it is possible to obtain the z-component of the energy flux Q_z (which changes when T varies over time) . Using the definition of E, with $\rho = mn$, and assuming that l is of order one diameter and v_z is of order $T^{1/2}$, one gets

$$Q_z \propto -\rho d T^{1/2}\frac{\partial T}{\partial z}. \tag{2.26}$$

The coefficient of proportionality of the energy flux with the gradient of the temperature is the conductivity λ (the transport coefficient of conduction of fluctuating energy). For a dilute granular gas it can be obtained

$$\lambda \propto \rho d T^{1/2}. \tag{2.27}$$

Notably, in the general case, the energy flux vector must be

$$\mathbf{Q} = -\lambda \nabla T. \tag{2.28}$$

In vector form, the direction of $\mathbf{Q}$ is from large values of T to small values of T.

2.3.4.6 Rate of collisional dissipation

Once more, the case of an assembly of particles having mean velocity $\mathbf{u}$ equal to zero is considered. Then, the particle velocity coincides with the fluctuating velocity, whose absolute value is, on average, proportional to $T^{1/2}$ from the definition of the granular temperature. If a certain volume W that contains N particles is taken, the total number of collisions occurring in that volume in the time interval dt is proportional to N^2, given that each of the N particles can have a binary collision with each of the remaining $N-1$ particles. The time interval dt is bounded by the average time that a particle takes to cross the domain, i.e., $W^{1/3}/T^{1/2}$. Each particle loses a fraction proportional to $(1-e_n^2)$ of the kinetic energy associated with the relative motion during one collision [111]. The normal coefficient of restitution e_n is the negative of the ratio between the pre- and post-collisional normal relative velocity between two colliding spheres. When $e_n = 1$ the collision is perfectly elastic (this is the case for a molecular gas); for $0 \leq e_n < 1$ the collision is inelastic (for granular gases). It is also assumed that the absolute value of the normal relative velocity between two colliding spheres is roughly equal to the absolute value of the fluctuating velocity, proportional to $T^{1/2}$. Hence, the energy lost per collision is proportional to $(1-e_n^2)mT$. The total energy lost in the volume per unit volume and unit time, i.e., the rate of collisional dissipation Γ is:

$$\Gamma \propto \frac{(1-e_n^2)N^2mT}{Wdt} = \frac{(1-e_n^2)N^2mT}{WW^{1/3}/T^{1/2}} = (1-e_n^2)mn^2W^{2/3}T^{3/2}. \tag{2.29}$$

With $\rho = mn$, $n = 6\rho/(\pi\rho_p d^3)$ and taking $W \propto d^3$, Eq. 2.29 reduces to:

$$\Gamma \propto (1-e_n^2)\frac{\rho^2}{\rho_p}\frac{T^{3/2}}{d}, \tag{2.30}$$

which represents the constitutive relation for the rate of collisional dissipation in a dilute granular gas.

2.3.4.7 Classic kinetic theory

While the first derivation of kinetic theory from the Boltzmann equations are limited to very dilute systems, those obtained by using the Enskog equations [51] extend the kinetic theory to higher density gases. The particles are not treated as point-like, instead they have non-negligible volume, which restricts the degrees of freedom, and, as a consequence, the possibilities of motion. They also take account of hysteresis effects since, in principle, the correlation of two colliding particles may be caused by their previous interactions occurring elsewhere in the system. These types of correlation behaviours become relevant when the concentration increases to a limit where particles are moderately or highly densely packed. When these equations are used, two classes of kinetic theory are possible: the Standard Enskog Theory (SET) and the Revised Enskog Theory (RET) [169]. The difference lies in the treatment of interacting particles. That is, the likelihood that, at time t, spheres with velocities near $\mathbf{v}_1$ and $\mathbf{v}_2$ are located in the vicinity of $\mathbf{x}_1$ and $\mathbf{x}_2$, respectively. This is also known as the pair distribution function, f_p. While in the SET f_p depends only on the local value of the volume concentration ν, in the RET this dependence is extended also to the gradient of ν. In the particular case of the RET, the radial distribution function g_0 appears in the definition of f_p. g_0 is a function of the volume fraction ν and takes into account two effects that are present when the particles have a non-negligible volume: the increased probability of having collisions due to excluded volume brought about by finite-size particles (i.e., less free space is available), and the decreased probability of having collisions due to shielding, i.e., binary encounters screened by other particles present along the colliding paths [167]. As for the kinetic theory derived from the Boltzmann equations, the additional constitutive relations are obtained using the Chapman-Enskog (CE) method in order to arrive at a solution for the evolution of the macroscopic variables of interest (ρ, $\mathbf{u}$ and T). Several classic (or standard) kinetic theories have been proposed in the literature. A summary and classification of several works based on kinetic theory can be found in Garzó et al. [60].

2.3.4.8 Breaking of the assumptions

So far the discussion has been focussed on rather dilute granular gas. If we are interested in particle flows of practical importance, gravity typically works to collapse flows into a dense regime. There are some important applications of flows with concentration in the range of $0 < \nu < 0.5$, but denser flows are most common.

Kinetic theory is based on the molecular chaos assumption which is most likely to hold at very low particle concentrations. However, it ceases to be valid at higher volume fraction, as shown through numerical simulations [102, 119, 120]. In particular, Mitarai and Nakanishi [120] numerically tested the predictions of classic kinetic theory under

uniform shear of frictionless particles in a rectangular periodic cell. Their results showed that for different values of the coefficient of restitution, the collisional dissipation rate Γ was poorly predicted when the concentration $\nu \gtrsim 0.4$.

The reason is due to the failure of one of the kinetic theory assumptions. Mitarai and Nakanishi [120] showed that, if the velocity distribution function for a single particle is computed, it will resemble a Maxwellian distribution. However, this is only true for every value of the volume fraction up to a value of $\simeq 0.49$ (for identical, rigid spheres in three dimensions this also called the freezing point [167], i.e., the lowest value for which a first order transition to an ordered (crystalline) state is possible). After this limit the distribution of the relative velocity between two particles is no longer Maxwellian. This means granular temperature is no longer a good measure of the collisions (or strength of the fluctuation velocity) because the particles can fluctuate together, hence introducing a certain degree of correlation.

Mitarai and Nakanishi [120] suggested that the rate of collisional dissipation Γ as defined by the classical kinetic theory should be modified as a possible way to extend its validity to dense flows, e.g., when $\nu \gtrapprox 0.49$.

2.3.4.9 Extended kinetic theory

Granular systems can exhibit sources of multistability such as clustering, and microstructures. Clusters, in particular, are characterized as stationary objects with low granular temperature, and once created they can be very long-lived entities unless they interact with other clusters in the flow. To take account of multistabilities and the overestimation of the dissipation rate due to the possible presence of correlated motion, Jenkins [83, 84] suggested to use a correlated length L in the denominator of the dissipation rate (Eq. 2.30) which differs from the single particle diameter d. L represents the typical size of the region of correlated particles and, in case of plane shear flows, its expression reads

$$L = \max\left(1, f_0 \frac{d}{T^{1/2}}\dot{\gamma}\right) d. \tag{2.31}$$

The term f_0 varies as a function of the solid volumetric concentration (ν) and other particle properties. On the basis of experimental and numerical simulations on inclined granular flows and shearing flows, different formulations of f_0 have been proposed [169]. The first expression of this term was proposed by Jenkins [83, 84] , where a constant value with poorly defined physical meaning was used, although recently Berzi [17] proposed a more robust expression for f_0 based on known physical particle properties and derived from previous numerical simulations of shear flows conducted by Mitarai and Nakanishi [120]. The kinetic theory modified by the addition of the correlation length has been dubbed

Extend Kinetic Theory (EKT). When L is equal to one diameter, the molecular chaos assumption is valid and EKT reduces to classic kinetic theory.

2.3.4.10 Frictional particles

One of the main assumptions of the classic kinetic theory is that the particles are frictionless. However, except for very special cases, real particles are frictional. In this case, the first important consequence is that the collisions are characterized by an impulse having normal and tangential components [89] leading to forces in the tangential direction and grain rotations. To take this effect into account, more constitutive relations have to be derived and introduced into kinetic theory. To do this, it is necessary to solve the balance of angular momentum and the balance of fluctuating energy associated with the rotational degrees of freedom, which involves consideration of the rotational granular temperature.
To tackle this problem there are essentially two approaches. A first rigorous one introduces an additional equation to the hydrodynamic equations in order to take into account the rotational degrees of freedom. However, this approach is very onerous from a computational point of view. A much simpler approach is the possibility to define an effective coefficient of restitution ϵ, as a function of the normal and tangential coefficients of restitution (e_n and e_t), and the interparticle friction coefficient (μ). The idea is that transforming linear momentum into angular momentum (i.e., translational granular temperature into rotational granular temperature) can be seen as an additional dissipation mechanism. Hence, a renormalized restitution coefficient may be theoretically used to absorb the effect of the tangential contact in collisions. This approach was first suggested and derived by Jenkins and Zhang [89] in the case of slightly frictional particles ($0 < \mu \lesssim 0.2$). Based on the same principles, this second approach has been recently revised and improved by Chialvo and Sundaresan [43].
The second consequence is that the friction coefficient μ affects the maximum value of the random close packing $\nu_{rcp} \approx 0.64$ (the maximum volume fraction achievable by disordered aggregates of rigid frictionless spheres in static conditions [167]) and the value at which the radial distribution function g_0 diverges. It is assumed that the divergence is reached when a critical value ν_s is approached. This is also referred to as the "shear rigidity concentration" [169], i.e., the mean interparticle distance is zero along the principal compression axis, so that random aggregates of rigid particles develop a shear rigidity. The concentration ν_s represents the densest possible packing for a disordered collection of identical frictional spheres. However, in monodisperse dry granular flows, the value is directly affected by the particle friction: ν_s corresponds to the random close packing when $\mu = 0$ (i.e. for frictionless particles), whereas when $\mu > 0$ the shear rigidity concentration ν_s is a decreasing function of μ. Estimations of this variable were obtained through nu-

merical simulations based on the varying value of μ. They can be found, e.g., in Chialvo et al. [42] and Silbert [153] but are also reported in Table 2.1. Conversely, in monodisperse saturated granular flow, the value of ν_s should not only take account for friction effects but also others, e.g., adhesion forces and lubrication in the particle-particle interaction zone. For this specific case, not systematic studies have been performed to extract the actual value of ν_s and should be considered in future research. Ultimately, for any kinetic theory dealing with frictional particles the value ν_s should be used instead of ν_{rcp}.

Table 2.1: Value of random close packing for different friction coefficient μ for 3D monodisperse spheres and 2D disks. Adapted from Silbert [153]

μ	0	0.001	0.01	0.1	0.2	0.5	1	10
ν_s^{2D}	0.843	0.843	0.842	0.836	0.827	0.801	0.779	0.767
ν_s^{3D}	0.639	0.638	0.634	0.614	0.595	0.574	0.556	0.544

2.3.5 The current state of kinetic theory

The application of kinetic theory to granular flows includes a series of problems, for example, the lack of scale separation [63] (i.e., the scale of spatial variation of variables has the same order of magnitude as the particle size [12]) and particle correlation motion. Indeed, a non-trivial key feature is the binary and instantaneous interaction of particles upon contact, which effectively limits the application of the classic theory to low volume fractions. This typically occurs for very rapid granular flows, but unfortunately most flows of practical interest are found in the intermediate regime where the mechanics are not only controlled by particle collisions but also by frictional contacts.

In Fig. 2.10 a comparison between different kinetic theories in terms of ratio of shear stress to pressure ($\mathrm{s/p} = \tan\theta$) versus solid volume fraction ν is shown. The classic kinetic theory [59] (dashed line) assumes that molecular chaos holds for every value of volume fraction. Because of this, the granular temperature is overestimated at volume fractions larger than $\approx$0.49, and the stress ratio slightly increases when the volume fraction increases. This is unphysical since, contrary to what is observed in simple inclined chute flows (i.e., on gentler slope the flow is generally denser), the result would imply that the volume fraction would decrease when the angle of inclination decreases.

Developing an understanding of densely packed systems and the role of the particle microproperties (e.g. friction) has led to the improvement of the theory, later dubbed extended kinetic theory (EKT), which is able to deal with such regime. Indeed, assumptions of classic kinetic theories, namely, frictionless particles (III), dilute systems (VII), and the

molecular chaos assumption (VIII), can be overcome, respectively, by deriving the theory from the Enskog Theory which can then be applied even to moderately dense systems, introducing an effective coefficient of restitution and accounting for the correlated motion of particles through a correlation length. In particular, the introduction of this characteristic length scale effectively extended kinetic theory [17, 85] to dense flows by considering that the particle motion is correlated. With this, the theory (dashed dotted line in Fig. 2.10) predicts that the stress ratio decreases at the freezing point, implying an inverse proportionality between particle concentration and slope angle beyond this threshold.
More recently, it has been shown [24] that a theoretical value of yield stress ratio can be predicted in the context of EKT (solid line). In principle, this yielding point allows a transition to be defined between a regime where the stresses are rate-independent (quasi-static regime in Fig. 2.10) and another where they are rate-dependent (collisional regime). In the context of granular flows down inclines, this becomes useful to characterize materials flowing over erodible beds [87].

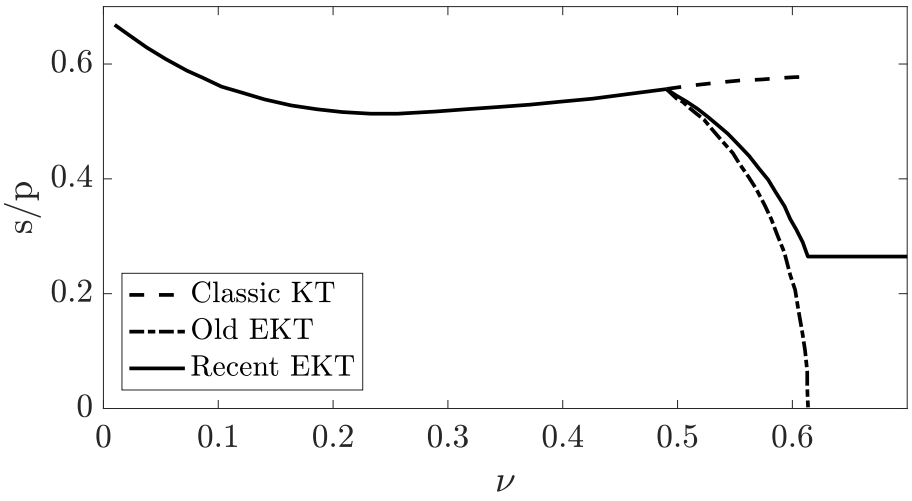

Figure 2.10: Stress ratio versus solid volume fraction as predicted by the classical kinetic theory (- - -), its extension that takes into account correlated motion (-·-·-) and a further modification that defines a yield stress ratio (——). For $\nu < 0.49$ all theories predict the same behaviour. Data courtesy of Diego Berzi (personal communication).

2.3.6 State of the art of kinetic theory for inclined chute flows

In the present thesis simple, dry granular flows are investigated numerically and experimentally on an inclined flow configuration and their results are tested against the predictions of kinetic theory. The comparison is made against the extended kinetic theory for inclined chute flows, as explained next. This includes the concepts of particle interaction and correlation motion in dense granular flows and the most recent derivation of boundary conditions. The Matlab implementation of the following extended kinetic theory can be found in `http://intranet.dica.polimi.it/people/berzi-diego/`.

In what follows, it is assumed that all quantities are averaged along the spanwise direction, with no change in notation for simplicity. Derivatives with respect to the z-direction are indicated with a prime. The spanwise averaged momentum balances along the z and x directions for steady and fully-developed inclined flows in the presence of sidewalls reduce to [85]:

$$p' = -\rho_p \nu g \cos\theta, \tag{2.32}$$

and

$$s' = -\rho_p \nu g \sin\theta + 2\frac{\mu_w}{l_y} p, \tag{2.33}$$

respectively, where s is the shear stress and μ_w is an effective wall friction coefficient, which accounts for the average force exerted by the sidewalls on the flow [93]. The expression for the sidewall force is just an approximation given that all particle-wall contacts are taken to be sliding and gradients in the velocity along the spanwise direction are ignored. In Eqs. (2.32) and (2.33), it is assumed that the normal stresses are isotropic and coincide with the pressure, although this is not strictly true for granular flows [141].

The balance of the fluctuation kinetic energy is

$$su' = Q' + \Gamma, \tag{2.34}$$

where u is the x-component of the particle velocity, Q is the fluctuation energy flux along z and Γ is the rate of collisional dissipation. The term on the left hand side of Eq. (2.34) represents the energy production through the work of the shear stress, while the divergence of the energy flux, Q', is the energy diffusion associated with the velocity fluctuations of the particles.

The constitutive relations for p, s, Q and Γ of kinetic theory [59, 170] are used:

$$p = \rho_p f_1 T, \tag{2.35}$$

$$s = \rho_p d f_2 T^{1/2} u', \tag{2.36}$$

$$\Gamma = \rho_p \frac{f_3}{L} T^{3/2}, \tag{2.37}$$

and

$$Q = -\rho_p d f_4 T^{1/2} T' - \rho_p d f_5 T^{3/2} \nu', \tag{2.38}$$

where f_1, f_2, f_3, f_4 and f_5 are explicit functions of the volume fraction, the coefficient of normal restitution and the interparticle friction and are listed in Table 2.2. There, g_0 is the radial distribution function at contact [167]. The expression suggested in [170] and valid for e_n less than or equal to 0.95 is used here:

$$g_0 = \frac{2-\nu}{2\left(1-\nu\right)^3}, \tag{2.39}$$

if $\nu \leq 0.4$; and

$$g_0 = \left[1 - \left(\frac{\nu - 0.4}{\nu_s - 0.4}\right)^2\right] \frac{2-\nu}{2\left(1-\nu\right)^3} + \left(\frac{\nu - 0.4}{\nu_s - 0.4}\right)^2 \frac{2}{\nu_s - \nu}, \tag{2.40}$$

if $\nu > 0.4$.

In Eq. (2.40), ν_s represents the critical value of the solid volume fraction at which g_0 is singular for perfectly rigid spheres which is only a function of surface friction [24]. An effective coefficient of restitution ϵ must be used in the function f_3 of Table 2.2 instead of e_n [89] to take account that surface friction also induces particle rotation (Sec. 2.3.4.10). Numerical simulations [43] have provided a simple expression for the dependence of ϵ on e_n and μ:

$$\epsilon = e_n - \frac{3}{2}\mu \exp(-3\mu). \tag{2.41}$$

In Eq. (2.37), L is the correlation length of extended kinetic theory, which decreases the rate of collisional dissipation due to the correlated motion of particles that occurs at solid volume fractions exceeding the freezing point [84, 103, 120]. When L is equal to one diameter, the molecular chaos assumption is valid and EKT reduces to classic kinetic theory. Jenkins [84], using heuristic arguments, suggested to use

$$\frac{L}{d} = f_0 \frac{u'}{T^{1/2}}, \tag{2.42}$$

where f_0 is a function of solid volume fraction, coefficient of normal restitution and surface friction (through ϵ) [17, 24]:

$$f_0 = \left[\frac{2J}{15(1-\epsilon^2)}\right]^{1/2} \times \left[\frac{26\left(1-\epsilon\right)}{15} \frac{\max(\nu - 0.49, 0)}{0.64 - \nu} + 1\right]^{3/2}. \tag{2.43}$$

The theory does not include the role of particle stiffness [21] because this is relevant only at solid volume fractions close to ν_c (i.e., where collisions cannot be considered instantaneous) and this does not occur in the numerical simulations performed in this work (see later).

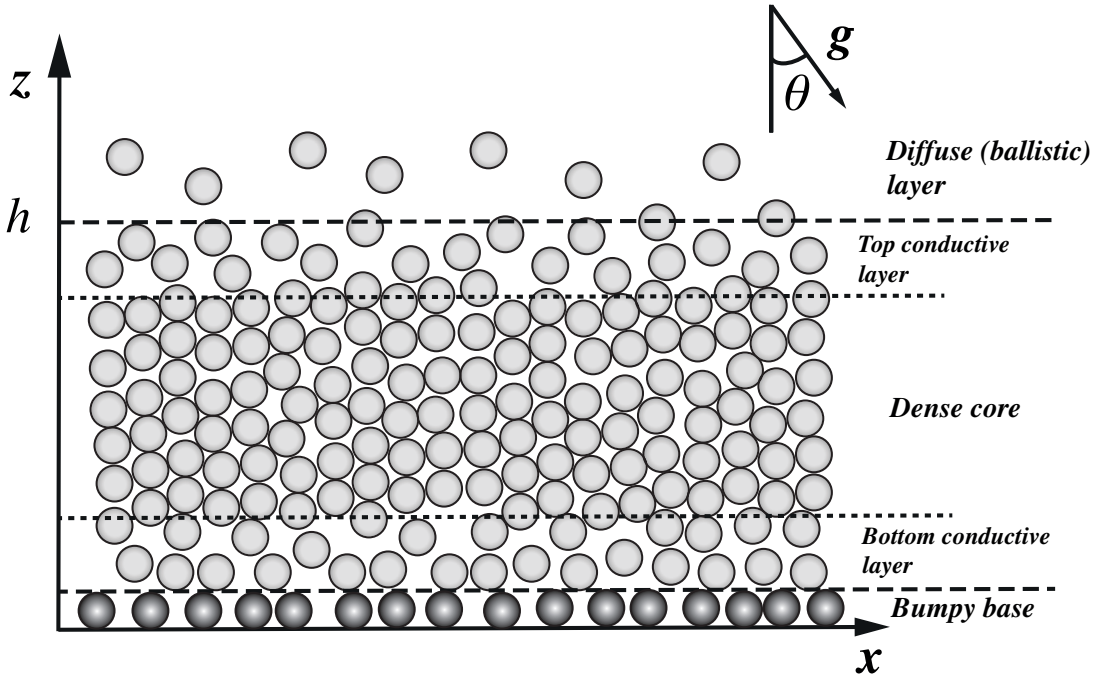

Figure 2.11: Theoretical subdivision of different layers in the flow domain

Table 2.2: List of auxiliary coefficients in the constitutive relations of kinetic theory.

$$
\begin{aligned}
f_1 &= 4\nu GF \\
f_2 &= \frac{8J}{5\pi^{1/2}}\nu G \\
f_3 &= \frac{12}{\pi^{1/2}}\left(1-\epsilon^2\right)\nu G \\
f_4 &= \frac{4M\nu G}{\pi^{1/2}} \\
f_5 &= \frac{25\pi^{1/2}N}{128\nu} \\
G &= \nu g_0 \\
F &= \frac{1+e_n}{2}+\frac{1}{4G} \\
J &= \frac{1+e_n}{2}+ \\
&\quad \frac{\pi}{32}\frac{\left[5+2(1+e_n)(3e_n-1)G\right]\left[5+4(1+e_n)G\right]}{\left[24-6\left(1-e_n\right)^2-5(1-e_n^2)\right]G^2} \\
M &= \frac{1+e_n}{2}+\frac{9\pi}{144\left(1+e_n\right)G^2}\times \\
&\quad \frac{\left[5+3G\left(2e_n-1\right)\left(1+e_n\right)^2\right]\left[5+6G\left(1+e_n\right)\right]}{16-7\left(1-e_n\right)} \\
N &= \frac{96\nu\left(1-e_n\right)}{25G\left(1+e_n\right)}\frac{5+6G\left(1+e_n\right)}{16+3\left(1-e_n\right)}\times \\
&\quad \left\{\frac{20\nu H\left[5+3G\left(2e_n-1\right)\left(1+e_n\right)^2\right]}{48-21\left(1-e_n\right)}-\right. \\
&\quad \left.e_n\left(1+e_n\right)G\left(1+\nu H\right)\right\} \\
H &= \frac{1}{G}\frac{\mathrm{d}G}{\mathrm{d}\nu}
\end{aligned}
$$

2.3.6.1 System of differential equations and boundary conditions

As in previous works [85, 170], a system of differential equations needs to be numerically integrated to solve for steady, fully-developed inclined flows.
Taking the derivative along z of Eq. (2.35), and using Eqs. (2.32) and (2.38), the equation governing the distribution of the solid volume fraction in the flow is obtained:

$$\nu' = \left(\frac{Q f_1}{\rho_p d f_4 T^{1/2}} - \nu g \cos\theta \right) \left[T \left(f_{1,\nu} - \frac{f_1 f_5}{f_4} \right) \right]^{-1}, \tag{2.44}$$

where $f_{1,\nu}$ represents the derivative of f_1 with respect to ν.
The distribution of the shear stress is governed by Eq. (2.33), which reads, with Eq. (2.35),

$$s' = -\rho_p \nu g \sin\theta + 2\rho_p \frac{\mu_w}{l_y} f_1 T. \tag{2.45}$$

The distribution of the particle velocity is given by Eq. (2.36):

$$u' = \frac{s}{\rho_p d f_2 T^{1/2}}. \tag{2.46}$$

Eq. (2.34), with Eqs. (2.46), (2.37) and (2.42), governs the distribution of the energy flux:

$$Q' = \frac{s^2}{\rho_p d f_2 T^{1/2}} - \frac{\rho_p^2 T^{5/2} f_2 f_3}{s d f_0}. \tag{2.47}$$

The governing equation for the distribution of the granular temperature is given by Eq. (2.38), with Eq. (2.44):

$$T' = \left(-\frac{Q}{\rho_p d f_4 T^{1/2}} + \frac{f_5 \nu g \cos\theta}{f_{1,\nu} f_4} \right) \left(1 - \frac{f_5}{f_{1,\nu} f_4} \right)^{-1}. \tag{2.48}$$

As in Jenkins and Berzi [85], the information about the number of particles in the system can be given in terms of the mass hold-up per unit basal area (the total mass of particles over unit area), $\mathcal{M}$. This can then be implemented as a boundary condition to a first order differential equation for the partial mass hold-up, $\mathrm{m}(z) = \int_0^z \rho_p \nu \, \partial z$,

$$\mathrm{m}' = \rho_p \nu. \tag{2.49}$$

Boundary conditions need to be specified at the top and the bottom of the flow. The top of the collisional flow is considered to be located at $z = h$; it is assumed that, above h, the mean inter-particle distance is larger than the mean free path of kinetic theory, so that particles follow the free falling trajectories and particle-particle collisions can be neglected

(ballistic layer). Pasini and Jenkins [127] determined the pressure at the interface with this ballistic layer, which by using the constitutive relation for the pressure in the dilute limit ($p = \rho_p \nu T$) gives:

$$\rho_p \nu_t T_t = \frac{1}{18\sqrt{2}} \approx 0.039, \tag{2.50}$$

where, here and in what follows, the subscript t indicates that the quantity is evaluated at $z = h$ (top). At the interface with the ballistic layer (Fig. 2.11), the shear stress and the energy flux have been evaluated by Jenkins and Hanes [88] as:

$$s_t = \rho_p \nu_t T_t \tan\theta \tag{2.51}$$

and

$$Q_t = -\rho_p \nu_t T_t^{3/2} \tan^2\theta, \tag{2.52}$$

respectively.

Richman [138] derived boundary conditions for the flow of spheres over a plane made bumpy by means of rigid, nearly elastic semi-spheres attached to it in a regular hexagonal fashion. Those boundary conditions apply at a distance of half a diameter from the top of the semi-spheres, i.e., at $z = 1.5d$ in the considered configuration (where whole spheres are glued at the bottom). In what follows, the subscript b indicates that the quantity is evaluated at $z = 1.5d$ (bottom). The slip velocity there results in:

$$\begin{aligned} \frac{u_b}{T_b^{1/2}} &= \left(\frac{\pi}{2}\right)^{1/2} \frac{s_b}{p_b} \\ &\quad \times \left[\frac{1}{3\sqrt{2}J_b} \frac{2^{3/2}J_b - 5F_b\,(1+B)\sin^2\psi}{2\,(1-\cos\psi)\,/\sin^2\psi - \cos\psi} \right. \\ &\quad \left. + \frac{5F_b}{2^{1/2}J_b}\right], \end{aligned} \tag{2.53}$$

where $B = \pi\,[1 + 5/(8G_b)]\,/\big(12\sqrt{2}\big)$, and J_b, F_b and G_b are obtained from the corresponding expressions of Tab. 2.2 with $\nu = \nu_b$. The boundary condition for the energy flux is [138]

$$Q_b = s_b u_b - \left(\frac{2}{\pi}\right)^{1/2} \frac{p_b T_b^{1/2} d}{L_b} (1-\epsilon) \frac{2\,(1-\cos\psi)}{\sin^2\psi}, \tag{2.54}$$

where, consistent with EKT, the correlation length and the effective coefficient of restitution have been introduced in the expression of the rate of collisional dissipation at the bumpy plane (second term on the right hand side of Eq. (2.54)). In Eqs. (2.53) and (2.54), ψ measures the bumpiness of the base and is defined as $\sin\psi = (d+l)/(2d)$ where l is the distance between the edges of two adjacent spheres glued at the boundary [138]. Although

ψ in Richman's boundary conditions refer to equally spaced semi-spheres attached in an hexagonal array, here the same definition is adopted by using, as l, the average distance between the edges of two adjacent spheres in the random configurations at the base. It is worth emphasizing that the analysis of Richman holds for $\pi/6 \leq \psi \leq \pi/3$: when $\psi = \pi/6$, the boundary particles are in close contact; while, when $\psi = \pi/3$, the flowing particles can fall, and therefore get trapped, in between two boundary particles.
Finally, the following boundary conditions for the partial mass hold-up are used:

$$\mathrm{m}_b = 0, \tag{2.55}$$

and

$$\mathrm{m}_t = \mathcal{M}. \tag{2.56}$$

The system of six differential equations (2.44) through (2.49) is solved for the six unknowns ν, s, u, Q, T and m using the Matlab 'bvp4c' two-point boundary value problem solver with the seven boundary conditions, (2.50) through (2.56). The additional boundary condition allows the value of h to be determined.

2.3.6.2 Algebraic and incompressible approximation

The μ(I) rheology described in Sec. 2.3.3 links the stress ratio to the Inertial parameter (Eq. 2.7) and suits flow regions, where the density is uniform; however, it fails close to the boundaries [98] and in describing phase transitions [56]. In the context of kinetic theory, a simplified approach to the solution of inclined, dense, granular flows consists of assuming that the solid volume fraction is also constant within the flow and that the divergence of the energy flux in the fluctuation energy balance (Eq. (2.34)) is negligible. The latter assumption implies, from Eq. (2.34) with Eqs. (2.36), (2.37) and (2.42),

$$\frac{du'}{T^{1/2}} = \left(\frac{f_3}{f_2 f_0}\right)^{1/3}, \tag{2.57}$$

i.e., there is a one-to-one algebraic relation between the shear rate and the square root of the granular temperature [20, 84]. The granular temperature is dependant on the gradient of velocity (u') and it is no longer an independent quantity in the problem. The algebraic assumption makes the constitutive relations of EKT formally analogue to the phenomenological local rheology based on the inertial parameter [61, 93], with the advantage that, unlike the latter, there are no parameters that need to be fitted against experiments.
In the dense limit, i.e., by retaining only terms proportional to G in the expressions of Table 2.2, the ratio of s over p can be expressed, using Eqs. (2.36), (2.35), (2.57) and

(2.43), as

$$\frac{s}{p} = \left[\frac{6(1-\epsilon^2)J}{5\pi F^2}\right]^{1/2} \left[\frac{26(1-\epsilon)}{15}\frac{\nu - 0.49}{\nu_c - \nu} + 1\right]^{-1/2}, \tag{2.58}$$

where J and F are now only functions of e_n. If the stress ratio is taken to be roughly equal to $\tan\theta$ (this is strictly true only in the absence of sidewalls), and invert Eq. (2.58), the relationship between the solid volume fraction varies and the slope of the channel is obtained:

$$\begin{aligned} \nu &= \left[\frac{26(1-\epsilon)}{15}0.49 + \frac{6(1-\epsilon^2)J}{5\pi F^2\tan^2\theta}\nu_c - \nu_c\right] \\ &\quad \times \left[\frac{26(1-\epsilon)}{15} + \frac{6(1-\epsilon^2)J}{5\pi F^2\tan^2\theta} - 1\right]^{-1}. \end{aligned} \tag{2.59}$$

If the mass hold-up $\mathcal{M}$ is given, the height of the flow can then be calculated as $h = \mathcal{M}/(\rho_p \nu)$.

The integration of Eqs. (2.32) and (2.33), with ν uniform and neglecting the stresses at $z = h$, gives

$$p = \rho_p \nu g\,(h - z)\cos\theta, \tag{2.60}$$

and

$$s = \rho_p \nu g\,(h - z)\sin\theta - \frac{\mu_w}{l_y}\rho_p \nu g\,(h - z)^2\cos\theta, \tag{2.61}$$

respectively.

From Eqs. (2.35) and (2.60) and the expression of f_1 in Table 2.2, the granular temperature is linearly distributed along z,

$$T = \frac{1}{4FG} g\,(h - z)\cos\theta. \tag{2.62}$$

From the constitutive relations for the shear stress and the pressure (Table 2.2):

$$u' = \frac{5\pi^{1/2}F}{2J}\frac{s}{p}\frac{T^{1/2}}{d}. \tag{2.63}$$

Using Eqs. (2.60), (2.61) and (2.62) in Eq. (2.63) and integrating gives

$$\begin{aligned} u &= u_b + \left(\frac{25\pi g F\cos\theta}{16GJ^2d^2}\right)^{1/2} \\ &\quad \times \left\{\frac{2}{3}\tan\theta\left[h^{3/2} - (h-z)^{3/2}\right]\right. \\ &\quad \left. -\frac{2}{5}\frac{\mu_w}{l_y}\tan\theta\left[h^{5/2} - (h-z)^{5/2}\right]\right\}, \end{aligned} \tag{2.64}$$

where u_b is given in Eq. (2.53).

2.4 Constitutive description of granular flows

2.4.1 Continuum description of granular flows

Gravity-driven flows commonly occurring on the Earth's surface can appear under various forms. Examples are dry rock avalanches, in which pore fluid may be considered negligible, or liquid-saturated debris flows, in which fluids may enhance their mobility. Obviously, the presence of an interstitial fluid renders theories that try to fully capture the interaction of the solid and liquid components much harder to handle. Robust theories for describing the mobilization and deposition of geophysical flow started with the pioneering works of Johnson [91] and Yano and Daido [181]. They recognized that debris flows have physical properties similar to both viscous fluids and plastic solids. These properties have been used as a basis to develop the Bingham model [92] for the continuum representation of debris flows. The mechanical behaviour of a Bingham material is characterized by an elasto-plastic stress-strain relationship. As it stands, this model is a one-phase approximation, i.e., a single constitutive equation is considered sufficient to describe the bulk properties. The Bingham model can be used to capture certain types of debris flows (i.e. clay rich) where segregation and pore water diffusion is not a major concern. It assumes that the momentum transport and energy dissipation in debris flows occur exclusively by viscous shearing [78]. However, the rate-dependent energy dissipation can also extend to the debris materials, where solid particles interact with each other through inter-particle friction, collision and basal friction. Consequently, viscoplastic models turn out to be inappropriate as they oversimplify the rheology of real debris mixtures. Indeed, their most relevant application boils down to the solely fines-rich fraction of debris flow mixtures and mud flows.

In the geophysical context, saturated granular flows can be more appropriately treated as multi-phase systems, i.e. consisting of interacting phases. In fact, debris flows are a combination of fluid and solid components with different grain size and shape. Viscoplastic models do not account for the interaction between these conditions, which play a relevant role in generating shear resistance and transfer of momentum. Indeed, inertial forces may dominate over viscous forces. Takahashi [162] considered a debris flow material as a suspension of particles within a viscous fluid whose interactions produce dissipative grain stresses. He applied Bagnold's [15] constitutive equations in the inertial regime to stony debris flows, i.e. when the dynamics are consistently collisional. This model, also referred as to as the dilatant model, provided the basis for inferring the stress development in grain-inertial flows, although it does not take into account the effects generated by the interstitial fluid on the solid phase during motion [79].

Model limitations, such as those embedded in the viscoplastic approaches, can alterna-

tively be overcome by using methods that adopt hydraulic approximations, for instance, depth-averaged theory. One example is the analytical description for the motion of granular materials by Savage and Hutter [149]. Although primarily conceptualized for dry granular mixtures, the original formulation has been proved successful for the prediction of the depositional pattern of the flows after runout [132]. However, to capture the more fundamental behaviour of debris flows, the inclusion of the fluid phase is necessary. This has been achieved by models (e.g., [78, 128]) which derive from a two-phase system of equations that describe two constituent phases, namely solid and fluid phases, and which go under the name of mixture theories. In these models, two separate sets of shallow-water equations are solved, one for the fluid phase and one for the granular phase. The assumption at the heart of mixture theory is that, wherever both phases are present, solid and liquid exchange momentum in a manner proportional to the volume fraction ν, i.e., during debris dilation and contraction. However, the assumption of a uniform distribution of particles throughout the flow greatly limits the capabilities of this approach. In particular, mixture theory is currently unable to appropriately represent segregation patterns observed in real debris flows, although such implementations in the model have been attempted (e.g., [68, 69]). Another problem in implementing the shallow-water equations is the treatment of pore fluid pressure variations, which in real debris flows can be in excess of the hydrostatic value (Sec. 2.2.1.2). Several model modifications have been recently proposed, e.g, [62], where explicitly independent equations account for sources of excess pore pressure and its dissipation which are in turn is connected with the evolution of porosity due to changes of effective normal stress and shearing of the grain-fluid mixture, leading to contraction or dilation of the pore space [97].

In the solid phase of geophysical flows, momentum transfer is mainly carried by frictional and collisional stresses. The contribution to the high mobility of debris flows due to particle collisions could be effectively introduced in constitutive models based on kinetic theory (Sec. 2.3.4). Notably, there are similarities with the shallow-water approximations, however, kinetic theory provides additional equations that take into account the exchange of energy during grain collisions. Since these types of models have only being intensively studied in the last few decades, it is justified to believe that they cannot be immediately used for full-scale applications. However, as our understanding advances, progress is being made to enlarge the range of application of these models. In simple laboratory small-scale realizations, kinetic theory is able to replicate and describe the behaviour of shearing granular flows in dry [17, 86] and saturated conditions [19]. It is also possible to bridge the gap between phase transitions (e.g. from an quasi-static erodible bed to a flowing state), as was done in [11, 87]. Further advanced models based on kinetic theory can also account for a first degree of segregation, e.g. [23], where only two species - or sizes -

are considered. The improvement of such models may allow us to better understand and include important additional mechanics into the modelling of granular flows.
More recently, Rauter et al. [136] applied a rheological model based on extended kinetic theory to depth-averaged snow avalanche simulations with the aim of reproducing the runout spread obtained from field observations. The results were tested against a more classical depth-averaged model based on Voellmy frictional relation [171]. The two models produced similar results although the one based on extended kinetic theory showed some improvements and in some situations a better fit to the observation field data. This is encouraging since models based on a Voellmy-type constitutive equation are also common tools used in practice for the predictions of the debris flow runouts [100] and help the generation of hazards maps.

2.4.2 Discontinuum description of granular flows via discrete element simulation

A different approach to the continuum models presented above is the use of discrete (discontinuum) methods, where even the movement of single particles can be tracked and analysed. With their use, the abstraction of treating the material as continuum as in depth-integrated methods is avoided. Advantages of these methods are, among others, the possibility of reproducing interaction with external objects, for instance Leornardi [106], or the study of segregation effects [168]. In the context of this thesis, discrete methods are particularly useful to reproduce the mechanics of simplified small-scale laboratory experiments (chute flows) and extract information that could be otherwise biased by the experimental measurement techniques or hindered by the opacity of the flows.
The focus of numerical simulations on inclined chute geometries has primarily been on free-surface granular flows in configurations with periodic lateral boundaries [114, 140, 154–156, 166, 173, 174], where measurements were deemed equivalent to those made along the centre line of laterally bounded flows. Simply changing the remaining bottom boundary condition, slope angles and flow rates produces remarkably different behaviours. Over a flat base, a shallow flow behaves as an agitated and dilute layer while, for increasing flow depth, a large region of plug flow with high slip velocity and vanishing shear rate develops [48]. Conversely, a rough bottom generally reduces slip at the base while sustaining a sheared flow. In this case, depth-averaged velocities strongly depend on inclination and flow height, which in turn determine whether a flow stops, steadily propagates or constantly accelerates [154], a feature similarly observed in experimental flow [129] as already mentioned in 2.3.3.
Conversely, very few works have attempted to numerically study flows down an inclined chute between sidewalls [33, 34, 70, 107, 172] and the literature reveals that the under-

standing of granular flows investigated in such a way is largely incomplete and the limited simulations are not able to complement the flow details reported in experimental works [34]. Moreover, such studies were either limited to just few particle layers or focussed only on flat bases. An important characteristic of sidewalls is their dual effect of supporting flows over rough bases at increasingly high slope angles and stabilizing flowing piles over erodible surfaces of a heap at inclinations greater than the angle of repose [93, 159]. However, these features have been barely studied by means of numerical simulations and investigations of flows over bumpy rough bases are still lacking.

Despite the good agreement between experimental and numerical works, the latter approach usually affords several simplifications to ease the computational cost or the mathematical complexities. An example is the necessity to use and assume that the particles are nearly rigid and perfectly spherical objects, whereas in nature this is rarely, if ever, the case. The shape anisotropicity of the grains can be taken into account by introducing additional torques (e.g., torsion and rolling) [112, 113] while keeping the same simplified approach used for spherical particles. Studies that have specifically used such components for a more realistic investigation of granular flows on inclines and their comparison with experiments are lacking in the literature. In the case of rolling, i.e. an artificial opposing moment that is used to mimic the relative surface resistance of two complex shaped particles at contact, a weak rolling resistance results from micro slidings between grain asperities while large rolling resistance is generated by particles with dendritic surfaces. The quantification of this resistance has been calculated and interpreted differently in experimental [57, 183] and numerical studies which mainly deal with shear tests, triaxial tests and granular column collapse [4, 52, 58, 90]. To date, there are different methods (summarized in [175]) that can be used to include the effect of rolling but there is no general agreement on parameter values leading to a wide range of different results.

2.5 Physical modelling of granular flow

2.5.1 Large and small scale tests

Phenomena such as liquefaction, entrainment, flow instability caused by the longitudinal sorting of material, and spread into depositional fans are common features in debris flows. Field observations are limited by the unpredictability and extent of these events. However, these processes can be simplified by scaled-down physical modelling without preconditioning the outcome.

There are several small-scale configurations that can be used to investigate the mechanics of debris flow behaviour: coaxial-cylinder rheometers (e.g. [7, 45]), which are usually used to validate viscoplastic models although are not compatible with the large size of particles involved in geophysical flow; conveyor belts (e.g. [75]) and rotating drums (e.g. [74, 96]), which allow steady flows, make observations taken over longer periods of time possible; and centrifuge testing (e.g. [30]), which recreates appropriate stress states for scaled pseudostatic geotechnical problems. A widely used arrangement consists in allowing material to flow down an inclined plane between well-defined boundaries. Many studies have employed this configuration, e.g. [5, 10, 11, 14, 110, 126, 129, 149]. The inclined chute provides a good base for studying gravity-driven granular flows. Indeed, tests can closely control the material properties and observations can be taken at the sides as well as at the free surface boundary.

On the other hand, small-scale behaviours obtained with the arrangements described above may not always be appropriate for the full characterization of field scale processes. In the case of saturated granular flows, Iverson [78], Iverson and Denlinger [80] argued that small models may not be sufficient to reflect the importance of Coulomb stresses and the reduced effect of viscous stresses when compared to field scale flows. This argument derives from the normalization of the depth-averaged Coulomb mixture equations which yield bulk scaling parameters. In particular, the authors define the quasi-Reynolds number (N_R) and the pore pressure number (N_p), the first is the ratio between inertial and viscous forces, the second represents the time scale for downslope movement divided by the time scale for consolidation, which in turn reflects the extent to which pore-pressures are able to mediate frictional resistance [95]. As flow size increases, values of N_R increase and indicate that viscous stresses diminish in importance, whereas values of N_p decrease and indicate that fluid pressure effects grow more pronounced [80]. According to 1997, the influence of flow size on N_R and N_p poses a severe problem in scale model experiments, hence miniature flows cannot emulate conditions in full-scale geophysical flows. For these reasons, large flume tests were conducted at the USGS debris flow site [78, 80, 116]. The flume was a rectangular concrete chute about 100 m long and 2 m with a fixed slope of

31°. Approximately 10 m^3 of debris can be released, spreading out at the end of the chute onto a planar unconfined runout zone. Common debris-flow features were observed, such as surge formation with dry stony head followed by thinner and more watery tail, and the formation of lateral levees. Importantly, their results showed that the interaction between the porous soil material and interstitial fluid is central to understanding the dynamics of debris flows [117]. In particular their mobility is greatly affected by the pore pressure generated within the mixture. Whether this pore pressure is greater than hydrostatic depends on the amount of fine material present in the solid-fluid system. In general, the content of fine materials (silt sized and below) for granular debris flows is less than 10-12%, with greater amounts leading to increased viscous effects [152]. When fine particles and fluid dominate in the rear interior of the flow, permeability is reduced and excess pore pressure develops. Sustained high fluid pressure reduces effective stresses generating low frictional resistance. This greatly affects the mobility of debris flows and the depositional runout.

According to Iverson [78], Iverson and Denlinger [79], the large-scale models may be fundamentally different from idealized, small-scale ones. This difference primarily lies in the fact that small models cannot reproduce the same stresses as those of real large debris flows. When the flow size increases, the dimensionless scaling parameters [80] indicate that the importance of viscous stresses may diminish and pore pressure may grow more pronounced. Essentially, high pore pressure persists much longer in large-scale flows than small-scale flows do with the same mixture composition. However, the dimensional analysis has some limitations. It assumes kinematics of a simple shear flow, it neglects variation in granular temperature and volume fraction, and it neglects energy conversion and dissipation that occur at flow boundaries [78]. Most importantly, it neglects that debris flows occur as unsteady, nonuniform surges, develop non-hydrostatic pore pressures, and especially, include grains of widely ranging sizes.

Bowman and Sanvitale [29] showed that comparison between the two scales does appear feasible and careful laboratory testing performed on small scale flumes can still inform on the mechanics behind debris flow behaviour. It was shown that the well-graded nature of debris flow is not incidental, but an important factor affecting their mobility and the capacity to travel far before the final deposition phase. The correct choice of the particle size distribution (PSD) enabled important aspects of debris flow behaviour to be replicated even at small scale, such as the effects of flow segregation and its influence on final deposit shape and grading profile. An experimental debris flow consisting of well-graded materials may generate low frictional resistance within the flow interior as the flow segregates with agitated finer particles reducing the propensity for fluid to exit from the mass. Hence pore pressures may be greater than hydrostatic and effective stress greatly reduced. This is

different from typical experiments characterized by a relatively uniformly-graded particle size distribution. In this case segregation cannot occur and the mixtures maintain a steady frictional resistance. The fluid is evenly distributed throughout the flow so that momentum is lost quickly due to the uniformly distributed frictional resistance and the reduced effect of pore pressure. Comparatively, for systems with the same masses of solids and fluid, well-graded mixtures showed higher velocity, smaller flow thickness and a larger runout extent than uniform flows [143]. These distinct behaviours may explain the difference in behaviour at large and small scale that is often observed. If well-graded materials are used for small scale work, high overall mobility can be achieved in this configuration despite the lower velocity attained.
Problems such as the effect of boundary conditions on the near-wall probing of opaque flowing material may arise. A random velocity component caused by the interaction between walls and flowing mass can be added to any measurements of granular temperature taken at the sidewalls. Rigid boundaries may also contribute to the local rearrangement of particles, thus making measurements of solid volume concentration very different from the flow interior. However, recent non-intrusive techniques can look inside the flow without influencing the measurements which in turn become independent from the boundary conditions. Some of the studies conducted using this approach are introduced in the following section.

2.5.2 Optical investigation of granular flows

Small scale studies can be advantageous because flows can be easily reproduced and particular mechanics isolated and studied in detail. Idealized laboratory set-ups, in which dry and saturated flows that use identical or near-identical spherical particles in simple geometries have proved useful to study simple idealizations. The simplification of the complex behaviour of these flows facilitates the acquisition of their properties and a closer comparison between experimental data, theory and numerical simulations. However, this information is obtained primarily at the boundaries due to the opaque nature of studied flows. As such, relevant internal characteristics are difficult to obtain and data on the internal behaviour of such solid-fluid mixtures is rare [96]. Moreover, it is well understood that boundary conditions (e.g the sidewalls in chute experiments) can at times alter the representativeness of the bulk motion and therefore the reliability of the measurements.
The effect of lateral boundary conditions can be overcome by using new non-intrusive techniques that require the refractive index matching of both grains and liquid to render the medium transparent. In general these types of experiments have the advantage over more traditional methods in which materials are opaque enabling insights to the internal flow behaviour and the visualization of fluid-grain dynamics away from the flow margins.

Optical techniques have been used in a soil permeameter [77], in a horizontal with channel recirculating granular materials (e.g. [13, 121]), in a shear cell [125] and, in the context most relevant for geophysical application, in an inclined flume (e.g. [6, 144]). In this thesis, the same planar laser-induced fluorescence (PLIF) technique and apparatus proposed and developed by Sanvitale and Bowman [144] was used. A more detail description together with the modifications applied for this work are reported in section 8.2.

2.5.3 Measurements of granular temperature for dry and saturated flowing materials

Granular materials are notorious for the difficulty they pose in obtaining microscale laboratory measurements. This is why many theories, such as kinetic theory, are chiefly compared to numerical simulations. Despite this, as tools and techniques to measure experimental granular flows become increasingly sophisticated, experimenters can now obtain robust measurements of granular temperature. Indeed, in many cases experimenters are now able to follow the motions of each or most of the particles, thus enabling a better assessment of the theoretical predictions [63].
Velocity and granular temperature profiles of four studies on dry and saturated granular flows using an inclined chute geometry [10, 14, 27, 110] were collected by Sanvitale and Bowman [145] and compared against their results (Fig. 2.12). They showed that the range of variability of these quantities can span different orders of magnitude, partially owing to the different measurement techniques, materials, and boundary conditions involved.
In many studies, Particle Tracking Velocimetry (PTV) is the preferred method adopted to extrapolate measurements from these flows. Theoretically, if all the visible particles can be precisely tracked, accurate values of granular temperature can be obtained. However, particle tracking techniques still possess some limitations for use on dense flows and especially for flows of irregular shaped particles. Interestingly, the experimental measurements by Sanvitale and Bowman [145] were obtained for unsteady quasi-uniform saturated granular flows down an inclined chute composed of angular material. They trialled a different method to measure granular temperature based on Particle Image Velocimetry (PIV). It was first proposed by Reynolds et al. [137] who performed tests in a high shear granulator. It was shown that, if fluctuation velocities are assumed to be normally distributed, granular temperature is given by the variance of the velocity field. The measurements are also dependent on the size of the interrogation region (or patch size) used to find the particle displacements via cross-correlation in PIV (more details are given in Sec. 3.2). It was found that an interrogation area of the order of the particles generates the most accurate values of granular temperature. Larger patch sizes caused a reduction in the measured fluctuation velocity that in turn reflected a reduction in granular temperature.

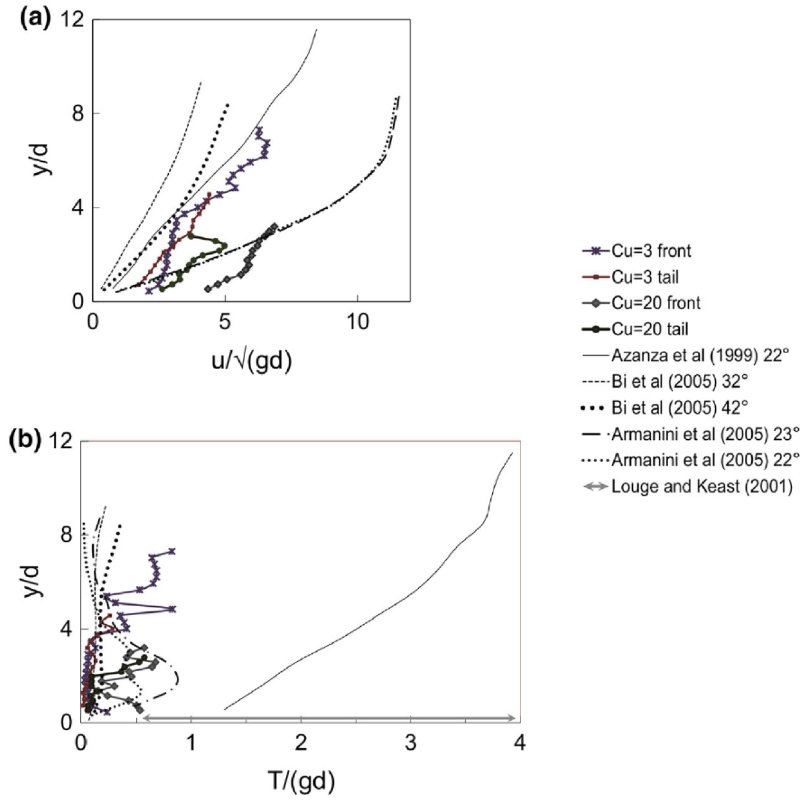

Figure 2.12: Measurements of normalized velocity (a) and granular temperature profiles (b) from different studies collected by Sanvitale and Bowman [145] and compared with their results.

More specifically, they found that if the interrogation size is increased by a factor of n_{sf}, granular temperature also decreases by the same factor n_{sf}. The same procedure was used in [145], however, since their flows were unsteady, it was not possible to take multiple measurements over long period of time. Instead, granular temperature was statistically measured as the variance of the velocities taken over 30 frames only. They also tested the dependence on the interrogation area. For these flows, the smallest ones contained high level of noise, although it was progressively damped when increasing the patch size. This study has given encouraging results in determining granular temperature even for agitated flows with a different range of particles sizes. However, further validation and supporting evidence are required to examine the validity of this technique to correctly capture granular temperature.

2.6 Conclusion

In the first part of this chapter the mechanics involved in real debris flows and in simple steady granular flows have been described. Then, the fundamental works and theories devoted to the study of granular flows have been reviewed. In particular, the focus was given to the recently developed extended kinetic theory. This theory considers the particle agitation induced by the collisional grain motions which is taken into account by introducing the state parameter called granular temperature. Different models have been developed to capture the behaviour of granular flows, e.g. the Bingham model and mixture theory, however, those based on kinetic theory represent a new approach that may lead to better understanding of complex debris flows.

Considering the configuration most relevant for this thesis, i.e., granular flows down an inclined chute, investigations in a dry condition have been carried out via experimental and numerical methods. Both have been used for the development and improvement of kinetic theory. In the experimental context, further validation and supporting evidence are required to examine the validity of non-intrusive measurement techniques, such PIV and PTV, to correctly measure granular temperature. In numerical analyses, discrete element method simulations should not be limited to simple situations (e.g., a representative element volume away from the boundaries) but should also be extended to provide new insights to the behaviour of simple flows reproduced in the experiments over a bumpy base and constrained by lateral sidewalls.

The physical investigation of debris flows has been conducted at large and small scales. In both cases, the mechanics behind granular flows behaviours can be captured with the correct choice of the particle size distribution. With this, the study of simple granular flows can now be extended and performed using new optical investigation techniques that provide valuable information of the flow interior. Mixtures of solids and fluid can be studied and the properties of real debris flows more closely matched.

Ultimately, it appears that the capability of a model or theory to reproduce the behaviour of a granular flow under well-controlled, uniform flow conditions is a first indispensable requirement. That is, before extending the analyses to complex debris flows, models should certainly be capable of describing the simpler situations. This particularly applies to new models, such as those based on kinetic theory. In this sense, the present thesis follows this concept. Experimental and numerical results from simple shearing flows in an inclined geometry relevant for the study of debris flows are given so that these two approaches, together with statistical and continuum mechanical models, are tested against each other.

3. Error frameworks for experimental measurement techniques

3.1 Introduction

As discussed in Sec. 2.5.3, experimental measurements of granular flows are mainly obtained via Particle Image Velocimetry (PIV) or Particle Tracking Velocimetry (PTV). This chapter aims to identify and minimize possible sources of error that affect the measurements obtained with these two techniques.
Non-intrusive measurement techniques, namely PIV and PTV, are reviewed first in Sec. 3.2. Methods for the outlier removal common to the two techniques are summarized in Sec. 3.3. PIV is a very established technique where notions and procedures to minimize potential errors already exist. These are briefly summarized in Sec. 3.4.1. Conversely, PTV guidelines to correctly investigate granular flows are lacking, therefore possible ways to minimise sources of errors are investigated and discussed in Sec. 3.4.2.

3.2 Non-intrusive measurement techniques

In laboratory experiments which use either opaque or transparent particle systems, non-invasive measurements of motion are usually obtained via imaging techniques such as Particle Image Velocimetry (PIV) and Particle Tracking Velocimetry (PTV). These are broadly used to estimate the velocity of groups of particles or the movement of single particles.

PIV and PTV were originally developed in the field of experimental fluid mechanics [1] for the study of single- and multi-phase fluid flows. In this context, the methodological principle is to add tracer particles to the flow, i.e. assuming that they move under the action of the flow structure of interest. While in fluids, seeding is necessary for the creation of reference features for image processing operations, granular flows have their own texture in the form of natural or idealized particles (usually spheres) which can be individually tracked. With an appropriate number of tracers or particles, a rigorous reconstruction of the entire flow and its essential properties can be achieved. The flow field is usually illuminated by a source of light (lighting system or laser light) to highlight the particle locations. A CCD or CMOS based camera is then used to capture a sequence of images separated by a defined time interval. The displacement of a characteristic interrogation region for PIV or a singular particle for PTV is determined differently according to the technique used.

3.2.1 Particle Image Velocimetry

Particle Image Velocimetry (PIV) is a well-established technique and exhaustive reviews may be found in the literature, for example, in [2]. The process followed by PIV to track the displacement of a small group of particles is shown in Fig. 3.1. The common approach is to divide the entire field-of-view into smaller regions, called interrogation areas (or patches ([178]). Extracting the displacement information between two consecutive images is performed by cross-correlating the interrogation areas at two sequential time steps using the calculation of correlation via Fourier Transform. The procedure for evaluating a single displacement vector is repeated for the entire grid of the patches, producing the displacement field between the image pair. The analysis is continued by cross-correlating the interrogation areas of the second image with those of the subsequent one and so on until all the images are analysed. Eulerian velocity vectors of the assemble of particles in the sub-images are provided in a regular raster by dividing each displacement by the time step chosen for the acquisition.

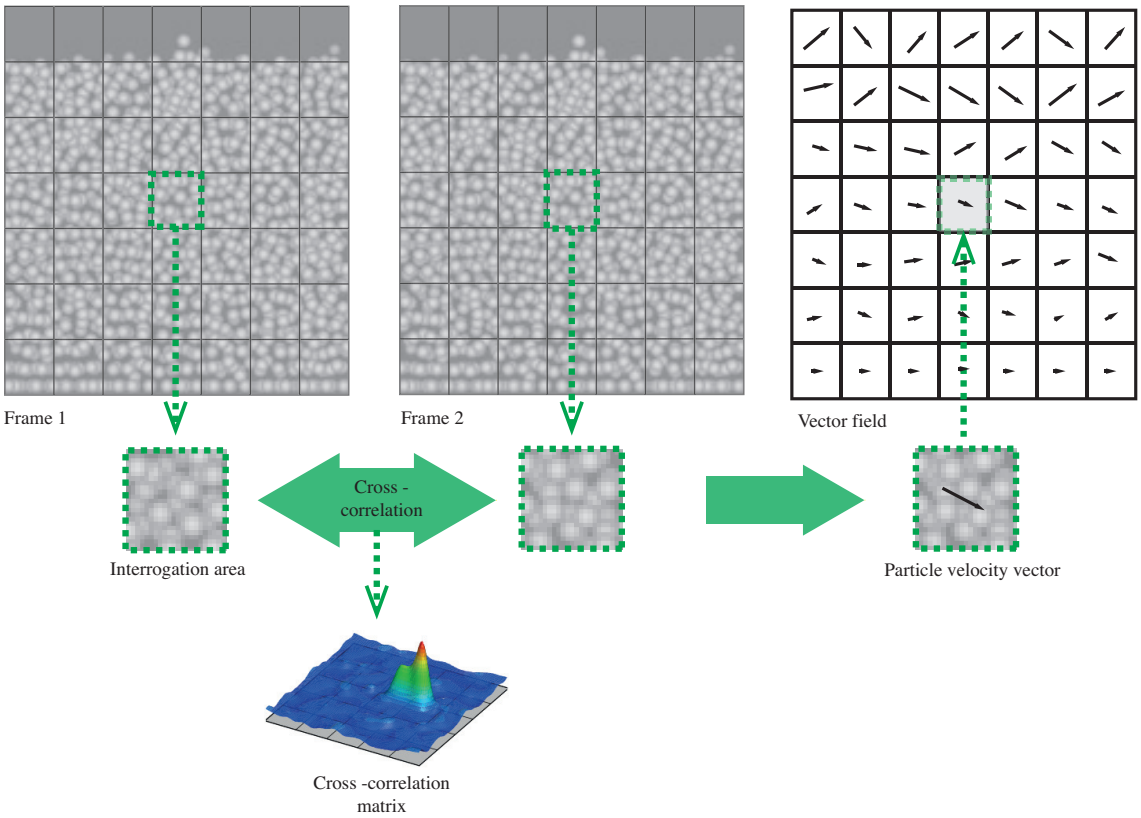

(a)

Figure 3.1: Depiction of the principle of PIV analysis.

3.2.2 Particle Tracking Velocimetry

3.2.2.1 Centroid estimations

An alternative image processing technique that is suitable to obtain the velocity field is two-frame particle tracking via PTV. Generally, a particle image has a brightness pattern with a peak near its centroid, with brightness progressively decreasing one pixel away from this peak. The process followed by PTV begins with the individualization of particles and the estimation of their centroids. Perhaps the simplest method for individual-particle detection from the image intensity distribution is the single-threshold binarization of a binarized image, commonly referred to as image segmentation [2]. Once found the particle is labelled, its position is calculated by means of a centre-of-mass estimator. This method finds its best applications in low density flows where the edge of each particle can be clearly identified. However, in dense granular flows, particles move randomly creating a non-homogeneous distribution of the intensity matrix over time. Moreover, due

to the high concentration, particles are prone to overlap, appearing with no sharp edges, leading to spurious detection or loss of the particle data. In order to handle such cases and also situations where the particle images are partly varied with respect to their size, mean brightness level, and intensity-distribution profile, other methods are available, such as dynamic threshold binarization [122] and particle-mask-correlation [164]. In dynamic threshold binarization, the binarization threshold is adjusted according to the mean intensity of each particle. This is done in such a way that the contrast or difference with the image background is kept constant. For the method to be successful the base threshold needs to be always higher than the noise level. In the particle-mask-correlation method, a Gaussian reference mask (i.e. a matrix) is convoluted to the intensity distribution around each particle. The centroid of the particle is identified when the correlation value between the mask and a sub-matrix, of the same size of the mask and centred on each image pixel, is above a predefined threshold level. Both methods, dynamic threshold binarization and the particle-mask-correlation method, are able to detect overlapped particles and can estimate their centroid position with sub-pixel accuracy. However, their limitation lies in the fact that they assume that the shape and intensity distribution is that of a circular particle.

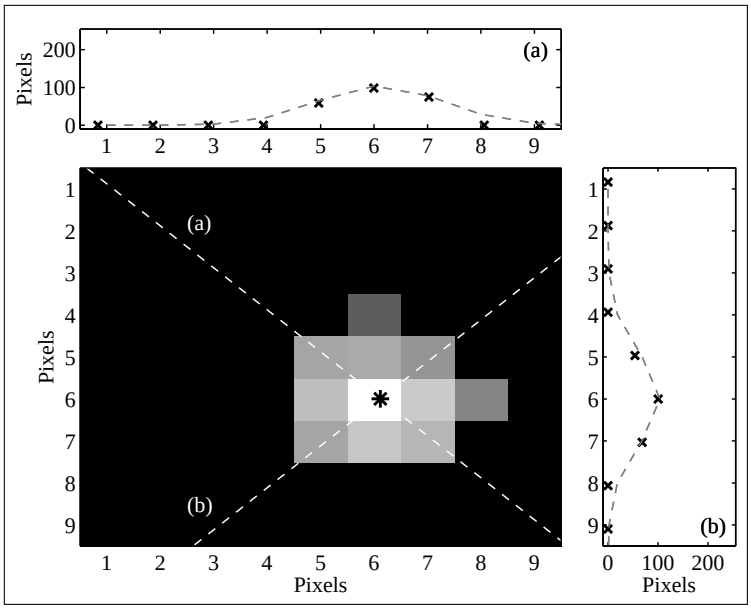

Figure 3.2: Determination of the particle centroid. To find the the peak of the distributions, i.e. the centre coordinates, the algorithm selected values (x-marks) of the intensity matrix are fitted by two curves (dashed-lines) in x- and y-direction, (**a**) and (**b**), respectively.

In case of dynamic threshold binarization, the subpixel accuracy is achieved by using techniques similar to the one used for the binary method (i.e. centre-of-mass estimator). In the particle-mask-correlation method, the threshold correlation level is chosen once, before the analysis, and is taken to be representative of all image particles. However, this can lead to uncertainties in the particle centroid estimation due to differences in the intensity matrix of nearly overlapping particles and those at the margins. An accurate estimation of the centroid position can be obtained by fitting a presumed functional shape to the intensity matrix centred individually on each particle. Generally, the estimate of a given parameter (e.g. the sub-pixel particle position) is attained by minimizing the sum of the squared difference χ^2 between the observation $\tau[m,n]$ in a MxN-pixel domain and a suitable model $H(X,Y;\boldsymbol{\theta})$ with respect to a parameter vector $\boldsymbol{\theta}$:

$$\chi^2 = \sum_{m}^{M}\sum_{n}^{N}\left(\frac{\tau[m,n] - H(X_m, Y_n; \boldsymbol{\theta})}{\sigma_{m,n}}\right)^2 \tag{3.1}$$

where $\sigma_{m,n}$ is a weighting factor and $\tau[m,n]$ the pixel intensities in the interrogation region. For circular particles the functional shape is well approximated by a Gaussian distribution and the parameter vector would consist of $\boldsymbol{\theta} = (\tau_{00}, X_0, Y_0, d)$, that is, the amplitude (τ_{00}), a guessed particle location (X_0, Y_0) and the characteristic diameter (d). The guessed particle location can be acquired, for instance, by the use of one of the other methods mentioned above. It may be expected that the least-square fit in Eq. 3.1 will give very accurate results in the case of low density flows. Conversely, in highly concentrated flows the size and the shape of the particle image are determined by the aforementioned factors (e.g. random movement and particle overlap). Care should be taken if the parameter estimates are not near the minimum of χ^2 or when a large number of fitting parameters is used. Otherwise the result may be an excessive increase in computational time which is a major drawback of this method.

A characteristic application of this method is illustrated in Fig. 3.2. A guessed location is first generated using the particle-mask-correlation method by correlating the Gaussian reference matrix to the particle image. A portion of the original image containing the particle of interest is then extracted around this value (surrounding particles are masked out). This information is then used as part of the parameter vector in Eq. 3.1. This equation enables the refinement of the guessed particle location, yielding a higher precision estimate. During the processing of the data, curves based on the presumed functional shape are fitted to the intensity sub-matrix (each curve gives the centroid coordinate in respect of one axis). The process stops when the sum of squared residuals (i.e. the difference between an observed value and the fitted value provided by the model) is minimized.

3.2.2.2 Tracking algorithms

Once the particle positions are found and stored, the next step is to track a large number of particles over time in order to achieve high spatial resolution (in the limiting case of steady flows) and obtain accurate results. Low seeding densities was generally deemed the limiting case for PTV [2] and the challenge of the tracking algorithms for use in measuring granular flows has been to achieve applicability to much higher particle densities than have thus far been needed. To do this, different tracking algorithms have been proposed, for example, Cowen et al. [46] proposed a hybrid technique that uses PIV results to guide the particle matching algorithm and more recently Brevis et al. [32] presented a two-stage integrated approach that combines cross-correlation with a relaxation algorithm. In the latter, during the cross-correlation phase the interrogation windows are centred on each particle candidate in the first image and a particle match is found in the second image when the highest correlation coefficient is detected. However, particle patterns associated with the interrogation areas can suffer from strong deformation due to non-linear gradients in the field. The consequence is a drop in the correlation level which would decrease the reliability of the PTV analysis. To improve the performance, the relaxation method is then applied to those unmatched candidates that were disregarded during the cross-correlation phase. Hence this method is based on the probability of particle matching between two frames defined for every possible pair of particles. This approach enables the particle-matching probability to be updated using the probabilities of the neighbouring particles which are then iterated until all the probabilities remain almost constant [122]. This strategy was found to be effective in establishing the correct inter-particle links from the others, as was shown by a higher value of the yield parameter Y_i [72] compared to similar approaches. The yield Y_i is obtained from synthetic benchmark studies and it is defined as the ratio between the known number of particle displacements available between two images and the valid displacements recovered from the images. Ultimately, the merits of this specific algorithm are its applicability to complex flows with local shearing boundaries and relatively strong velocity gradients.

3.3 Outlier removal for PIV and PTV

Even with the best practice, PIV and PTV can return spurious velocity vectors. The median filter, also known as universal outlier detection, and mean local filter can be used to remove these vectors. The first is based on defining a threshold value of the normalized residual velocity fluctuation of one data point relative to its neighbourhood. The data point is rejected when its residual is greater than the normalized residual threshold. This approach is simple, computationally efficient and universal [50]. The second filter com-

pares the direction and magnitude of each velocity vector with the local mean value of a pre-defined neighbourhood. This filter is very sensitive to the user-defined parameters required to consider a vector as an outlier (size and number of points within the neighbourhood, maximum magnitude and angle difference between points), which can result in the elimination of a large number of correct vectors. Westerweel [176] and Westerweel and Scarano [177] give more information on these two methods. A pseudo code implemented in Matlab for the universal outlier detection is given by Westerweel and Scarano [177].

3.4 Experimental investigation of sources of error

Without due caution, PIV and PTV can generate errors that severely affect the results. While the complete removal of these is practically impossible, some useful guidelines can be followed to minimize them. Here the notions of PIV analysis that are useful to obtain valid results are summarized in Sec. 3.4.1 while more in-depth experimental investigations are described for PTV in Sec. 3.4.2. The results presented for PTV are given in dimensionless form and the translation to dimensional forms can be obtained by dividing with the following scaling. From the experiments (see Ch. 4), the characteristic real diameter is that of spherical ceramic beads $d' = 1.5$ mm with density $\rho_p = 2430$ kg m^{-3} (Table 4.1). Using a the gravitational acceleration $g' = 9.81$ ms^{-2}, the time scale length is $t' = \sqrt{d'/g'} = 0.0124$ s, the velocity scale is $\mathbf{v}' = \sqrt{d'g'} = 0.121$ ms^{-1} and, with the mass calculated as $m' = \rho_p \frac{\pi}{6} d'^3 = 4.29 \times 10^{-6}$ kg, the kinetic energy scale is $KE' = m'd'g' = 6.31 \times 10^{-8}$ kg m^{-2}s^{-2}. Here, $d', g', t', \mathbf{v}', m', KE'$ indicate the respective dimensional forms.

3.4.1 PIV error type and reduction

The choice of the interrogation window size (or patch) has a strong influence on the PIV results [71]. The chosen size depends on the experimental conditions (i.e. lighting, image texture, etc.) and the particle diameter. In the simple case of monodisperse flows, to increase the level of accuracy it is necessary to increase the image texture. This can be achieved by use of textured particles (i.e. non smooth or differently coloured) or increasing the image density N_i, i.e., the mean number of particles per interrogation window. Both signal strength (the peak of the correlation matrix) and the noise (i.e. the random correlations) increase in proportion to the image density. However, when the correlation is normalized with respect to the highest peak, the relative noise level (defined as the highest random correlation peak) decreases with increasing N_i. Examination of the normalized correlation function has shown that for a correct peak detection, the mean number of particles per interrogation area should vary between 5 and 10 [2]. Additionally, empirical estimates for the optimal particle image diameter suggest a range that varies from 2 to 4 pixel units [131, 134]. Note that this is may be true for spherical particles, although other particle shapes are also possible.

The boundaries of a granular flow can be frictional and generate local shearing. For instance, granular flows down chute geometries with highly frictional bottom boundaries form shearing layers, producing an in-plane velocity gradient. For methods that use standard static spatial domain correlation (i.e. when the shape of the interrogation region is fixed) in the vicinity of the bottom boundary, faster particles may leave the sub-images

and the remaining slower particles act to generate in-plane loss-of-correlation, hence biasing the displacement estimates. This is referred to as gradient biasing [99]. To reduce this error, the experimenter may resort to algorithms that allow iterative sub-image deformation [150, 151]. This type of scheme starts with a standard static correlation pass over the entire image. This pass then provides an initial estimated displacement vector for each node (nodes are found in the corners and the centre of the sub-image). The results are then used to determine the amount by which to dynamically deform the second sub-images, as shown in the example of Fig. 3.3. The next interrogation pass cross-correlates the undeformed sub-images in the first frame with the deformed ones in the second frame. There is an image displacement range within which the image deformation scheme guarantees correct results. The cross-correlation in each pass is performed within an area in the next frame that cannot be larger than the chosen interrogation size and a correct correlation peak is found if the particle displacement is half the interrogation window size [134]. In fact, the interrogation areas are assumed to be periodic, i.e., they repeat themselves in all directions [165]. If the displacement is larger than half the patch size, the correlation peak is folded back into the matrix and will appear in the opposite side, i.e., the sampling criterion (Nyquist theorem) is violated causing the measurement to be aliased [134]. Therefore, before undertaking any application it should be made sure that the flow under investigation is not subjected to overly long particle displacements. A simple way to control this is by varying the sampling interval of acquisition (or frame rate).
In highly sheared flows, with algorithms that use the image deformation technique, the interrogation accuracy and robustness is significantly improved, however, the computational cost is generally increased owing to the iterative structure of such advanced algorithms, and by the additional image re-sampling process [150].

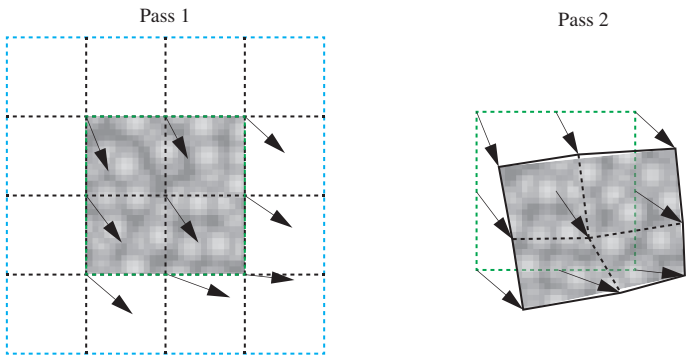

Figure 3.3: Principle of the window deformation technique.

3.4.2 PTV error type and reduction

PTV does not suffer from gradient biasing since particles are tracked individually and the particle image is not affected by displacement gradients. However, PTV operations inherit two main sources of error, namely the inaccuracy in determining a particle position and errors arising from the linear approximation of the particle trajectory during the time taken to move from one image to the next. In the following, the errors and simple investigations designed to determine their magnitude are described in detail.

3.4.2.1 Particle position error

Particle position error can induce unrealistic disturbances to the measured velocity field. It is likely to be significant at very high acquisition rates due to the large relative errors induced by the centroid estimates in the total displacement. In Sec. 3.2 it was pointed out that there are different algorithms to detect particles and determine their locations. Cowen et al. [46] suggested that the optimal algorithm may also be a function of particle image diameter (i.e. the diameter of the particle in number of pixels). Based on this consideration, the effect of particle size on centroid-detection error during a rotational motion were experimentally investigated. The motivation for using a circular motion was to facilitate the experimental procedures, hence allowing the effect changes in lighting conditions and camera settings to be determined while isolating the motion of an individual particle, and providing the possibility of changing its position (or radius) with respect to the centre of the circular motion.

An aluminium disk covered with matt black paint was mounted on an electric motor to allow for rotation. A single white bead (with diameter d=1.5 mm, see Table 4.1) taken from the experimental monodisperse flows was then glued onto the disk contrasting with the dark background (Fig. 3.4). The particle linear velocity was estimated as $\mathbf{v} = r\omega$, where r is the radius for the midpoint of the disk and ω the measured (in RPM) angular velocity. Knowing the radius from the midpoint of the disk allowed a comparison to be made of the measurements with the true particle positions during the circular motion. Measurements were taken for different particle image diameters by outdistancing the camera. The linear speed and the acquisition frequency were varied and it was found that they had negligible effect on the centroid-detection error magnitude. In addition, the results from the particle-mask-correlation method alone and its implementation with a least-square fit (Fig. 3.2) collapsed onto the same curves.

Fig. 3.5(a,b) presents data for two linear speeds. Note that in Fig. 3.5(a) a minimum error is found for a particle image diameter of three pixels. That is, when the particle is approximated by an intensity profile which spans three pixels in diameter and with an intensity peak located in its centre, the sub-pixel position estimated using the three-point Gaussian

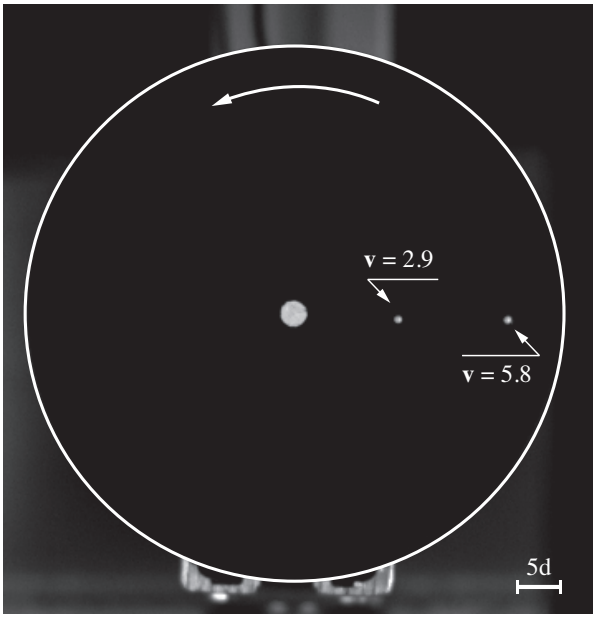

Figure 3.4: Apparatus used to investigate the particle position error for PTV.

approach performs best. For smaller diameters, measurements are primarily influenced by pixel-locking, whereas for larger diameters, the Gaussian fit tends to be skewed, acting to bias the particle positions. At three pixels the magnitude of the RMS error was expected to be close to zero, however, added to the uncertainties of the particle-mask-correlation method is a slight eccentricity of the disk that affected all of the measurements. A further control depicted in Fig. 3.5(b) was made by dividing the uncertainty by the respective particle diameter. This plot shows that three pixels is again the minimum size of particle that should be considered. The ratio being somewhat flat for diameters larger than three pixels suggests that the result is insensitive to the choice of particle image larger than this value.

The analyses were restricted to a maximum particle image diameter of ten pixels. To further validate the quality of the results additional analyses should be conducted at resolutions greater that this value. In fact, with higher particle resolutions and an illumination that enables the peak to be found always at the particle centre, it could be also possible to obtain accurate results without considering only certain particle resolutions. However, in the chute experiments conducted with dry granular flows, it was difficult to perfectly control all the experimental conditions (e.g. illumination). The use of a low particle resolutions ($\approx$ three pixels) to extrapolate measurements with minimized particle position uncertainties was considered the most appropriate and computational efficient choice.

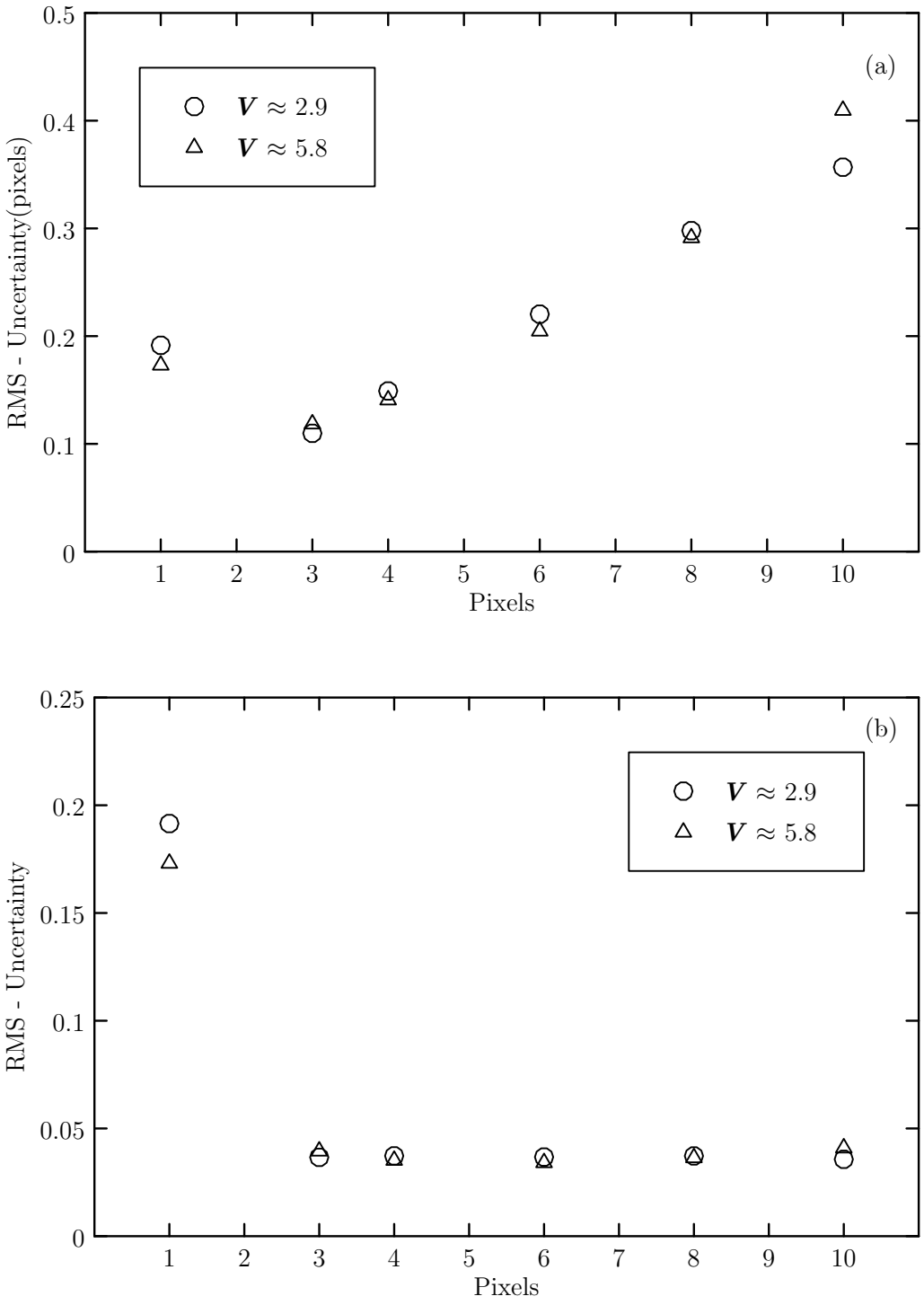

Figure 3.5: Particle position uncertainties associated with a single particle undergoing a circular motion. Data are shown for two different linear velocities: ≈ 2.9 (0.35 ms^{-1}) and ≈ 5.8 (0.7 ms^{-1}). (a) Uncertainty versus particle diameter; (b) ratio of uncertainty to respective particle diameter. For particle tracking the minimum error is found when the particle image is three pixels in diameter.

3.4.2.2 Linear approximation error

The second source of error is associated with the acceleration of the particles, i.e. that the real particle trajectory is approximated by linear displacement. This error is strongly affected by the choice of the acquisition frequency (or frame rate). Feng et al. [54] pointed out that a high frame rate is not always necessary to capture the true behaviour of the process under analysis. The simplest tracking method assumes that the particle travels between two images in a straight line at a constant speed. If the positions of a particle before and after a time interval Δt are $\mathbf{x}_i$ and $\mathbf{x}_{i+1}$ respectively, then the velocity $\mathbf{v}_i$ can be estimated as:

$$\mathbf{v}_i = \frac{\mathbf{x}_{i+1} - \mathbf{x}_i}{\Delta t} \tag{3.2}$$

In the work of Feng et al. [54], a uniform circular motion was used to show the error arising from the particle accelerations. Assuming zero position error, at large Δt the two-frame tracking method in Eq. 3.2 approximates this ideal circular motion to that of a polygon. At smaller Δt, the polygon has more sides, resembling the circle more closely.

When the particle position uncertainties are added to the process, the polygon deforms in a manner proportional to the magnitude of the error. Motivated by this and having information about the particle position errors from the previous analysis, an experiment similar to that of Feng et al. [54] was reproduced. A simple simulation was carried out where a single particle performs a uniform circular motion. A position error with maximum magnitude equivalent to that at three pixels, as in Fig 3.5, was randomly added to the particle. The distorted positions of the particle were updated during motion and recorded at different sampling intervals Δt. The velocity calculated in Eq. 3.2 was then used to compute a time series for the kinetic energy, $KE(t) = m|\mathbf{v}(t)|^2/2$, and the ensemble average, $\langle KE \rangle$, was extracted over 1000 circular periods. The values of $\langle KE \rangle$ were then compared to the true kinetic energy $KE_{true} = m|\mathbf{v}_p|^2/2$, where $\mathbf{v}_p$ is the selected particle velocity having zero position error (i.e. the radius is constant).

The radius of the particle from the centre was varied in order to change the magnitude of $\mathbf{v}_p$ under the same experimental condition. The influence of the sampling interval Δt was also analysed. The choice of differing radius, and as a consequence $\mathbf{v}_p$, is based on the fact that in a typical free-surface granular flow the velocity profile changes with depth, i.e. a typical measurement is exposed to a large dynamic range. Three different velocities $\mathbf{v}_p$, and radii representative of the experiments were chosen: 4.1 at $6.7d$ (0.5 ms^{-1} at 10 mm), 8.2 at $13.3d$ (1 ms^{-1} at 20 mm), and 12.8 at $20d$ (1.5 ms^{-1} at 30 mm), respectively. The data produced from these simulations are reported in Fig. 3.6.

Fig. 3.6 is useful to illustrate the combination of errors. Positive errors that increase

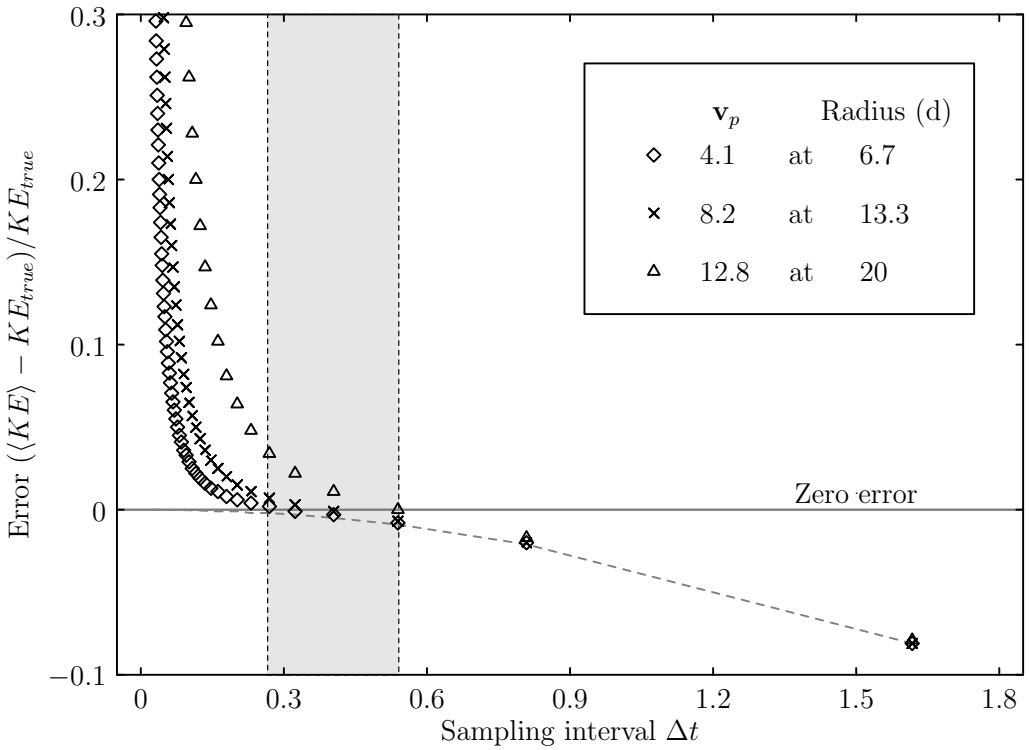

Figure 3.6: Velocity errors associated with particles undergoing a circular motion at different velocities ($\mathbf{v}_p$) and radii. The value of $\langle KE \rangle$ is compared with the true kinetic energy $KE_{true} = m|\mathbf{v}_p|^2/2$ for different sampling intervals (Δt). Positive errors due to particle position uncertainties arise at small Δt (i.e. fast frame rate) whereas negative errors originate as a result of particle acceleration at large Δt (i.e. slow frame rate). The dashed-line in the negative region represents errors produced by particle acceleration only. There is a range (shaded area) along the zero-error line where the total error should be the smallest.

the measured KE above the true value, above the zero-error line, originate due to the enhanced influence of centroid detection errors relative to the total displacement between two time intervals. This issue becomes increasingly severe for small sampling intervals (i.e. fast frame rate). Conversely, negative errors that decrease the measured KE are mainly due to the error involved in approximating the particle displacements to a straight line (Eq. 3.2). It is evident that for large sampling intervals, the real particle trajectories developed during their normal evolution is non-linear (e.g. curved). This means that the movement is undersampled and as a consequence it can result in a strong aliasing of the measured position signal. For reference, the dashed-line in Fig. 3.6 represents the error due to this effect only. This source of error is effective for large Δt (i.e. for slow frame rate). However, there is a value of Δt when the data crosses the zero-error line, that corresponds to the minimization of errors. Such information can be used to help the

choice of a sampling interval that reduces the total error within the range of velocities considered for a given experiment .

The velocities $\mathbf{v}_p$ analysed here with their respective radii yield a sampling interval that ranges approximately between 0.26 and 0.54 (shaded area in Fig. 3.6), corresponding roughly 150 fps (frames per second) to 350 fps. The limits of the shaded area were drawn by simply observing where the minimum and maximum velocities (4.1 and 12.8) touched the zero-error line. Within these values the expected total error should be minimized. Notably, Fig. 3.6 suggests that there is no unique value of Δt suitable for examining the whole of a granular flow. Best practice would then require a combination of different acquisition frequencies obtained by analysing different regions of interest at different Δt. However, there is also need to consider that in most physical experiments, particles do not experience the same idealized circular motion as investigated here, with the motion of individual particles varying from that of surrounding ones. Hence, while the values reported in Fig. 3.6 have been used here to guide the choice of an indicative initial (highest) frame rate before undertaking the laboratory experiments on granular flow, they should be treated with some caution.

From their simplified simulation, Feng et al. [54] proposed a scheme to minimize the total error. The process should be analysed not only at the initial frame rate but also at different Δt obtained by skipping frames (i.e. increasing Δt) from the original recording. This strategy should continue until convergence to a single averaged value for a quantity (e.g. $\langle KE \rangle$) is reached. For granular flows, this is difficult to achieve, since as stated above, the flow characteristics (e.g. velocity gradient) vary with depth. A better choice would be to study the convergence of the KE profile rather than an averaged value. Analyses can be iterated by skipping frames until a value of Δt deemed close enough to those found in Fig. 3.6 is reached. This unique value will not be the correct one in all parts of the flow due to the change of velocity with depth, however, by employing values similar to those reported in Fig. 3.6, these can be used to avoid using overly slow or fast frame rates, i.e., falling into areas where the error is severely dominated by particle position or acceleration uncertainties.

3.5 Conclusion

In the first part of this chapter particle image velocimetry (PIV) and particle tracking velocimetry (PTV) were briely reviewed and the common sources of error and the methods used for their reduction were discussed. While there are known procedures to mitigate the error in PIV, error frameworks for PTV were lacking. It should also be noted that, to the knowledge of the author, error frameworks associated with PTV only exist for steady and long-lasting granular flows (e.g in a recirculating flume [10]). The difficulties with quasi-steady and short-lasting flow measurements (as in dam-break experiments) is that, by definition, steady states are not obtained. Hence, for this technique, the work carried out in this chapter focused on the removal of potential sources of error affecting measurements of granular temperature that could be *a priori* avoided, rather than methods to deal with these in a *post hoc* situation. For this reason a series of controlled experiments of a circular motion was used to illustrate the errors associated with the particle centroid uncertainties and the linear approximation of particle trajectories. The former was reduced for a minimum particle image diameter of approximately three pixel. The latter required an appropriate choice of the sampling interval (or frame rate). The results reported in Sec. 3.4 have been used to guide the choice of image resolution and of an indicative initial (highest) frame rate before undertaking the laboratory experiments.

4. Experimental investigation of dry granular flows

4.1 Introduction

In the first stage of this research, simple dry monodisperse granular flows were studied at small-scale. The reasons for this were easy control over the experimental conditions and test repeatability. These experiments were used to investigate simple flows down an inclined and assess the capability of non-intrusive measurement techniques in measuring second-order statistic fields (e.g. granular temperature).
The description of the apparatus and material properties are given first in Sec.4.2. The dimensionalization of the different flow properties is given in Sec. 4.3. Next, Sec. 4.4 outlines the procedure used to estimate the flow fields of interest, namely, velocities, granular temperature and solid concentration. A preliminary test conducted to assess the performance of the two measurement techniques previously introduced in measuring granular temperature is presented in Secs. 4.5.1 and 4.5.3. Finally, once the performance of the two techniques has been assessed based on the preliminary tests and the validation presented in Ch. 6, additional dry granular flows down an inclined chute are analysed and described in Sec. 4.5.4.

4.2 Apparatus and materials

The flume used in this study is a sloping rectangular 10 cm wide and 150 cm long channel that can tilt from horizontal up to 45° (Fig. 4.2(a,b)). At one end, the material is held inside a hopper, which can contain approximately 20 kg of material. The release of the material was controlled by a double-slider gate mechanism. The outer gate held the material inside the hopper, while the inner gate was set at a certain height from the flume bottom enabling control of the releasing flow height (or flow rate) that develops downstream. The basal roughness is created by gluing to the flume bottom the same material used to produce the granular flows. The walls are made of Perspex, allowing observation at the sides. The sidewall surface of the granular flow of interest is illuminated by two 50W DC LED floodlights and captured via a high-speed camera (Phantom Miro 310).

The materials used for the experiments are sand (David Ball Ltd, Fraction A) and almost spherical ceramic beads (Sigmund Lindner Gmbh). A batch of sand was sieved to produce a nearly monodisperse material. While sand has grains with angular shape, the ceramic beads were selected for several practical reasons: spherical particles are used in the majority of granular flow experiments, accordant behaviour is assumed in many theories and the majority of centroiding algorithms require spherical particle shape.

The circularity of spherical beads was also assessed in order to estimate an average value of shape anisotropy. Images of a single layer of static and evenly arranged particles on a plane (Fig. 4.1) were analysed and the edges identified via a Canny edge detector in Matlab. It was then straightforward to measure areas (A) and perimeters (P) of each particle and calculate an average value of circularity $\xi = (4\pi A)/P^2$. Assuming an ellipsoidal shape of the particles it was also possible to estimate an average aspect ratio ($\mathcal{A}_\mathcal{R}$) calculated as the ratio of the major axis to minor axis of the detected particles [175]. This measure, together with all the other material characteristics, are listed in Table 4.1.

Table 4.1: Dry granular material characteristics. $^{(\star)}$ shear box test; $^{(\dagger)}$ tilt test.

Material	Size - (mm)	Mean diam. (d) (mm)	Friction (ϕ) (deg °)	Density (ρ_p) (kg·m^{-3})	Circularity (ξ) (-)	Aspect ratio ($\mathcal{A}_\mathcal{R}$) (-)
Beads	1.4 - 1.6	1.5	$22^\star$ - $24^\dagger$	2430	0.88	1.1
Sand	1.4 - 1.7	1.55	$34.5^\dagger$	1520	-	-

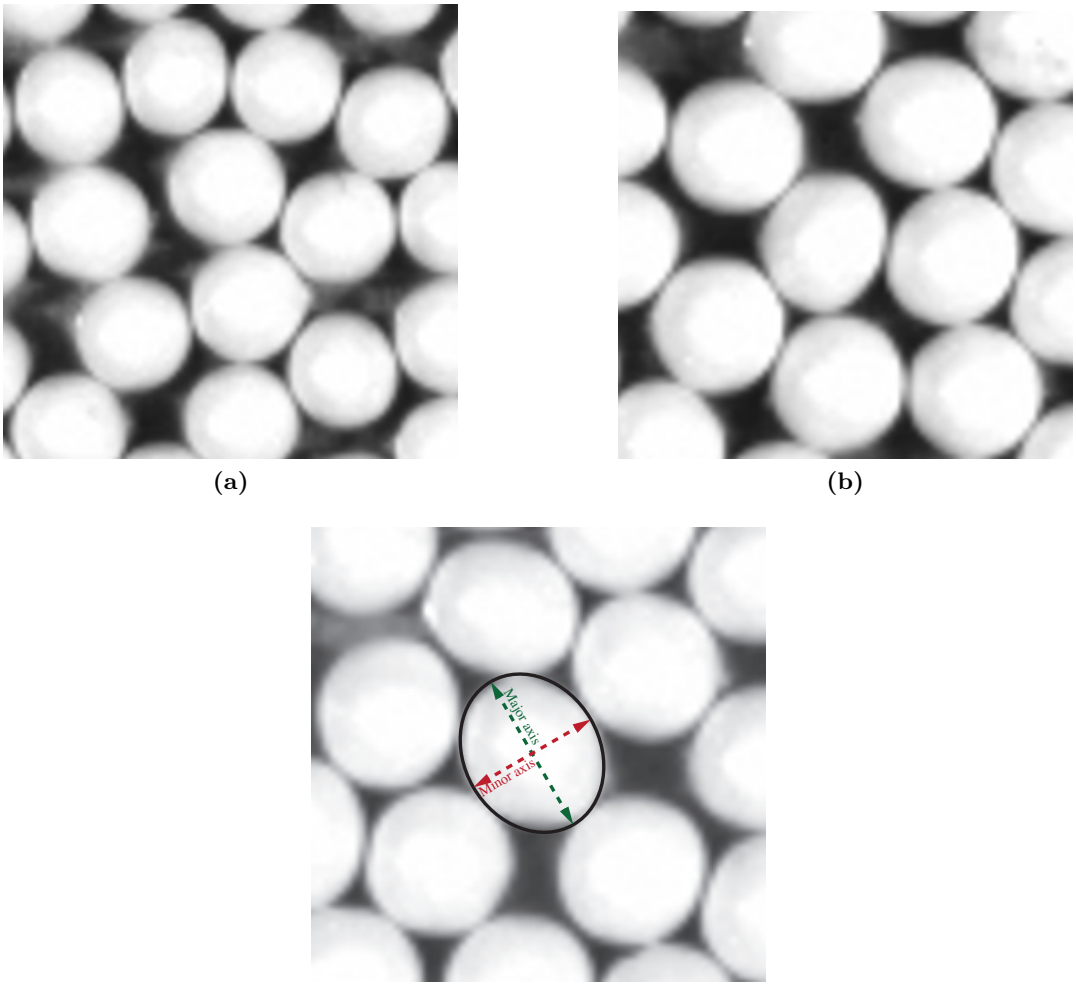

Figure 4.1: Shape anisotropy of ceramic beads. (**a**,**b**) Zoomed views of the ceramic beads highlighting the different shapes. (**c**) An ellipsoidal shape of the particles was assumed and the aspect ratio ($\mathcal{A}_\mathcal{R}$) calculated as the ratio of major axis to minor axis.

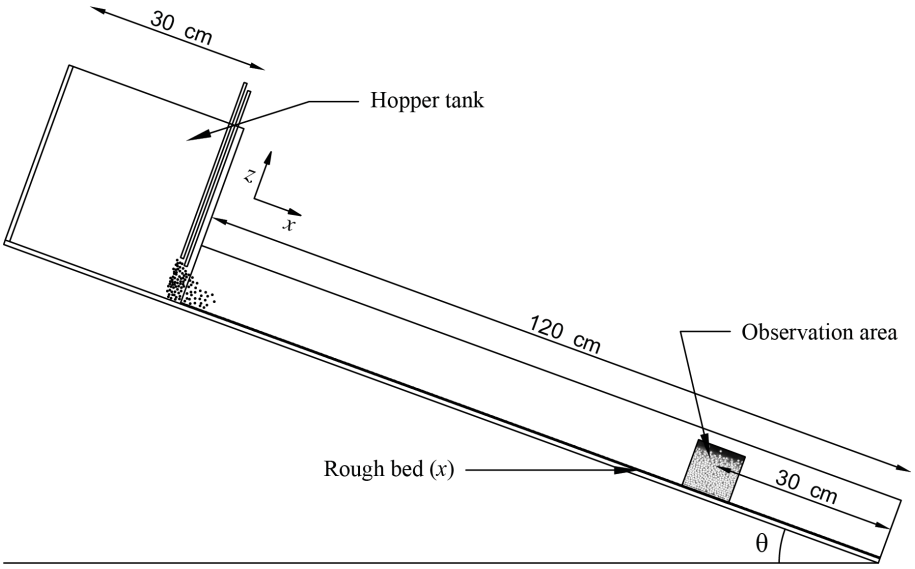

(a)

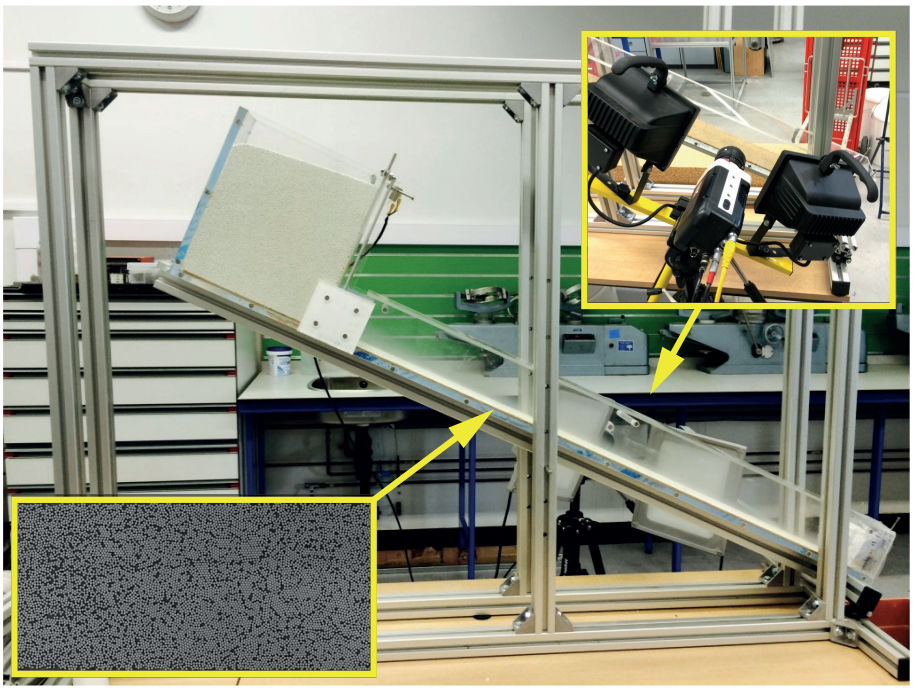

(b)

Figure 4.2: Small scale apparatus for the study of dry granular flows. Sketch and dimensions (**a**); example of the set-up ready for the experiment (**b**)

4.3 Unit description

In the following, the analyses refer to monodisperse flows with a characteristic mean diameter d' (differing slightly for the two materials used here, see Table 4.1), using the gravitational acceleration $g' = 9.81$ ms^{-2} and particle mass $m' = V\rho_p$, where for a sphere the volume $V = \frac{1}{6}\pi d'^3$. The results are given in nondimensional form by defining the following normalization for the distances, times, velocities (in the flow direction u, normal-to-bed direction v and the resultant $\mathbf{v}$, respectively), granular temperatures, stresses, kinetic energies and shear rates ($\dot{\gamma}(z) = (\partial u/\partial z)$):

$$d = 1, \qquad t = t'/\sqrt{d'/g'}, \qquad u = u'/\sqrt{g'd'}, \qquad v = v'/\sqrt{g'd'}, \qquad \mathbf{v} = \mathbf{v}'/\sqrt{g'd'},$$

$$T = T'/g'd', \qquad p = p'/(m'g'/d'^2), \qquad KE = KE'/m'g'd', \qquad \dot{\gamma} = \dot{\gamma}' \cdot \sqrt{d'/g'}.$$

where $t', u', v', \mathbf{v}', T', s', p', KE'$ and $\dot{\gamma}'$ indicate the respective dimensional forms.

4.4 Outline of the PIV and PTV procedures

The high-speed camera was positioned and aligned to visualize the side of the chute, i.e., no systematic measurements at the top of the flows were made. Digital images of the moving mass were then recorded with a resolution of 256 x 256 pixels (Fig. 4.3(a,b)). The maximum frame rates were 1000 and 1400 fps (Δt of 0.08 and approx. 0.06, respectively) depending on the velocity of the flow. Because of the finite memory of the high-speed camera, the resolution was chosen so that the flows could be recorded for their entire durations. The initial frame rates were higher than those recommended in Fig. 3.6, however the goal was to highlight the effect of small sampling interval on the measurements. More details are given in Sec. 4.5.3. For each test, a time series lasting $t = 162$, or equivalently 2 s, (i.e. within the limit of the apparatus) was extracted from the original recording in the fully developed, steady region of the flow, about 30 cm before the outlet (Fig. 4.2(a)).

Following the scheme mentioned in Sec 3.4.2.2, the flows were investigated at the original frame rate and by progressively increasing the sampling interval by skipping one frame, i.e. doubling Δt, in each previous set. The additional frame rates obtained from the 1000 fps case were 500 fps, 250 fps and 125 fps (Δt equal to 0.16, 0.32 and 0.64). Similarly, for the 1400 fps case, 700 fps, 350 fps and 175 fps (Δt of approximately 0.12, 0.24 and 0.46), were produced. Note that increasing Δt to this extent brings its values within the interval highlighted in Sec. 3.4.2.2, Fig. 3.6.

For the PIV analysis of sand and beads flows an open source algorithm PIVLab [165] was employed. This particular PIV method uses a multi-pass approach to deform the interrogation areas in the second pass based on the estimate obtained in a previous one. Hence the analysis includes a state-of-the-art image deformation technique (e.g. [150]) which reduces the error associated with the correlation calculation by deforming the interrogation windows according to the local velocity gradient (shear deformation). The effect of smaller or larger areas was not studied on all the flows as in some cases the signal to noise ratio, defined as the ratio between the primary and secondary peaks in the correlation plane, was always reliable.

For PTV, the particle-tracking algorithm proposed by Brevis et al. [32] was used. Since the application of PTV is strictly connected to the particle centroid recognition, the following procedure is limited to spherical particles since the centroid identification of sand grains affects the measurements of granular temperature, i.e., the centroids estimated form angular particle shapes visualized in 2D images will not be the same over time thus increasing the particle position error. Upon the application of the centroid estimators, the outermost faint edges of the particles were removed by a morphological image opening. To do this the particles were allowed to have a diameter of approx. five pixel. This conflicts somewhat with the minimum diameter by which a particle should be approximated for a proper analysis in both PIV and PTV (three pixels as shown in Fig 3.5(a)). However, diameters smaller than five pixels would make the edges very difficult to recognize. Considering smaller particle diameters, i.e. three pixels, the particles could still be separated by a background subtraction. However, some particles would then result in being incorrectly approximated by single pixels and hence would be prone to pixel locking. For larger diameters, e.g. five pixels, the background subtraction affects the estimation of the centroid position only slightly. Following this procedure, the particle diameters in the image frames were reduced from the original five pixels down to approx. three pixels (e.g. see Fig. 3.2).

Although the particle images could be resized using background subtraction in this way, the particle-mask-correlation method alone still led to poor position estimates, due to the necessary thresholding used to remove the background. This was clearly revealed when the centroids were plotted over several frames. However, this information could be used to estimate particle locations for a least-squares method (e.g. as in Eq. 3.1), as discussed in Sec. 3.2.2.1.

The functional model for Eq. 3.1 was a Gaussian distribution, in this case a good approximation due to the spherical shape of the experimental material. The chosen parameter vector was $\boldsymbol{\theta} = (\tau_{00}, X_0, Y_0, d, \varrho)$, where ϱ is an additional factor in radian units, which allows for rotation of the pixel intensity grid associated with each particle, thus compen-

sating for the surrounding particles. A sub-matrix was extracted from the original image around the guessed location. The characteristic brightness of a particle was isolated from the others (each giving the centroid coordinate with respect to one axis) and curves were fitted to the data (e.g. Fig. 3.2). This process was iterated for all the particles in the image. This scheme rendered the system considerably more stable over consecutive frames while improving the localization of the particle centroids at the same time.
The aforementioned processing steps were applied automatically to all successive images in the sequence. At a later stage, the tracking algorithm was initiated to sequentially match the particles in each pair of consecutive frames, producing arrays of particle displacement vectors. This arrangement was then filtered to remove erroneous and spurious displacements that can contaminate the data by using the two filters mentioned in Sec. 3.3.

4.4.1 Calibration

Ultimately, both PIV and PTV require a transformation for relating information in pixels to physical lengths. Prior to each experiment, a calibration grid (Fig. 4.3(c)) composed of regular circular marks spaced by 4 mm was located at the wall exactly in the region of interest. An image of this target grid was captured before each test and the coordinates of the calibration marks detected with sub-pixel accuracy. These coordinates were then associated with an undistorted grid (mm units) and then interpolated by using the built-in Matlab function ScatteredInterpolant [31] as shown in Fig. 4.3(d). The latter is an approach based on linear interpolation that uses Delaunay triangulation. The displacements are converted into real world coordinates and corrected for distortion induced by the imaging device and the optical distortions induced by the experimental facility.

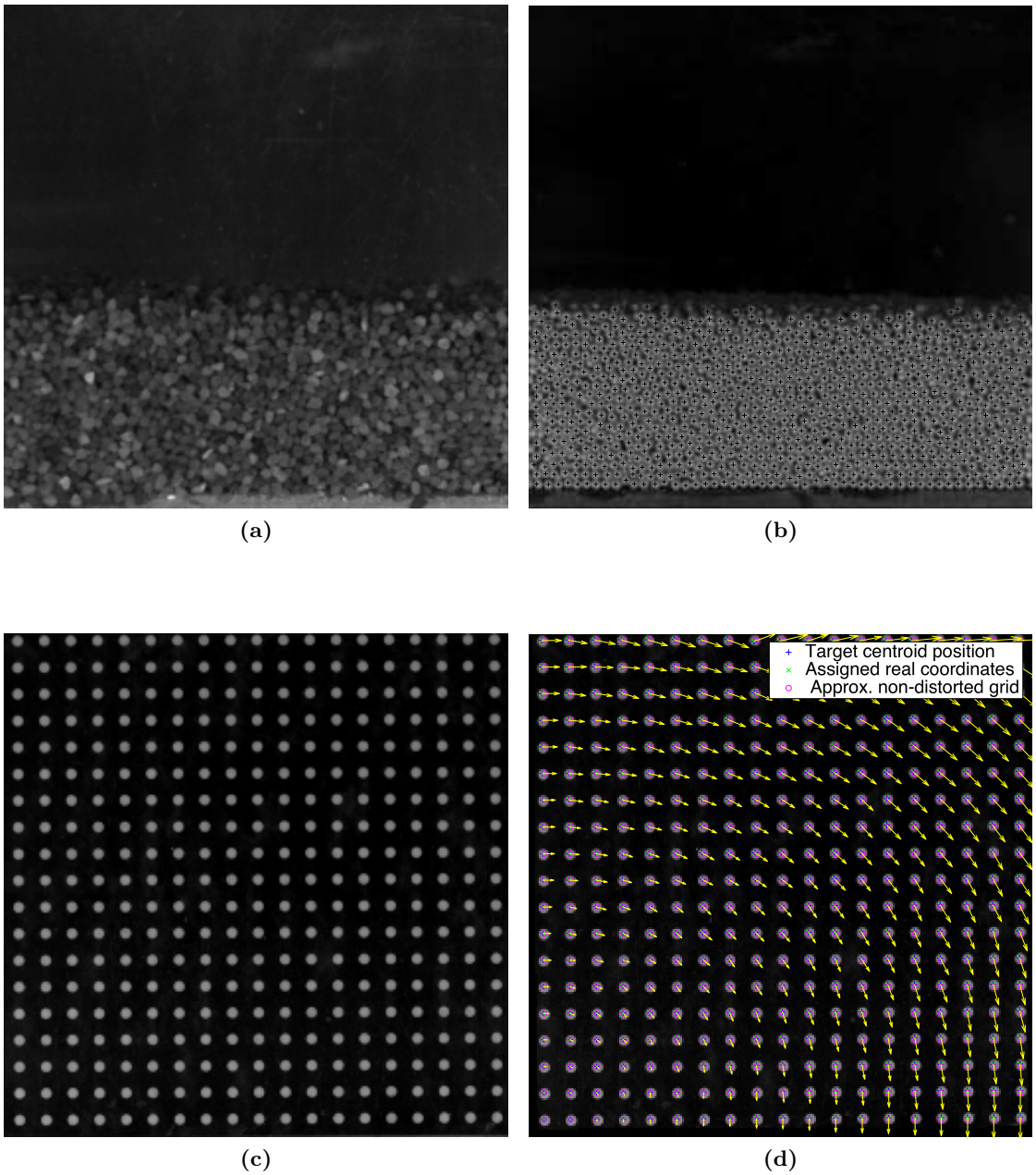

Figure 4.3: Typical flow images for (**a**) sand and (**b**) bead flows at a resolution of 256x256 pixels detailed with positioned particle centres. Calibration target: (**c**) original image and (**d**) during the calibration procedure. In this example the target was tilted from the horizontal with respect to the first centroid in the bottom left corner. Vectors indicate the translation with respect to a non-distorted grid.

4.4.2 Data processing

Upon completion of the PIV and PTV analyses, the resulting displacement data were used to compute the corresponding instantaneous and mean velocities. In PIV, the displacements obtained from cross-correlation divided by the sampling interval yields the components of the instantaneous velocity field (u_i, v_i), generally given in a regular mesh partitioned into rows and columns. The mean velocity is obtained as the temporal average of all velocities belonging to the same rows of interrogation regions (or columns depending on the flow direction) for the entire duration of the flow.
In PTV the in-plane instantaneous velocity is approximated by Eq. 3.2. Binning is then used to extract velocity profiles. The flow is subdivided into non-overlapping horizontal slices of thickness one particle diameter. The mean velocities are then constructed by separately taking the ensemble-average velocities of each bin in the two directions.
As a general reference, the slope-parallel (streamwise) mean velocity component $\bar{u}$ for each K^{th} bin/row is given by:

$$\bar{u} = \frac{\sum_{N_k}^{i=1}(u_i)_k}{N_k} \tag{4.1}$$

where N_k is the total number of velocity vectors in the K^{th} bin/row across the entire flow. Another field property of interest in granular flows is the square of the velocity fluctuation, also known as the granular temperature. It provides a measure of the energy associated with the fluctuating nature of the granular motion, i.e. the agitation within the flow and is of importance to the transfer of stress via collisions.The granular temperature (T) is defined from the measurement of fluctuation components. The slope-parallel fluctuation component is given as:

$$(u_i^*)_k = (u_i)_k - \bar{u}_k \tag{4.2}$$

The mean of the squares of this quantity is calculated for each bin/row as follows:

$$\langle (u^*)^2 \rangle_k = \frac{\sum_{N_k}^{i=1}[(u_i^*)^2]_k}{N_k} \tag{4.3}$$

Eqs. 4.1, 4.2 and 4.3 similarly apply to the slope-normal (transverse) velocity component v. The third component of velocity j was not measured in these experiments, thus the granular temperature is:

$$T_k = \frac{1}{2}\langle [(u_i^*)^2]_k + [(v_i^*)^2]_k \rangle, \tag{4.4}$$

where the angle brackets denote ensemble averaging. By following this definition, granular

temperature has units of squared velocity.

4.4.3 Estimation of density profiles

Measurements of solid concentration ν (or, alternatively, porosity $\varphi = 1 - \nu$), defined as the ratio of volume occupied by the solid to the total volume, are useful to examine the dependency of basic flow properties such as velocity and granular temperature on ν. To date, simple, cost effective and very accurate measurements of this quantity are still challenging to reproduce, especially for dense and opaque systems. This section describes simple methods used to estimate two- and three-dimensional solid concentration profiles based on image analysis and information obtained from the centroiding procedure for PTV.

For spherical particle flows, the fact that the flows are made of spherical, nearly uniform, particles can be exploited to obtain concentration profiles. If the particles can be visualized at a sufficient pixel scale, their edges can be easily distinguished and an algorithm can be used such as that based on the Hough transform for finding circles in a image [16]. While keeping the same chute conditions (i.e. inclination and gate height), similar flows to those used to measure other properties derived from the velocity fields were performed, but at a larger spatial resolution of 768 x 576 pixels. In these experiments the particles were approximated to ≈ 27 pixels in diameter compared to the five pixels adopted to minimize the particle position errors. This was necessary to improve the robustness of the Hough transform detection and remove spurious circular shapes developed at smaller scales. Prior to the direct application of the Hough transform, a morphological image opening was applied to the image to enhance the foreground particles. The particle circumferences of the first layer closest to the side-wall were then outlined by the edge detector. Images were subdivided into bins (27 pixels in height Fig. 4.4(a)), which in turn allowed for the calculation of the particle areas (the entire area or part if the particle was shared across two bins). The sum of all areas divided by the total area of the corresponding bin yielded the value of two-dimensional solid concentration.

It should be noted that the results are affected by the side-walls and do not represent accurately the local solid concentration throughout. The algorithm also is not able to isolate particles leaving the side-walls unless the particle partially disappears behind the first layer. It was assumed that the particles remained close to the side-walls for a long enough period of time, although this may not be the case, especially at steeper slopes. Furthermore, the algorithm has the tendency to construct smaller circumferences than the real particle edges leading to underestimations in the solid concentration. To examine this issue, specific parameters (e.g. the minimum and maximum radii required for the detection of circles) were varied which resulted in slight differences in magnitude of solid

concentration while the profiles changed little.

In the three-dimensional case, concentrations may be theoretically estimated from the point density of visible particles per unit image surface [1]. However, this method is limited to sparse dispersions and becomes unsuitable for dense flows due to the prevalence of occlusion effects [36]. On the other hand, when the mean interparticle distance becomes of the order of the diameter (as in the case of dense systems), neighbouring particles are forced to organize with respect to each other into increasingly ordered assemblies. This creates short-range correlations between grain positions allowing the characterization of the local particle arrangement with local descriptors, as proposed by Capart et al. [36]. The ordering can be estimated based on the roundness of the Voronöi polygons. From the centroiding procedure for PTV, these can be constructed based on the known position of each particle and those of the surrounding ones (Fig. 4.4(b)). Depending on the local concentration of the system, each particle has its own configuration (a polygon with a certain number of sides). The shape of the polygon can then be related to the concentration via a Voronöi-based indicator. This is provided by the ratio $\xi = 4\pi A/P^2$, i.e. circularity, where A and P are the area and perimeter of the polygon, respectively. Once the flow has been divided into horizontal slices (or bins as described in Sec. 4.4.2) a local average value of ξ is obtained for a sufficient number of individual polygons over time. This average value ($\bar{\xi}$) is then used to determine a three-dimensional granular concentration profile based on the normalized power law relation calibrated by Capart et al. [36]:

$$\frac{\nu}{\nu_s} = \left(\frac{\bar{\xi} - \xi_{min}}{\xi_{rcp} - \xi_{min}} \right)^{\beta} \tag{4.5}$$

where ν is the solid concentration of the solid material, ν_s^{3D} is the 3D random close packing for frictional spheres (with $\mu = \tan(24°) \approx 0.45, \nu_s^{3D} \approx 0.59$ in Table 2.1) and $\xi_{min} \approx 0.72$, which is derived from Monte-Carlo simulations [123]. The other parameters, $\xi_{rcp} = 0.84$ and $\beta = 3.5$ were calibrated by Capart et al. [36] based on fluidization cell tests.

The validity of this method has also been tested by Larcher [105] based on a comparison with 3D stereoscopic measurements. He found that correct values of solid concentration based on a roundness estimate of the Voronöi polygons can be extended up to $\nu \approx 0.55$. Hence, it is not expected that Eq. 4.5 applies for very densely packed systems. Other effects (e.g. particle shape or sidewalls) in addition to volume exclusion can contribute to the ordering of the particles, leading to an erroneous solid concentration estimation. When the roundness-based estimator is used, such effects can lead to unreasonably high concentration values. Therefore, a limiting maximum concentration (ν_s) must be imposed [10]. In other words, all the values that exceed this threshold are assumed to be in the maximum packing state ν_s. It is also expected that in the range $0.55 < \nu < \nu_s$ the results

yield only an approximate indication of ν. Applications of the two methods are reported and compared in Sec. 4.5.

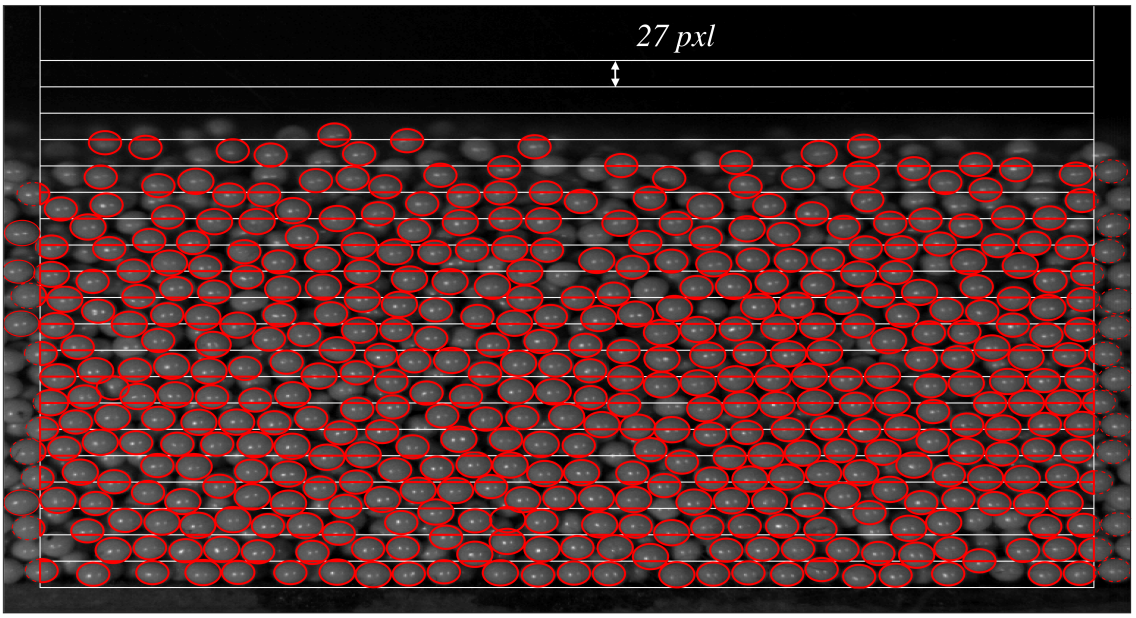

(a)

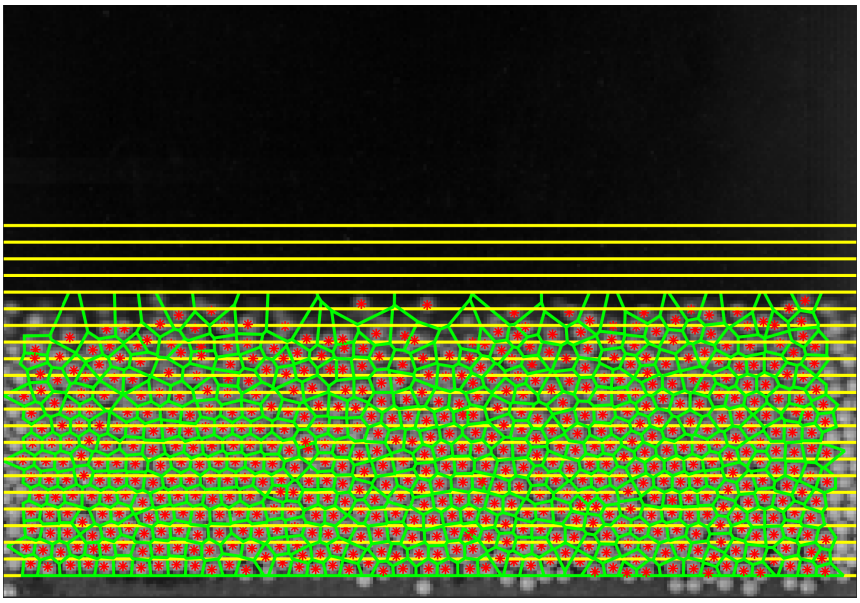

(b)

Figure 4.4: Methods for the estimation of solid concentration from flow images. Partition of particle edges for the determination of an areal fraction in 2D (**a**). Voronöi tessellation based on particle centroids for a 3D volume fraction estimation (**b**).

4.5 Experimental dry granular flows on an inclined channel

4.5.1 Flows of sand

A first series of analysis was conducted using the sieved batch of sand. While keeping the same experimental conditions, i.e., mass and flow rate, flows were released for three different inclinations, 35°, 37.5°, and 40°. These inclinations were chosen so that the shallowest slope was just above the material friction angle (Table 4.1) and the steepest still permitted sufficiently long steady states. For slopes greater than 40° steady states may also be possible for short periods of time, however, at such angles granular flows tend to accelerate, so steady states are hard to capture. Once released, the flow front was generally very disperse and chaotic. After this phase a uniform flow height was reached for a certain period of time until there was no more material available inside the hopper. The shape and texture of the particles did not allow the use of PTV, for this reason PIV was employed. Particles were assumed to be five pixels in diameter, although this slightly varied due to the irregularity of the grains. For the multi-pass method followed by PIV the selected interrogation regions were 24 x 24 and 12 x 12 pixels, for the coarse and refined grid, respectively. This set a maximum of approx. 5 particles in the smallest interrogation region (i.e., the least seeding concentration required for a correct correlation peak localization). This implies that the measured values are not referred to a single particle but to a group of particles. It is known that the interrogation area has an effect on the final measurements. While velocity profiles are less sensitive to this, very small interrogation regions (of the order of a particle diameter) produce high levels of noise whereas larger areas progressively reduce the noise (or fluctuation velocity) and hence, granular temperature measurements [145]. Here, only the framework outlined in Sec. 3.4.1 for the reduction of potential measurement errors in PIV was considered, while the effect of the different interrogation regions was studied in more detailed with synthetic images in Ch. 6.

The first analysis was conducted to verify whether the flows reach a steady state, in other words, if the flow properties (e.g. mean velocity) do not change considerably over time. Using PIV, the flows were analysed for their entire duration in order to assess how the mean velocity of all visible particles changed over time. The flow was deemed at a steady state when the mean velocity (black lines) was approximately constant over time. These results are depicted in Fig. 4.5 for the three chosen inclinations. It can be seen that apparent steady mean velocities (shaded areas) were sustained after some time from the commencement of the recording, i.e., after the dispersed and less steady front (black line). This part together with the slowing final part during the cessation of the flows were disregarded from the computations. At 40° a steady mean velocity was possible for a

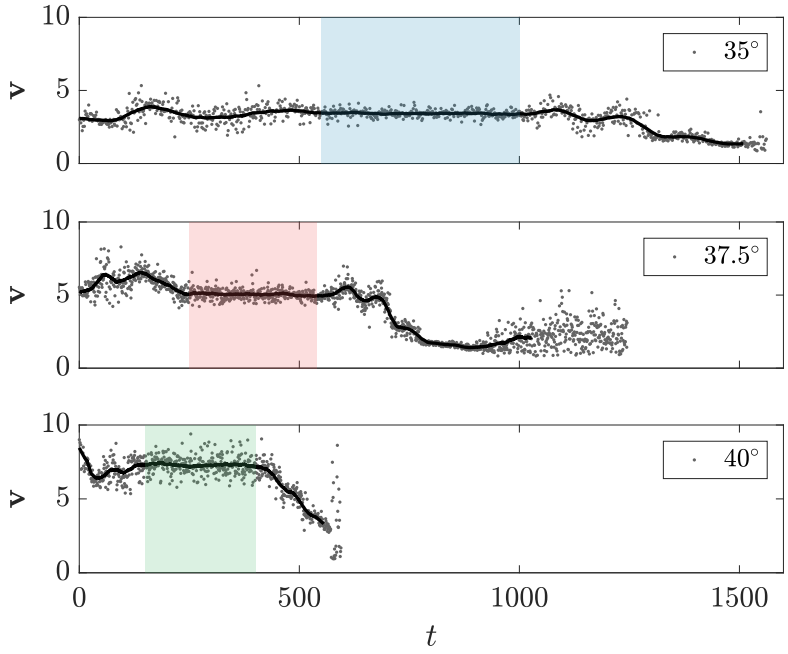

Figure 4.5: Depth-averaged velocity of all visible particles over the entire duration of sand flows. The black line shows the mean velocity over time. Shaded areas represent the duration of the steady states, i.e. where the mean velocity remained roughly constant over time.

shorter period of time when compared to the other inclinations. However, avoiding the initial and final parts of the flow, it was still possible to obtain a minimum time series lasting $t = 162$ (i.e. 2 s). All measurements were averaged over this time interval also for 35°, and 37.5° (although they sustained a steady state for longer) to allow comparisons. Using the procedure explained in Sec. 4.4, i.e., by progressively increasing the sampling interval Δt, velocity profiles averaged over the time series considered are shown in Fig. 4.6(a,c,e). Note that some measurements are affected by large displacements, a direct consequence of increasing Δt. As it is clear at 37.5° and 40° for $\Delta t > 0.16$, when this happened, the level of correlation needed for PIV dropped and the profiles became corrupted. Disregarding these measurements, the profiles show a clear change in velocity with depth. The shape agrees with those experimentally and theoretically presented by Jop et al. [93], although obtained with different material, and for sand flows down an incline and over a heap [26, 160, 161]. Interestingly, a static, erodible layer formed at the bottom of the flows which became thinner for increasingly steep slope angles. This layer may be a consequence of the highly frictional resistance of sand (i.e. for bead flows this did not happen, see later) and the effect induced by the sidewalls which allows the stabilization of the flowing piles over an erodible surface of a heap (the static layer) at inclinations greater that the angle

of repose [159]. If the static layer is present only locally at the flume corners or a is feature extending the entire length of the channel, is difficult to assess by simply visualizing an opaque flow from the side.
Granular temperature profiles are shown in Fig. 4.6 (b,d,f). Since the slope-normal component of velocity (v) shows, in all cases, a gradient very close to zero, in the calculations of granular temperature the two velocity components (u, v) in Eq. 4.4 are summed together and only one curve is plotted for each experiment at different Δt. The magnitude of granular temperature varies according to the flow velocity profiles, i.e., being zero in the static layer while progressively increasing above it until the free surface is reached. In addition to the corrupted measurements taken at large displacement (37.5° and 40° for $\Delta t > 0.16$), at the free surface very fast moving particles occasionally disrupt the application of PIV and measurements should also be considered with care. The granular temperatures in Fig. 4.6 (b,d,f) are not in complete disagreement, at least in terms of magnitude, when compared with profiles from previous works (Sec. 2.5.3, Fig. 2.12) where, for most of the flows, $0 < T < 1$. However, considerations should to be made as to whether these are representative and correct values of granular temperature, what is the influence induced by the correlation-based procedure followed by PIV, the chosen interrogation areas and Δt. For real granular flows, it is very difficult to make, for angular particles, a true comparison with exact values of granular temperature because the particle tracking is very unreliable and measurements based on numerical simulations of angular material from which synthetic images can be created are, in general, not very common due to the extended computational time. However, this can be easily done for spherical particles as reported later in Ch. 6, where a first validation of PIV is given against synthetic images and the influence of the patch size and Δt is investigated in more detail.

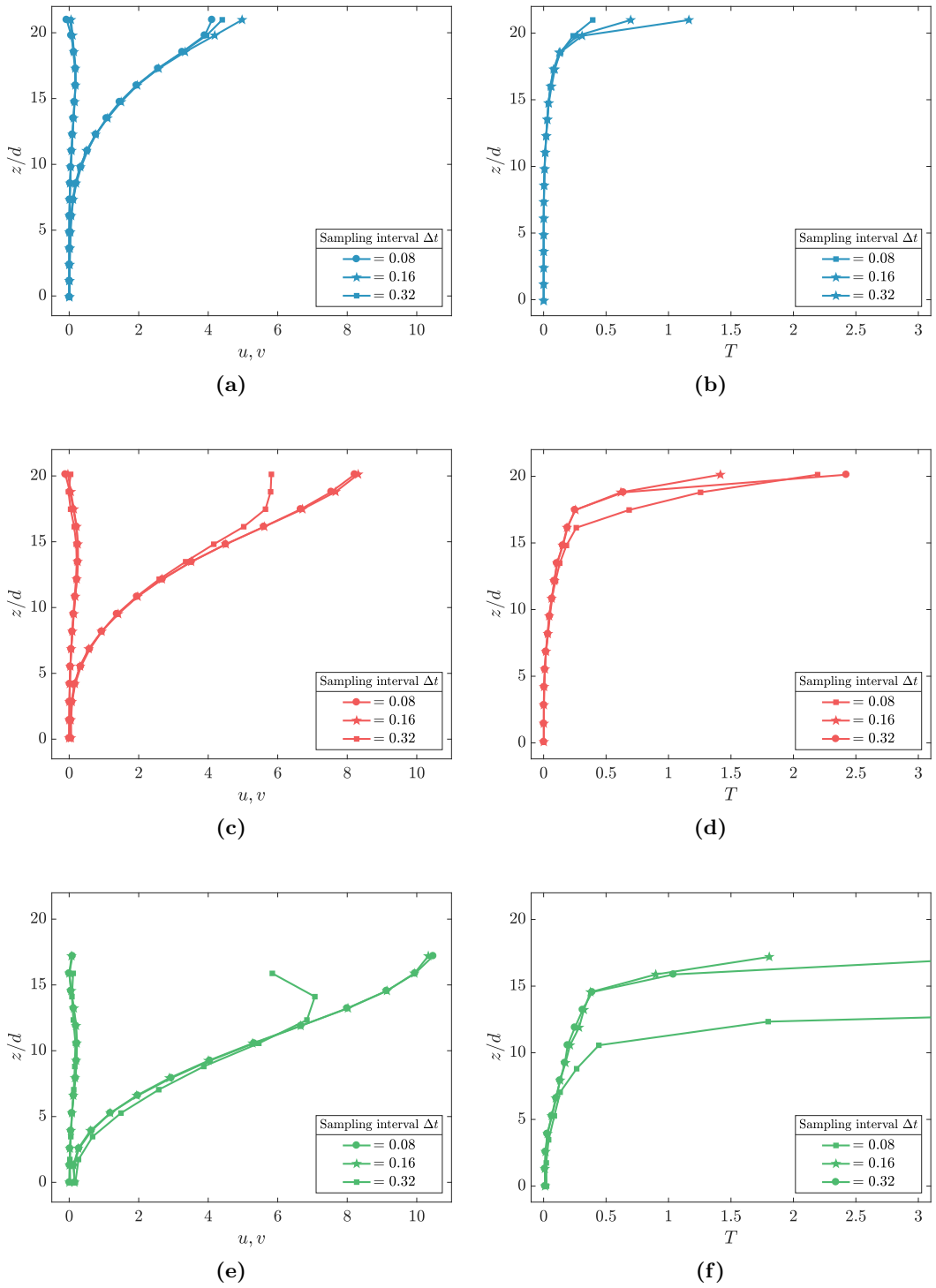

Figure 4.6: Slope-parallel (u) and slope-normal (v) velocity components (for each component, profiles at different Δt are given) for sand flows studied at three inclinations, 35° (**a**), 37.55°(**c**), and 40°(**e**) and different sampling time Δt. Profiles of granular temperature are shown for the corresponding inclinations and sampling intervals Δt in **b**,**d**,**f**.

4.5.2 Flows of ceramic beads

Keeping the same experimental conditions (mass and flow rate) and varying the sampling interval Δt, flows of ceramic beads were released at five different slope angles, 24°, 26°, 28°, 30°, and 32°, respectively. These are within the limits given by the friction angle of the material and the steepest angle that allows steady state for a sufficient period of time. As in sand flows, very agitated and diffuse flow fronts at the beginning of the recording, followed by flowing materials with constant heights and reducing flow depths at the end, were observed.

When the mean overall velocity of all visible particles obtained with PIV and interrogation regions 24x24 and 12x12 (coarse and refined grid, respectively) was plotted against time for a single event at different inclinations (Fig. 4.7) it was revealed that steady states (shaded areas) were possible up to an angle of 30°. At this slope angle, a duration of $t = 162$ was still possible, therefore this time was set as reference for the other inclinations to allow equal comparisons between the averaged measurements. Note that the results at 24° is not shown in Fig. 4.7 since the recording was only taken avoiding the unsteady part of the flows while the actual one for the entire flow duration was lost. However, it is clear that below 26° steady flows are possible for a relatively long period of time.

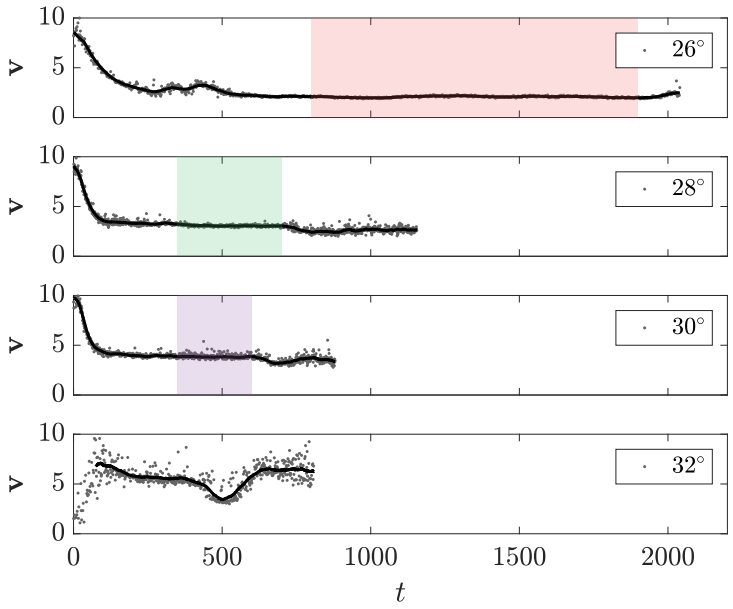

Figure 4.7: Depth-averaged velocity of all detected particles over the entire duration of bead flows. The black line shows the mean velocity over time. Shaded areas represent the duration of the steady states, i.e. where the mean velocity remained roughly constant over time.

4.5.3 Preliminary tests and comparison between PTV and PIV results

A preliminary comparison between PTV and PIV measurements of particle flows was made considering only two flows at an inclinations of 26° and 30°. Distributions of the mean (ensemble-averaged) velocities obtained from the PIV algorithm and interrogation regions 24x24 and 12x12 for a coarse and refined grid, respectively, are given in Fig. 4.8 (a,b). For each flow, the velocity profiles collapse onto a single curve for different Δt, indicating a lack of sensitivity to the time step over the range considered. The magnitude of the streamwise mean velocity increases with steeper inclination as expected and a higher velocity is found at the free-surface, decreasing with depth until the bed of the chute is encountered. The first layer of particles appearing at the bottom through the side-wall is firmly glued, so that no-slip velocity is exhibited. Thus, zero basal slip velocity is always found.

Profiles of granular temperature using PIV are given in Fig. 4.8 (c,d). This ensemble-average quantity achieves its maximum value at the free surface and decays to zero with depth. When plotted on the same graph, the granular temperature distributions in each flow have similar values but when the flows are processed with the two largest Δt (0.24 and 0.46) some dissimilarities in the profile of granular temperature arise. They are caused by faster moving particles that leave the sub-image causing loss of correlation. Most importantly, the magnitude of granular temperature profiles is rather less than that measured by PTV (Fig. 4.9 (c,d)) as discussed later in more detail. The reason for this may be due to the size of the interrogation region. In these experiments the smallest interrogation window was 12 x 12 pixels which can contain a maximum of approx. 5 particles. As before, averaging and smoothing of the data is introduced, which may damp the fluctuations measured. The analysis could be performed with very small interrogation areas to mitigate this, although this would make the correlation peak very difficult to identify, resulting in potentially inaccurate displacement estimates.

An alternative approach was presented by Reynolds et al. [137]. From a coarse PIV analysis, i.e. using interrogation regions larger than the particle diameter, they showed that the values of granular temperature can be theoretically scaled to the characteristic length scale of one particle diameter. When scaled, the results are useful to directly compare with the PTV results which are obtained from the tracking of single particles. Following their approach, the measurements were scaled up by a factor of 9 with values reported in Fig. 4.8 (e,f). The scale factor can be calculated considering the actual interrogation size (δ_{act}), in this case 12 pixels, and as the interrogation area is decreased by a factor n_{sf} the calculated granular temperature will increase by the same factor leading to $n_{sf} = (\delta_{act}/\delta_p)^2$, where δ_p is the presumed interrogation area including one image particle. With $\delta_p = 4$ (somewhat larger than three pixels to take into account any

change in particle shape and dimension) the scale factor by which the measurements are increased is $(12/4)^2 = 9$.

Mean velocity profiles produced by PTV are shown in Fig. 4.9 (a,b). As with PIV, velocity profiles collapse onto a single curve for different sampling intervals, although the velocity measured at $\Delta t = 0.46$ becomes corrupted above a depth of 12 particles. At this frame rate the PTV algorithm is incapable of correctly performing the matching routine due to the large displacements and a few velocity vectors from which to calculate the average. Without considering this particular case, the magnitude of the velocities is very similar to those found for PIV (Fig. 4.8 (a,b)), which cross-validates the particle tracking and particle image velocimetry algorithms, at least in terms of mean velocity.

Distributions of granular temperature obtained with PTV are shown in Fig.4.9 (c,d), where the most notable feature is the variability of granular temperature with Δt (or frame rate). That is, although the mean velocity measurement is insensitive to Δt, the determined granular temperature is greatly influenced by it. As is clear in Fig.4.9 (c,d), there is a shift of the granular temperature profiles to the left with increase in Δt, converging somewhat at large Δts, although the exact values do not (they are still declining with Δt). However, this trend disappears for sampling intervals smaller than 0.16 and approx. 0.12, respectively. The reason for this is that errors in the determination of the square of the fluctuation velocities accumulate (rather than cancel out) during the ensemble-average calculations. Conversely, for the mean velocities, the errors in instantaneous velocities are reduced by averaging.

As discussed in Sec. 2.2.2.1, dry granular shear flows down inclined geometries exhibit different regimes that span from a quasi-static to a collisional-dominated rapid flow state. These regimes are strictly connected to the shear rate ($\dot{\gamma}(z) = \partial u/\partial z$, i.e., the rate of change of velocity across the shear flow) and the solid fraction profile. When the particle concentration decreases with the shear rate, i.e., when the system becomes diluted, individual particles experience random collisions which are converted through grain velocity into higher flow mobility. This can be expected to happen close to the free surface of simple dry granular flows where the stress associated with the granular temperature acts to force the particles apart thus creating a dilute region represented by lower solid fraction.

After these considerations, the values of granular temperature calculated with PTV are also compared with the solid fraction profiles in two and three-dimensions (Fig.4.9(e,f)). Note that the profile for $\Delta t = 0.06$ is affected by the high accumulation of errors and should not be considered below. The gradient of granular temperature developed in the body of the flow at an angle of 26° steadily increases, remaining close to zero until greater agitation (or granular temperature) is produced at the free surface. In contrast, the flow released at 30° shows a clear change of granular temperature above 10-12 particle

diameters (depending on the solid concentration considered) which is accompanied by a growing dilated region. These features are captured by the solid concentration profiles shown in Fig.4.9 (f). For 26° it can be seen that the solid concentration is nearly uniform in the central part of the flow but changes when the free-surface is approached. For 30° the solid concentration decreases significantly above 10-12 particle diameters showing the flow to be more diluted. The good agreement between the changes of granular temperature and the profiles of solid fraction confirms the general variations expected in these flows and supports the validity of the measurements.

When PTV data is compared to PIV results, the shape of the granular temperature profiles show similar trends, i.e., increasing values moving towards the free-surface and an apparent change in the gradient above 10 particle diameters in the flow at 30°. For the same flow at 26° the magnitude is slightly higher while at an inclination of 30° the dimensionless granular temperature reaches values up to 4.2 at the flow surface (4.8(f)) which are well beyond the average magnitude showed in the rest of the analyses. This is probably caused by the errors arising during the cross-correlation process in PIV which are then magnified when granular temperature is scaled up.

Looking at the data for both PIV and PTV expected changes of granular temperature can be recognized. High-speed images at the base near the side-wall indicates frictional dependence of the motion with occasional brief contacts between neighbouring particles and more long-lived contacts (i.e. less granular temperature is generated). In contrast, particle collisions become more prominent towards the free-surface (i.e. more granular temperature is produced). Additionally, the granular temperature increases with increasing tilt angles, as the kinetic energy of the system increases.

However, granular temperature results obtained from the PIV and PTV analyses were unexpectedly variable and both methods had shortcomings when applied to dense granular flows. An analysis, reported later in Ch. 6, was conducted where results from discrete element simulation of dry granular flows were used to generate synthetic images with known particle locations. It is anticipated here that the analyses revealed that, with the correct choice if sampling interval Δt, PTV is a more appropriate technique for the analysis of the flows presented here, while PIV tends to wrongly predict the profiles and magnitudes of granular temperature.

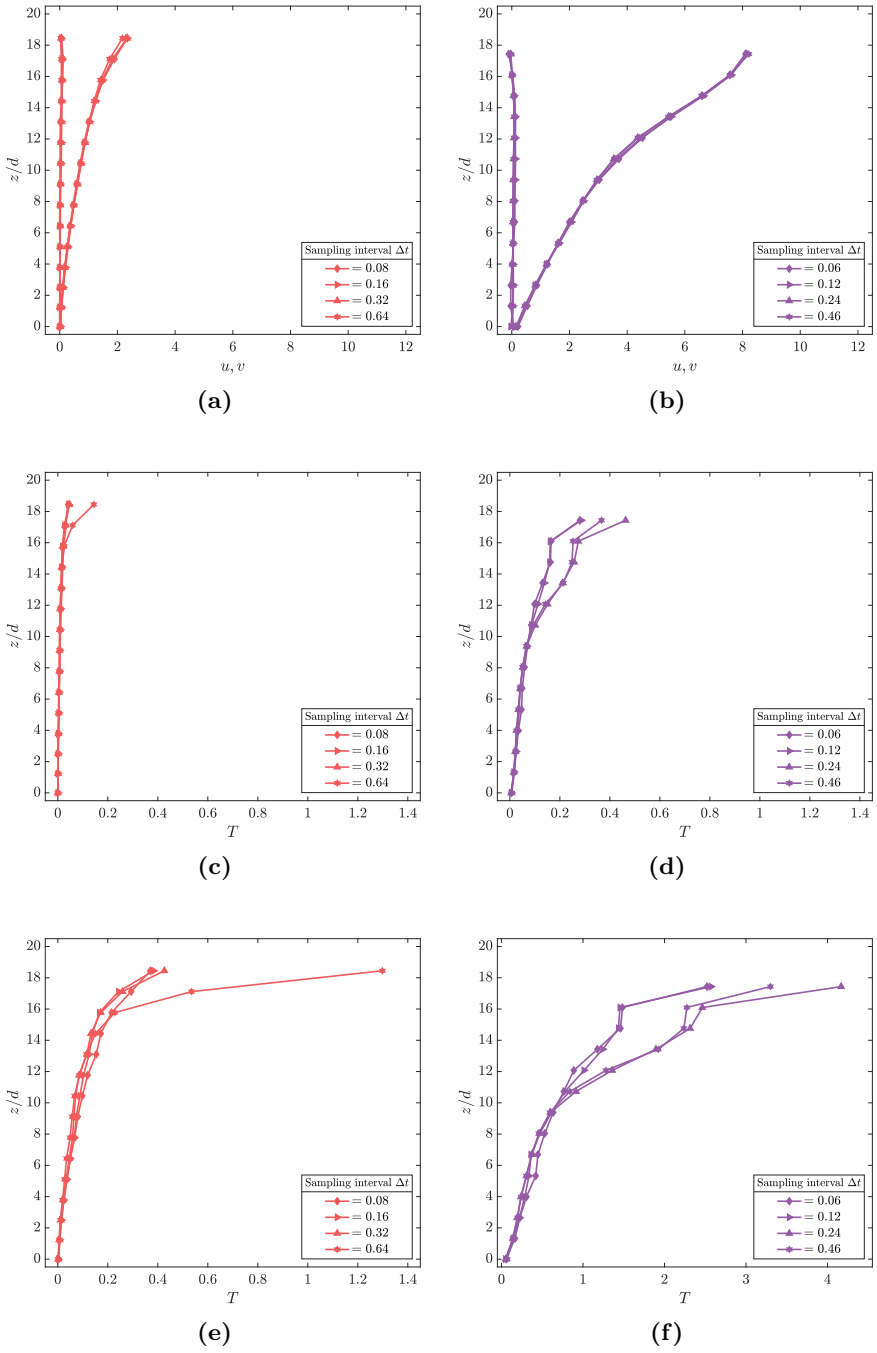

Figure 4.8: Depth-averaged flow property profiles obtained with PIV at different sampling intervals (Δt): (**a**,**b**) slope-parallel (u) and slope-normal (v) velocity components (for each component, profiles at different Δt are given) for the flows released at an inclination of 26° and 30°; (**c**,**d**) granular temperature at 26° and 30°; (**e**,**f**) granular temperature scaled up by a factor of 9.

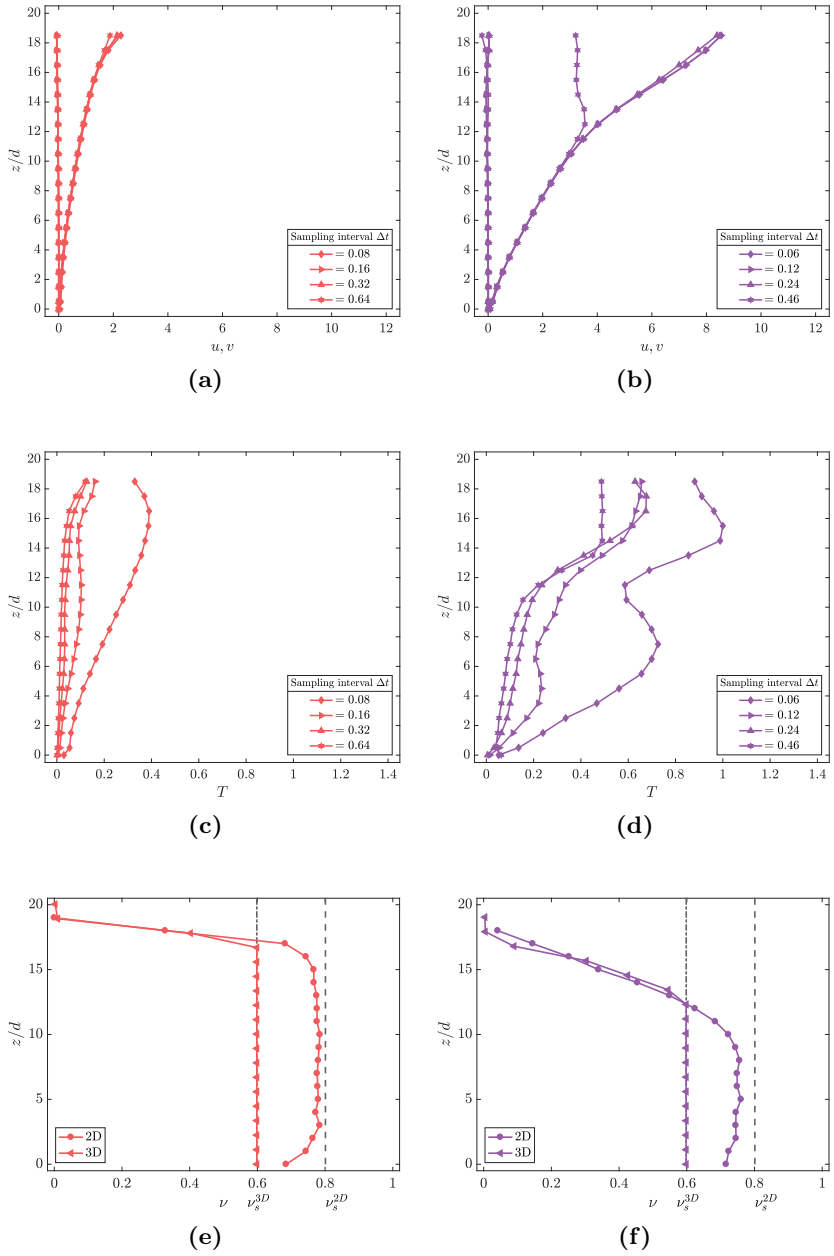

Figure 4.9: Depth-averaged flow property profiles obtained with PTV at different sampling intervals (Δt): (**a**,**b**) slope-parallel (u) and slope-normal (v) velocity components (for each component, profiles at different Δt are given) for the flows released at an inclination of 26° and 30°. (**c**,**d**) granular temperature at 26° and 30°; (**e**,**f**) 2D and 3D solid concentrations. Dashed and dash-dotted lines represent the two theoretical limits ν_s^{2D} and ν_s^{3D}.

4.5.4 Additional tests of ceramic beads

After the previous analyses and considering the validation performed in Ch. 6, further investigations of bead flows were conducted for all inclinations. Measurements were taken only with PTV for the reasons mentioned in Sec. 4.5.3. The only difference with the previous flows is that the flow rate (controlled by the height of the inner gate) was reduced to better assure that enough material was available to generate sufficiently long steady state at steep inclinations. In addition to this, the results reported below are averaged over 10 tests conducted at the same inclination to confirm the statistical reliability of the measurements. For a collection of these tests, at each inclination, kinetic energy of the entire system at each time step and the expected value (i.e., the long-run mean velocity) for each bin were calculated and plotted over time. The almost constant value of kinetic energy and the convergence of the expected value supported the persistence of steady state. Since these are additional information that confirms what was already showed in Fig. 4.7, the results are given in Appendix A.

Averaged velocity profiles for these flows are given in Fig. 4.10 for selected sampling intervals that did not cause any data corruption close to the free surface. They are $\Delta t = 0.32$ for 24°, 26°, 28° and $\Delta t = 0.24$ for 30°, respectively. Profiles obtained at smaller Δt collapsed onto the same curve as shown in the inset of Fig. 4.10. The flow at 24° was higher compared to the others since, additionally to be very close to the angle of repose of the material, at the release of the flows only a certain amount (i.e. flow rate) of material can escape from the gate depending on the inclination of the slope. That is, at steep angle, flows are generally shallower because they are faster. Measurements taken at the sidewall showed that the velocity changed almost linearly with depth and the magnitude increased for steeper slope angles. Linear velocity profiles were also observed at lateral boundaries down inclined flows in previous studies [3, 5, 70, 129, 135, 148] for different spherical materials. Further, the granular flows showed different avalanching behaviour with respect to sand. This should be expected since flow properties depend on the shape anisotropy of the material and the velocity profile is strongly controlled by the angularity of the particles.

Solid volumetric profiles obtained with the approach introduced in Sec. 4.4.3 are presented next. In two dimensions (Fig. 4.11(a)) it can be seen that for each inclination, the magnitude of ν remained very close to the value of random close packing for frictional disks (with $\mu = \tan(24°) \approx 0.45$, $\nu_s^{2D} \approx 0.8$ in Table 2.1) until the flows became more diluted at some distance from the bottom boundary. Some discrepancies are noticeable in the bottom layer, however, this point represents firmly glued particles and should not be taken into consideration. The method used to extract measurements in three-dimensions required the truncation of the data at the random close packing limit, as shown in Fig. 4.12(a) where

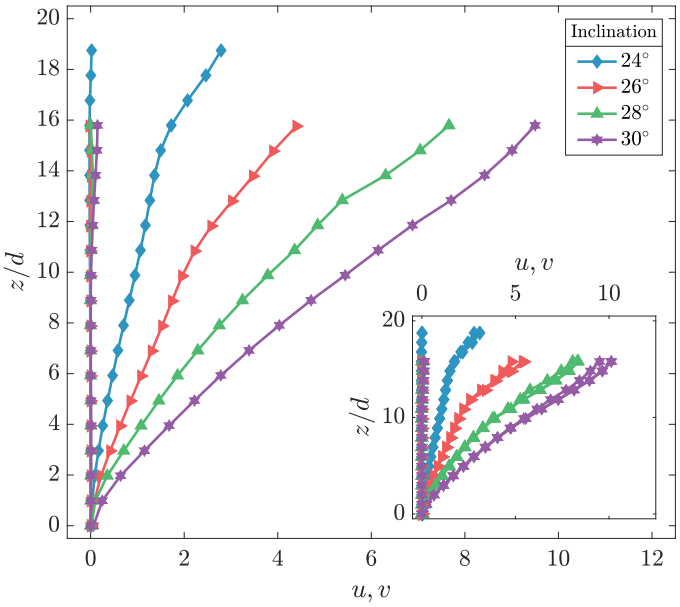

Figure 4.10: Slope-parallel (u) and slope-normal (v) velocity components (for each, profiles at different Δt are given) for the bead flows measured with $\Delta t = 0.32$ for 24°, 26°, 28° and $\Delta t = 0.24$ for 30°, respectively. The inset shows how the velocity collapsed on the same curve for different sampling intervals Δt at the same inclination.

the data beyond this value are also depicted. For clarity, the same profiles are shown in Fig. 4.12(b) only up to this maximum value. Apart from their magnitude, when 2D and 3D profiles were compared, the only subtle difference is that the deviation from ν_s occurred at slightly lower depths in the 3D approach as it is evident when comparing the profiles at 24°. At this slope angle the deviation occurred at $18d$ and $16d$ in 2D and 3D, respectively. While this difference is generally within $2d$, the same trends were captured by the two methods which cross-validates them at least in terms of profile shape. The analyses performed with different Δt revealed the insensitivity of solid volume fraction to this parameter. Most importantly, it is seen that both 2D and 3D approaches have their strengths and limitations. The use of high resolution images tends to lead to an underestimate of the concentration. Conversely, the roundness indicator leads to an overestimation in most cases which is corrected by limiting the maximum value of concentration that can be achieved. Despite this, both methods can still be used to assess the variation of other properties of the flows.

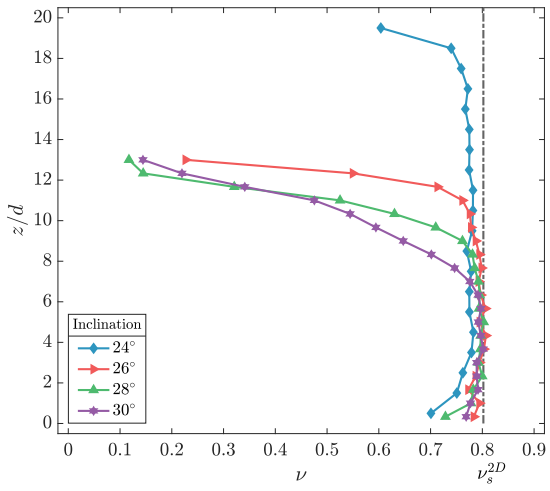

Figure 4.11: Solid concentration for the bead flows in 2D.

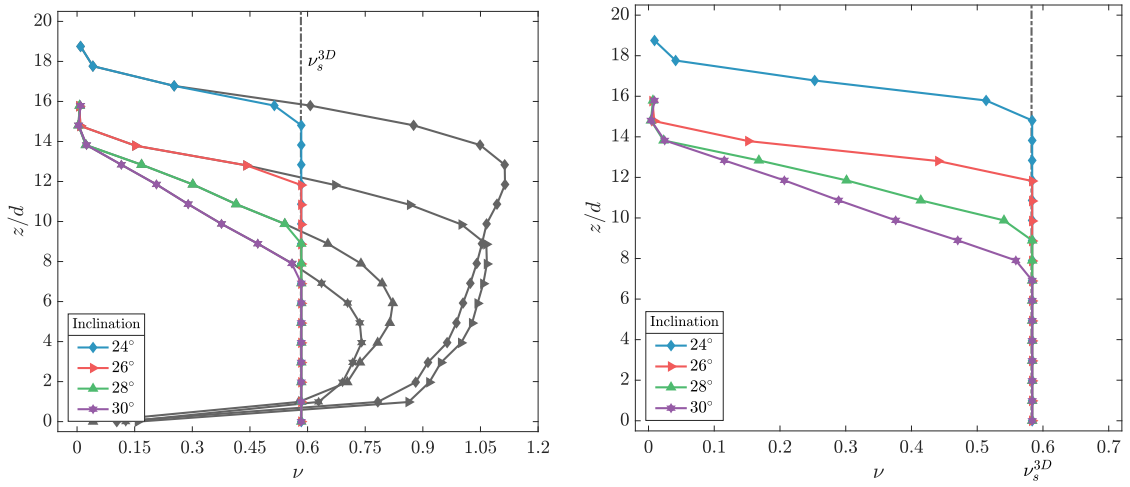

Figure 4.12: Solid concentration for the bead flows in 3D with actual (**a**) and truncated results (**b**).

The distribution of pressure p was obtained from a numerical integration of the concentration profiles as:

$$p = \rho_p \nu g \cos(\theta) \tag{4.6}$$

where the prime indicates a derivative with respect to z (the slope-normal direction). Specifically, only the values in 3D were used in order to make possible comparison with existing theory in three-dimensions. Results given in Fig. 4.13 showed linear (hydrostatic) profiles with values that increased with depth.
Profiles of granular temperature are shown in Fig. 4.14. As before, this quantity increased with progressively steeper slope angles, showed a variability from bottom to the free surface that could be related to changes of solid volumetric concentration and was sensitive to the choice of Δt.

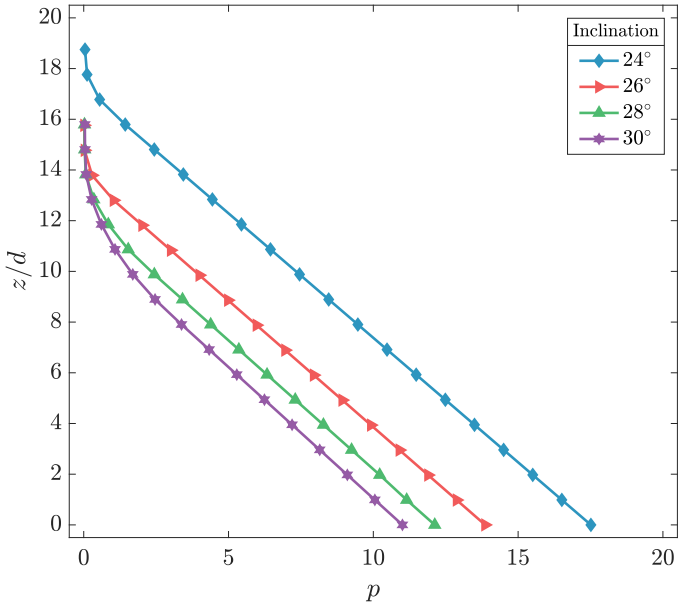

Figure 4.13: Estimated pressure distribution for the bead flows.

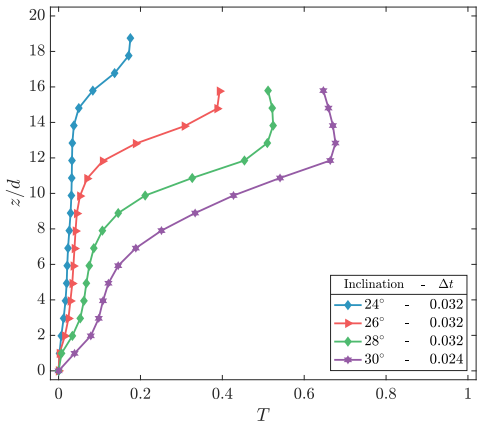

(a)

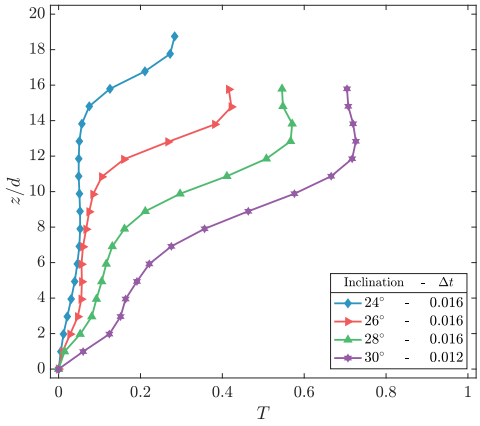

(b)

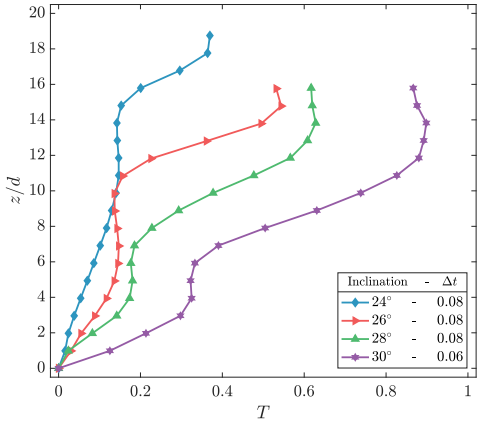

(c)

Figure 4.14: Granular temperature profiles (**a**,**b**,**c**) of the additional bead flows for different sampling interval Δt.

4.6 Conclusion

The influence of errors related with the procedure of PIV and PTV was examined in preliminary experiments on dry monodisperse granular flows made of angular sand and spherical ceramic beads down an inclined chute geometry. For sand flows PIV was trialled to measure granular temperature although it was not clear, after following the strategy for the error minimization of PIV, whether this quantity was accurately measured. A direct comparison with an approximate true value was not available and the influence of the size of the interrogation region and sampling intervals Δt were best studied for the bead flows to allow easier testing of the PIV technique.

Preliminary tests conducted with ceramic beads that considered the error framework of Ch. 3 generated the following outcomes. Granular temperature profiles for PIV were somewhat sampling-interval dependent with magnitudes that increased at larger Δt. This effect was associated with the selection of the sample interval which caused loss of correlation at large Δt. Moreover, errors in the PIV results were also likely to be connected with the scale of scrutiny used in the analysis. An interrogation size that included several particles in order to minimize the error associated with the correlation peak localization was selected. Considerably different values for the directly measured and theoretically scaled granular temperature were obtained when compared to PTV results. Conducting a scaling analysis based on the method proposed by Reynolds et al. [137] enable granular temperature to be derived from measurements over large interrogation regions did not generate the expected results. The sampling interval dependency but with an opposite trend was seen in the PTV results, with both changes in granular temperature magnitude and profile shape. The accumulation of errors for the smallest Δt produced very different profiles when compared to the rest. If these values were disregarded, the remaining agree qualitatively with those of PIV, i.e., although the shape of the profiles were similar the values were not. For PTV data the general variation of granular temperature were also supported by our estimations of the solid concentration.

Finally, steady monodisperse bead flows were examined in more detail over a range of inclinations considering the validation of the two imaging techniques conducted in Ch. 6 with the use of synthetic images. Velocity, granular temperature, solid concentration and normal stress profiles were obtained with PTV. The results obtained are used later in Ch. 7 to test the predictions of extended kinetic theory in terms of dimensionless granular pressure.

5. Numerical investigation of dry granular flows

5.1 Introduction

In this chapter simple dry granular flows are investigated numerically via Discrete Element Method (DEM) simulations. Simulations are undertaken considering two different flow configurations. The first consists of an idealized element volume where the flow dynamics are only dominated by external forces and a rough basal boundary condition. The goals are identify the main rheology developing in such flows and probe regions of the interior flow difficult to access in experiments. The second configuration is designed to reflect the experimental conditions of granular flows over a rough, inclined base bounded by rigid, flat and frictional side walls. These simulations together with the work conducted experimentally were then used to test the current predictions of kinetic theory.
A brief description of DEM based on the simple contact model used here is given in Sec. 5.2. The post-processing tool used to extract the continuum fields from numerical simulations via coarse-graining is described in Sec. 5.3. Next, methodology, parameters and the description of the two configurations are given in Sec. 5.4. The results of flows in absence of sidewall are discussed in Sec. 5.5. Finally, the results of simulated chute flows in presence of sidewalls are summarized in Sec. 5.6 and 5.7.

5.2 Discrete element method

In Discrete Element Method (DEM), the material is treated as an ensemble of discrete particles, where every grain i is resolved as a Lagrangian point with position $\mathbf{x}_i$, mass m_i, velocity $\mathbf{v}_i$, moment of inertia I_i, and angular velocity $\boldsymbol{\omega}_i$. Considering a simple system of soft spherical particles of diameter d, contact forces are generated when particles interact with each other. This produces deformation to the particles which may be determined via Hertz-Mindlin contact mechanics or similar. In this analysis, to simplify this behaviour, interaction forces are related directly to rigid particles by an ideal particle overlap δ.

This can be schematically visualized by considering a system where the interaction occurs between a pair of identical particles i, j (Fig. 5.1(a)). The two are in contact if $\delta^n > 0$, i.e., the normal overlap is positive. The overlap is easily defined as:

$$\delta^n_{ij} = (d_i/2 + d_j/2) - (\mathbf{x}_i - \mathbf{x}_j) \cdot \mathbf{n}_{ij}, \tag{5.1}$$

where the normal contact vector $\mathbf{n}_{ij} = (\mathbf{x}_i - \mathbf{x}_j)/|\mathbf{x}_i - \mathbf{x}_j|$. It is assumed that the contact takes place at the centre of the overlap, a justifiable assumption as long as the overlap remains small.

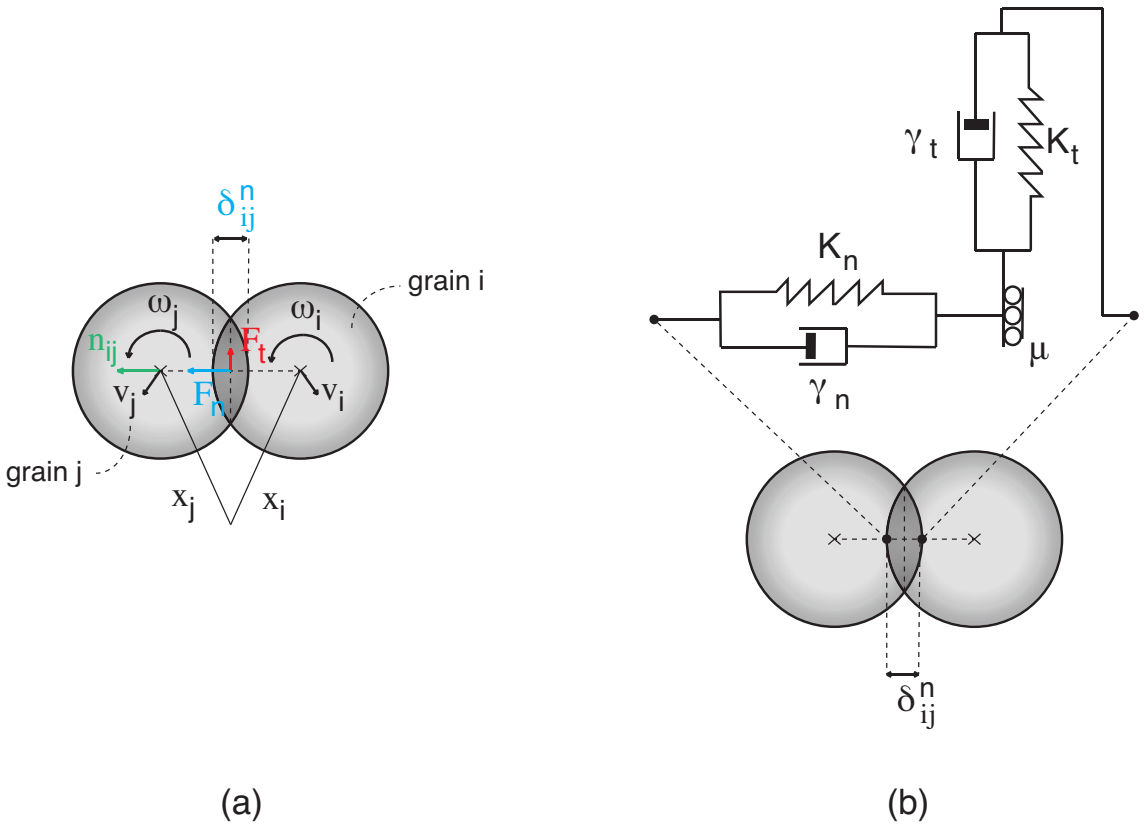

Figure 5.1: Two particles at contact (a). Sketch of the spring-dashpot contact model (b).

The forces acting on particles i, j are determined using a standard spring-dashpot model (Fig. 5.1(b)). Following this approach, the force acting from particle i to particle j can be decomposed into normal and tangential contributions, $\mathbf{F}_{ij} = \mathbf{F}^n_{ij} + \mathbf{F}^t_{ij}$. These are calculated in both normal and tangential directions as the combination of a linear

repulsive and a linear dissipative component:

$$\begin{aligned} \mathbf{F}_{ij}^{n} &= k_n \delta_{ij}^{n} - \gamma_n \mathbf{v}_{ij}^{n}; \\ \mathbf{F}_{ij}^{t} &= -k_t \boldsymbol{\delta}_{ij}^{t} - \gamma_t \mathbf{v}_{ij}^{t}, \end{aligned} \tag{5.2}$$

where, k_n and k_t are, respectively, the normal and tangential spring constants, γ_n and γ_t, the normal and tangential viscous damping constants and the relative velocities in normal and tangential directions are defined as:

$$\mathbf{v}_{ij}^{n} = (\mathbf{v}_{ij} \cdot \mathbf{n}_{ij})\mathbf{n}_{ij} \tag{5.3}$$

$$\mathbf{v}_{ij}^{t} = \mathbf{v}_{ij} - \mathbf{v}_{ij}^{n} + \mathbf{l}_{ij} \times \boldsymbol{\omega}_i - \mathbf{l}_{ij} \times \boldsymbol{\omega}_j. \tag{5.4}$$

Here, the relative velocity of the pair is defined as $\mathbf{v}_{ij} = \mathbf{v}_i - \mathbf{v}_j$ and, for equal size particles, the vector $\mathbf{l}_{ij} = -(\mathbf{x}_i - \mathbf{x}_j)/2$.

It is straightforward to derive the collisional time t_c between two particles and the coefficient of normal restitution e_n and normal dissipation γ_n from the normal component of the force as:

$$t_c = \pi / \sqrt{\frac{2k_n}{m_{ij}} - \left(\frac{\gamma_n}{m_{ij}}\right)^2} \tag{5.5}$$

$$e_n = \exp\left(-\frac{\gamma_n}{m_{ij} t_c}\right) \tag{5.6}$$

$$\gamma_n = -\frac{m_{ij}}{t_c \ln e_n} \tag{5.7}$$

where $m_{ij} = m_i m_j/(m_i - m_j)$ is the reduced mass (m_i and m_j being the masses of particles i and j, respectively).

The tangential component of the force is used to recreate the effect of particle surface roughness and to determine whether the particles stick or slide against one another. This effect is reproduced taking into account the generated force proportional to the elastic tangential displacement $\boldsymbol{\delta}_{ij}^{t}$. At the time of contact this is set to zero and its rate of change is given by [153, 174]:

$$\frac{d\boldsymbol{\delta}_{ij}^{t}}{dt} = \mathbf{v}_{ij}^{t} - \frac{(\boldsymbol{\delta}_{ij}^{t} \cdot \mathbf{v}_{ij})\mathbf{n}_{ij}}{r_{ij}}. \tag{5.8}$$

Due to the possible rotation of the reference frame at the contact over time, the second term on the right hand side makes sure that the tangential displacement is always rotated: thus, at every time interval, it is kept tangential to the contact point. The magnitude of

the tangential displacement is truncated to satisfy a yield criterion based on Coulomb's law, $|\mathbf{F}_{ij}^t| \leq \mu |\mathbf{F}_{ij}^n|$, where μ is the interparticle friction. Tangential sliding at a contact takes place when $|\mathbf{F}_{ij}^t| = \mu |\mathbf{F}_{ij}^n|$. Note that the static μ^s and dynamic μ^d coefficients of friction, which usually follow the relation $\mu^d < \mu^s$, are assumed here to be equal.
The tangential contact model also sets a single routine for the determination of the additional torques at contact $\mathbf{q}_r$. Since in this work only rolling is used, other torques, e.g torsion, are not discussed further. For the determination of this additional torque, the only requirement is a relative velocity as input [112]. The relative velocity for rolling is calculated as:

$$\mathbf{v}_{ij}^r = r'_{ij}(\mathbf{n}_{ij} \cdot \boldsymbol{\omega}_i - \mathbf{n}_{ij} \cdot \boldsymbol{\omega}_j). \tag{5.9}$$

This is used to determine the torque $\mathbf{q}_i^r = r_i \mathbf{n}_i \cdot \mathbf{F}^r$ where, similarly as before, the force $\mathbf{F}^r$ is determined as:

$$\mathbf{F}_{ij}^r = -k_r \boldsymbol{\delta}_{ij}^t - \gamma_r \mathbf{v}_{ij}^r. \tag{5.10}$$

The additional stiffness (k_r) and the viscosity (γ_r) for rolling need to be specified independently. Similarly to what was done previously, the force is truncated to satisfy $|\mathbf{F}_{ij}^r| \leq \mu^r |\mathbf{F}_{ij}^n|$, where μ^r is the rolling "friction" coefficient. Note that the additional rolling resistance acts to modify the angular velocity whose direction is opposite to the rolling motion (Fig. 5.2). This fact can be used to reproduce the asphericity of real particles while keeping a simple contact model based on spherical ones.
If all the contact forces $\mathbf{F}_i^c = \sum_{j=1, j\neq 1}^N \mathbf{F}_{ij}^c$ acting on a single particle i are known (e.g. from the contact with particles or the boundaries), its translational and rotational degrees of freedom can be solved by integrating Newton's equations of motion:

$$\begin{aligned} m_i \frac{d_2 \mathbf{x}_i}{dt_2} &= \mathbf{F}_i^c + m_i \mathbf{g}; \\ I_i \frac{d\boldsymbol{\omega}_i}{dt_2} &= \mathbf{j}_i, \end{aligned} \tag{5.11}$$

where $\mathbf{g}$ is the gravitational acceleration and $\mathbf{j}_i = \sum_{j=1, j\neq 1}^N (\mathbf{l}_{ij} \times \mathbf{F}_{ij} + \mathbf{q}_r)$ is the total torque. Once the forces are known, these equations are a set of ordinary differential equations that can be solved numerically to update the particle positions at a chosen time step. The same process is performed for particle-wall interactions, with a new set of parameters (stiffness, dissipation and friction) that needs to be specified independently.

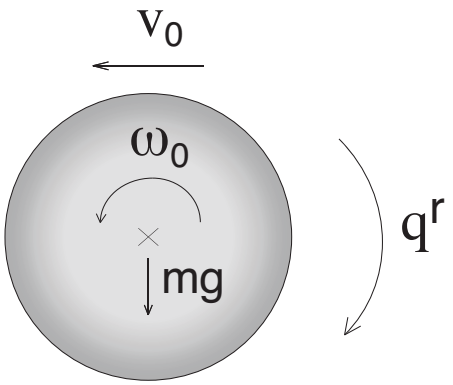

Figure 5.2: Rolling resistance torque ($\mathbf{q}^r$).

5.3 Coarse-graining

Coarse-graining is a technique used to simplify highly detailed and complex (anisotropic) microscopic quantities of heterogeneous materials and extract macroscopic continuum fields. The advantages of coarse-graining are that the equations of continuum mechanics are automatically satisfied, the particles can have different stiffness and shape and the results are even valid for a single time step, i.e. no ensemble-averaging is required [168]. The fields of interest in particle simulations are obtained by applying a local smoothing kernel (the coarse-graining function) characterized by a specific smoothing length (coarse-graining scale) denoted as w. A Gaussian defined with its standard deviation and scale (or variance) is a common example of a coarse-graining function. The scale, or resolution, is essential for obtaining correct measurements. Considering a general field, very fine resolutions (smaller than the particle scale) lead to strong fluctuations of the same field. However the value can plateau at a spatially dependent number and thereafter becomes independent of the scale. The plateaued value is what is usually referred to as the macroscopic field [65]. Narrower plateaus can also be found at large resolutions (larger than the particle scale) but they are strongly dependent on the field macroscopic gradients.

In explaining the procedure for coarse-graining, only the following fields of interest are explained and derived: velocity, solid volume fraction, granular temperature, and stresses. A system of N flowing particles is considered with particles fixed at the boundaries labelled N_f.

The microscopic (point) mass density ρ^{mic}, at a point $\mathbf{r}$ and time t is defined from statistical mechanics as

$$\rho^{mic}(\mathbf{r}, t) = \sum_{i=1}^{N} m_i \Theta(\mathbf{r} - \mathbf{r}_i(t)), \tag{5.12}$$

where Θ is the Dirac delta function. The macroscopic mass density is calculated by convoluting the ρ^{mic} with a coarse-graining function $\Psi(\mathbf{r})$:

$$\rho(\mathbf{r}, t) = \sum_{i=1}^{N} m_i \Psi(\mathbf{r} - \mathbf{r}_i(t)). \tag{5.13}$$

Here we use a Gaussian function, with coarse-graining width w. The volume fraction ν is expressed as

$$\nu(\mathbf{r}, t) = \sum_{i=1}^{N} V \Psi(\mathbf{r} - \mathbf{r}_i(t)), \tag{5.14}$$

where (for a sphere) $V = \frac{1}{6}\pi d^3$ is the volume of the particle and ρ_p its density.

The momentum density vector $\mathbf{M}(\mathbf{r},t)$ is defined as:

$$\mathbf{M}(\mathbf{r},t) = \sum_{i=1}^{N} m_i \mathbf{v}_i \Psi(\mathbf{r}-\mathbf{r}_i). \tag{5.15}$$

The ratio of momentum to mass densities leads to the macroscopic velocity $\mathbf{V}(\mathbf{r},t)$:

$$\mathbf{V}(\mathbf{r},t) = \mathbf{M}(\mathbf{r},t)/\rho(\mathbf{r},t). \tag{5.16}$$

This allows the particle fluctuation velocity to be defined as:

$$\mathbf{C}_i(\mathbf{r},t) = \mathbf{v}_i(t) - \mathbf{V}(\mathbf{r},t). \tag{5.17}$$

The macroscopic stress can be obtained considering the momentum conservation equation [173]. This stress is subdivided into kinetic (i.e., streaming) and collisional stresses, $\boldsymbol{\sigma} = \boldsymbol{\sigma}^k + \boldsymbol{\sigma}^c$ whose explicit formulation reads:

$$\boldsymbol{\sigma}^k = \sum_{i=1}^{N} m_i \mathbf{C}_i \mathbf{C}_i \Psi(\mathbf{x}-\mathbf{x}_i); \tag{5.18}$$

$$\boldsymbol{\sigma}^c = \sum_{i=1}^{N}\sum_{j=i+1}^{N} \mathbf{F}_{ij}\mathbf{x}_{ij} \int_0^1 \Psi(\mathbf{r}-\mathbf{r}_i+s\mathbf{r}_{ij})ds + \sum_{i=1}^{N}\sum_{k=N+1}^{N+N_f} \mathbf{F}_{ik}\mathbf{a}_{ik} \int_0^1 \Psi(\mathbf{r}-\mathbf{r}_i+s\mathbf{a}_{ij})ds, \tag{5.19}$$

with the interaction force between two particles $\mathbf{F}_{ij} = -\mathbf{F}_{ij}$, vectors $\mathbf{x}_{ij} = \mathbf{x}_i - \mathbf{x}_j$ and $\mathbf{a}_{ij} = \mathbf{x}_i - \mathbf{b}_{ij}$, where $\mathbf{b}_{ij}$ is the contact point between the particle i and a fixed wall particle j.

Once the stresses are known, the pressure, p, and the granular temperature, T, can be calculated as [173]:

$$p(\mathbf{r},t) = tr(\boldsymbol{\sigma}(\mathbf{r},t))/3 \tag{5.20}$$

and

$$T = tr(\boldsymbol{\sigma}^k)/3\rho, \tag{5.21}$$

respectively.

For granular systems, the definition of the particle fluctuation velocity (Eq. 5.17) leads to scale dependency effects [173] due to gradients developing in the flow. For inclined flows, it has been suggested [173] that the scale dependency can be removed *a posteriori* from

the kinetic stress $\boldsymbol{\sigma}^k$, which becomes:

$$\boldsymbol{\sigma}^{k\prime} = \sum_{i=1}^{N} m_i \mathbf{C}_i \mathbf{C}_i \Psi(\mathbf{r} - \mathbf{r}_i) - \rho\dot{\gamma}^2 \frac{w^2}{3} \tag{5.22}$$

where $\dot{\gamma}$ is the shear rate while the factor 3 appearing in the denominator in the right hand side expression is an integration constant [173]. The corrected granular temperature and pressure can then be calculated as:

$$T'_{corr} = T - \rho\dot{\gamma}^2 \frac{w^2}{3} \tag{5.23}$$

$$p'_{corr} = p - \nu\rho\dot{\gamma}^2 \frac{w^2}{3} \tag{5.24}$$

where the prime indicate the derivatives with respect to the z-direction. Following the procedure described above, correct coarse-grained fields can be obtained near boundaries made of fixed particles (e.g. those at the bottom of the inclined chute). Other boundaries (e.g. lateral periodic or flat rigid walls) lead to local underestimations of these fields due to "vacuum" effects [139]. This happens when the coarse-graining function has to be partially defined also beyond these boundaries (Fig. 5.3). There are strategies to correct for this, e.g. [139], but they are not implemented here.

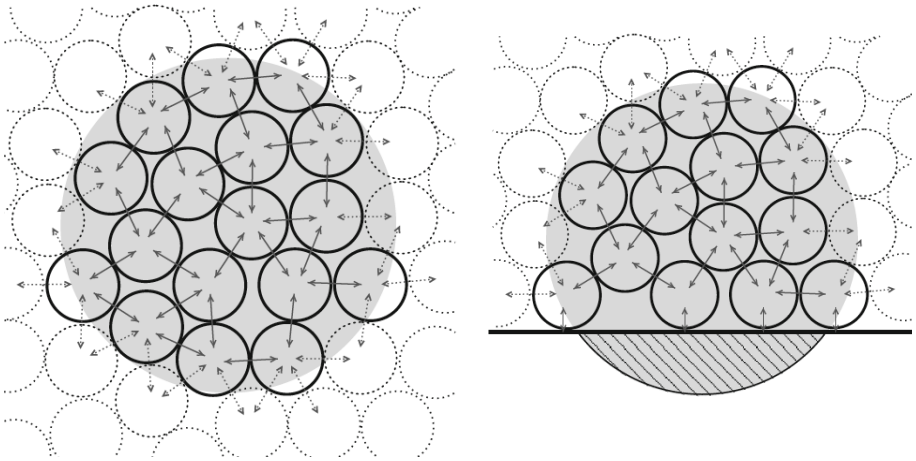

(a) **(b)**

Figure 5.3: Example of coarse graining in the bulk (a). The grey region indicate where the contribution of particles (circles) or contacts (arrows) to the coarse grained field is not negligible. Coarse graining at the boundary (b). The contribution to all quantities by the region beyond the boundary (hatched area) is zero leading to "vacuum" effects. Adapted from [139]

5.4 Numerical simulations

Numerical simulations were performed via the Discrete Element Method (DEM). This is a well-known tool in contact mechanics and many works [33, 154, 166, 174] have previously used this approach for the study of granular flows. The simulations presented here were carried out using the open-source DEM software mercuryDPM (`http://www.mercurydpm.org`). This particular code has been validated against single-particle experiments [58], shaken systems [179] and compared against the previous DEM work of Silbert et. al. [154] where similar systems to those presented here were studied. An additional advantage of this code is that it offers a post processing tool to extract the continuum fields from numerical simulations via coarse-graining (CG). This technique has been used here to retrieve the fields of interest for the comparisons with the results of experiments and kinetic theory.

The DEM code was employed to perform three-dimensional numerical simulations of granular systems flowing over a bumpy inclined plane in the absence and in the presence of flat, frictional sidewalls. In the reference coordinate system used here, x represents the streamwise (flow) direction, y the spanwise (vorticity) direction, and z is the direction perpendicular to the bed. The particles are identical spheres of diameter d and mass m which are subjected to the gravitational acceleration g. The results presented here are given in dimensionless form and the translation to dimensional forms can be obtained with the following scaling. From the experiments (Ch. 4), the characteristic real diameter is that of ceramic beads $d' = 1.5$ mm (Table 4.1). Using a the gravitational acceleration $g' = 9.81$ ms^{-2} the time scale length is $t' = \sqrt{d'/g'} = 0.0124$ s, the stream-wise dimensional velocity scale is $u' = \sqrt{d'g'} = 0.121$ ms^{-1} (also valid for the other components), the dimensional granular temperature scale is $T' = d'g' = 0.0147$ m^{-2}s^{-2}, the stress scale is $p' = m'g'/d'^2 = 18.70$ kg/m^{-1}s^{-2} and, with the density of the ceramic beads $\rho_p = 2430$ kg m^{-3} (Table 4.1) and the mass of a bead calculated as $m' = \rho_p \frac{\pi}{6} d'^3 = 4.29 \times 10^{-6}$ kg, the kinetic energy scale is $KE' = m'd'g' = 6.31 \times 10^{-8}$ kg m^{-2}s^{-2}. Additional scaling factors for the simulation input parameters are given later for each separate set of simulations.

To simulate flows in the absence of lateral confinement, a simulation cell with lateral periodic boundaries along x and y was employed. Any particles crossing a periodic boundary re-enters the opposite periodic boundary in the same direction with the corresponding position and velocity. The system had dimensions $l_x \times l_y = 20d \times 10d$. A single layer of 180 particles was glued at random spacing on the flat surface at $z = 0$ (so that their centres of mass are located at $z = d/2$). These particles cover the entire $x - y$ plane, although a few gaps are always present (see Fig. 5.4(c)). These are generally filled during the simulations although particles trapped there are allowed to recirculate, i.e., are not fixed. This is due to the fact that the simulation base was an accurate representation

of the experimental bottom boundary condition (Fig. 4.2). Images of the flume rough base were taken in the same location 30 cm before the outlet, positions found with the same centroiding techniques used for PTV and then adapted to the dimensional simulation domain. The distances between edges of adjacent glued particles were calculated via Delaunay triangulation in Matlab with an estimated average value of $0.4d$. This measurement was used as an input to define the bumpyness in the equation of kinetic theory (Sec. 2.3.6). Note that, in these simulations, the base and flowing particles have the same size. Choosing different base particle sizes have an effect on the shape of the flow property profiles [174]. All the simulations consisted of 3500 flowing spherical particles which, within the simulation domain, can reach heights that are approximately $20d$. In the following this configuration is referred to as the periodic cell.

When flat, frictional sidewalls were added, the domain was enlarged and periodic boundaries were used only along x (flow direction). The domain of simulation was $l_x \times l_y = 30d \times 66d$. The bumpy bottom was generated as described above, using 1760 particles so that the average distance between the edges of two adjacent particles was still $0.4d$ on average. A total of 27500 flowing spheres were simulated with typical heights of approximately $15d$.

Examples snapshots of the DEM simulations obtained in the presence and in the absence of lateral confinement are reported in Fig. 5.4 and Fig. 5.5, respectively.

For the spring-dashpot contact model, parameters similar to those used in other studies [33, 154, 173] were employed. The constant particle stiffness in the normal direction was set to $k_n = 2 \times 10^5 mg/d$. This was set to be much lower than the physical elastic constant since a larger value would necessitate a very small time step ([154]), thus increasing the computational time considerably, however, general behaviours could still be captured. In addition, it has also been shown [21] that stiffness has an influence in numerical simulations only after the jamming point, i.e., after a transition from a flowing to a jammed solid-like state.

The damping γ_n is adjusted in Eq. 5.7 to obtain the desired value of the coefficient of normal restitution e_n. Here, results are given for e_n having values of 0.5, 0.6, and 0.7. These values of e_n are lower than that typical for real ceramic beads $e_n \approx 0.98$ (`http://grainflowresearch.mae.cornell.edu/impact/data/Impact%20Results.html`). However, as in other works [61, 120], this is an assumption afforded to reproduce the typical behaviour of granular flows composed of nearly elastic particles. The collisional time determined from Eq. 5.5 was set to $t_c = 0.005$. For accurate simulations, a sufficiently small integration time step could then be defined as $\Delta t = t_c/50$ [154]. The tangential stiffness and damping were set as $k_t = \kappa \cdot k_n$ and $\gamma_t = \kappa \cdot \gamma_n$, respectively. The prefactors κ, derived from numerical simulations on the impacts of spheres [82, 111], were different for tangential and

rolling contacts, being 2/7 and 2/5, respectively. In this way the frequency of normal and tangential contact oscillation is made equal so that time step is the same in both directions and the normal and tangential dissipation are made equal, i.e., $e_n = e_t$. In principle, if the normal contact oscillation is not equal, the tangential spring will still be loaded at the instant when two particles detach. This implies that energy is stored in the spring causing an energy imbalance over the contact period. However, the contact dynamics are not very sensitive to the precise value of these ratios [154]. All these parameters are used as inputs for both particle-particle and particle-flat wall collisions. Only the coefficients of sliding and rolling friction, μ and μ_r, are changed, with μ being set at 0.45 for particle-particle interactions and 0.35 for the particle-flat wall contacts (in the absence of physical measurements specific for the experimental flume, this value was based on impact parameters between a ceramic bead and a flat plate of Lexan, a perspex-like material `http://grainflowresearch.mae.cornell.edu/impact/data/Impact%20Results.html`) while rolling friction μ_r was varied in the range of $0 < \mu_r < 0.3$ for different set of simulations. Once chosen, a single value of this parameter was used for all contacts, i.e., there was no distribution of values within a given simulation. Notably, at present, there is no general consensus on the precise value of this parameter nor it is widely used in the literature. Wensrich and Katterfeld [175] estimated the values of rolling friction based on the aspect ratio of an elliptical particle. Based on their data and using the average value of this ratio in Table 4.1, rolling friction should be ≈ 0.1. However, as stated by the same authors, the validity of their estimations was entirely untested and a degree of caution must be exercised, hence a range of values was tested.

At the beginning of the simulations, the bumpy plane was set horizontally and particles were randomly allocated within the simulation domain so that they did not overlap. Then, under the imposed force of gravity, particles settled until they form a packing. At this stage, the inclination was increased to give the particles enough energy to flow. Simulations were run until a steady state was reached, as shown later for different sets of simulations. Due to computational reasons, simulations had to be stopped when the maximum run time (168 hours) permitted by the high-performance computer used (Iceberg HPC Cluster) was reached. For example, using one processor only, the system with 27000 flowing spheres at 26° required nearly a week (168 hours) to overcome the first phase of the simulation where the kinetic energy increases up to a constant value. However, simulations were restarted several time with positions and initial velocities of the latest time step and it was made sure that, after the first phase, collectively KE was constant for sufficient amount of time in order to remove hysteresis effects.

Finally, coarse-graining was used to obtain the fields of interest and, after the steady state was reached, measurements were averaged over a time interval of $200t$ (longer time

intervals did not alter the results). For the coarse-graining scale w, a value of $1d$ was used in the absence of sidewalls and $1d$ and $0.1d$ in the presence of sidewalls. These two are plateaued values (Sec. 5.3) where macroscopic fields exist in these types of flows [173].

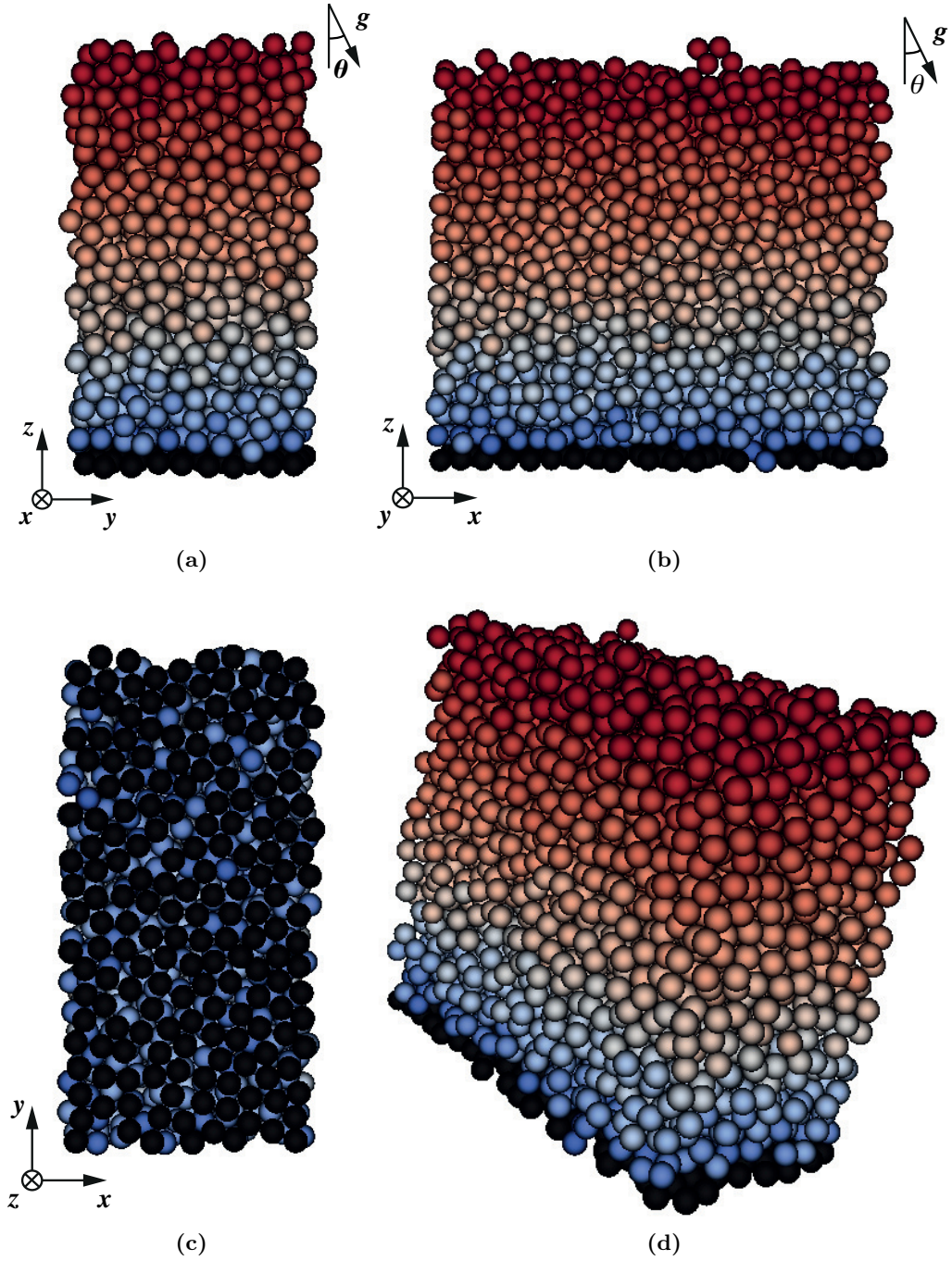

Figure 5.4: Simulation cell with periodic boundaries of size $l_x \times l_y = 20d \times 10d$. A total of $N = 3500$ particles are simulated at different angles of inclination (θ). Front and side views (**a**,**b**) show the velocity gradient from slow (blue), at the bottom, to fast (red) particles, at the free-surface. The rough bottom base (**c**) is made by random placed particles (black) with centres at $z = d/2$ based on the experimental bottom boundary. (**d**) Flowing particle system.

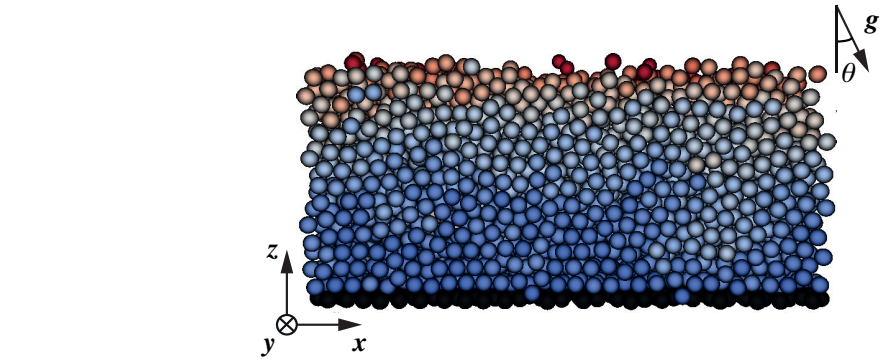

(a)

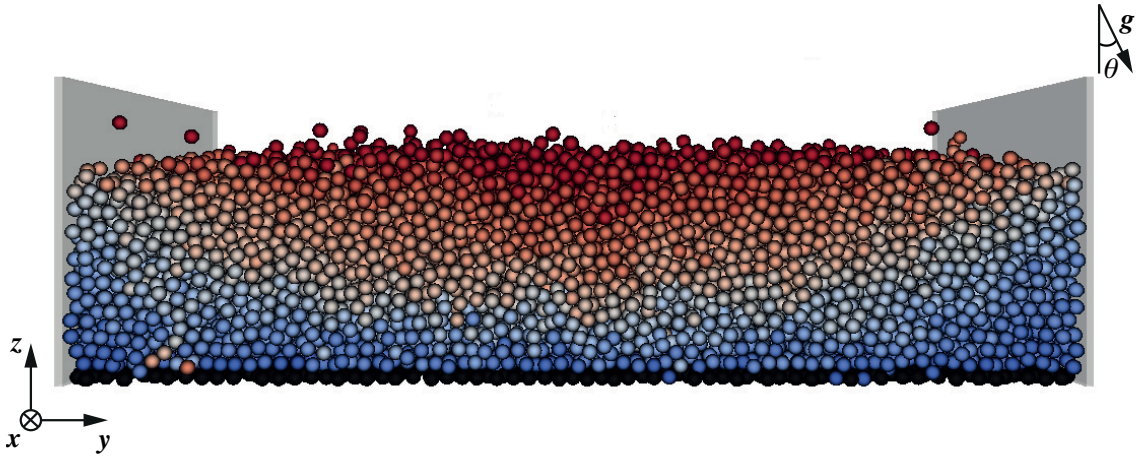

(b)

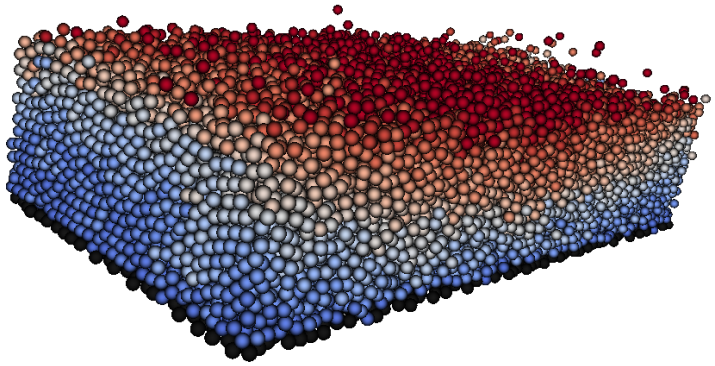

(c)

Figure 5.5: Front and side views (**a**,**b**) of a flow laterally confined by flat, rigid and frictional sidewalls. The simulation domain is $l_x \times l_y = 30d \times 66d$ with a total of $N = 27500$ particles simulated. As in Fig. 5.4, glued (black) particles make the base bumpy and the colour gradient represents slow (blue) to fast (red) particles as z increases. Notably, there is an additional influence of wall friction in the spanwise (y) velocity gradient. (**d**) Flowing particle system.

5.5 Periodic cell

Simulations in the periodic cell were conducted with parameters listed in Table 5.1 for slope angles of 24°, 26° and 28°, respectively. The steady state of the systems was assessed knowing that it can generally exist over a range of inclination angles. For comparable simulation domains, flow heights and contact parameters, it has been shown in numerical simulations [174] that this range is approximately between 21° and 29°. However, this was further verified since different roughness bases affect these values slightly [155]. Fig. 5.6 depicts the kinetic energy (KE) several simulation restarts after the initial phase of the simulation, i.e. when KE increases before reaching a steady value, and over the time considered for coarse-graining. Notably, the magnitude of KE increases with the restitution coefficient e, clear for $e = 0.7$ (green lines). More details on the effect of the restitution coefficient are given below when discussing the profiles of velocity and granular temperature. A slope angle of 30° was not tested since the chosen inclinations were sufficient to demonstrate the general flow behaviour for this configuration. A more detailed analysis over a larger range of tilt angles was conducted in the presence of sidewalls.
Measurements away from periodic boundaries at different locations in the spanwise direction had a negligible variation in magnitude, therefore flows are treated as one-dimensional and only measurements taken along the central line ($l_y = 5$) of the flows are presented. Furthermore, due to the coarse-graining width also being applied to particles glued at the bottom, those immediately above may partially contribute to measurement fields at this level. In addition, the bottom roughness has gaps where particle can fall and move, i.e. measurements are never zero in the static layer. However, the transition can be identified by a change in magnitude at approximately $z = 1d$ in most cases. For clarity these measurements are depicted with dotted lines.

Table 5.1: Contact parameters for flows in the absence of sidewalls.

Parameter	Symbol	Scaling	Value
Normal restitution	e_n		0.5, 0.6, 0.7
Normal stiffness	K_n	mg/d^2	2×10^5
Tangential stiffness	K_t	mg/d^2	$\frac{2}{7} \cdot K_n$
Normal damping	γ_n	$\sqrt{g/d}$	135, 100, 70
Tangential damping	γ_t	$\sqrt{g/d}$	$\frac{2}{7} \cdot \gamma_n$
Sliding friction coefficient	μ		0.45

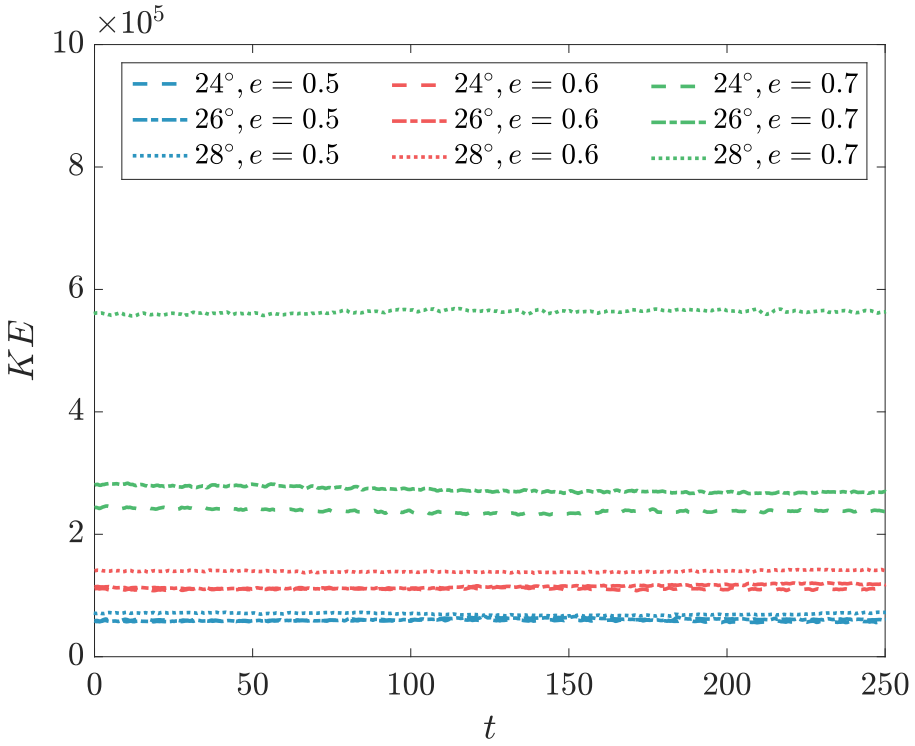

Figure 5.6: Kinetic energy plotted against time for flows in a periodic cell with different restitution coefficient e.

Velocity profiles obtained for different coefficients of restitution are shown in Fig. 5.7(a,c,e). While the slope-normal velocity component is negligible, a slip velocity always develops with stream-wise velocities that increase from the base to the surface, resembling a Bagnold-like profile (Fig. 2.4), thus in agreement with previous studies [156, 166, 174]. Velocity magnitudes are similar for $e = 0.5$ and $e = 0.6$, however, a considerable shift in velocity appears for $e = 0.7$ at 28°, i.e. the shape shows only little variation compared to lower values of e but the magnitude is much greater throughout. Greater values of restitution (0.8 and 0.9) were also tested, however they caused an increase in this shift with a constant KE considerably above the average.

Granular temperature profiles are given in Fig. 5.7(b,d,f), again in agreement with previous numerical simulations [61, 119, 154, 173]. Granular temperature is greater closer to the bottom and decays with height until the free-surface is reached. This indicates that the bumpy base acts as a source of fluctuation energy. The work carried out by the grains at this level give rise to a production of fluctuation energy resulting in a temperature gradient. A higher temperature by almost a factor of two appears again for $e = 0.7$ at 28°.

It has been shown [61] that the restitution coefficient influences the transition from dense to dilute collisional regimes. In several studies [114, 154, 156] the typical value of coefficient of restitution was greater than 0.7, flow depths were equal or greater than 40 particle diameters, flows were studied in a range that featured also gentler slopes than those analysed here and the base was designed to represent the internal particle flow configuration, i.e., by translating and fixing particles in the interior to the bottom. In such flows the effect of the base is also hindered by the weight of the material above it and the effect is felt only locally, e.g., between 15-20 particle diameter for flows $80d$ thick [114]. Conversely, the flows studied here are generally around $20d$ in height and the base is much more energetic, i.e., the overall system behaviour is expected to be much more affected by it. The variation of the restitution coefficient towards greater value (so that increasingly less energy is dissipated) may be much more evident for the thin flows studied here. Granular temperature is progressively higher at the base, while, when $e = 0.7$, the velocity magnitude is greater throughout the whole depth leading to a higher but constant kinetic energy. Ultimately, greater coefficient of restitution could also be used but a limiting value of $e = 0.7$ was set in order to avoid considerably changes in velocity and granular temperature for different angles of inclinations.

Another peculiar aspect of these flows is the profile of solid volume fraction (Fig. 5.8). As observed in some of the studies mentioned above [61, 119, 154, 173], two regions, one deep in the flow and one near the free surface, where the concentrations decayed to lower values, bound a core region with approximately constant density. For thick flows ($20d \geq z \geq 100d$) this feature is very clear [154], however, for the thin flows ($z \leq 20d$) studied here this is still observed but it is less pronounced. A constant concentration suggests that the rheology is local in this part of the flow, an assumption that was previously used to derive the Inertial number (Sec. 2.3.3). In line with velocity and granular temperature measurements, the concentration for $e = 0.7$ at 28° was less at the base and differed from the rest. A constant profile could not be recovered due to the height of the flow and the slightly higher agitation throughout the flow (as seen from the profile of granular temperature when $e = 0.7$).

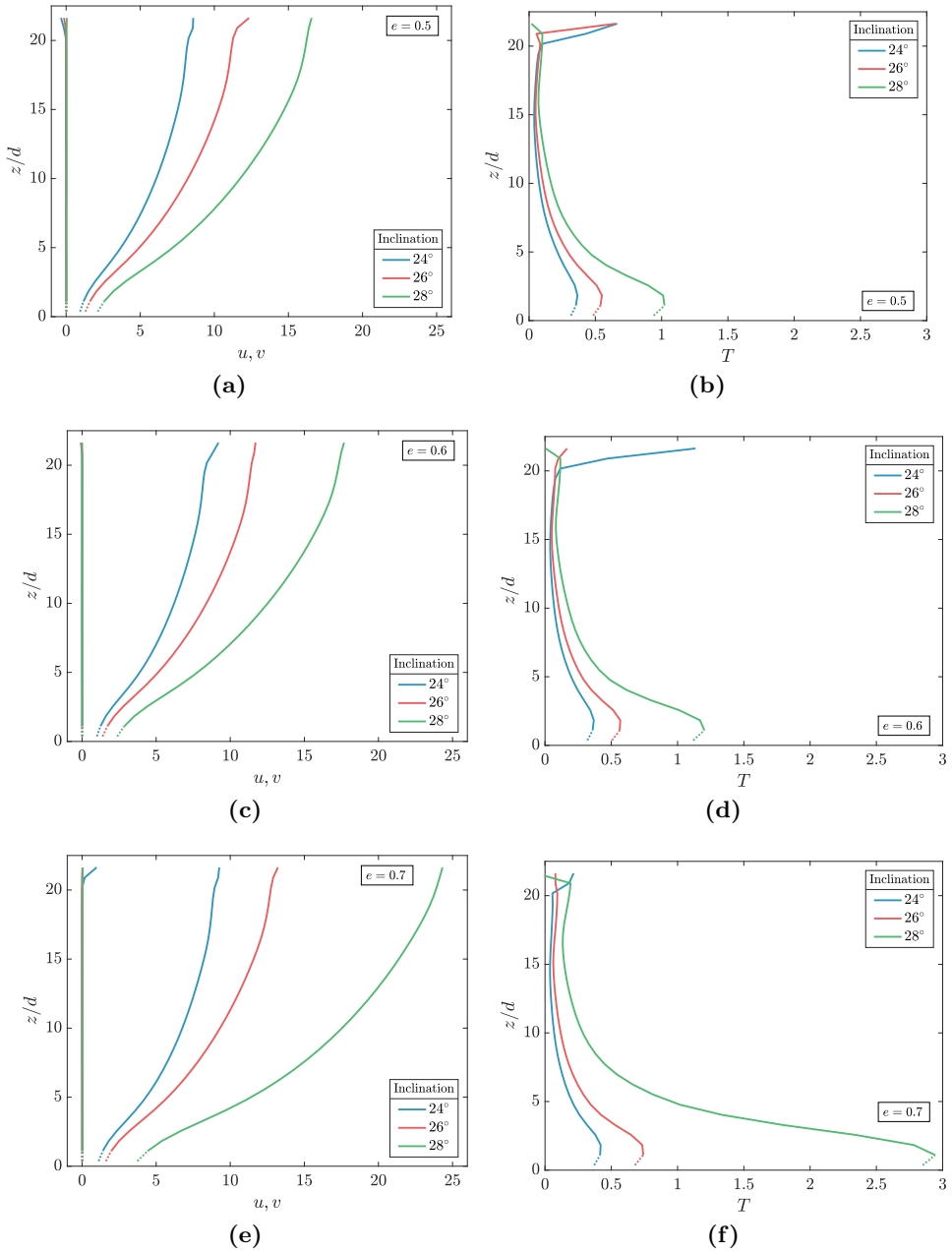

Figure 5.7: Velocity (**a**,**c**,**e**) and granular temperature (**b**,**d**,**f**) profiles from the simulation without sidewalls for different restitution coefficients and slope angles.

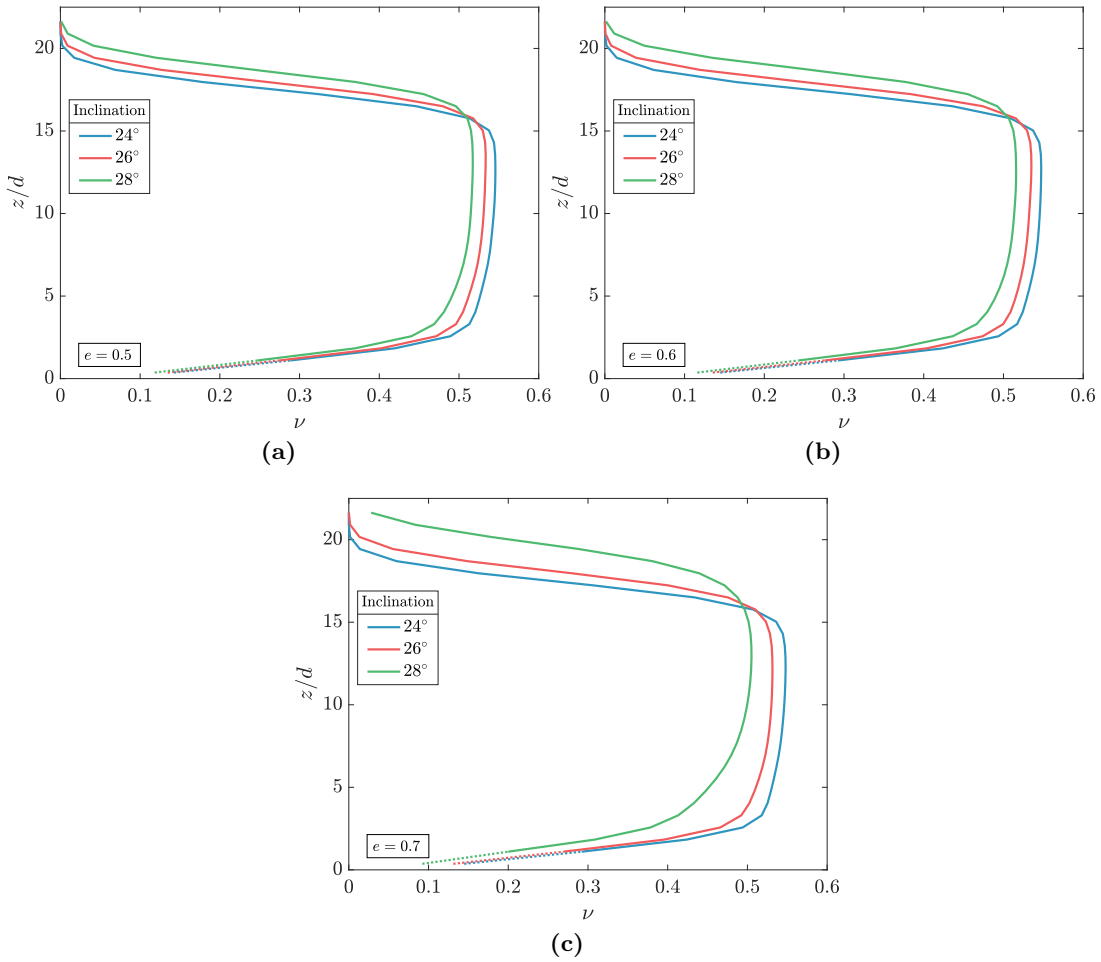

Figure 5.8: Solid volume concentration profiles from the simulation without sidewalls for different restitution coefficient and slope angles.

5.6 Flows between sidewalls without rolling friction

The kinetic energy of the simulations, obtained with the parameters listed in Table 5.2, was assessed to verify the influence of sidewalls. The insets of Fig. 5.9 show the results for angles above 28° where KE did not reach a constant value, hence steady flows were not possible at these inclinations. Comparing to the kinetic energy of the flows at $\theta < 28°$, it was clear that the flows at an inclination $\theta > 28°$ were constantly accelerating. For this reason they were stopped (causing the truncation of the data) in order to minimize computational time for other simulations run simultaneously. Interestingly, for $e = 0.6$ and $e = 0.7$ at 24°, fluctuations of KE were observed. They were quite random for $e = 0.6$ but assumed a sinusoidal shape for $e = 0.7$. In this case, during the simulation time the system was subject to sudden vertical "explosions" and later relaxed again to a compact state. Similar behaviour was observed in numerical simulations [34, 155] when approaching the angle of repose of the material. The data of Silbert et al. [155] suggested that this may be caused by a periodic build up and relaxation of the stress in the system. Fluctuations were also observed experimentally by Louge and Keast [110], although over a flat base. Only flows that reached a steady state were selected for further analysis. Again they were within the range of $24° < \theta < 28°$, i.e., inclinations greater than 28° did not show the stabilizing effects of sidewalls [160]. In regard to this, it has been previously shown [154] that the angle of maximum stability is also dependent on the model parameters such μ and e. Moreover, the rough base, the flow thickness and the distance between sidewalls might hinder the development of stabilizing effects for such wide simulated systems (e.g. in Taberlet et al. [160] the distance between sidewalls was only $l_y \approx 25d$ whereas here $l_y = 66d$).

Table 5.2: Contact parameters for flows in the presence of sidewalls without rolling friction. Superscript $(_w)$ indicates the wall contact; subscripts $(_n)$ and $(_t)$, normal and tangential contact parameters, respectively.

Parameter	Symbol	Scaling	Value
Normal restitution	e_n		0.5, 0.6, 0.7
Normal stiffness	K_n	mg/d^2	$2 \cdot 10^5$
Sliding stiffness	K_t, K_t^w	mg/d^2	$2/7 \cdot K_n$
Normal damping	γ_n	$\sqrt{g/d}$	135, 100, 70
Sliding damping	γ_t, γ_t^w	$\sqrt{g/d}$	$2/7 \cdot \gamma_n$
Particle-particle friction	μ		0.45
Particle-wall friction	μ^w		0.35

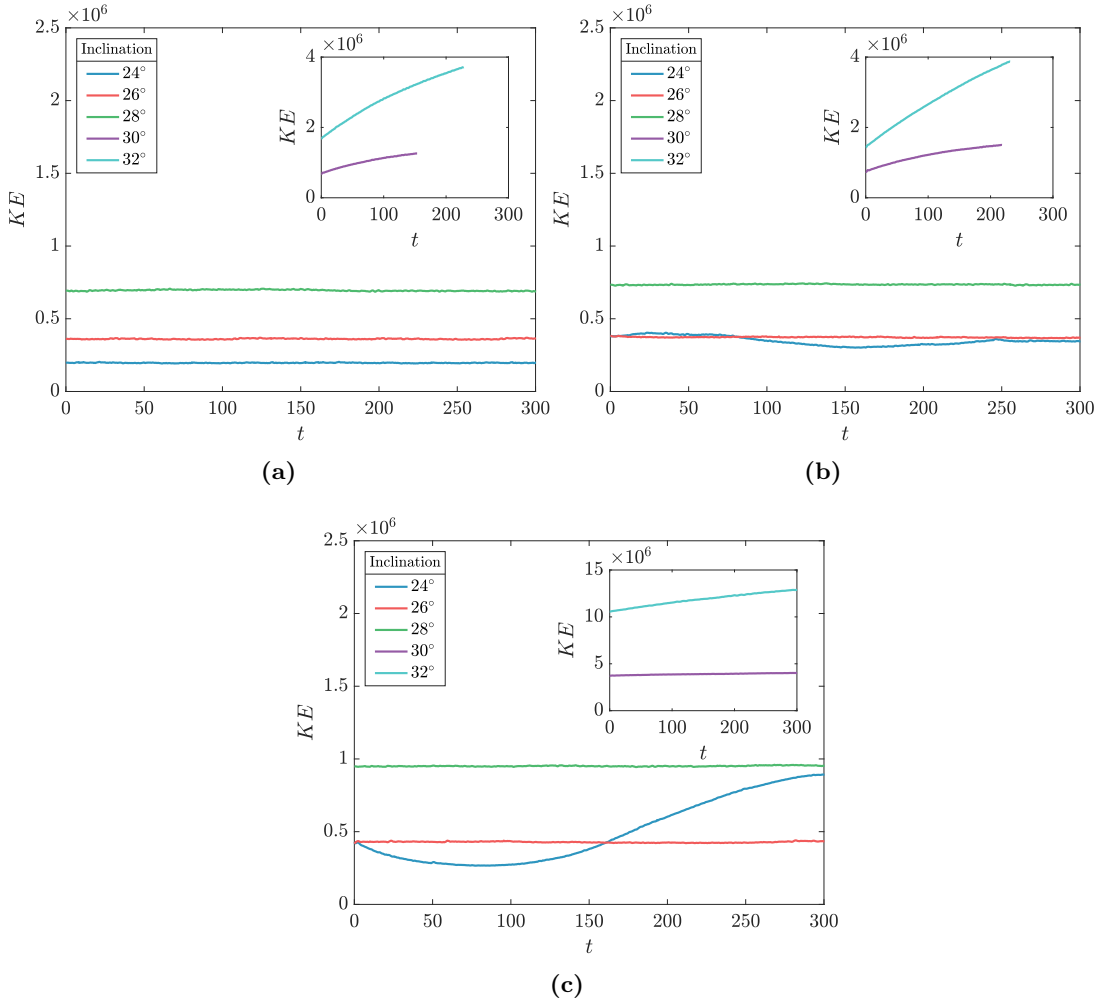

Figure 5.9: Kinetic energy plotted against time for flows in the presence of sidewalls without rolling friction with different restitution coefficient e.

Velocities were measured at different locations in the flows. Profiles were taken at $1d$ (circles) and $2d$ away (solid lines) from the sidewall (Fig. 5.10(a,c,e)) and then averaged in the spanwise direction (dashed lines) and compared to those along the centre line (triangles) (Fig. 5.10(b,d,f)). The velocity profiles are linear at the sidewall and recover a Bagnold-like shape in the middle of the channel. The particle-wall friction is felt by the particles in the proximity of lateral boundaries, then it dissipates away from them. This can also be visualized in the snapshots of Fig. 5.5 where it is clear that there is a "corner effect" [3, 70] between the sidewalls and rough base where the velocity is less compared to the bulk, a feature that was not possible to observe non-intrusively in the

opaque bead flows (Ch. 4). Nearly linear velocity profiles at the sidewall were observed in the experiments suggesting that a qualitative comparison with the simulations is possible. However, as it will be shown later, the magnitudes differ by almost a factor of two, e.g., at 26° the velocity is roughly 7 (0.84 m/s) at the top of the flow while in the experimental bead flow (Fig. 4.10) the maximum is only about 4 (0.48 m/s). The reason for this might be connected to the fact that, in the simulations the dynamics refer to a system of perfectly spherical particles, while the material used in the experiments has a certain degree of shape anisotropy (Table 4.1). This may induce a rolling resistance to motion and explain the difference in magnitudes. To take into account this possibility, simulations were also run by adding rolling resistance as explained later in more detail.

Sidewall, middle and averaged granular temperature profiles are shown in Fig. 5.11. At the centre of the flows (triangles) the temperature evolves from the base to the free-surface similarly to what was observed in the absence of sidewalls. The flow at 28° with $e = 0.7$ has a value of granular temperature in the middle and in the layer just above the base (Fig. 5.11(f)) that is less compared to that found in the periodic cell (Fig. 5.7(f)) by almost a factor of three. This indicates that there are some stabilizing sidewall effects which cannot be simply seen by analysing the kinetic energy of the system, but are highlighted by the magnitude of fluctuation velocity. At the sidewall granular temperature is less and varies almost linearly with depth compared to the middle cross section. More interestingly, there is an inversion of the profile at the sidewall which is directly affected by the coefficient of restitution. For $e = 0.5$ the granular temperature is nearly constant with height while for $e = 0.7$ the inversion it the strongest. Profiles that oppositely sloped near the sidewalls were also observed by Hanes and Walton [70]. Lateral boundaries, and particularly the corners, are very dissipative, providing sinks of fluctuational energy. Strikingly, profiles measured at $1d$ from the sidewall (circles) show a higher granular temperature than those $2d$ away (solid lines). Higher granular temperature at the sidewalls was also observed in chute flow simulations, although for thicker flows at steep slopes and over a flat base [33]. Particle-wall collisions may occur, thus increasing granular temperature, but sidewalls would also induce local ordering (or layering) in the flowing structure [70] where granular temperature is less. Furthermore, the experimental results previously presented (Sec. 4.5.4, Fig. 4.14) would suggest that granular temperature is oppositely sloping at the sidewalls. In principle, it should be possible to verify the accuracy of the measurements by analysing the profiles of solid concentration which is done next.

Solid concentration profiles are shown in Fig. 5.12 at the same distances $1d$ and $2d$ from the sidewall, along the centreline and then averaged in the spanwise direction. At the centre line (dashed lines in Fig. 5.12(b,d,f)), the same characteristics as in the absence of sidewalls are observed, i.e., two diluted regions approximately $3d$ thick at the bottom and

free-surface bound an almost constantly dense core region. Notably, at the sidewall, all the profiles measured at $1d$ (circles in Fig. 5.12(a,c,e)) also show a considerable reduction of ν indicating that the flows should be in a more dilute state close to lateral boundary. This is in contrast with experimental density measurements of bead flows. The cause may be connected to vacuum effects that corrupt coarse-graining. To verify this, snapshots of the simulations were taken at the distance of $0.5d$ and in the middle cross section to highlight this problem. From one of these snapshots in Fig. 5.13, it is clear that the concentration is much higher at the sidewall, contrary to the results of coarse-graining. The uncertainty might not just affect the concentration profiles but also those of velocity (although to a lesser extent as seen in Fig. 5.10(a,c,e)) and granular temperature. The uncertainty in terms of granular temperature and solid concentration profiles was also observed when the coarse-graining width was reduced to $w = 0.1d$, therefore to make sure that this did not alter the comparison with kinetic theory (made later in Ch. 7), measurements within $2d$ of the sidewall were disregarded. Once excluded, only a negligible variation of the spanwise average profiles was observed.

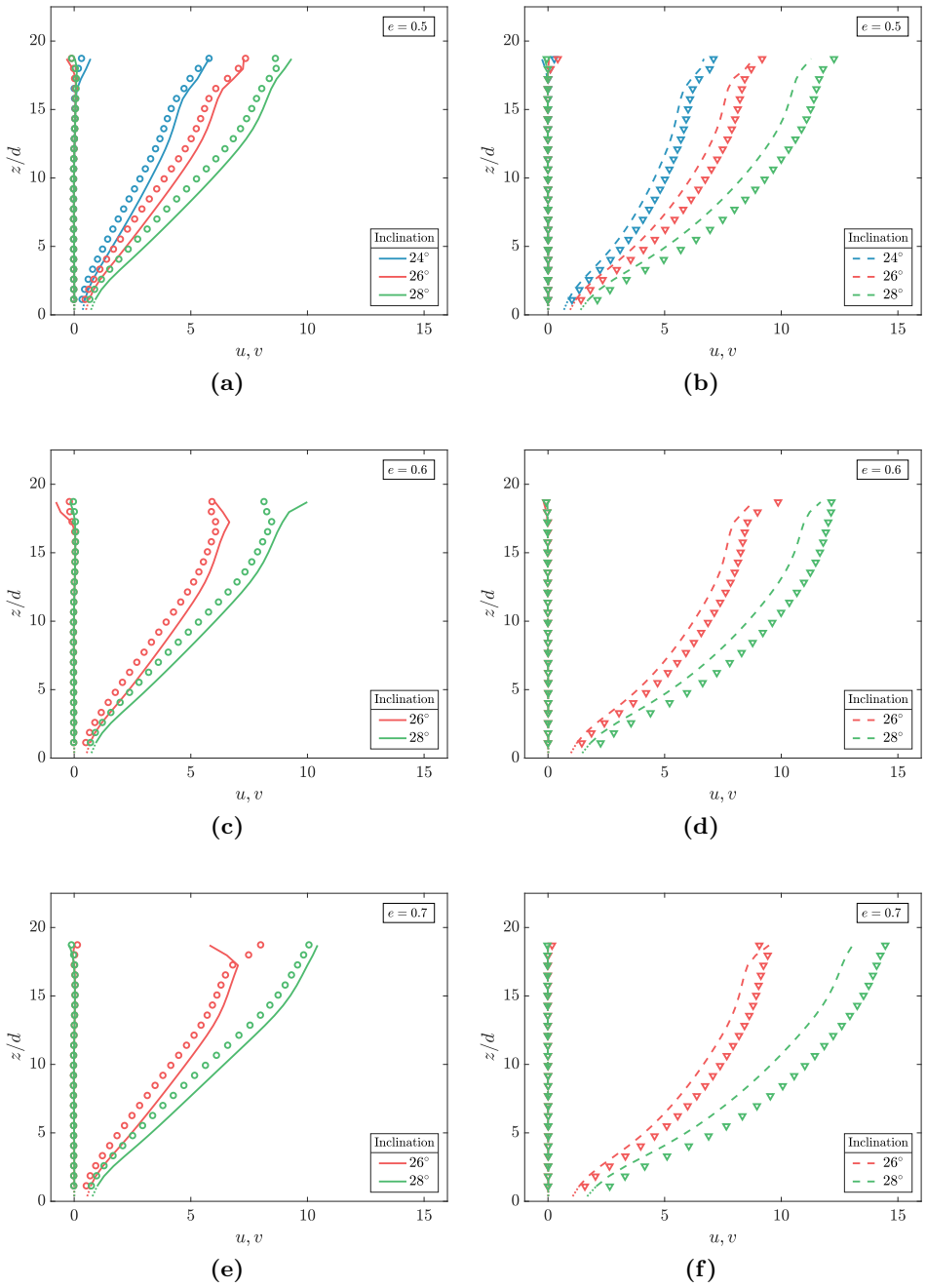

Figure 5.10: Velocity profiles from the simulations in the presence of sidewalls without rolling friction for different e: (**a**,**c**,**e**) profiles obtained at $1d$ (circles) and $2d$ away from the sidewall (lines); (**b**,**d**,**f**) profile in the middle of the channel (triangles) and averaged profiles in the spanwise direction (dashed lines).

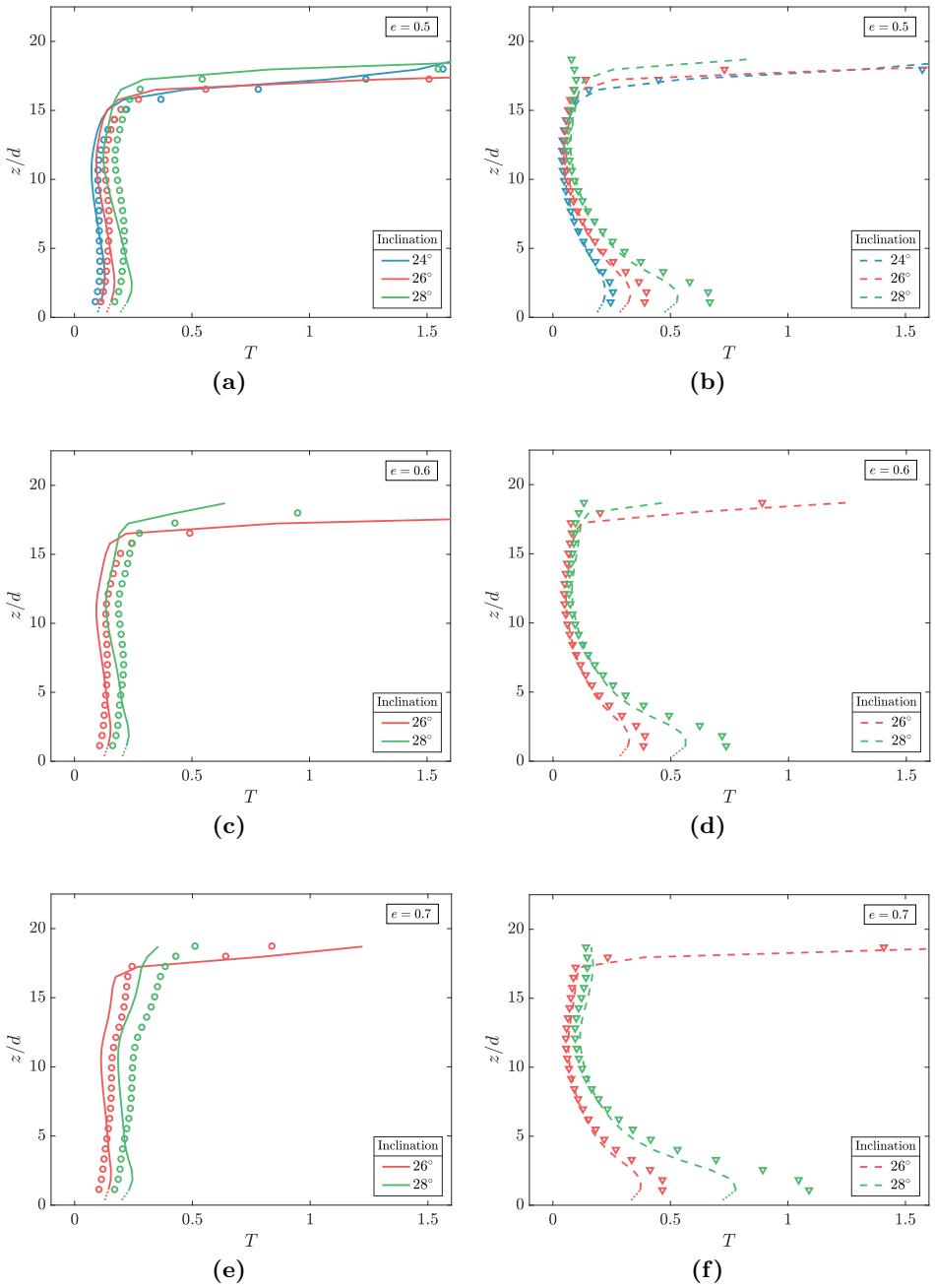

Figure 5.11: Granular temperature profiles from the simulations in the presence of sidewalls without rolling friction for different e: (**a**,**c**,**e**) profiles obtained at $1d$ (circles) and $2d$ away from the sidewall (lines); (**b**,**d**,**f**) profile in the middle of the channel (triangles) and averaged profiles in the spanwise direction (dashed lines).

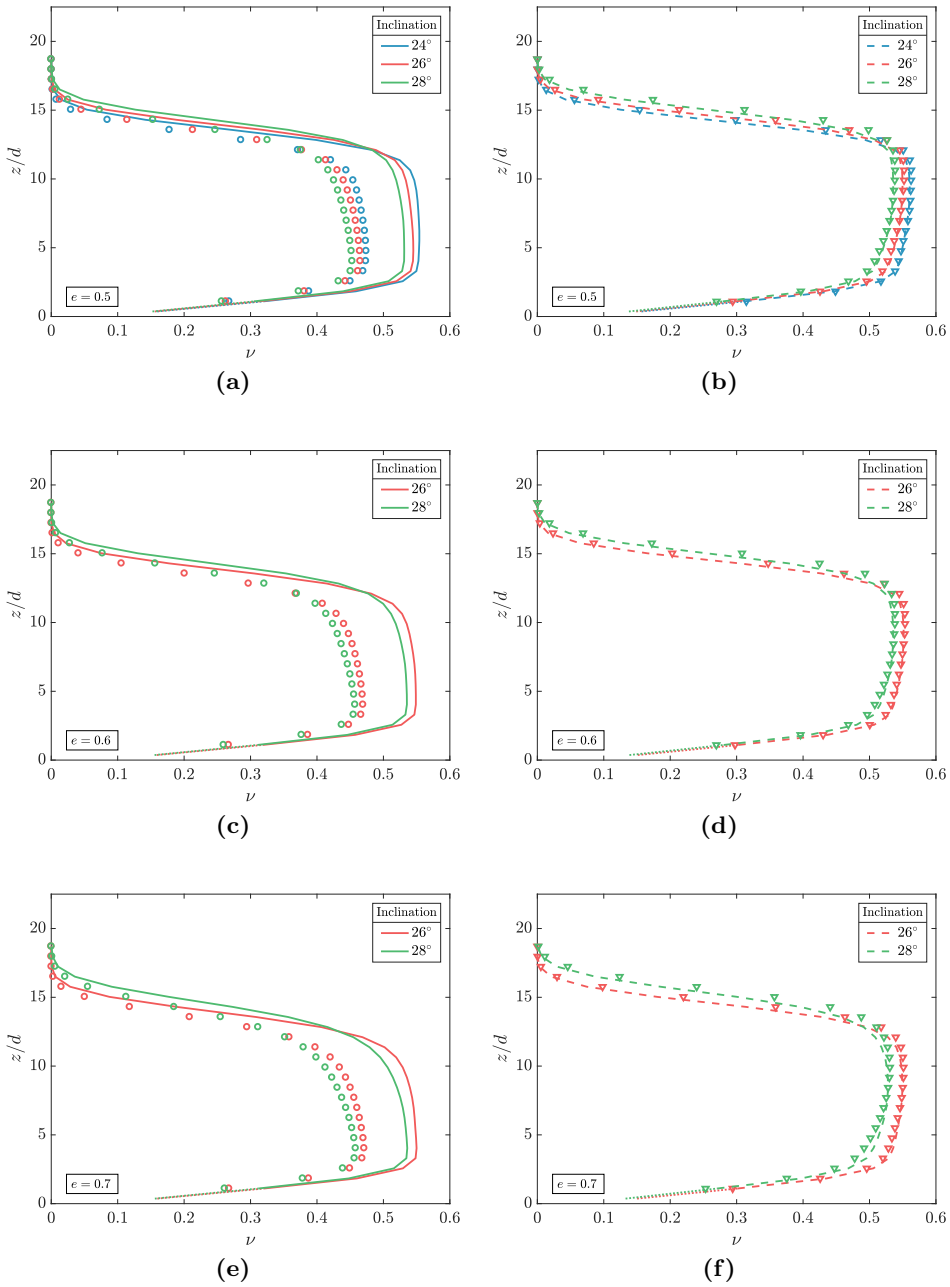

Figure 5.12: Solid concentration profiles from the simulations in the presence of sidewalls without rolling friction for different e: (**a**,**c**,**e**) profiles obtained at $1d$ (circles) and $2d$ away from the sidewall (lines); (**b**,**d**,**f**) profile in the middle of the channel (triangles) and averaged profiles in the spanwise direction (dashed lines).

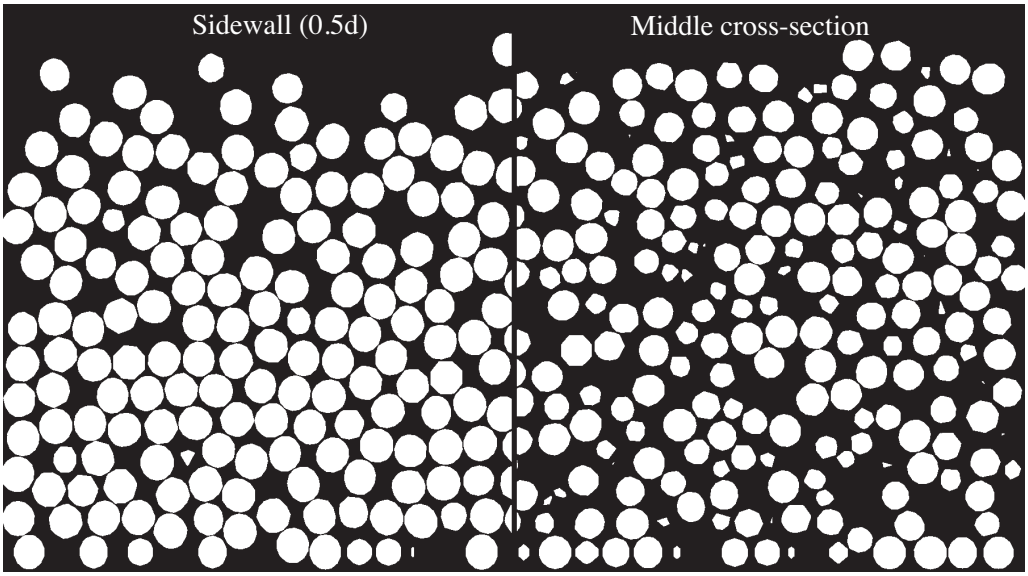

Figure 5.13: Snapshots of particle ordering for a simulation in the presence of sidewalls without rolling friction taken at $0.5d$ from the sidewall (left) and in the middle of the flow (right).

5.7 Flows between sidewalls with rolling friction

As already mentioned, the velocity profiles measured in the simulations did not match those obtained experimentally. Rolling resistance was added in order to reduce the velocities and bring their values close to those measured with PTV. In addition to the indicative value of rolling friction $\mu_r = 0.1$ based on the work of Wensrich and Katterfeld [175], other values were trialled. These are reported in Table 5.3 together with the other parameters used in the simulations.

Table 5.3: Contact parameters for flows in the presence of sidewalls with rolling friction. Superscripts $(_p)$ and $(_w)$ indicate particle and wall, respectively; subscripts $(_n)$ and $(_t)$, normal and tangential contact parameters, respectively; subscript $(_r)$ indicates rolling.

Parameter	Symbol	Scaling	Value
Normal restitution	e_n		0.7
Normal stiffness	K_n	mg/d^2	$2 \cdot 10^5$
Sliding stiffness	K_t, K_t^w	mg/d^2	$2/7 \cdot K_n$
Rolling stiffness	K_t^r	mg/d^2	$2/5 \cdot K_n$
Normal damping	γ_n	$\sqrt{g/d}$	70
Sliding damping	γ_t, γ_t^w	$\sqrt{g/d}$	$2/7 \cdot \gamma_n$
Rolling damping	γ_t^r	$\sqrt{g/d}$	$2/5 \cdot \gamma_n$
Particle-particle friction	μ_p		0.45
Particle-wall friction	μ_p^w		0.35
Particle-particle rolling friction	μ_r		0.1, 0.2, 0.3
Particle-wall rolling friction	μ_r^w		0.15

Velocity profiles for different rolling friction coefficients are given in Fig. 5.14 where the simulation results (solid lines) are compared against the experimental data (symbols). By varying the value of rolling friction it was possible to shift the velocity profiles, however, it was difficult to find a best match for all the flows. A rolling friction of 0.1 still overestimates the data while 0.3 tends to underestimate the majority of the experimental measurements. A value of 0.2 was chosen as the reference value which gives a good fit at least for the flow at 26°. The comparisons between DEM and experiment results for this specific flow are further discussed later.

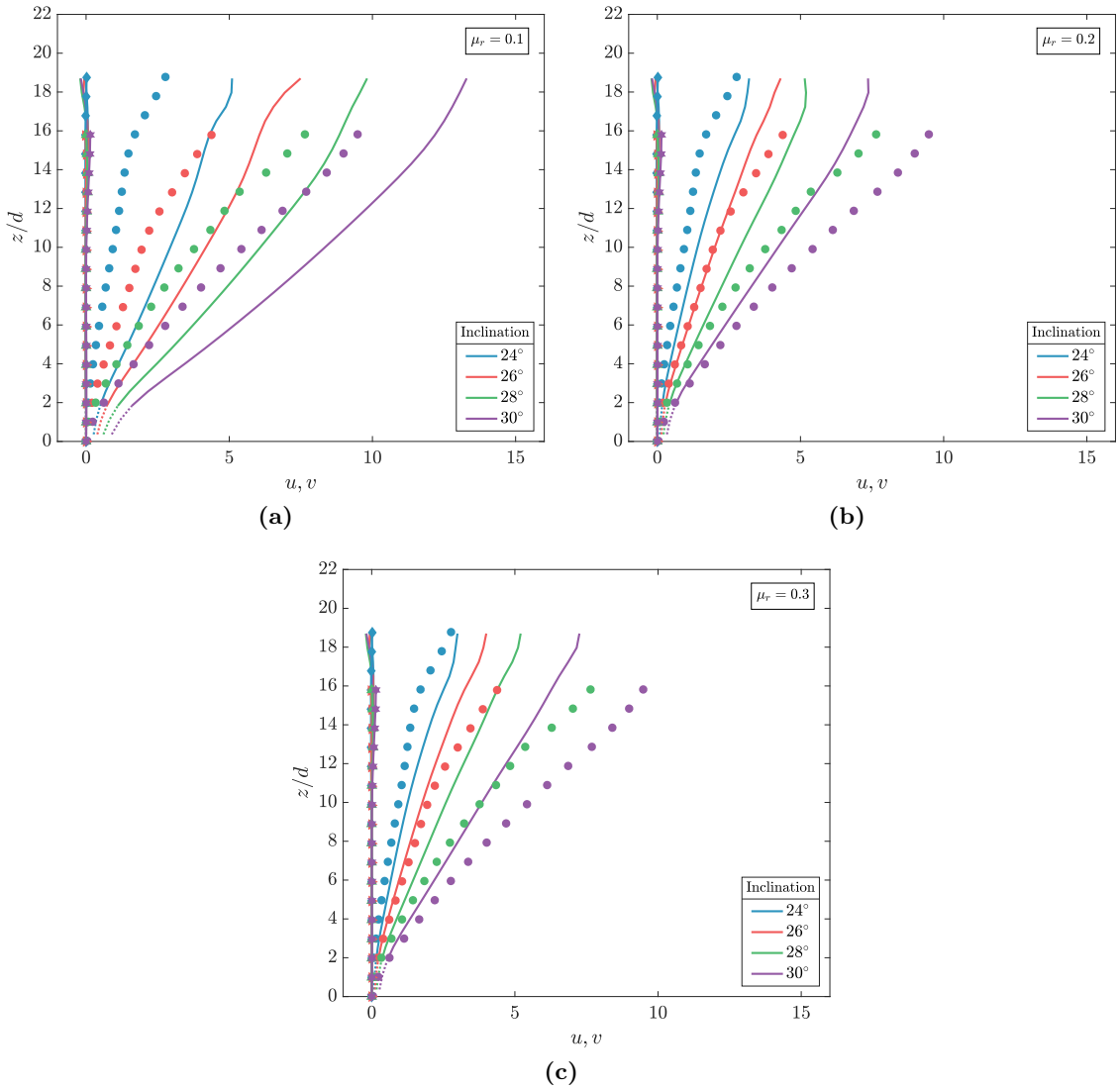

Figure 5.14: Velocity profiles from the simulations in presence of sidewalls with different values of rolling friction (solid lines) are compared against the experimental velocity profiles (symbols).

In Fig. 5.15 the kinetic energy for the systems with $\mu_r = 0.2$ highlights the fact that the addition of rolling resistance makes possible steady flows up to an angle of 30°, a greater inclination compared to the previous numerical results and within the range measured experimentally.

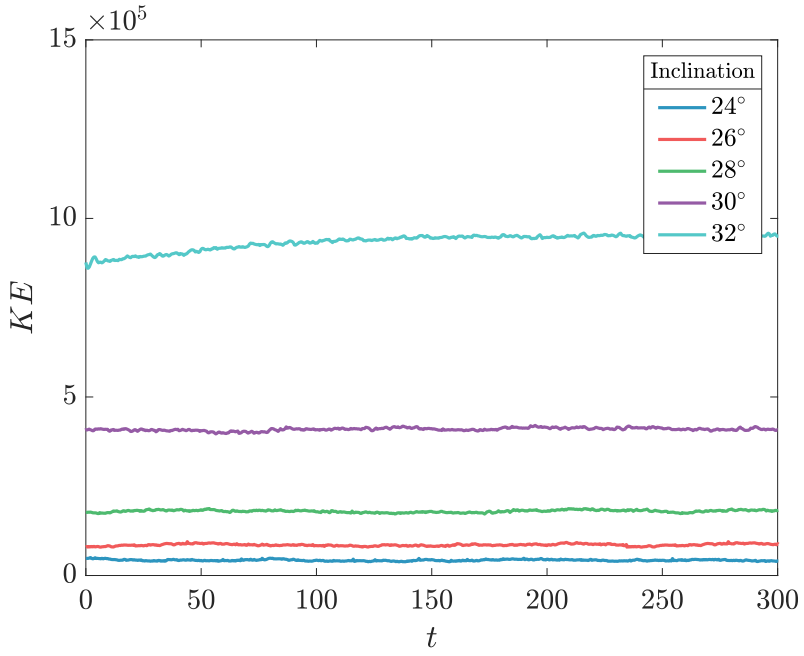

Figure 5.15: Kinetic energy plotted against time for flows in the presence of sidewalls with rolling friction.

Measurements of velocity, granular temperature and solid concentration are shown with their respective profiles taken at a distance of $1d$ (circles) and $2d$ away (solid lines) from the sidewall (Fig. 5.16(a,c,e)) and averaged in the spanwise direction (dashed lines) against those in the centre line (triangles) (Fig. 5.16(b,d,f)). Apart from the reduced magnitude of velocity and granular temperature, similar characteristic behaviours as are found in the absence of rolling friction are obtained, thus the previous discussions in Sec. 5.6 are valid also here.

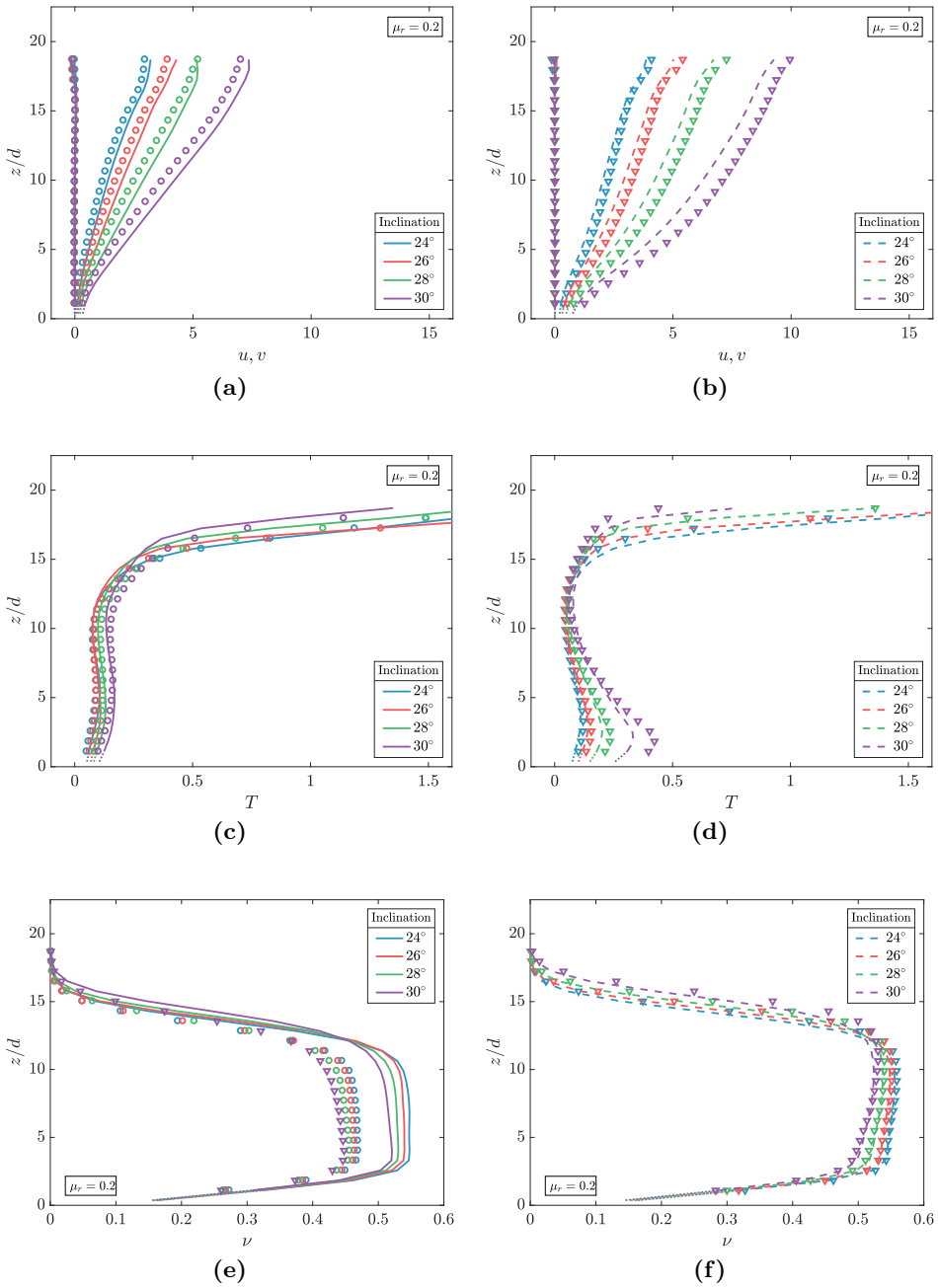

Figure 5.16: Velocity (**a**,**b**), granular temperature (**c**,**d**) and solid concentration (**e**,**f**) profiles from the simulations in the presence of sidewalls with rolling friction: profiles obtained at $1d$ (circles) and $2d$ away from the sidewall (lines); profile in the middle of the channel (triangles) and averaged profiles in the spanwise direction (dashed lines).

5.7.1 Comparison of chute flows results between simulations and experiments

The flow at 26° was chosen to give a first comparison between the numerical (DEM) and experimental (PTV) results. For the other angles of inclination, the results are given in Appendix C. It might be questionable to compare the two approaches since in principle a correction of granular temperature should be also applied to PTV when different binning widths are used. However, the validation of PTV measurements conducted with a binning width of $1d$ (see Sec. 6.4) shows that there is a narrow range of Δt where the values tend converge close to the granular temperature measured numerically. That is, although the errors affecting PTV cannot be completely removed, this method can give a good estimation of granular temperature magnitude and its gradient variation across the flow height. Because coarse-graining is less reliable close to the sidewall, here the comparison is made by taking measurements $2d$ away. A coarse-graining width of $w = 1d$ and a PTV post-processing binning width of $1d$ were used, thus the measurements are compared at the same averaging scale.

In Fig. 5.17(a) a good agreement between the velocity profiles is found up to a height of approximately $12d$. Above this height the experimental data slightly deviate from the numerical values. A good match is also found for the granular temperature (Fig. 5.17(b)) with a discrepancy at the top of the flow, however there, PTV is less reliable since particles are moving too fast and hence the measurements should be treated with care. The overestimation of the DEM model below $12d$ is connected to the fact that measurements refer to different locations from the sidewall, i.e., a better agreement may be achieved if the coarse-graining procedure would be valid also at the sidewall. The shear rate is well matched by the two approaches, showing an almost constant variation with depth (Fig. 5.17(c)), thus leading to a linear velocity profile [135, 156]. Pressure is related to the solid concentration through Eqs. 5.24 and 4.6. In Fig. 5.17(d,c) a good match is found also for these two quantities although experimental measurement of ν are valid up to ≈ 0.55. For greater values, the data are overestimated and truncated at the random close packing limit leading to the slight overestimation of the experimental pressure. Conversely, the high value of pressure at the base of the simulation profile is a direct consequence of the coarse-graining smoothing width (as was shown in Fig. 7.2), thus a smaller width may lead to better agreement.

Through the fitting of the simulation parameters, a general agreement is found with the experimental measurements. Rolling friction was added based on the experimental velocity profiles. However, the particle property known as “rolling friction” is accepted with different levels of enthusiasm [175], thus further research needs to be done before claiming that this is the correct approach. A better approach would be to use DEM simulations

able to reproduce the real contacts of spheroidal shape (e.g., elliptical particles) or angular material without the use of rolling resistance. However, such simulations are, in general, not very common due to the extended computational time. Assuming perfectly spherical particle in DEM is still preferred since this enables a simple mathematical implementation and the ease of computational costs.

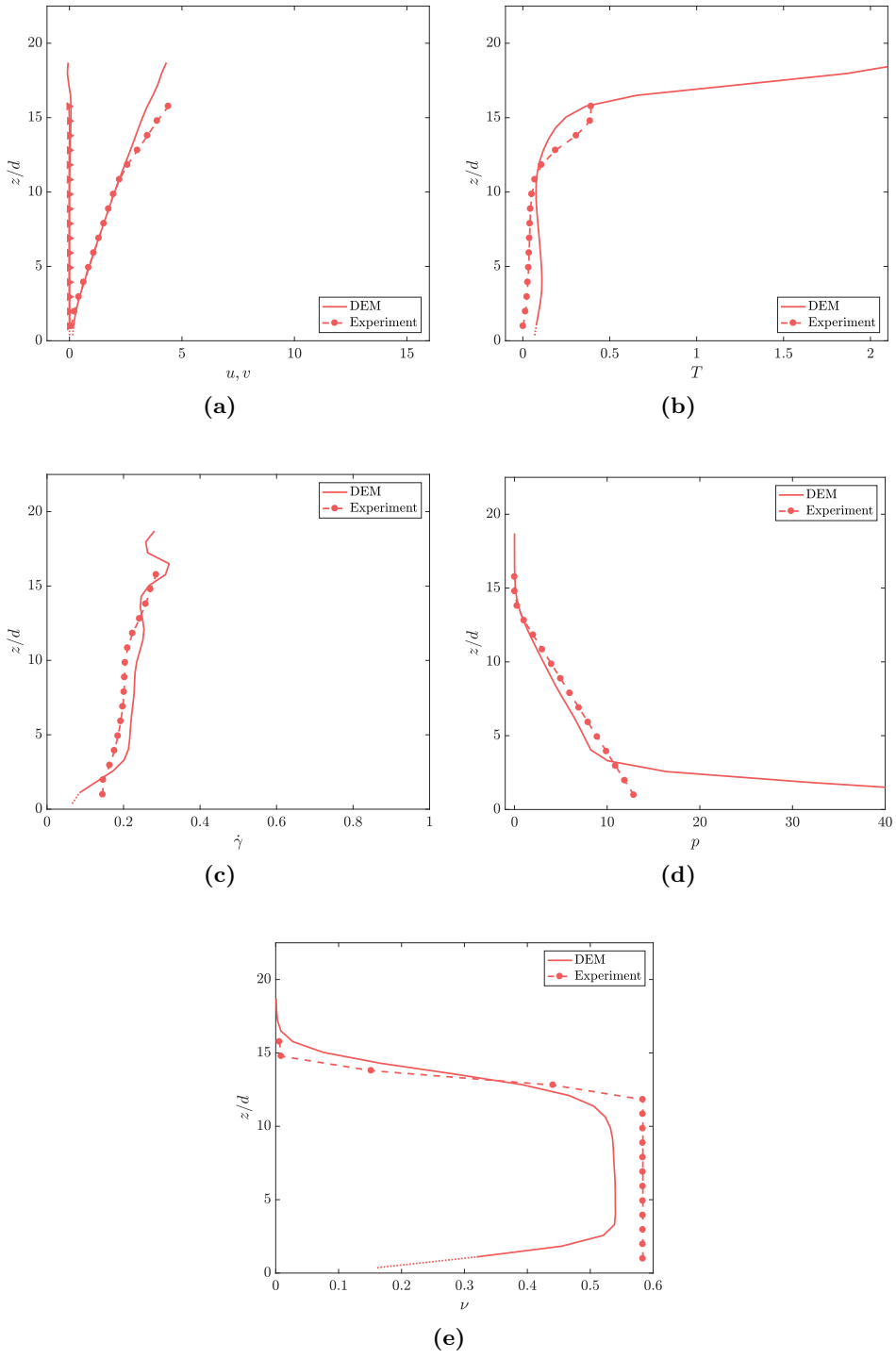

Figure 5.17: Comparison between experimental measurements (dashed-line with symbols) and numerical results (red solid lines) with rolling friction ($\mu_r = 0.2$) for the flow at 26°: velocity (**a**), granular temperature (**b**), shear rate (**c**), pressure (**d**), solid concentration (**e**).

5.8 Conclusion

Numerical simulations of dry granular flows were performed via discrete element method (DEM) in the absence and presence of sidewalls to identify the main rheology developing in such flows and to test the prediction of kinetic theory.
In the periodic cell, flows were only controlled by the gravitational force and the rough base. Over a range of inclinations the velocities resembled a Bagnold-like profile while the granular temperature had the characteristic gradient for flows over a bumpy base, i.e., the energy injection of the base generated higher grain agitation within a region of approximately three diameters above the bumpy base which progressively decayed towards the free-surface. The solid concentration profiles confirmed that these flows are, in general, characterized by a core region where the concentration is constant bounded by two less dense regions, one close the base and one at the free-surface. The influence of the simulation parameters, in particular the coefficient of restitution e that caused a shift in velocity towards faster profile in one case, was also reported.
A simulation flow configuration based on the experimental apparatus was also studied numerically. In general, the behaviour away from the sidewalls was similar to the periodic cell over the same range of inclination and for the possible steady flows. At the lateral sidewalls the measurement were erroneously interpreted by coarse-graining which led to an underestimation of the solid concentration. Taking profiles $2d$ away from the sidewalls where the such problems did not occur showed that the velocities had linear profiles and granular temperature was generally less and varied almost linearly with depth compared to the middle cross section. The match of experimental results was achieved by adding the rolling resistance to the simulations which, at least for a flow at an inclination of 26°, led to a good agreement between the two approaches.

6. Validation of PIV and PTV for the measurements of granular temperature

6.1 Introduction

Comparison of experimental results with extended kinetic theory predictions require the measurement of granular temperature. However, knowing that errors affect the measurements of PIV and PTV, the true value of granular temperature is generally not known from experiments. Considering a steady dry granular flows made of identical spherical particles, synthetic images and accurate measurements of granular temperature can be obtained from numerical simulations that closely match the experiments. While rolling resistance is introduced to take account for the shape anisotropy of the particles and match the results of experimental flows, synthetic images represent systems of perfectly spherical particles. Despite the discrepancy that may arise, this approach is used in this section to give a quantitative validations of PIV and PTV for the measurement of granular temperature.

After describing the simulation procedure and results in Sec. 6.2, the method to generate synthetic image is explained in Sec. 6.3. Based on the images generated, measurements of granular temperature obtained from PTV are validated in Sec. 6.4 while those obtained from PIV are validated in Sec. 6.5.

6.2 Numerical simulations

Numerical simulations used for the validation of PIV and PTV refer to the periodic cell configuration described in Sec. 5.4. The system had dimension $l_x \times l_y = 20d \times 10d$ with lateral periodic boundaries along x and y. A single layer of 180 particles was glued at random spacing on the flat surface. All the simulations consisted of 3500 flowing spherical particles which led to typical flow height of $\approx 20d$. The results are given in dimensionless form but the transformation to real units can again be obtained using the scaling factors already introduced in Sec. 5.4. The simulation parameters are listed in Table 6.1. Rolling

resistance was used to reduce the velocity of the systems (Fig. 6.1(a)) and bring the magnitudes close to those found in the experimental flows. This was necessary to achieve similar particle displacements and set initial sampling intervals Δt (or frame rates) to be comparable to those used in the experiments.
The kinetic energy of the system (Fig. 6.1(d)) was tested for different angles of inclination revealing that at 24°, 26° and 28° steady flows were possible, whereas at lower or steeper angles they either stopped or continuously accelerated. The solid concentration profiles (Fig. 6.1(c)) have the same characteristic core regions seen in Sec. 5.5 with approximately constant densities bounded by other two less dense regions at the bottom and top of the flows.
The choice to use a periodic cell was led by the profile shape of the granular temperature. In the experiments conducted at the sidewall with ceramic beads, the granular temperature gradient varied in accordance with the solid concentration, i.e., when the flows were dense, the granular temperature close to the base was generally less and increased linearly upwards. Conversely, the periodic cell simulations are characterized by having a higher granular temperature close to the rough base (Fig. 6.1(b)). This fact was used to test the capability of PIV and PTV in reproducing this feature. Whether the two imaging techniques were able to give comparable temperature magnitudes was also tested.

Table 6.1: Simulation parameters used in the generation of synthetic images for the validation of PIV and PTV.

Parameter	Symbol	Scaling	Value
Normal restitution	e_n		0.7
Normal stiffness	K_n	mg/d^2	$2 \cdot 10^5$
Sliding stiffness	K_t	mg/d^2	$2/7 \cdot K_n$
Rolling stiffness	K_t^r	mg/d^2	$2/5 \cdot K_n$
Normal damping	γ_n	$\sqrt{g/d}$	70
Sliding damping	γ_t	$\sqrt{g/d}$	$2/7 \cdot \gamma_n$
Rolling damping	γ_t^r	$\sqrt{g/d}$	$2/5 \cdot \gamma_n$
Particle-particle friction	μ_p		0.45
Particle-particle rolling friction	μ_r		0.12

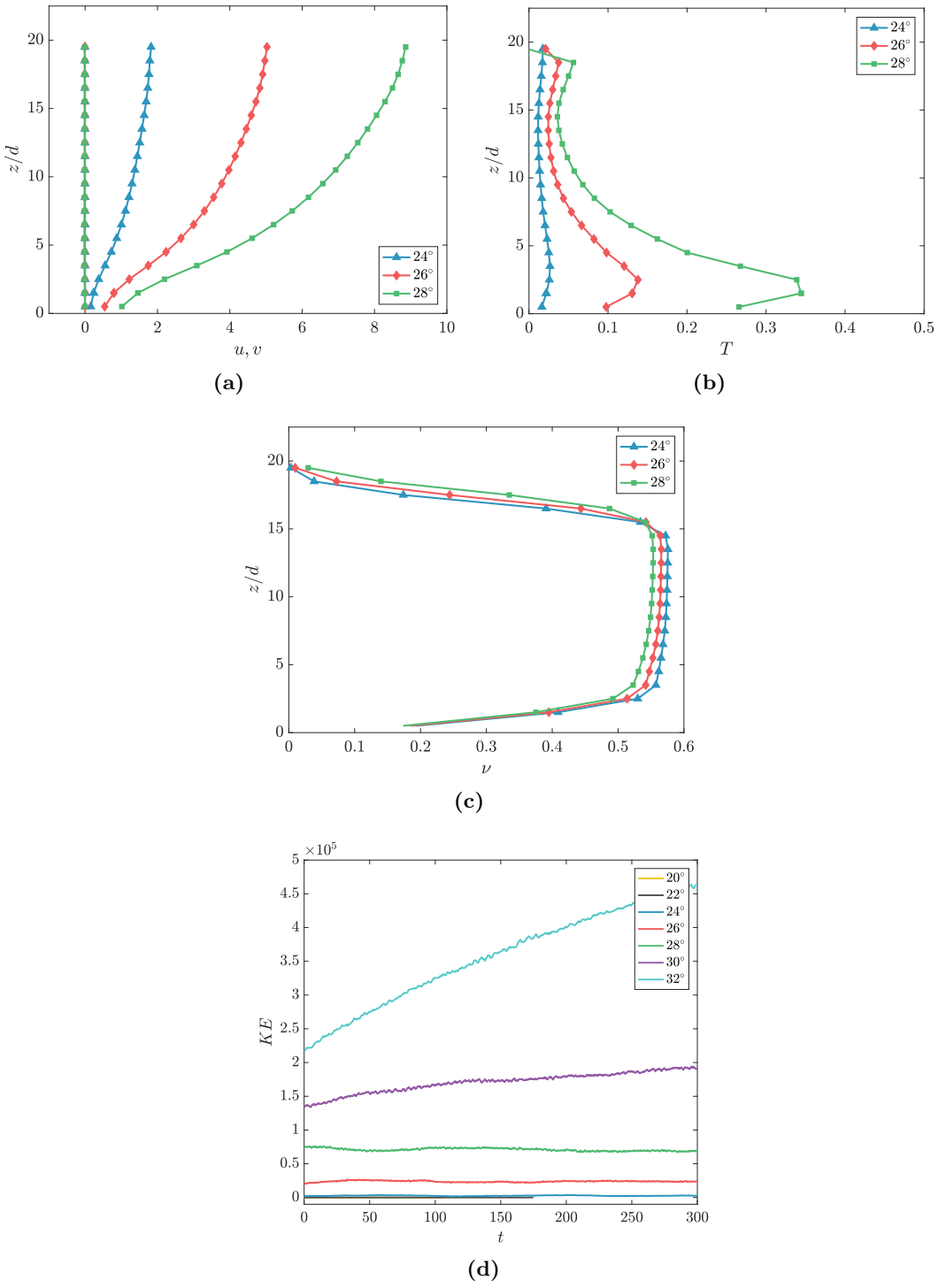

Figure 6.1: Velocities (**a**), granular temperature (**b**) and solid concentration (**c**) for the simulations used in the generation of synthetic images. Kinetic energy of the systems used in the generation of synthetic images (**d**)

6.3 Synthetic Image Generation

Synthetic images were generated based on particle positions extracted from periodic cell simulations. For the results presented here, the individual particle images are described by a Gaussian intensity profile [134]

$$\mathcal{I}(x,y) = \mathcal{I}_0 \exp\left[\frac{-(x-x_0)^2-(z-z_0)^2}{(1/8)d_\tau^2}\right], \tag{6.1}$$

where the centre of the particle image is located at (x_0, z_0) with a peak intensity of $\mathcal{I}_0$. The magnification factor between object plane and image plane is chosen to be unity, such that $(x, y, z) \equiv (X, Y, Z)$, where X, Y, Z are coordinates in unit pixels. The particle diameter, d_τ, is defined by the intensity of the Gaussian bell. The factor $\mathcal{I}_0$ is a function of the particle's position, Y_0, within the simulation domain. For a light sheet centred at $Y = 0$ with a Gaussian intensity profile (Fig. 6.2(a)), $\mathcal{I}_0$ is expressed as [134]

$$\mathcal{I}_0(Y) = \Upsilon \exp\left[\frac{Y^2}{(1/8)\Delta Y_0^2}\right], \tag{6.2}$$

where Υ is the maximum level of intensity set to 180 considering a grey scale between 0 (black) and 255 (white) and estimated based on the average intensity value of experimental images and ΔY_0 is the thickness of the light sheet. Eq. 6.2 represents the amount of light received by the particle i inside the flow, i.e., when particle i is at $Y = 0$ its intensity peak is $\mathcal{I} = \Upsilon$ which reduces at a distance $|Y_i - Y_0|$ from the centre plane following a Gaussian profile.

The peak of the light sheet was located in the central section of the simulation domain ($l_y = 5$) and half of the light sheet disregarded (hatched area in Fig. 6.2(a,b)). In this way the first layer of particles had the maximum level of intensity (peak of the Gaussian) which reduced with Y hence recreating similar light penetration conditions as the experiments. To generate a particle image, a single particle's position (X_1, Y_1, Z_1) was taken within the selected half section. No substantial changes were observed when particles deeper than $2.5d$ where included due to the occlusion of the foreground ones. For this reason, the computation was restricted to particles within $0 < Y < 2.5d$ only. The peak intensity $\mathcal{I}_0(Y_1)$ was estimated using Eq. 6.2 and the value substituted into Eq. 6.1 to define the light captured by each pixel. This operation was repeated for all particles at each time step for a total duration of $t = 324$ (4 s). Typical synthetic generated images are shown in Fig. 6.2(c,d). Noise was not added to the images.

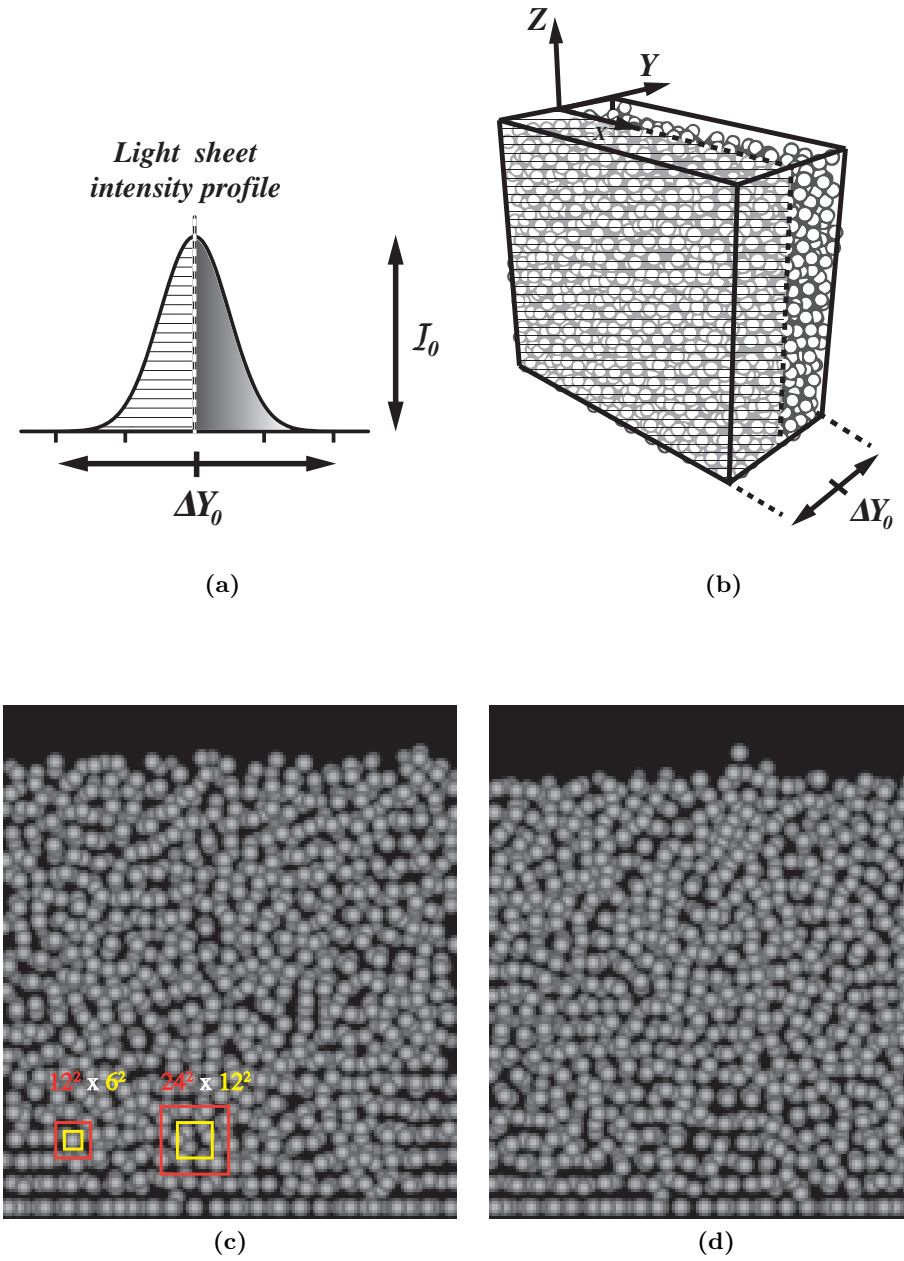

Figure 6.2: Synthetic image generation: light sheet profile (**a**) and section of the simulation domain where particle positions where taken (**b**). Typical synthetic images at an inclination of 24° detailed with interrogation sizes for PIV (**c**) and at 28° (**d**).

6.3.1 Synthetic images processing

One of the issues encountered during the generation of synthetic images was the transformation of particle centroids from the simulation, given up to ten decimal points, to the image plane which consisted of a matrix with integer pixel values. That is, the original centroid positions from the simulations were required to be rounded at an integer value to be allocated in the image matrix. This resulted in a spurious centroid allocation which severely disrupted the profile of granular temperature. To decrease this effect, the particle images were initially created with $d_\tau = 100$ pixels, then both particle images and centroids downscaled by a factor of 20 with a final maximum diameter of five pixels. Initial particle diameters greater than 100 pixels would have been possible, thus leading to improved quality of the image outputs, although this would have required considerable computational effort and therefore were not considered. With the procedure given, particle centroids were positioned with subpixel accuracy. However, a residual error remained in the data which did not allow a direct comparison with the simulation results for all Δt as explained in more detail in the next section.
The matching of the particle centroids between frames was done with the sub-routine followed by the particle tracking algorithm used in this thesis (i.e., a combination of cross-correlation and relaxation algorithms, see Sec. 3.2). Knowing positions and displacements of each particle in the synthetic images, it was straightforward to extrapolate the velocity and granular temperature profiles following the procedure of Sec. 4.4.2. Following the procedure used in the experimental analyses, initial sampling intervals Δt (or frame rates) were defined depending on the flow velocity magnitudes and later reduced by skipping frames (i.e. increasing Δt) through the original set of synthetic images created. All the sampling intervals considered with the corresponding frame rates are reported in Table 6.2.

Table 6.2: Sampling intervals and frame rates used for validation of PIV and PTV

24°		26°		28°	
Δt	fps	Δt	fps	Δt	fps
0.04	2000	0.025	3000	0.02	4000
0.08	1000	0.05	1500	0.04	2000
0.16	500	0.10	750	0.08	1000
0.32	250	0.20	375	0.16	500
0.64	125				

6.4 Validation of PTV

The first step of the validation was to verify that the procedure explained above (Sec. 6.3.1) was able to reproduce the same velocity and granular temperature profiles measured in the middle cross section of the DEM simulations. The results obtained are compared to coarse-graining measurements obtained with an averaging width $w = 1d$. Note that is the same scale length used in binning of the velocity vector field in PTV where a bin height of $1d$ was used (see Sec. 4.4.2).

The velocity profiles in Fig. 6.3(a,c,e) collapsed onto the same curve for different values of Δt and, apart from a small underestimation at the bottom of the flows ($z < 10d$), they closely matched the simulation velocities, therefore validating the synthetic image approach, at least in terms of this quantity. The small underestimation at the bottom of the flows ($z < 10d$) develops since the residual error generated during the centroid allocation form the simulations is more severe for slow moving particles.

Granular temperature profiles shown in Fig. 6.3(b,d,f) were influenced by Δt and tended to converge to the same curve for increasingly long sampling intervals, although a full convergence was never reached. Notably, the residual error in the image is clearly evident when the shortest Δt is analysed. The magnitude of granular temperature is considerably higher than the rest and profile peaks (especially at 24°) are more pronounced. This fact can be related to what was previously seen in the preliminary experimental tests carried out for spherical beads (Sec. 4.5.3). Once the sampling interval Δt is increased, this error is minimized, thus longer Δt may be indeed require for a better estimation of granular temperature. Compared to the direct application of PTV which is subjected to the two sources of error investigated in Sec. 3.4.2, the only difference is that, in this case, the error is caused by the synthetic image down-scaling procedure used to better allocate the particle centroids. It should be possible to see the same effect even when PTV is applied to the synthetic image as shown below.

The time independent procedure used to extract the profiles from simulations (dashed-lines) was used as reference to verify whether any of the sampling intervals at a specific inclination were able to approximate these values. This was obtained only for selected Δt and their respective profiles (grey lines with squares) were used as an additional reference against PIV and PTV measurements. Ultimately, the profiles obtained were determined to be suitable benchmarks when selected for specific Δt and synthetic images were, in general, able to generate the patterns and magnitudes of granular temperature found in the simulations. For simplicity, in the following the selected profiles at specific Δt are termed SIG (synthetic image generation).

The second step of the validation was to apply PTV to the synthetic images and test the results against those of SIG and simulation. Following the same procedure of Sec. 4.4,

profiles of velocity and granular temperature were obtained. While velocity profiles (Fig. 6.4(a,c,e)) collapsed onto the same curves and showed an insensitivity to Δt, the granular temperature (Fig. 6.4(b,d,f)) was again influenced by it. For the two longest sampling intervals at 24° and 26°, the profiles of this quantity were in good agreement with those of SIG and simulation. Results were similar at 28° although for the longest Δt the large displacement caused the failure of PTV above 10 particle diameters.
The results show that a correct choice of Δt is indeed necessary for a proper estimation of granular temperature. The good matching of the PTV data to those of SIG and simulations supports the quality of experimental measurements in terms of PTV when longer time intervals are used. A specific value of Δt that gives the best match is difficult to obtain and would probably require an adjustment of the PTV parameters, however, the validation performed here shows that very fast Δt (or high frame rate) cause the measurements to be dominated by noise, while there is a narrow range of Δt where the values approximate closely the granular temperature measured numerically.

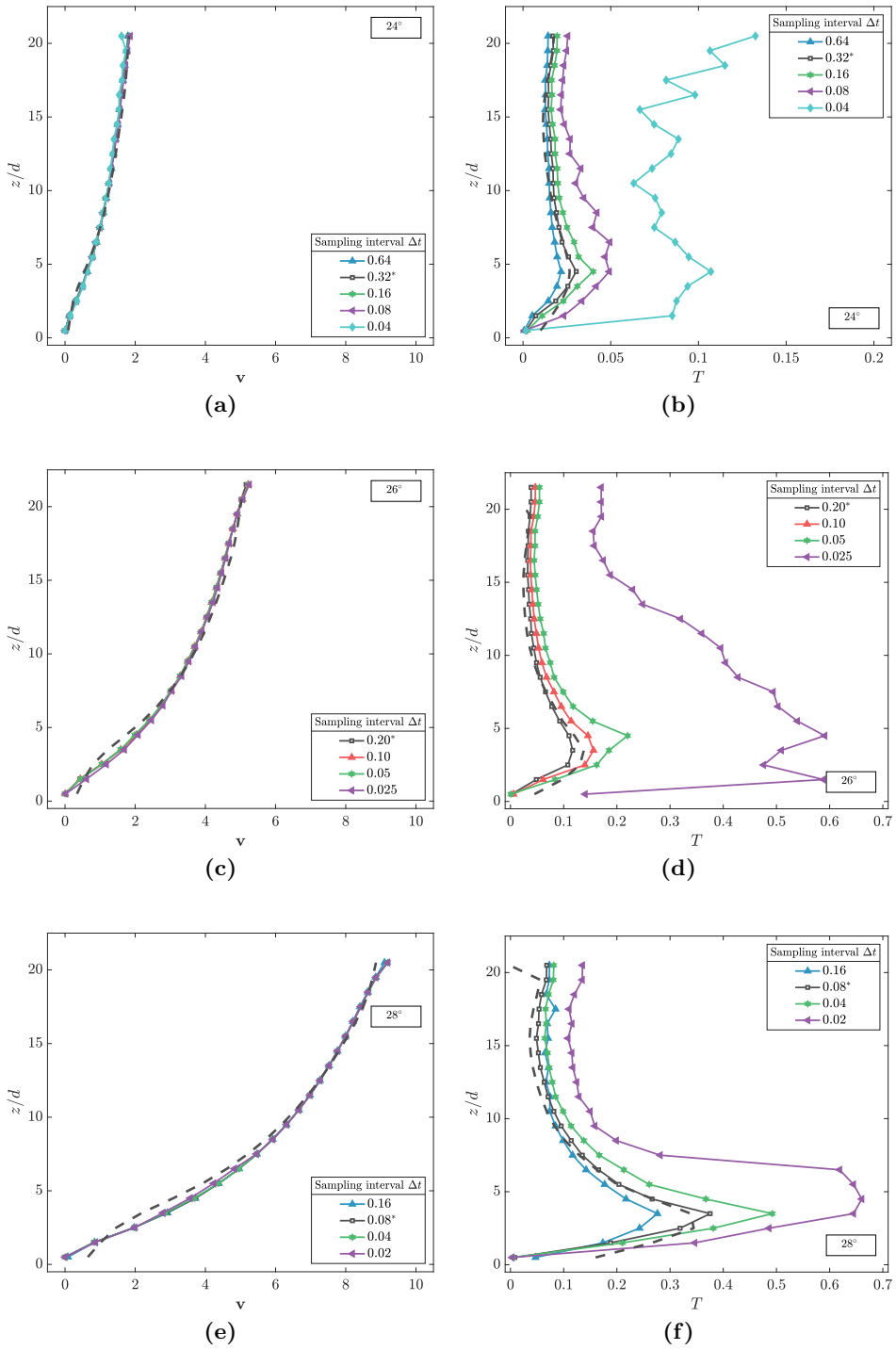

Figure 6.3: Velocity (**a**,**c**,**e**) and granular temperature (**b**,**d**,**f**) profiles calculated from known particle positions of synthetic images for different inclinations and Δt as reported in Table 6.2. Selected profiles (⊟) with the best match to the simulation measurements (▪ ▪ ▪).

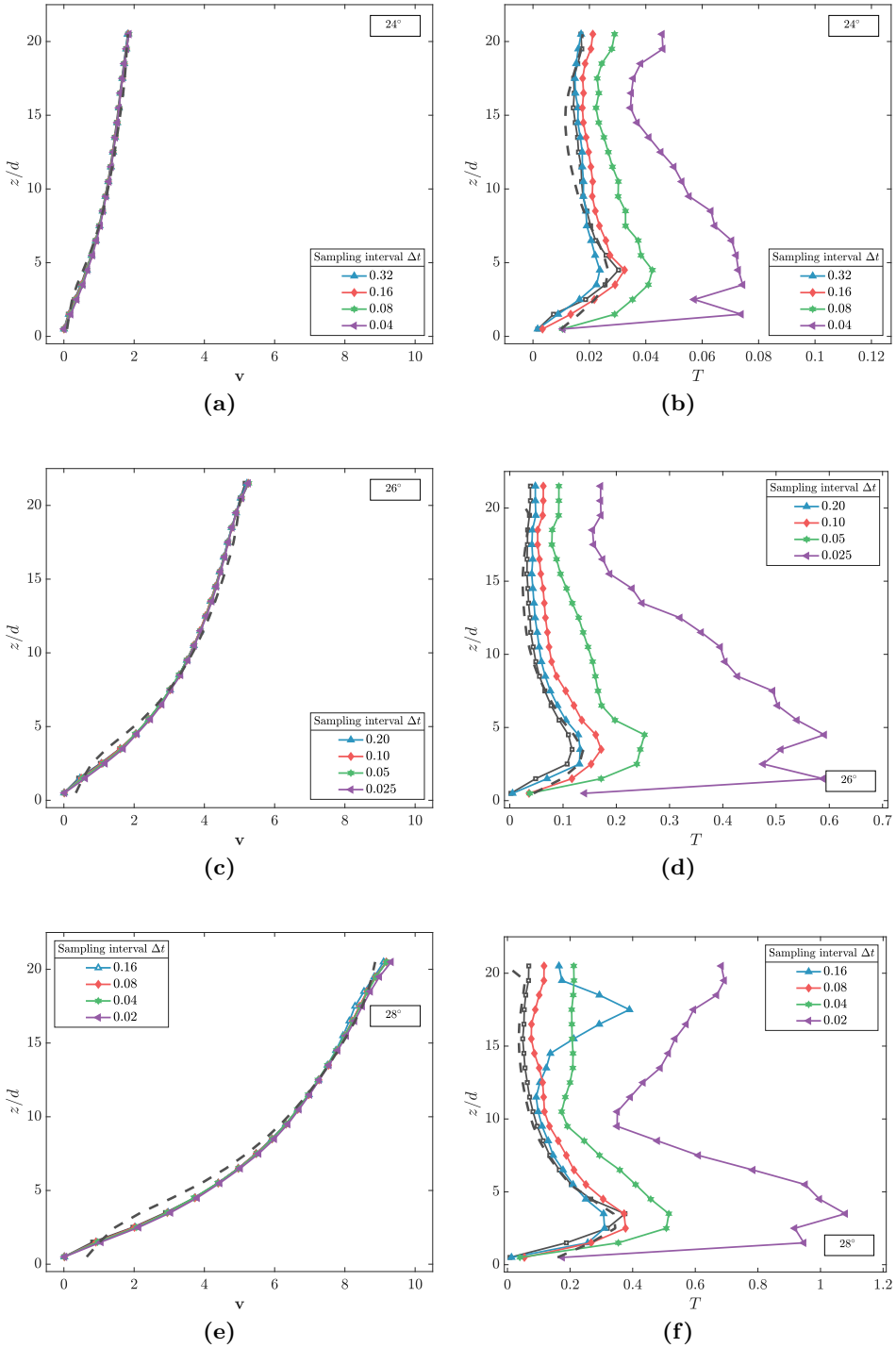

Figure 6.4: Velocity (**a**,**c**,**e**) and granular temperature (**b**,**d**,**f**) profiles calculated with PTV from synthetic images for different inclinations and Δt as reported in Table 6.2. Selected SIG profiles (–□–) with the best match to the simulation measurements (▪ ▪ ▪).

6.5 Validation of PIV

Particle image velocimetry was also applied to the synthetic images and tested against the results of SIG and simulation. Again, the results obtained from DEM refer to those measured in the middle cross section of the flows. Knowing that the particle displacements must be half the interrogation window size (Sec. 3.4.1), average displacement profiles were obtained based on known positions of the synthetic particle images. Based on these measurements it was possible to define the correct patch to be used in order to avoid aliasing. Two sets of interrogation areas of 24x24 - 12x12 pixels and 12x12 - 6x6 pixels (for the coarse and refined grids, respectively) were selected. To give a unit of measure, an example of their sizes compared to a flow image is given in Fig. 6.2(c). Considering that the particle image diameter is five pixels, in the case of 24x24 - 12x12 pixels the measurements refer to an ensemble while in the case of 12x12 - 6x6 pixels they are obtained nearly at the particle level. The analyses were conducted only for specific Δt, i.e., those that produced overly large displacements were avoided. For clarity, when plotted the selected displacement profiles are represented by coloured lines with squares.

At 24° the particle average displacement profiles used to define the interrogation areas are given in Figs. 6.5(a) for all Δt. The velocity profile shown in Figs. 6.5(b,d) matched well those of SIG and simulation. The profiles of granular temperature in Figs. 6.5(c,e) differ in magnitude for different patch sizes when compared to the same Δt. This can be expected since smaller patches increase the level of noise. Most importantly, at 24° the results show that the granular temperature above the base is always underestimated while it is well matched above $10d$ when the interrogation areas 24x24 - 12x12 pixels are used.

The selected particle displacement profile at 26° in Figs. 6.6(a) are comparable to those measured at 24°. The velocity is again well matched (Fig. 6.6(b,d)). In contrast with previous measurements at 24°, in Figs. 6.6(c,e) the granular temperature is now better matched below $10d$ for $\Delta t = 0.10$. However, when the sampling interval is decreased to $\Delta t = 0.05$ the profiles for the two sets of interrogation area disagree with the SIG and simulation reference profiles, even at the top of the flow.

At 28° the displacement profiles are shown in Figs. 6.7(a). Velocities profiles in Fig. 6.7(b,d) are well matched but, for patch sizes of 12x12 - 6x6 pixels, PIV becomes corrupted due to larger displacements at the top of the flow which did not allow a correct identification of the correlation peaks. A slight underestimation is displayed at the bottom of the flows when the set of interrogation areas 24x24 - 12x12 pixels is used. The granular temperature in Figs. 6.7(c,e) is quite clearly underestimated at the base for all Δt when 24x24 - 12x12 is used. For interrogation sizes of 12x12 - 6x6 the measurements are corrupted for $z > 10d$ and $\Delta t = 0.08$ while when $\Delta t = 0.04$ the peaks in the profiles indicate that the measurements are dominated by noise.

The overall PIV results shows a marked variability in the measurements. However, it is worth noting that, encouragingly, at least the overall magnitudes in granular temperature are captured by PIV (i.e. the differences between the flows at different angles of inclinations) although the profiles are less accurate than PTV. That is, for some applications it might be more important to assess the mean value than the full profile and PIV does have the advantage of potentially being more suited to polydisperse or non-spherical particles. A better agreement might be achieved by analysing additional sampling intervals and interrogation areas, however, it appears that there is a need to adjust these parameters for each specific event and for different part of the flows. In most cases, the disarrangement is clearly evident at the bottom of the flows where it seems that it is hard for PIV to correctly track agitated (i.e., with high granular temperature) systems. A possible cause may be connected to the synthetic image generation process. Particles crossing the middle cross-section of the simulations are more likely to randomly disappear near the bottom due to the bumpy base randomizing their flowing directions, i.e., particle images also randomly disappear causing loss of correlation. A solution may be to produce synthetic images with information obtained at the sidewalls where local ordering was observed (Fig. 5.13). However, here this was not done since the reference measurements obtained via coarse-graining are unreliable close to the lateral boundaries.

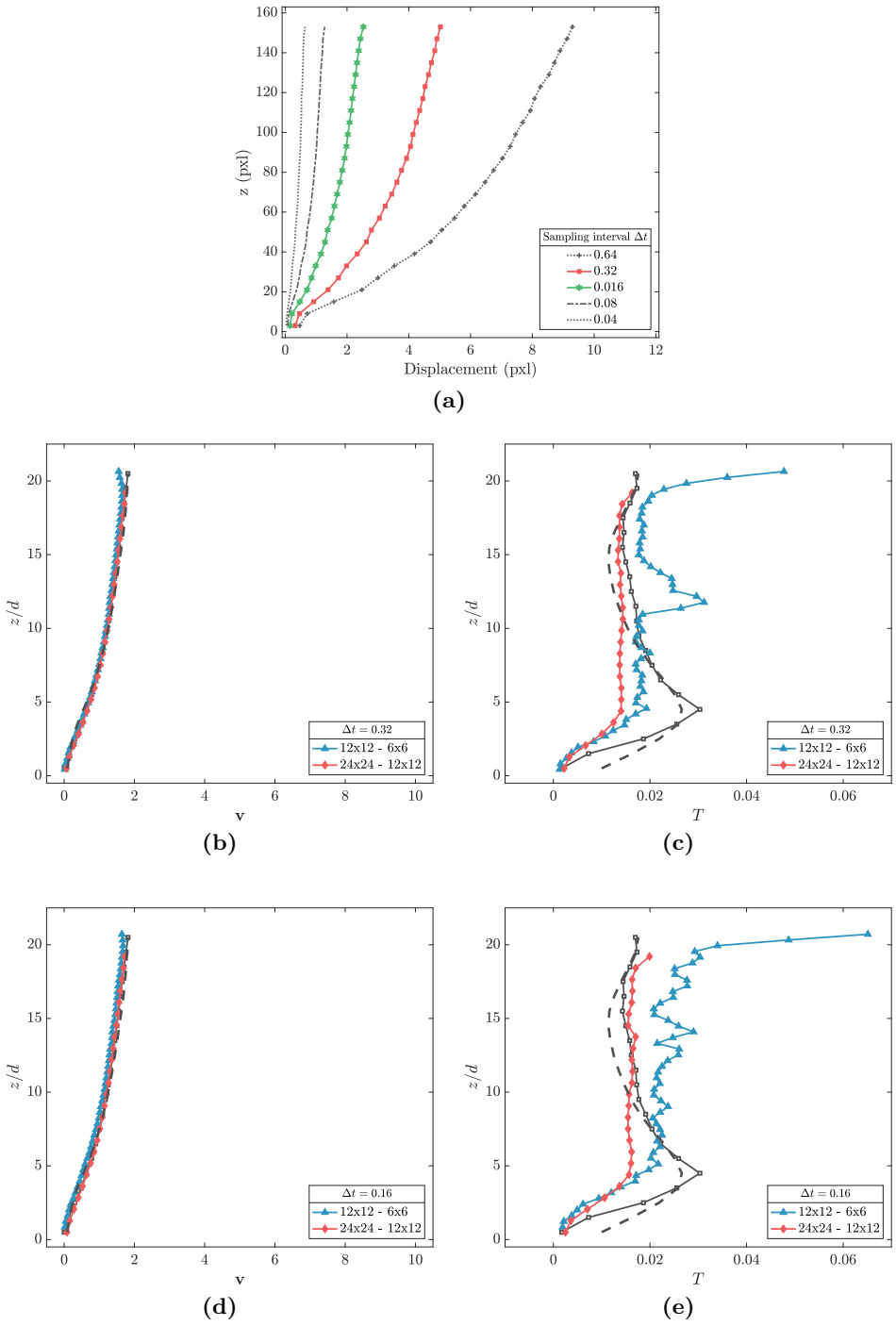

Figure 6.5: Velocity (**a**,**c**) and granular temperature (**b**,**d**) profiles calculated with PIV from synthetic images at an inclination of 24°, interrogation areas (for coarse and refined grid) of 24x24 - 12x12 and 12x12 - 6x6 and Δt as reported in Table 6.2. Selected SIG profiles (—⊟—) with the best match to the simulation measurements (▪ ▪ ▪).

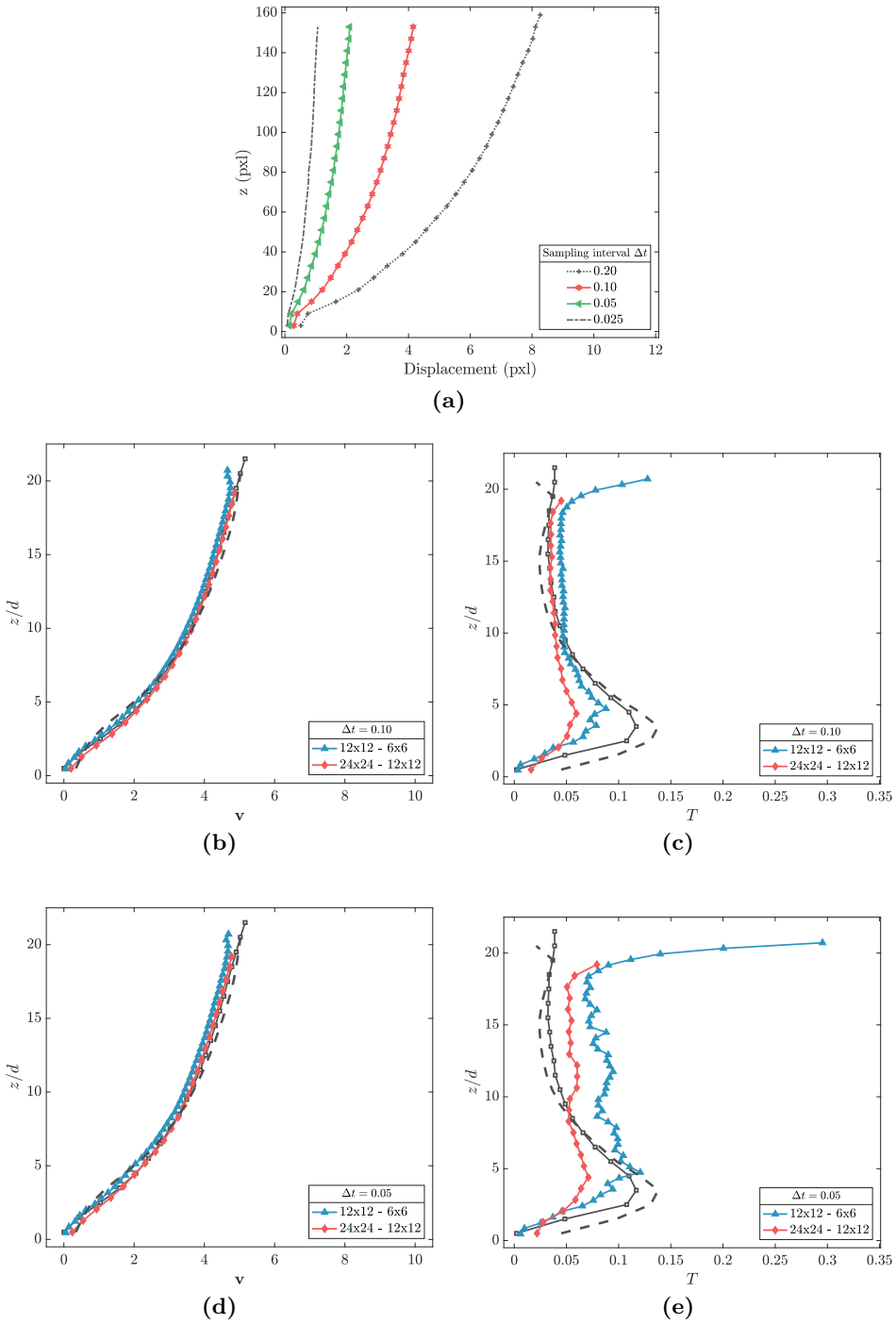

Figure 6.6: Velocity (**a**,**c**) and granular temperature (**b**,**d**) profiles calculated with PIV from synthetic images at an inclination of 26°, interrogation areas (for coarse and refined grid) of 24x24 - 12x12 and 12x12 - 6x6 and Δt as reported in Table 6.2. Selected SIG profiles (⊟) with the best match to the simulation measurements (▪ ▪ ▪).

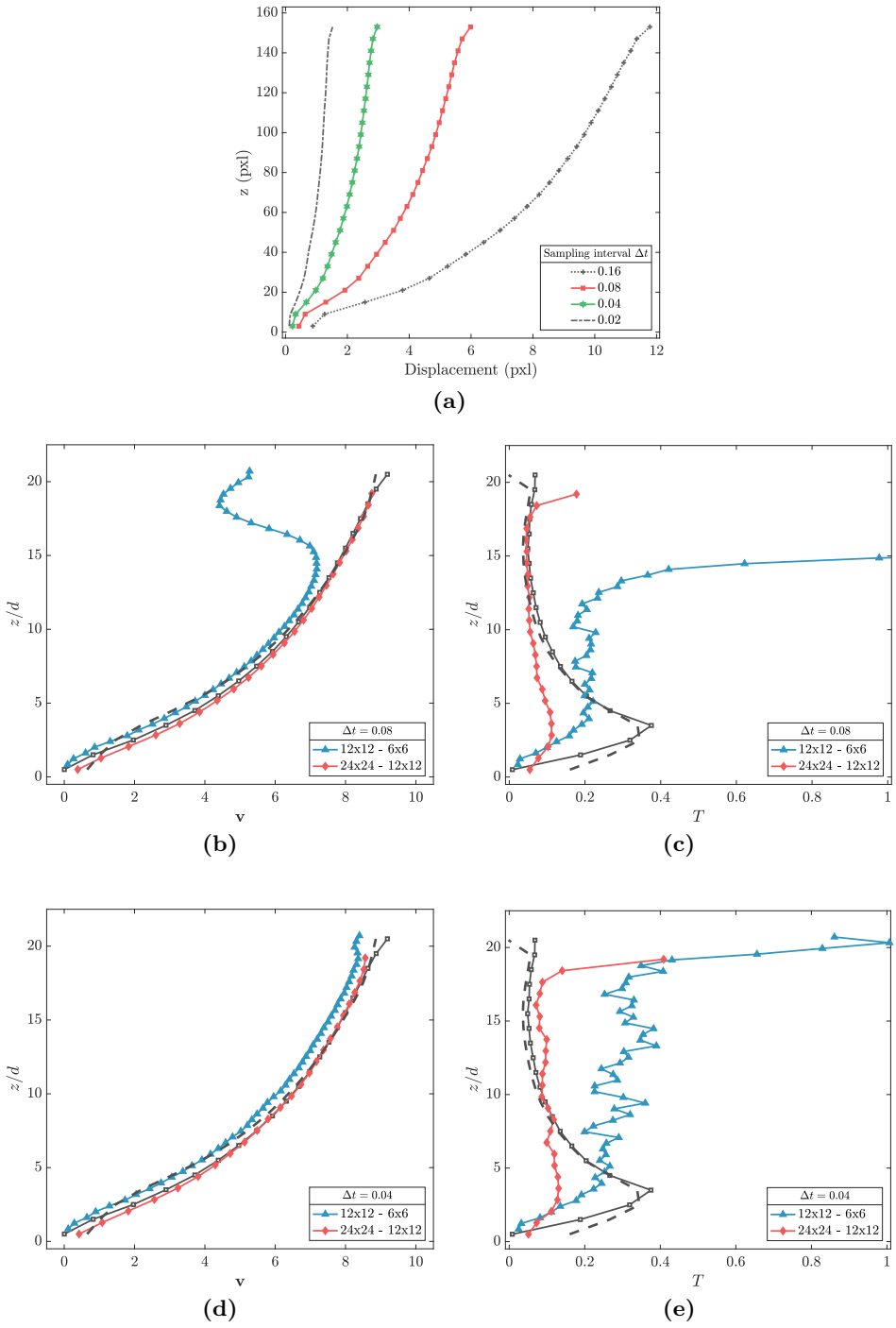

Figure 6.7: Velocity (**a**,**c**) and granular temperature (**b**,**d**) profiles calculated with PIV from synthetic images at an inclination of 28°, interrogation areas (for coarse and refined grid) of 24x24 - 12x12 and 12x12 - 6x6 and Δt as reported in Table 6.2. Selected SIG profiles (⊟) with the best match to the simulation measurements (▪ ▪ ▪).

6.6 Conclusion

A validation of PIV and PTV for the measurement of granular temperature was undertaken based on synthetic images created from numerical simulations. It was shown that PTV was a more reliable technique for the measurement of granular temperature, at least for the spherical particle flows investigated in this thesis, but this could only be achieved for certain sampling intervals where the values tend to collapse close to the numerical values. It was confirmed that very short sampling intervals (or high frame rate) generate measurements that are indeed dominated by noise. These observations reassured the validity of the experimental measurements presented in Sec. 4.5.4. Conversely, PIV results of granular temperature were highly variable and were not able to completely match the shape and magnitude of the numerical profiles.
Since both PTV and DEM refer to lagrangian reference systems, it might not be surprising that they are in better agreement than PIV. The corrections applied to remove the scale dependency from the measurements of coarse-graining (Sec. 5.3) made difficult a direct comparison between PIV and DEM results obtained with different coarse-graining widths. Further analysis could be performed by employing another method to extrapolate measurements from DEM (e.g. a slicing method [169]), however, since it was already implemented in the DEM software chosen for the simulations (Sec. 5.4), only coarse-graining was used. Ultimately, it appeared that, considering the same averaging scale length, coarse-graining and the binning method for PTV gave comparable results, thus reassuring the quality of the comparison between these two techniques.

7. Kinetic theory applied to dry granular flows over a bumpy base

7.1 Introduction

The predictions of extended kinetic theory (EKT), where the roles of surface friction and correlation in fluctuation velocities are taken into account are compared to the experimental results presented in Ch. 4 and the discrete element simulations of steady, fully-developed, inclined flows of identical spheres over bumpy bases presented in Ch. 5. The predictions of EKT in terms of dimensionless pressure are tested in Sec. 7.2.1 against the experimental results and in Sec 7.2.2 against numerical results for flows in the presence of sidewalls only. The same results hold also for flows in the absence of sidewalls, therefore they are reported in Appendix D. Then, the EKT described in Sec. 2.3.6 is directly applied and profiles of velocity, granular temperature and solid concentration obtained. These are compared in Sec 7.3.1 to the results of simulations performed in the absence of sidewalls and in Sec. 7.3.2 to those in the presence of sidewalls without rolling friction. Finally, in Sec. 7.3.3 a comparison with the experimental results is made. The disagreement of the theory when rolling resistance is introduced is also discussed.

7.2 Testing the prediction of extended kinetic theory

7.2.1 Experimental results

With experimental measurements of granular temperature and pressure obtained with PTV in Sec. 4.5.4 for the bead flows, it was possible to test the predictions of extended kinetic theory in terms of dimensionless pressure (Eq. 2.35) with results presented for all Δt in Fig. 4.14(b,d,f). The agreement is good, despite the effect induced by the sampling interval to the granular temperature profiles, at least up to $\nu \approx 0.55$. Unsurprisingly, this is the limit for correct measurement of solid concentration obtained with the 3D approach (Sec. 4.4.3). In fact, for $\nu > 0.55$ the theory overpredicts the measurements while, for $\nu < 0.55$, the collapse of the data suggests that the particle pressure scales

with the granular temperature giving support that kinetic theory may provide the correct framework to describe such bead flows. It should be noted that, while the use of different restitution coefficients e_n has little effect on the ratio $p/\rho_p T$ predicted by the theory, the value of particle friction μ affects its behaviour [18, 24]. Here, a value of $\mu \approx 0.45$ estimated from the tilt test for the ceramic beads was used.

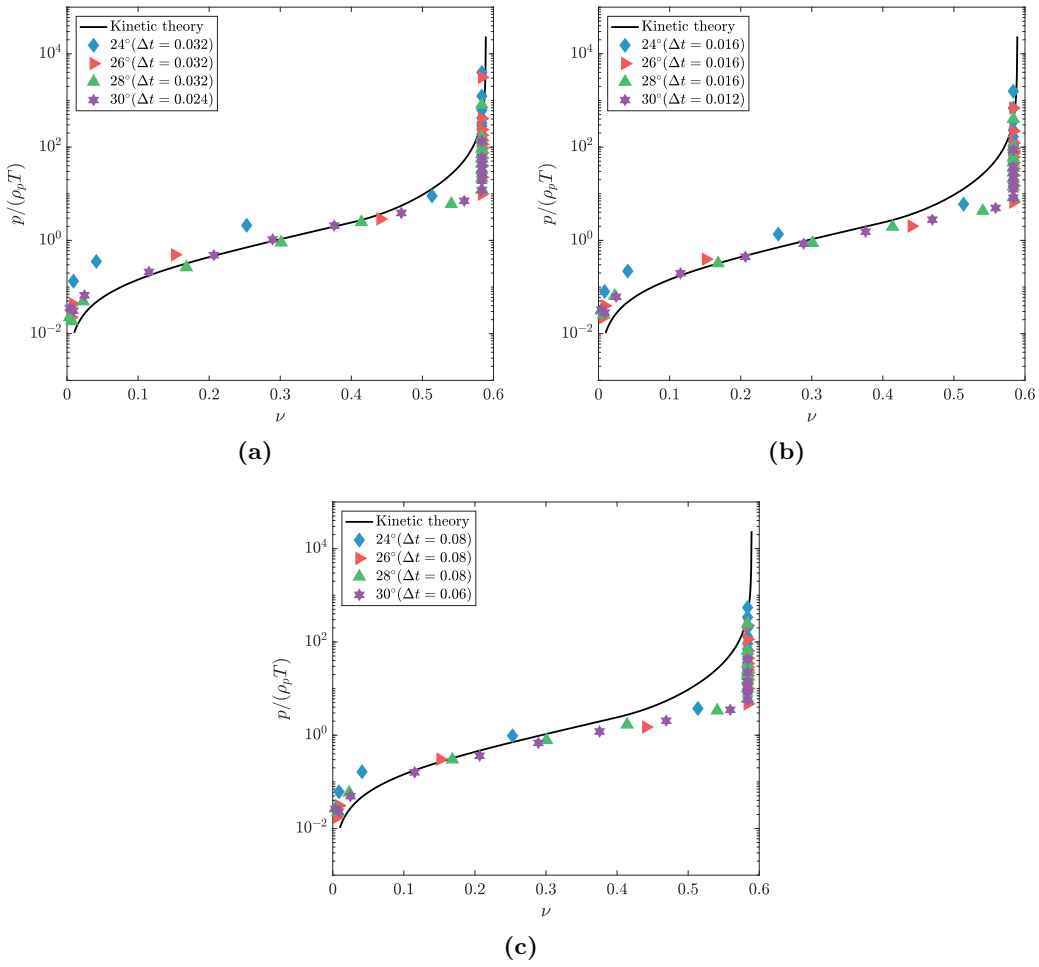

Figure 7.1: Comparison of ratio $p/\rho_p T$ from experiments of bead flows against kinetic theory equation of state (Eq. 2.35) for appropriate sampling interval Δt.

7.2.2 Numerical results

7.2.2.1 Simulations in the presence of sidewalls without rolling friction

Before testing the results of DEM obtained in Sec. 5.6 against the predictions of kinetic theory, it is useful to illustrate the results of coarse-graining when the smoothing lengths $w = 1d$ and $w = 0.1d$ are used. This is done by comparing the spanwise averaged profiles of granular temperature, pressure and solid concentration profiles. These are only given for $e = 0.5$ in Fig. 7.2 (similar results are obtained for other e) where lines indicate a length of $w = 1d$ and the dashed line with empty symbols a length of $w = 0.1d$. When Eq. 5.23 is used to eliminate the scale dependency from the granular temperature, the data for the same flow and slope angle collapse onto the same curve, i.e., the correction gives equivalent results. However, some discrepancy arises in the first layer above the base and at the free-surface since the smaller scale represents sub-particle measurements. The collapse of the data is similarly observed for the pressure profile but a clear divergence appears close to the rough base when $w = 0.1d$ is used. This is a direct consequence of using solid concentration ν in Eq. 5.24. In fact it is known [12, 173] that smoothing lengths smaller than the particle diameter display layering profiles, i.e., when particles close to the bottom boundary organize locally in layers.

To verify that the constitutive relations of kinetic theory are suitable to describe inclined granular flows, in Fig. 7.3 the dimensionless pressure $p/(\rho_p T)$ against the solid volume fraction measured in the DEM simulations is plotted with the theoretical predictions of kinetic theory in terms of dimensionless pressure (Eq. 2.35). The results given here are obtained using the DEM spanwise average measurements since the kinetic theory specifically derived for flows over a bumpy base used in this work (Sec. 2.3.6) predicts only a spanwise average behaviour of the flows.

If a smoothing length $w = 1d$ is employed in the coarse-graining procedure (Fig. 7.3(a,c,e)), and Eq. 5.22 is used to eliminate the scale dependency from both the pressure and the granular temperature, the numerical results are characterized by two branches for solid volume fractions less than approximately 0.5. The solid concentration ν is less than 0.5 in two layers, one layer close to the bumpy bottom and one close to the diffuse free-surface. In these layers, the divergence of the energy flux cannot be neglected in the energy balance and thus they are termed conductive layers [101]. The theoretical curve of kinetic theory predicts that the dimensionless pressure increases when the solid volume fraction increases. The lower branch of the numerical results (measurements obtained in the proximity of the diffuse top layer) follows the theory, at least qualitatively, while the upper branch (which comprises measurements in a region within three diameters of the bottom plane (empty symbols)) slightly decreases for increasing ν. For ν greater than 0.5 (the dense core region

of the inclined flow), the numerical measurements collapse onto the theoretical curve. This means that the the lack of agreement of the DEM with EKT shown in Fig. 7.3(a,c,e) has to do with the spatial variation of the velocity gradient.

If the smoothing length is reduced to $w = 0.1d$ (Fig. 7.3(b,d,f)), a scattering of the measurements around the theoretical curve due to layering is observed: solid volume fractions well beyond ν_c (as large as 0.8) are now possible. On the other hand, the measurements at the top of the flow, which belonged to the lower branch of Fig. 7.3(a,c,e), are now well fitted by Eq. 2.35. This indicates that there is a residual, but substantial, scale-dependency of the measurements on the smoothing length that cannot be simply corrected through Eq. 5.22. The measurements at the bottom of the flow still completely disagree with Eq. 2.35 (empty symbols in Fig. 7.3(b,d,f)). This might be due to the fact that the radial distribution function at contact g_0 in Eq. 2.35 only takes into account excluded volume and shielding in particle-particle interactions, while there are analogous mechanisms involved in particle-boundary interactions [180]. Defining a radial distribution function at contact in the proximity of solid boundaries is still an open question since g_0 is generally only well defined [37, 167] for a general element volume where the particles are sufficiently far from them. More details on what are the implications of using an incorrect g_0 near to such boundaries are given below in Section 7.3.1.

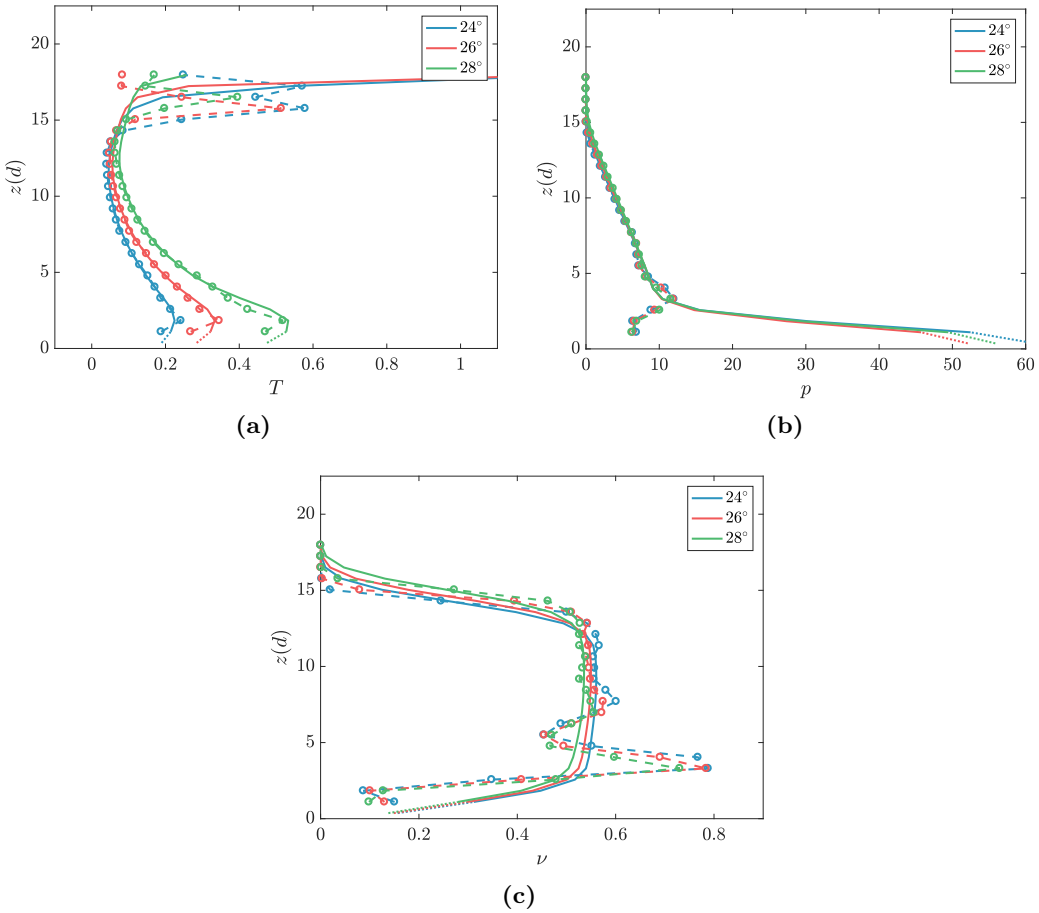

Figure 7.2: Granular temperature (**a**), pressure (**b**) and solid concentration (**c**) of the simulation in presence of sidewalls without rolling friction with $e = 0.5$. Solid lines represent measurements when coarse-graining $w = 1d$ whereas the dashed line with symbols represent measurements when $w = 0.1d$. In (**c**) the layering effect in the concentration profiles when $w = 0.1d$ is evident.

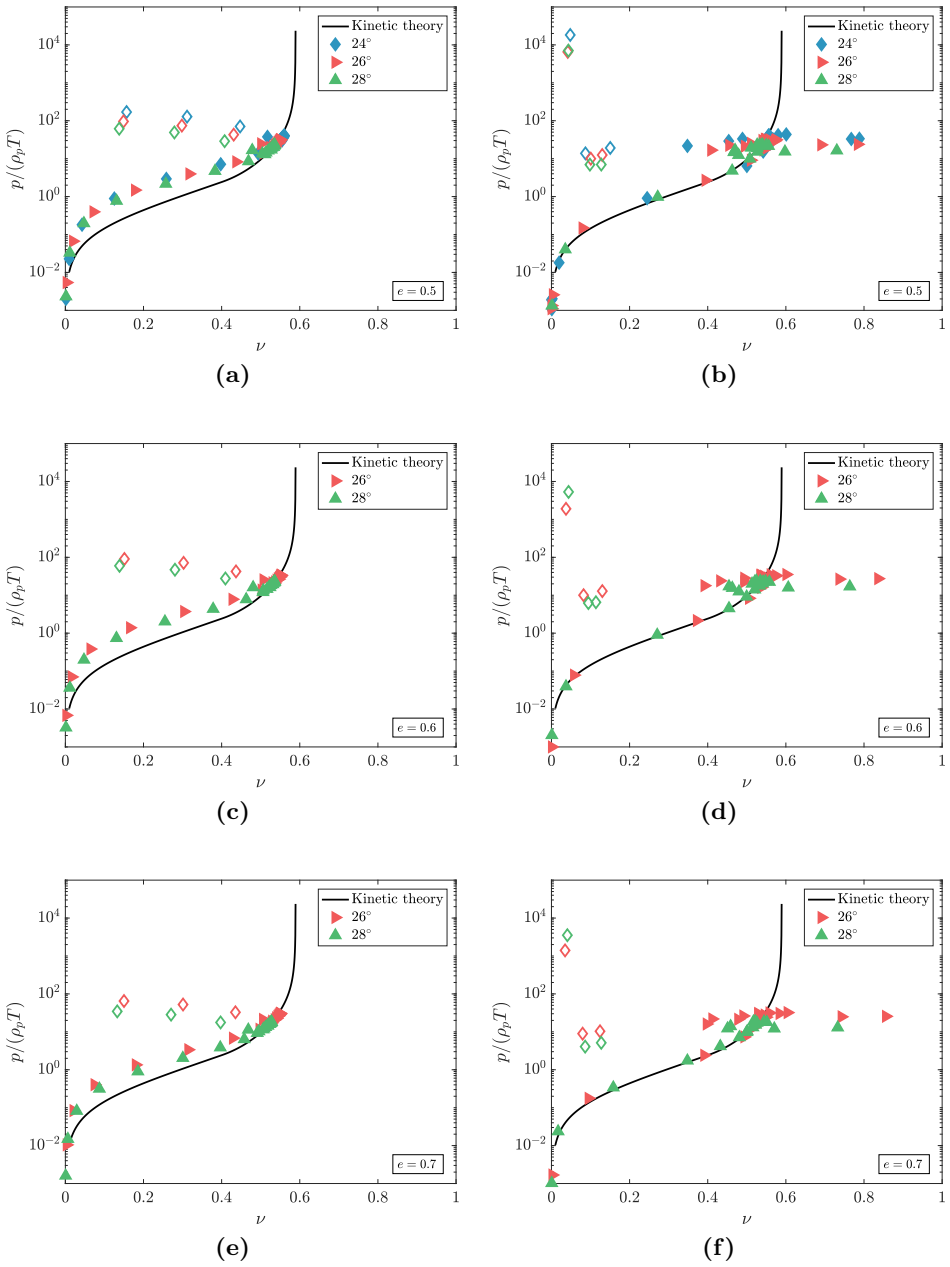

Figure 7.3: Dimensionless pressure $p/(\rho_p T)$ against the solid concentration measured in the DEM simulations without rolling friction with smoothing lengths of $w = 1$ (**a**,**c**,**e**) and $w = 0.1$ (**b**,**d**,**f**), respectively. Empty symbols indicate DEM results referring to a region within three particle diameters from the base. Theoretical predictions of kinetic theory (solid line) obtained from Eq. 2.35.

7.2.2.2 Simulations in the presence of sidewalls with rolling friction

In Sec. 5.7, the results of numerical simulation of granular flow down a inclined chute when rolling friction ($\mu_r = 0.2$) was introduced, were presented. When tested against the prediction of kinetic theory in terms of dimensionless pressure in Fig. 7.4, the results are similar to what was presented above (Sec. 7.2.2.1) and the same considerations in regard to the effect of different coarse-graining widths hold also in this case. For the flow at 30°, when the smoothing length is $w = 1d$, the numerical results fit the profile of EKT better than those at gentler inclinations which, conversely, plot above the theoretical curve. At 30° and with a smoothing length $w = 0.1d$, the dimensionless pressure is overestimated throughout by EKT when $\nu \lessapprox 0.5$, although no particular reasons for this were found.

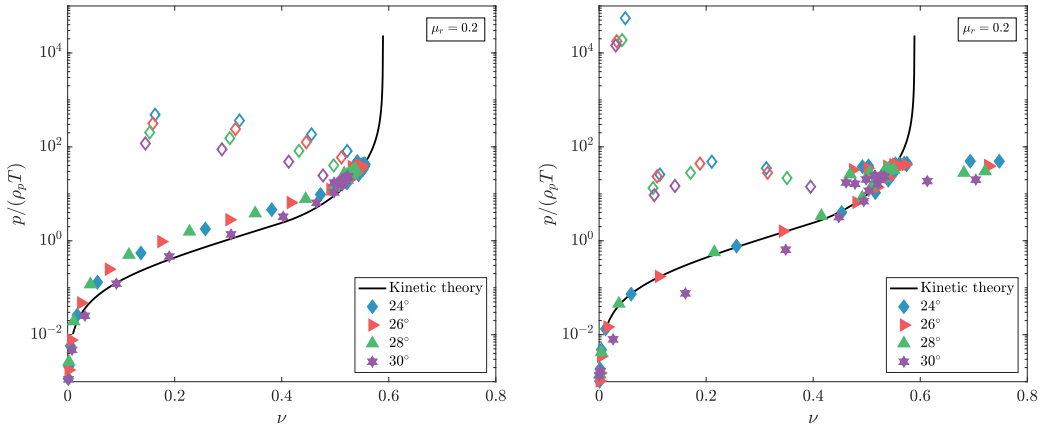

Figure 7.4: Dimensionless pressure $p/(\rho_p T)$ against solid concentration measured in DEM simulations with rolling friction and smoothing lengths of $w = 1$ (**a**) and $w = 0.1$ (**b**), respectively. Empty symbols indicate DEM results referring to a region within three particle diameters from the base. Theoretical predictions of kinetic theory (solid line) obtained from Eq. 2.35.

7.3 Extended kinetic theory (EKT) applied to inclined granular flows

The good agreement of the experimental and numerical results with the prediction of EKT in terms of dimensional pressure supports the fact that kinetic theory may be the correct framework to describe such flows. In what follows a width of $w = 1d$ is used to coarse-grain the profiles of velocity, granular temperature and solid volume fraction from DEM simulations. Considering the discussion in Sec. 7.2.2.1, in the granular temperature profiles, to further eliminate the scale-dependency in the upper part of the flows ($\nu \lessapprox 0.5$ in Fig. 7.3 and 7.4) a coarse-graining width $w = 0.1d$ can be used. Apart from a region near the flow free-surface, velocity and granular temperature profiles are qualitatively similar to those obtained with $w = 1d$, while the profiles of solid volume fraction are effected by layering effects as already discussed in Sec. 7.2.2.1. The results obtained with a width $w = 0.1d$ are presented in Appendix E.

7.3.1 EKT compared with DEM simulations in the absence of sidewalls

DEM simulations on inclined flows in the absence of lateral confinement (Sec. 5.5) were carried out using 3500 particles on a basal area of $l_x \times l_y = 200d^2$ (Sec. 5.4). The mass hold-up was calculated as $\mathcal{M} = 3500(\rho_p \pi d^3/6)/(200d^2) = 9.16\rho_p d$. Using the average distances between edges of adjacent glued particles at the bottom ($0.4d$) the bumpiness is $\xi = \arcsin[(d + l)/(2d)] \approx \pi/4$. The other parameters used to solve the full system of differential equations of EKT and its incompressible, algebraic approximation are listed in Table 7.1.

Table 7.1: Parameters used to solve the equations of EKT in absence of sidewalls. Subscript $(_n)$ indicate normal contact.

Parameter	Symbol	Scaling	Value
Normal restitution	e_n		0.5, 0.6, 0.7
Slope angle	θ		$24°, 26°, 28°$
Bumpiness	ξ		$\pi/4$
Hold-up	$\mathcal{M}$	$\rho_p d$	9.16
Shear rigidity concentration	ν_s		≈ 0.59
Particle-particle friction	μ		0.45

Figs. 7.5 and 7.6 show the comparisons between the results of the DEM simulations in the absence of sidewalls and the predictions of EKT, in terms of profiles of solid volume fraction, velocity and granular temperature.

For $e_n = 0.5$, the numerical solutions of EKT overestimate the velocities in the upper part of the flow, while the incompressible algebraic approximation underestimates them (Fig. 7.5(a)). The numerical solution of EKT can also reproduce the greater than linear increase of the granular temperature in those two dilute regions when approaching the diffuse (ballistic) layer and the bumpy bottom (Fig. 7.5(b)); while the incompressible, algebraic approximation simply predicts a linear decrease of T with z (Eq. 2.62). In Fig. 7.6(a) the numerical solution of the full system of differential equations of EKT satisfactorily reproduces the characteristic regions observed in DEM simulations and schematically represented in Fig. 2.11, unlike, evidently, its incompressible, algebraic approximation.

Similar considerations apply also to the case $e_n = 0.6$ (Figs. 7.5(c,d) and 7.6(b)) and $e_n = 0.7$ (Figs. 7.5(e,f) and 7.6(c)) but with a crucial difference: in these cases, numerical solutions of the full system of differential equations of EKT of Sec. 2.3.6.1 are possible only up to angles of inclination slightly above 24° and 26°. In other words, steady, fully-developed flows cannot be sustained at larger angles, and the theory predicts that the flow would continue to accelerate along the plane. The fact that the incompressible, algebraic approximation does not present the same limitation indicates the crucial role of the boundaries in controlling the maximum angle for which steady, fully-developed flows are possible.

The maximum angle of inclination that allows steady, fully-developed flows is underestimated in the EKT. It is possible that this is due to the underestimation of dissipation at the bumpy bottom, as imposed by the boundary conditions of Richman [138]. To verify this, the measured values of $u = 2.26(gd)^{1/2}$ and $Q = -0.13\rho_p(gd)^{3/2}$ at $z = 1.5d$ in the DEM simulation with $e_n = 0.7$ and $\theta = 26°$ were directly employed as boundary conditions for solving the corresponding differential integration problem of EKT. Fig. 7.7 shows that the modification of the boundary conditions at the bottom is indeed sufficient to obtain a solution for $\theta = 26°$, previously forbidden (for $e_n = 0.6$ and $\theta = 28°$ the same result was found). However, the negative value of the fluctuation energy flux, which indicates the dissipative nature of the bumpy bed in the DEM simulation, induces an increase of the solid volume fraction near the bottom, in contrast to the DEM results (Fig. 7.7(c)). Increasing the energy dissipation at the bottom will cause a further increase of the solid volume fraction there, that eventually will approach the singular value ν_c and prevent a numerical solution to the differential equations from being obtained. For this reason, even if the boundary conditions are taken from the DEM simulations, steady and fully-developed solutions to the flow for θ larger than 26° are not possible. As discussed in Sec. 5.6, this may relate to issues with the radial distribution function at contact near the bottom. It is likely that modifying g_0 to take into account the influence of the boundary would allow EKT to predict a decrease of the solid volume fraction when approaching the

dissipative bottom, as in the DEM simulations.
Comparing the results between the numerical solutions of EKT and its incompressible algebraic approximation (Fig. 7.5), it is clear that a correct definition of the energy flux at the bottom boundary is crucial to identify the correct dynamics involved in granular flows over bumpy bases. Using the algebraic approximation, the granular temperature is underestimated and a reduced basal slip velocity is obtained. While improvement in the solution for the slip velocity (Eq. 2.53) has already been proposed [25], the development of a correct solution for the energy flux (Eq. 2.54) strongly depends on the assumption afforded in the formulation of kinetic theories, e.g. that, in equilibrium systems (i.e, no velocity and temperature gradients, and no energy dissipation [35]), the velocity distribution function resembles a Maxwellian distribution. However, this is not always true since rapid granular flows are often in non-equilibrium states [64], i.e subject to constant driving forces, and the velocity distribution may be far from Maxwellian. Although accounting for the correct definition of the velocity distribution function may further increase the complexity of EKT, this may be required to improve the prediction of this theory.

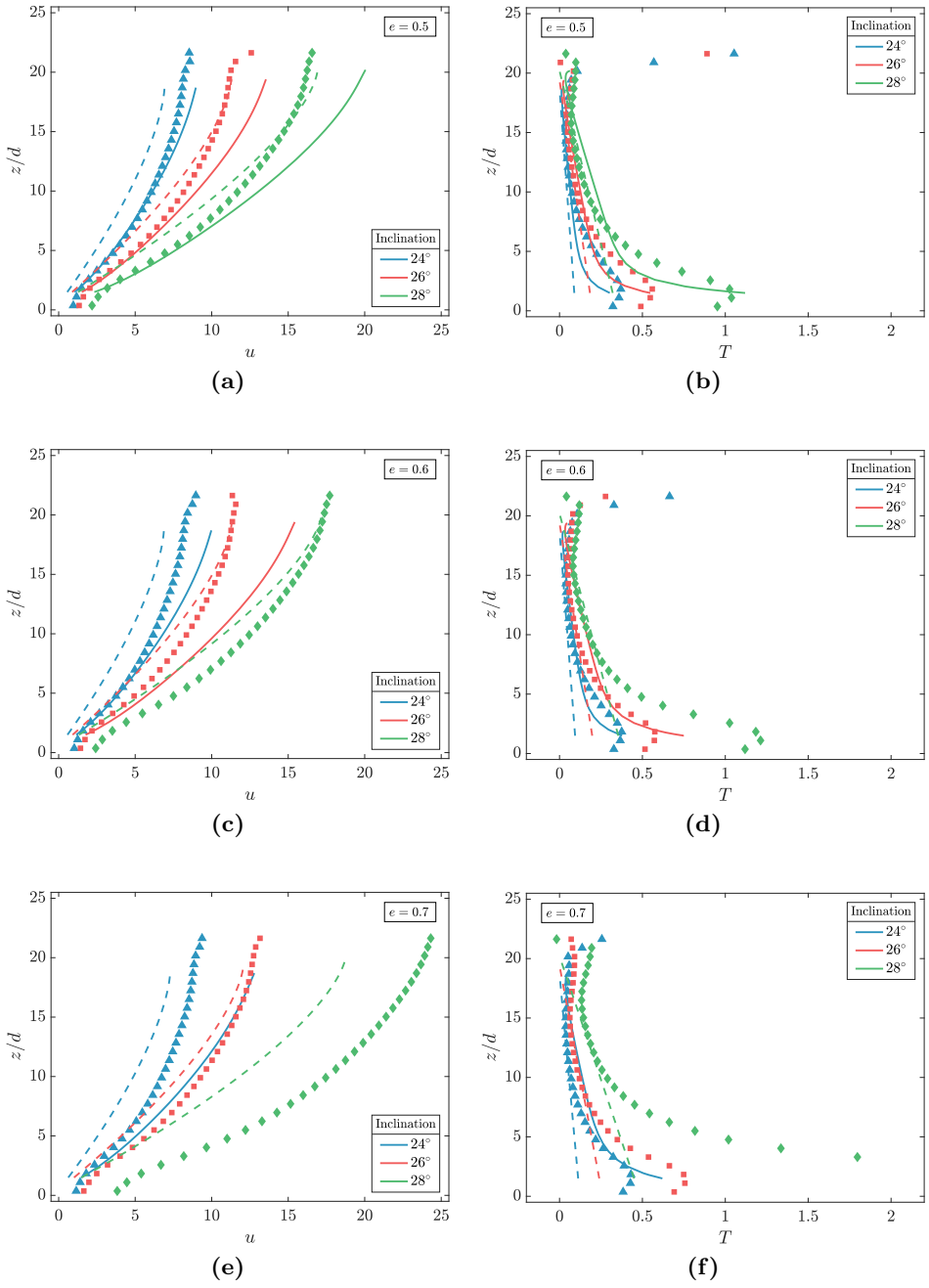

Figure 7.5: Numerical (symbols) profiles of (**a**,**c**,**e**) dimensionless particle velocity and (**b**,**d**,**f**) dimensionless granular temperature obtained from DEM simulations of inclined flows in the absence of sidewalls for different value of e, $\mu = 0.45$ and $\theta = 24°$ (triangles), $\theta = 26°$ (squares) and $\theta = 28°$ (diamonds). Coarse-graining width $w = 1$. Solid and dashed lines represent the results of the numerical integration of the full system of differential equations of EKT and its incompressible, algebraic approximation (Eq. 2.62), respectively.

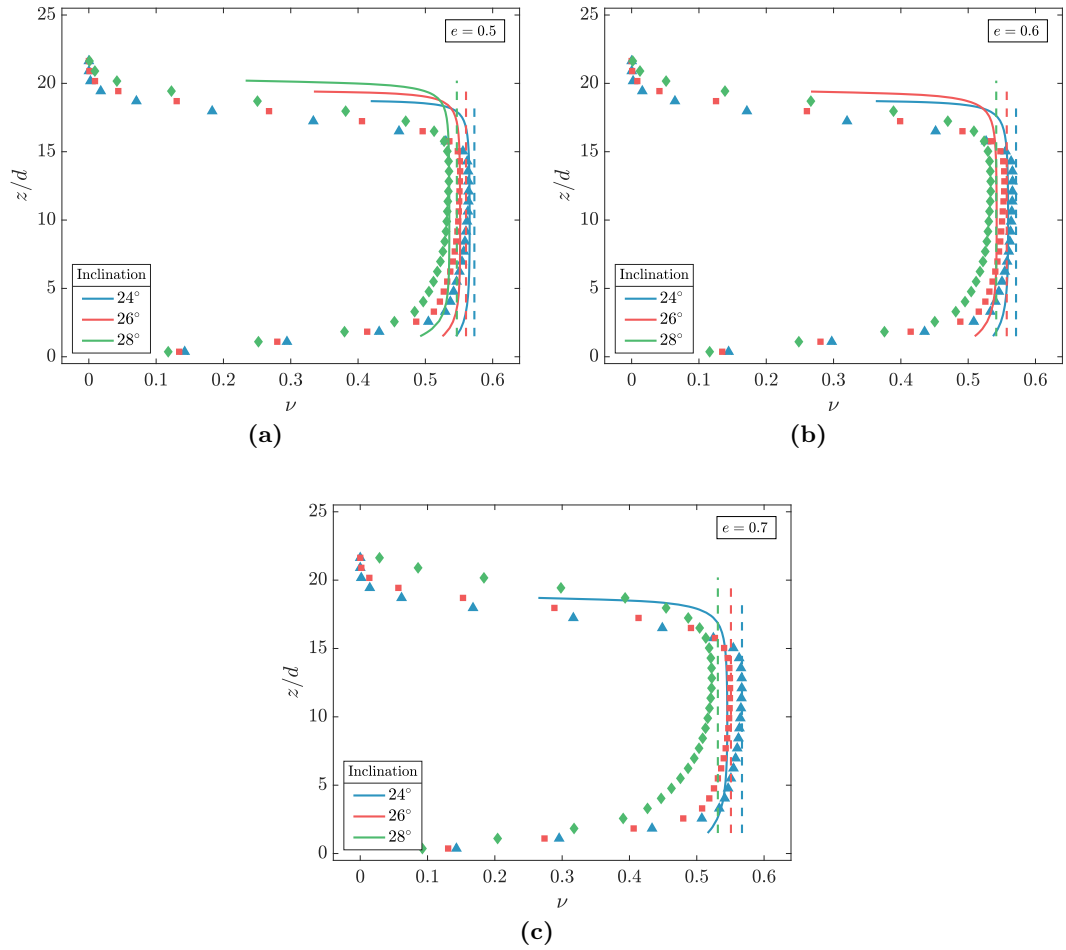

Figure 7.6: Numerical (symbols) profiles of (**a**,**b**,**c**) solid concentration obtained from DEM simulations of inclined flows in the absence of sidewalls for different value of e, $\mu = 0.45$ and $\theta = 24°$ (triangles), $\theta = 26°$ (squares) and $\theta = 28°$ (diamonds). Coarse-graining width $w = 1$. Solid and dashed lines represent the results of the numerical integration of the full system of differential equations of EKT and its incompressible, algebraic approximation (Eq. 2.62), respectively.

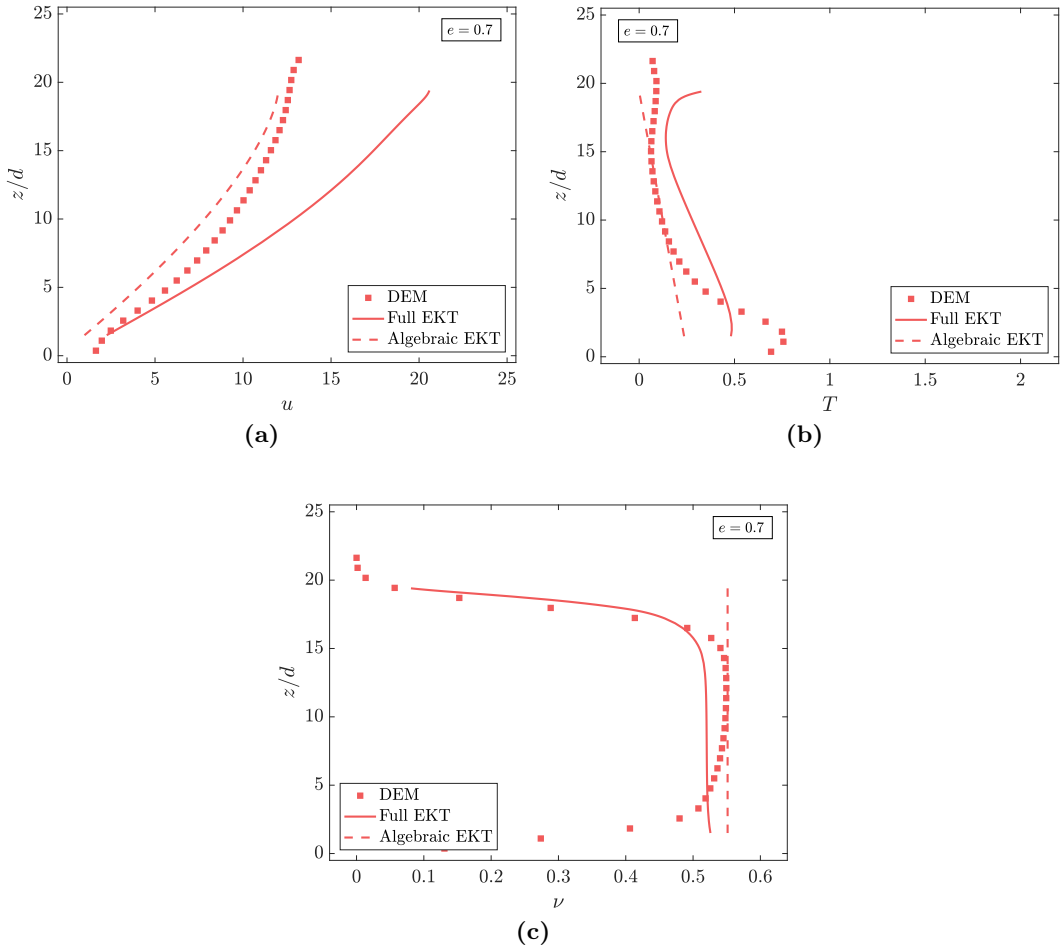

Figure 7.7: Numerical (symbols) profiles of (**a**) dimensionless particle velocity (**b**) dimensionless granular temperature and (**c**) solid concentration obtained from the DEM simulation of an inclined flow in the absence of sidewalls when $e_n = 0.7$, $\mu = 0.45$ and $\theta = 26°$. Coarse-graining width $w = 1$. The solid lines represent the results of the numerical integration of the full system of differential equations of EKT when the boundary conditions at the bottom are those measured in the DEM simulation. The dashed lines are the results of the incompressible, algebraic approximation of EKT (Eq. 2.62).

7.3.2 EKT compared with DEM simulations in the presence of sidewalls without rolling friction

DEM simulations were also performed on inclined flows in the presence of flat, frictional sidewalls (Sec. 5.6) using 27500 particles on a basal area of $1980d^2$, so that the mass hold-up was $\mathcal{M} = 7.27\rho_p d$. The other parameters used to solve the full system of differential equations of EKT and its incompressible, algebraic approximation are listed in Table 7.2. The sliding friction coefficient of particles in contact with the sidewalls was set equal to 0.35 (Table 5.2).

Table 7.2: Parameters used to solve the equations of EKT in presence of sidewalls. Subscript $(_n)$ indicate normal contact. For friction μ, subscripts $(_p)$ and $(_w)$ indicate particle and wall, respectively.

Parameter	Symbol	Value
Normal restitution	e_n	0.5,0.6,0.7
Slope angle	θ	$24°, 26°, 28°$
Bumpiness	ξ	$\pi/4$
Wall distance	W	66
Hold-up	$\mathcal{M}$	7.27
Shear rigidity concentration	ν_s	≈ 0.59
Particle-particle friction	μ_p	0.45
Effective wall friction	μ_w	0.15

From the ratio of shear stress (Eq. 2.61) to pressure (Eq. 2.60), it can be obtained:

$$\frac{s}{p} = \tan\theta - \frac{\mu_w}{l_y}(h - z), \tag{7.1}$$

i.e., the stress ratio linearly decreases when moving from the free surface to the bottom of the flow. This approximate relation explains why frictional sidewalls allow for steady and fully-developed flows over erodible beds at angles of inclination that are much larger than the angle of repose of the granular material [159]. Eq. 7.1 has been widely used in analytically solving for laterally confined surface flows [20, 85, 86, 93]. The advantage is that one can transform two-dimensional into one-dimensional flows by simply taking into account the average resistance of the sidewalls. It is not clear whether Eq. (7.1) is able to accurately represent the distribution of mean stress ratio along the flow. However, to

verify this, the spanwise averaged profiles of stress ratio for the three angles of inclination were plotted, shown in Fig. 7.8. In the core region of the flows, where the solid volume fraction (Fig. 7.10) is approximately constant (the assumption behind Eq. (7.1)), the stress ratio is indeed linearly distributed, with a slope which is independent of both θ and e_n. In addition, by fitting the results of the numerical simulations, a value of $\mu_w = 0.15$ is obtained: the effective wall friction coefficient is much less than the actual value of the sliding friction for the particle-flat wall interaction, $\mu_w = 0.35$. This might relate to the fact that only some of the contacts at the wall are actually sliding while others are rolling or bouncing, thus decreasing μ_w. The value $\mu_w = 0.15$ is then used in both the full system of differential equations of EKT and its incompressible, algebraic approximation (Eq. 2.62) and the results are shown in Figs. 7.9 and 7.10.

Figs. 7.9 and 7.10 demonstrate that the quantitative agreement between EKT and the DEM results for $e_n = 0.5$ is improved when flat, frictional sidewalls are present. Solutions of EKT for $e_n = 0.6$ and $\theta = 28°$ and $e_n = 0.7$ and $\theta = 26°$ were found, however, as in the case without sidewalls, the maximum angle of inclination for having steady and fully-developed flows is still underestimated for the other values of the coefficient of normal restitution due to the incorrect radial distribution function at contact near the bumpy base.

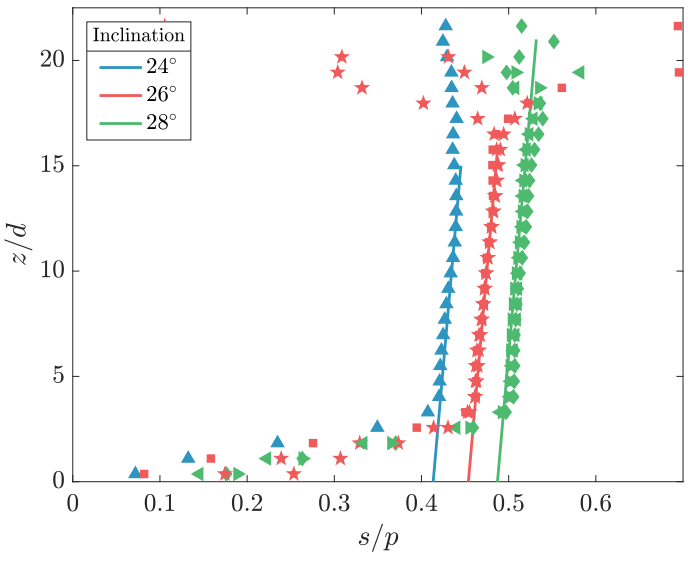

(a)

Figure 7.8: Spanwise averaged profiles of stress ratio (symbols) along the flow obtained from DEM simulations of inclined flows in the presence of sidewalls for different coefficients of restitution studied (0.5,0.6,0.7) with $\mu = 0.45$ and $\theta = 24°$ (triangles), $\theta = 26°$ (squares) and $\theta = 28°$ (diamonds). Solid lines represent Eq. 7.1.

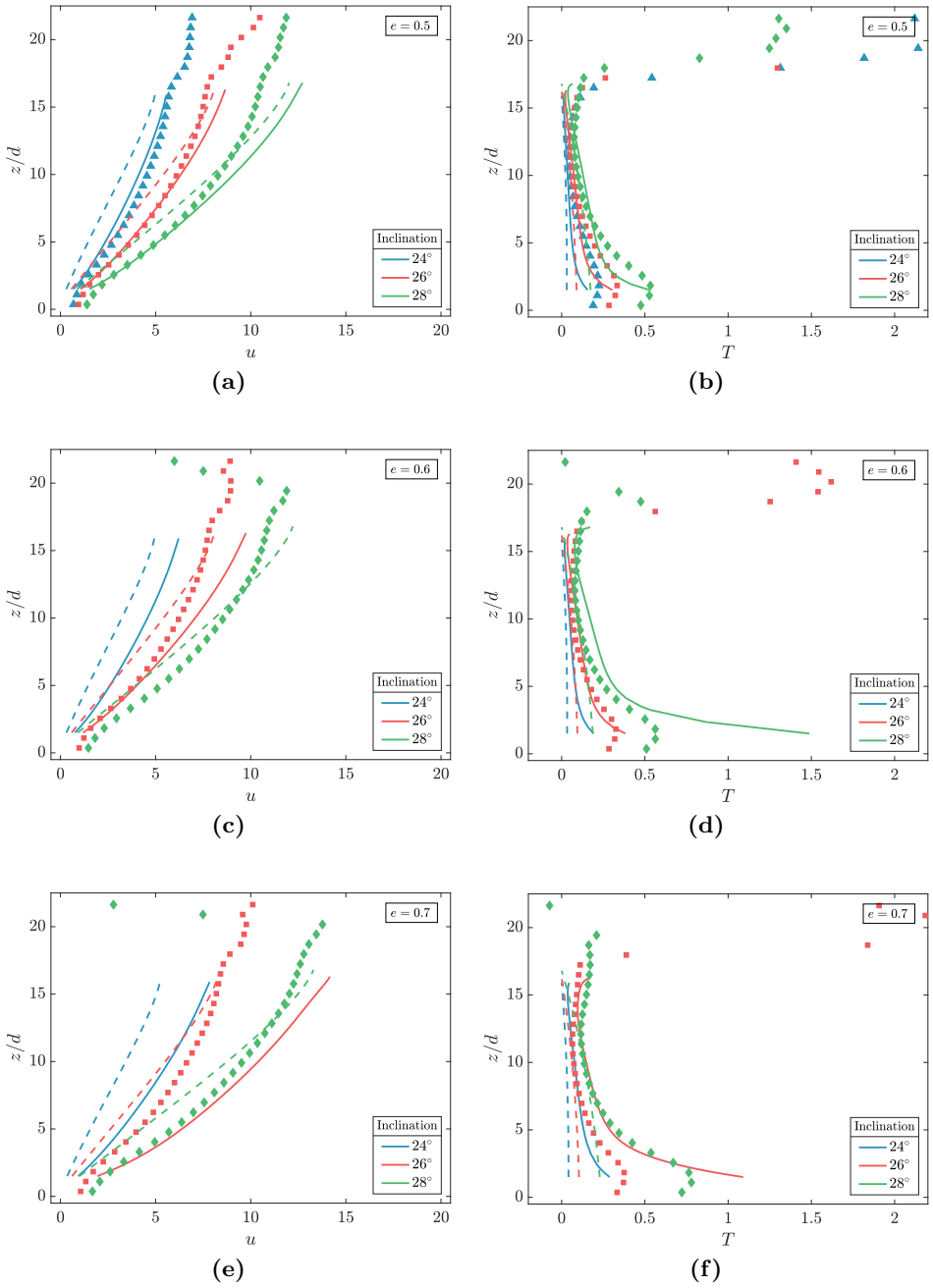

Figure 7.9: Numerical (symbols) profiles of (**a**,**c**,**e**) dimensionless particle velocity and (**b**,**d**,**f**) dimensionless granular temperature obtained from DEM simulations of inclined flows in the presence of sidewalls for different value of e, $\mu = 0.45$ and $\theta = 24°$ (triangles), $\theta = 26°$ (squares) and $\theta = 28°$ (diamonds). Coarse-graining width $w = 1$. Solid and dashed lines represent the results of the numerical integration of the full system of differential equations of EKT and its incompressible, algebraic approximation (Eq. 2.62), respectively.

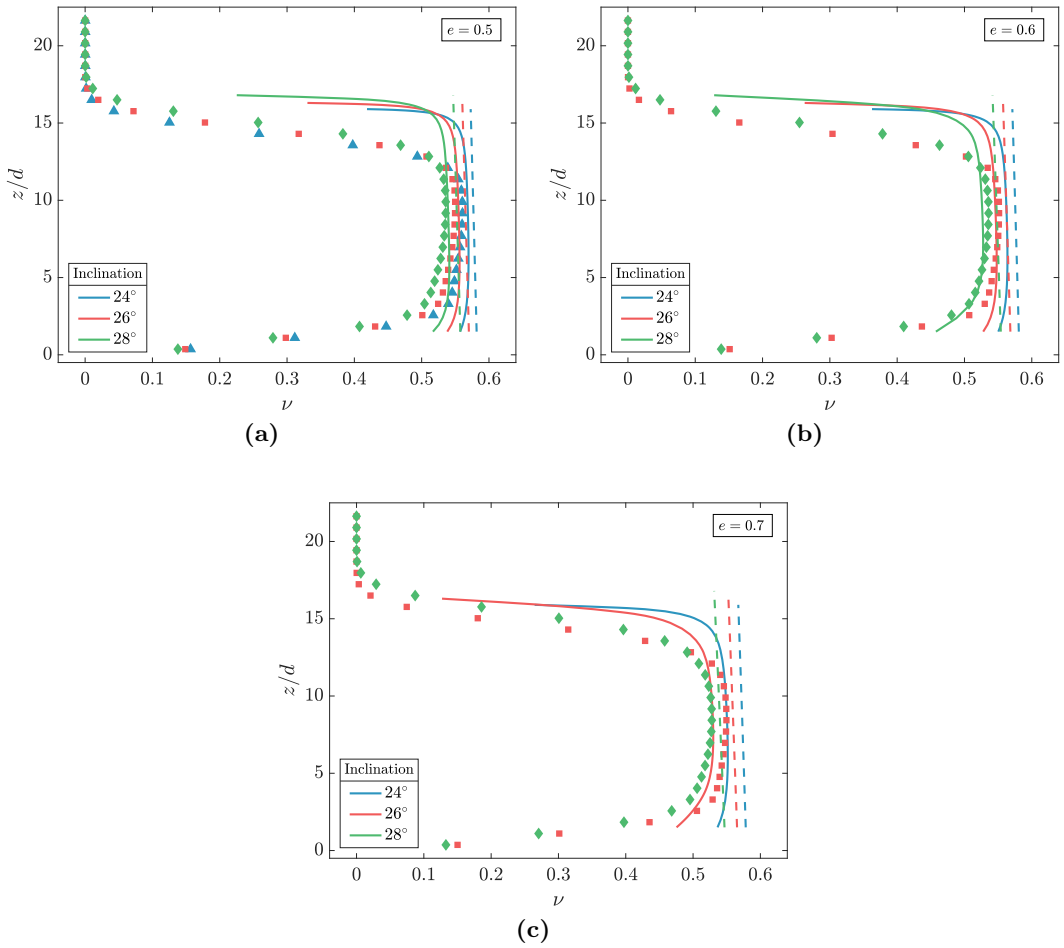

Figure 7.10: Numerical (symbols) profiles of (**a**,**b**,**c**) solid concentration obtained from DEM simulations of inclined flows in the presence of sidewalls for different value of e, $\mu = 0.45$ and $\theta = 24°$ (triangles), $\theta = 26°$ (squares) and $\theta = 28°$ (diamonds). Coarse-graining width $w = 1$. Solid and dashed lines represent the results of the numerical integration of the full system of differential equations of EKT and its incompressible, algebraic approximation (Eq. 2.62), respectively.

7.3.3 EKT compared with experiments and the influence of rolling resistance

Numerical simulation provides a useful tool to qualitatively reproduce the dynamics of granular flows down inclines. However, they should also be able to represent quantitatively, simple real situations such as the flows performed experimentally in this thesis. As discussed in Sec. 5.6, to match the experimental results, rolling resistance was introduced in the simulations based on the experimental velocity profiles and shape properties of the particles. In the previous section (Sec. 7.3) it has been also shown that good agreement between results of DEM simulations and the predictions of extended kinetic theory were obtained as long as the additional rolling resistance was not introduced in the simulations. Conversely, when rolling resistance is used, kinetic theory fails to predict the flow behaviour as it is shown below in terms of velocity profiles.

With additional modification of kinetic theory it should be possible to obtain good agreement also with the experiments. If the lack of agreement is caused by the shape anisotropicity of the particles, modelling additional energy dissipation induced by particle shape (causing rolling resistance) may be possible by modifying the coefficient of effective restitution, as has been done for the sliding friction (Sec. 2.3.4.10).

A modification of the effective restitution coefficient in EKT should allow, in principle, to take account of some rolling resistance and reduce the flow velocity. While a rigorous implementation of this in EKT goes beyond the purpose of this thesis, a first verification of this hypothesis was made by manually varying the effective coefficient of restitution.

With the full system of differential equations, solutions are not possible for steep slope angles and values of $e > 0.7$. Conversely, the algebraic approximation is computationally easier to handle and allows a variety of solutions for all values of e and within a wider range of slope angles where steady flows are possible. Using this approach and assuming that in Table 7.2 $\xi, W, \mathcal{M}, \nu_s, \mu_p$ and μ_w are constant, several iterations of the algebraic approximation were computed with all possible matches of $0 < e < 0.9$ and $0 < \epsilon < 0.7$ (Eq. 2.41), where $\epsilon = 0.7$ is the maximum value found before the measurements are considerably overpredicted. The results of these iterations are given in Fig. 7.11 for an inclination of $\theta = 26°$ (the result holds for all other inclinations) in terms of their mean velocity (solid line) and standard deviation (dashed lines), i.e. the range of velocities that was obtained by modifying these two parameters alone. It can be seen that the velocity is always overpredicted compared to the experiments (symbols) for all combinations of the two modified parameters.

The approach trialled did not produce the expected reduction of velocity. Ultimately, further research needs to be done to obtain agreement with the experiments. A possible solution can be to derive a simple model based on experiments or simulation data with

rolling friction as it has been previously done for the sliding friction by Chialvo and Sundaresan [43] and thus allow a better agreement with the experiments once this new model is introduced.

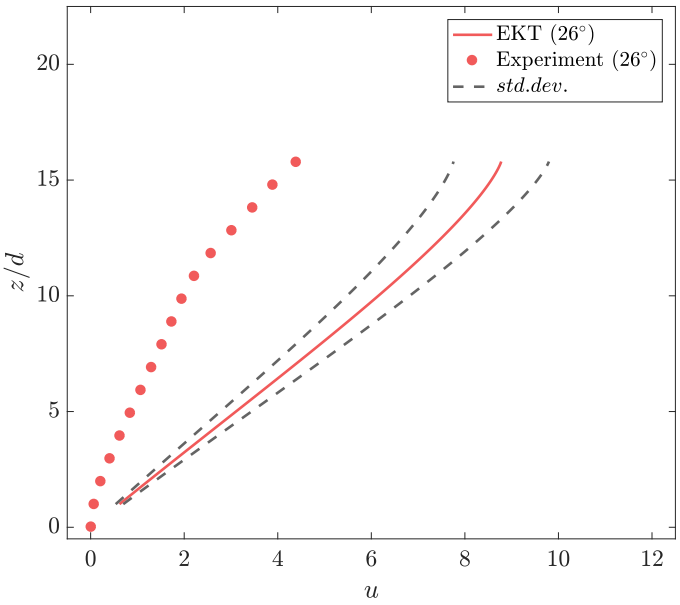

(a)

Figure 7.11: Dimensionless particle velocity profile of EKT incompressible, algebraic approximation (Eq. 2.62) with different values of normal restitution coefficient $0 < e < 0.9$, effective restitution coefficient $0 < \epsilon < 0.7$ and $\mu = 0.45$ of an inclined flow in the presence of sidewalls at $\theta = 26°$.

7.4 Conclusion

The predictions of extended kinetic theory (EKT) in terms of dimensionless granular pressure were found to be in good agreement with the experiment, although only within the solid concentrations that could be reliably measured. It was concluded that kinetic theory may provide the correct framework to describe such experimental bead flows.
The results of numerical simulation were also tested against the prediction of EKT. At the free-surface and in the core region, a good agreement with the predictions was found when different coarse-graining smoothing widths were used, while within a region up to approximately $3d$ above the bumpy base the data competently disagreed with kinetic theory. It was pointed out that the cause may be related to the radial distribution function which is as yet not known in the proximity of solid boundaries, so that further research needs to be done to address this aspect.
When extended kinetic theory was directly applied and compared to the numerical results for flows in the absence of sidewalls, it was shown that the constitutive relation for the pressure of EKT must be modified in the proximity of the boundary, because of the influence of excluded volume and shielding associated with collisions of particles with the boundary itself. It was also noted that currently available boundary conditions for flows over bumpy planes in kinetic theory underestimate the energy dissipation. These two observations explain the lack of agreement of EKT with the simulations, in terms of the maximum angles of inclination for which steady, fully-developed flows are possible. That is, for some high angles of inclination, EKT does not have solutions, while steady flows are predicted in DEM. However, whenever a solution to the system of differential equations of EKT does exist, the predicted distributions of velocity, solid volume fraction and granular temperature satisfactorily match the numerical measurements. The incompressible, algebraic approximation of EKT, which ignores the conduction of energy in the energy balance, admits solutions for a wider range of angles of inclination, as in the simulations, but fails to reproduce the quantitative and qualitative behaviour of solid volume fraction and granular temperature in the two conductive layers at the top and bottom of the flow.
When frictional sidewalls were added to the domain, it has been shown that the spanwise ratio of shear stress to pressure is linearly distributed in the dense core region of the flow, confirming that the sidewalls exert, on average, a Coulomb-like resistance to the flow with an effective friction coefficient which is less than half the actual particle-wall friction.
Extended kinetic theory was also tested against the experimental results in terms of velocity profile. The disagreement was quite evident and even changing the normal and effective coefficient of restitutions over a wide range of possible combinations did not result in major improvements. This highlights the fact that EKT finds good agreement with numerical simulation but there is the need to overcome the disagreement with the

results of more fundamental and simple experimental granular flows before applying EKT to more complex situations such as debris flows.

8. Experimental investigation of saturated granular flows

8.1 Introduction

In this chapter, a series of flume experiments designed to study the internal behaviour of monodisperse and polydisperse concentrated granular-fluid flows is examined. A non-intrusive technique called Planer Laser Induced Fluorescence (PLIF) originally developed for use in physical model debris flow testing by Sanvitale [142], Sanvitale and Bowman [144] is used to investigate saturated granular flows in small scale experiments.
The apparatus and materials used are presented first in Sec. 8.2. Then the PLIF technique used to visualize the flows is described in Sec. 8.3. Modifications to the original flume design used by Sanvitale [142], Sanvitale and Bowman [144] were made in terms of flow release, basal roughness, light source and laser optics. The new laser system installed to improve the quality of internal images and to provide more flexibility during test preparation is described in Sec 8.4. The test procedure and data processing of the flows investigated are given in Secs. 8.5 and 8.6, respectively.
Monodisperse flows made of spherical particles are studied first in Sec. 8.7.1. Spherical shaped particles were used for the following reasons: to compare the results with the work done with spherical particles in dry systems; to enable PTV to be assessed; to enable solid concentration to be measured using the method previously developed in Sec 4.4.3. Similarly to what was done for flows under dry conditions (Sec. 4.5.2), once the flow properties are extracted from the flows via PTV, a comparison with the predictions of extended kinetic theory in terms of dimensionless pressure is made.
Finally, different particle size distributions comprised of polydisperse spherical particles only or a combination of angular and spherical particles are investigated in Sec. 8.7.2. With the intention of not reducing overmuch the complexity involved and to closely match the properties of real debris flows, spherical shaped particles were used to assist with later data processing and analysis. Internal velocities of the flows and their depositional spreads are examined and compared.

8.2 Apparatus and materials

The flume used in this study is similar to that used by Sanvitale and Bowman [144]. A description of the apparatus along with the modifications required for this work is given here. The apparatus is a sloping rectangular 150 mm wide and 2000 mm long channel that can tilt from horizontal up to 45° (Fig. 8.1). For this specific work the flume was firmly bolted to the surrounding frame for security. Specific locations for rigid supports were selected at 10°, 15°, 20°, and 25°, respectively. The original design had an aluminium hopper with a curved chute that guided the flow from the mouth of the hopper to the top of the slope (Fig. 8.2(a)). This was used for a first series of tests and subsequently modified by removing the aluminium hopper and curved chute with a manually operated rectangular tank directly attached to the 2000 mm long channel (Fig. 8.2(b)). In this rectangular tank, the release of the material was controlled by a double-slider gate mechanism. The outer gate held the material inside the hopper, while the inner gate was set at a certain height from the flume bottom enabling control of the releasing flow height (or flow rate) that develops downstream. Attached at the bottom of the inner gate was a flexible flap with holes that held a small pocket of liquid (inset of Fig. 8.2(b)). At the opening of the gate, this liquid exited first, avoiding any entrainment of air bubbles which would be otherwise become trapped in the solid phase and were carried down the channel, thus creating unwanted visible micro lenses in the images and interfering with the laser plane. The rough base was making 3D-printing of a plastic material (Nylon SLS) which covered the entire length of the channel (Fig. 8.3(a)). Semi-spherical particles of diameter 3 mm at the circular edge were organized in a hexagonal pattern and positioned at the bottom. Near the end of the flume a planar laser light was shone from beneath the flow through a slit 150 mm in length and 1.5 mm wide (Fig. 8.3(b)) at the base of the channel in order to illuminate the flowing material 50 mm away from the borosilicate glass sidewall (Fig. 8.3(c)). A flat deposition area 750 wide and 2000 mm long made of plywood and varnished but not roughened was situated at the end of the channel where the material is collected and measurements of final runout length and area recorded (Fig. 8.3(d)).

Given that one of the focuses was on maximizing image quality, manufactured spherical particles which are nearly flawless enabled a better visualizations of the flow interior and allowed particle tracking. However, the cost of very fine spherical particles ($d < 2$mm) was prohibitive, hence fines were also made of angular materials for specific particle size distributions. The materials used were crushed angular particles made of borosilicate glass with size 0.6 and 1.18 mm, respectively, taken from the previous tests of Sanvitale [142], and high precision spherical particles (Sigmund Lindner GmbH, Glass beads Type P Borosilicate) of the same material with diameters of 1, 3, 7.5, 15, 20 and 25 mm, respectively (Fig. 8.4). The additional characteristics of these materials are given Table

8.1. In Fig. 8.4, some 15 mm beads do not look spherical. Due to the unavailability of spherical beads after the first purchase, a small batch of this size with shapes that slightly deviated from an almost prefect sphere was acquired separately. However, they were only used when there were not enough 15 mm particles to compose the wanted particle size distributions (i.e. PSD_3, see Sec. 8.7.2.1). The small amount used was not deemed influential on the final results.

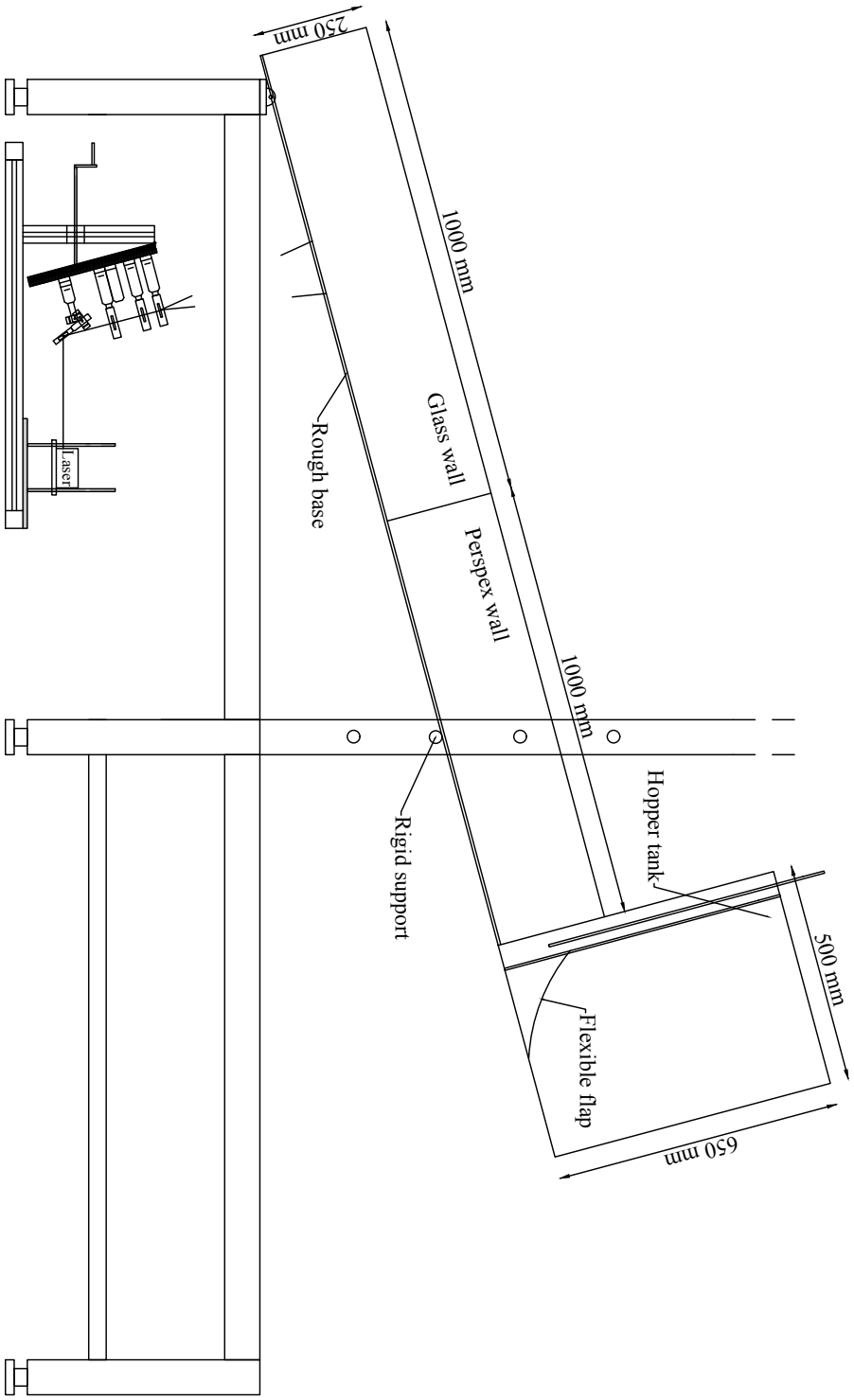

Figure 8.1: Sketch of the large scale apparatus used for the study of flowing solid-fluid mixtures.

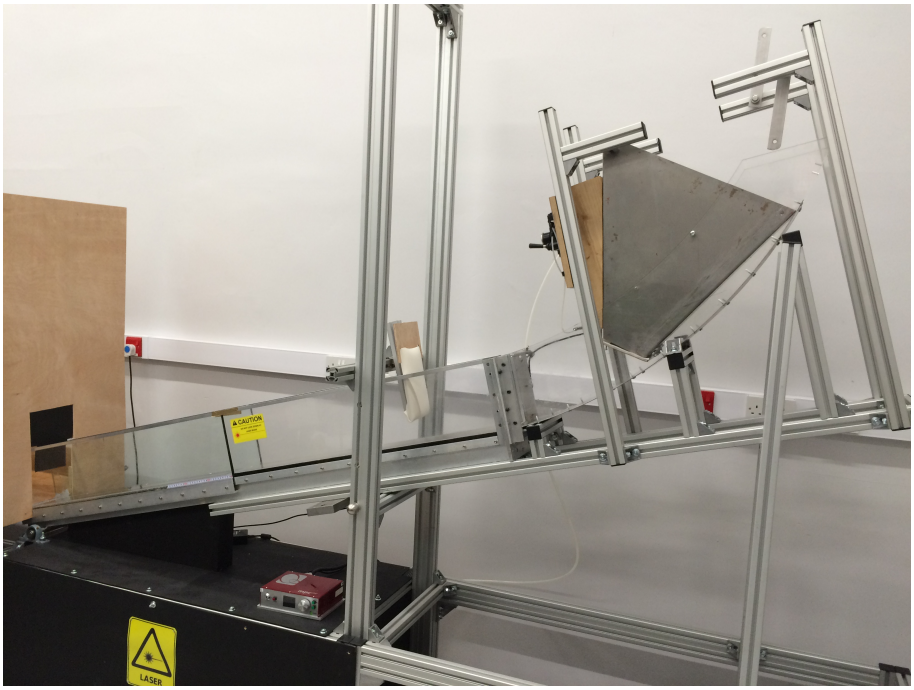

(a)

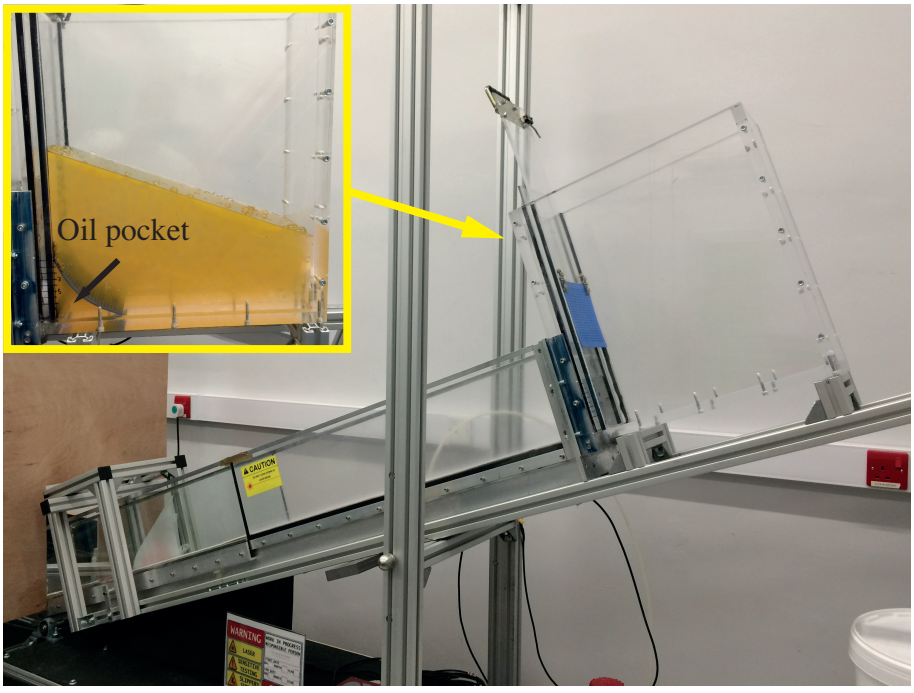

(b)

Figure 8.2: Front views of the experimental apparatus for the study of saturated granular flows highlighting the original flow release via an aluminium hopper with curved chute (**a**) which was later modified with a rectangular tank (**b**).

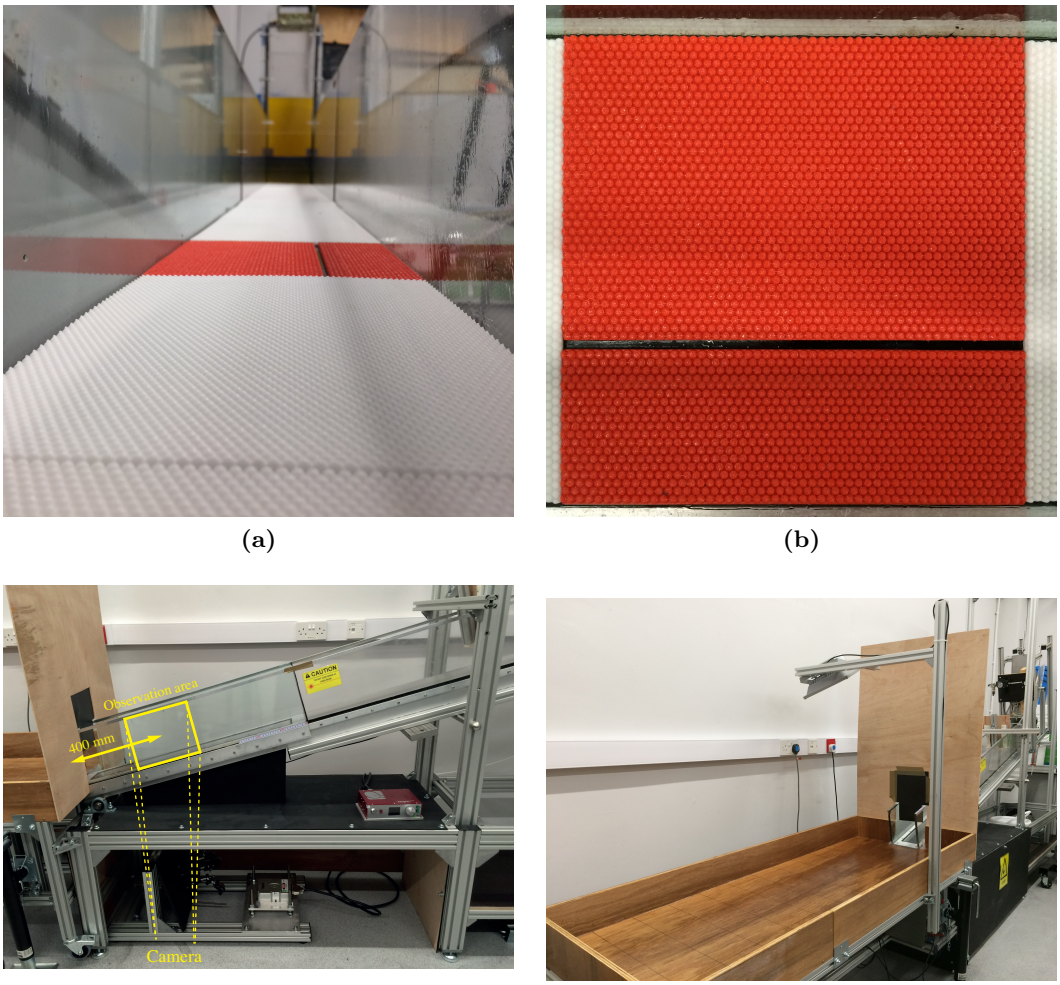

(a) **(b)**

(c) **(d)**

Figure 8.3: Different sections of the apparatus for the study of saturated granular flows: (**a**) rough based made of 3 mm plastic semi-spherical particles, (**b**) slit in the rough base 50 mm away from the sidewalls where the laser sheet is located, (**c**) observation area and (**d**) depositional area.

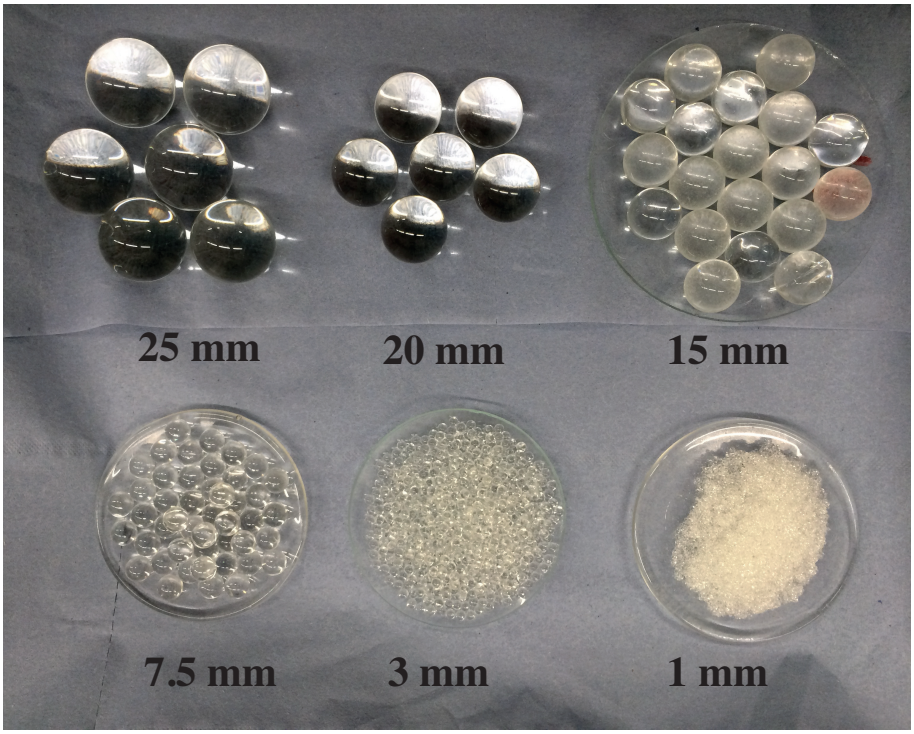

Figure 8.4: Spherical shaped particles used in the investigation of monodisperse and polydisperse granular flows.

8.3 Internal flow visualization

The visualization of solid-fluid mixtures is obtained via planer laser induced fluorescence (PLIF) [142, 144]. The key aspect of this laboratory method is the optical access to the interior of the flow which requires the matching the solid and liquid refractive indices (RI). The fluid (a hydrocarbon oil produced by Cargille laboratories, Liquid code 5095) was refractively matched to the glass (Table 8.1) and a fluorescent dye (Nile Red manufactured by Sigma-Aldrich) added so as to distinguish the particles from the brighter background. A fully saturated flow is required for this method to work properly, i.e., flowing particles that are above the saturation line are difficult to fully distinguish from the fluid. All tests were conducted at a controlled room temperature which was chosen with the following procedure. A mixture of fluid and 3 mm glass beads was prepared inside a beaker. A cylindrical red object was inserted in the liquid 50 mm away from the furthest edge with the top end just above the saturation line to allow the focusing of the camera. Images of the static object were recorded within a range of temperature from 15 °C to 26 °C (Fig. 8.5). While at these two extremes the immersed object edges were blurred, the best temperature was found in the range of 22 °C to 23 °C, i.e., when the edges became neat and clear. Temperature variations of a few degrees generally produces negligible changes in the refractive index [142] and, based on experimental flow images of glass spheres in a fluid with varying refractive index, an index mismatch of 0.003 nm is generally the largest tolerable before the the shape of the particles start to deviate from spherical [49]. Although the precise variation of the solid and liquid refractive indices with temperature was not tested, the quality of the images suggested that the room temperature and the distance of the laser plane from the sidewall were good enough to provide a clear particle visualization.

Table 8.1: Fluid and glass material characteristics

	Refractive index at 589.3 nm	Density at 25 °C ($kg \cdot m^{-3}$)	Kinematic viscosity at 25 °C (cSt)
Immersion oil	1.4715 (at 25 °C)	846	16
Borosilicate glass	1.4718 (at 21 °C)	2230	

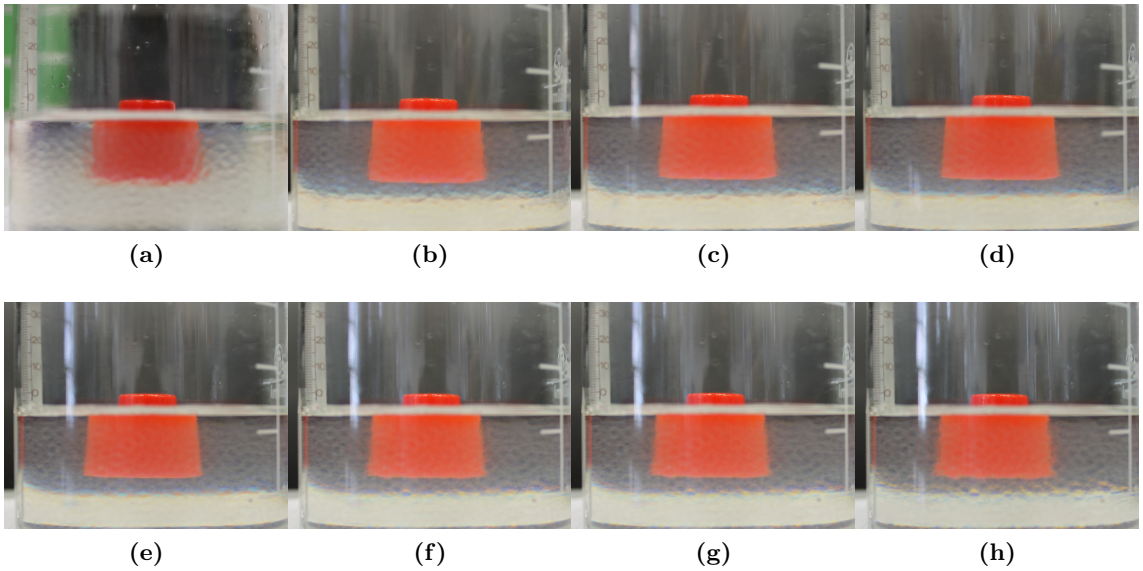

Figure 8.5: Static object viewed in the transparent mixture of fluid and 3mm glass beads at a temperature of (**a**) 15 °C , (**b**) 20 °C, (**c**) 21 °C, (**d**) 22 °C, (**e**) 23 °C, (**f**) 24 °C, (**g**) 25 °C and (**h**) 26 °C.

8.4 Light source and optics

In the previous work of Sanvitale [142] the source of light was a solid state green laser operating at 532 nm with an output up to 800 mW. The wavelength of 532 nm was within the range of 500-600 nm where the the refractive indices of the oil and glass are close and light scattering effects due to the RI mismatch are minimized [144]. This wavelength also guaranteed high intensity of emitted light when the dye is excited hence providing enough light to capture images at a high frame rate [142]. The laser beam was coupled into an optical fibre and then sent through a Powell lens to generate the light sheet. The problem with this system is that the beam needs to be carefully aligned manually to the fibre optic collimator. If the alignment is not done correctly there is the risk to damage one end of the fibre optic cable. With a degree of caution and keeping the laser power to a minimum this can be avoided, however, even if the alignment is done properly, the light travelling in an optical fibre loses power over distance [134] due to absorption by the core, cladding and impurities hence only a percentage of the signal would arrive at the other end.

To ease the alignment effort and remove the fibre losses, a new system was designed where the laser light was generated by directly sending the beam to a series of lenses. The system is shown schematically in Fig. 8.6 and mounted to the final frame in Fig. 8.7(a). The beam is first positioned perpendicular to the bottom of the flume via a mirror then sent through three uncoated plano-convex cylindrical lenses (purchased from `www.thorlabs.com`). The advantage of using a cylindrical lens is that the anamorphic shaping of the beam is provided by each lens only in one dimension, i.e., the first lens splits the beam and opens the fan and the other two, tilted by 90° with respect to the first one, control the other perpendicular dimension, i.e., the thickness of the line. Based on the lens focal lengths f different sheet width x_{ls} and thickness can be obtained. The sheet width x_{ls} at a working distance L_{ls} from the beam source to the bottom of the flume is control by the the focal length of the first lens. With the needed line width x_{ls} the fan angle can be calculate as:

$$\phi_{ls} = 2\tan^{-1}\frac{x_{ls}}{2L_{ls}} \tag{8.1}$$

The Effective Focal Length (EFL) is then obtained as:

$$EFL = \frac{d_b/2}{\tan(\phi_{ls}/2)} \tag{8.2}$$

where d_b is the beam diameter. The Class IV laser used (Opus Quantum 532) has an adjustable power up to 2150 mW, a working wavelength of 532 nm and a diameter $d_b = 1.85 \pm 0.2$ mm. With the flume at an inclination of 15°, a working distance L_{ls} of 600 mm assuming $d_b = 2$ mm and the needed sheet width of 240 mm the calculated EFL is 10

mm. The laser operates with Gaussian beam profile and once split, the fan will also have a Gaussian light distribution where the maximum intensity at the centre decays towards the margins. The less intense margins can be removed by an aperture (Fig. 8.7(a)) placed after the second or the third lens.
The major downside of this open-air lens system is that the laser light is unshielded which means that the setup needed to be enclosed to avoid any scattering of harmful laser light. The frame supporting the laser and the lens system was placed below the flume apparatus and enclosed with appropriate panels. Only a narrow gap corresponding to the slit in the rough base was let open. Before testing, outside the laboratory door the laser illumination sign was switch on and a strap put in place to limit the access in the room, which was also only accessible to authorized laser-users. The laser was connected to an appropriate power socket that switches the laser off in case someone enters the laboratory accidentally. The power was kept at a minimum during alignment of the laser sheet with the bottom slit and any adjustment of the lens system. The laser power was increased just before testing and switched off immediately after. Appropriate eye-protection was worn whenever the laser was activated and with any output power.
This system allows for the generation of light sheets thinner than the laser beam. To get the thinnest possible line, the focal length of the third lens should coincide with the distance between the centre of this lens and the observation area. The thickness was generally kept around 1 mm, although it varied slightly when the slope of the channel was changed since the working distance Lx_{ls} (set initially for an inclination of 15°) varied from the fixed laser frame below the flume (Fig. 8.3(c)). Light sheets thinner than 1 mm were possible but they required a very accurate adjustment of the lens system. A series of preliminary tests conducted with 3 mm glass beads was used to assess the quality of the image revealing that a thickness of approximately 1 mm was good enough to clearly visualize the particles.
The lit surface of the granular flow was captured by a high-speed camera (Phantom Miro 310) (Fig. 8.7(b)). During the recording of the flows, a long pass filter (Schott OG550), with the cut-point at 550 ± 6 nm, was placed in front of the camera lens to limit the imaging to these emission wavelengths of the fluorescent dye and to screen unwanted scattered light.

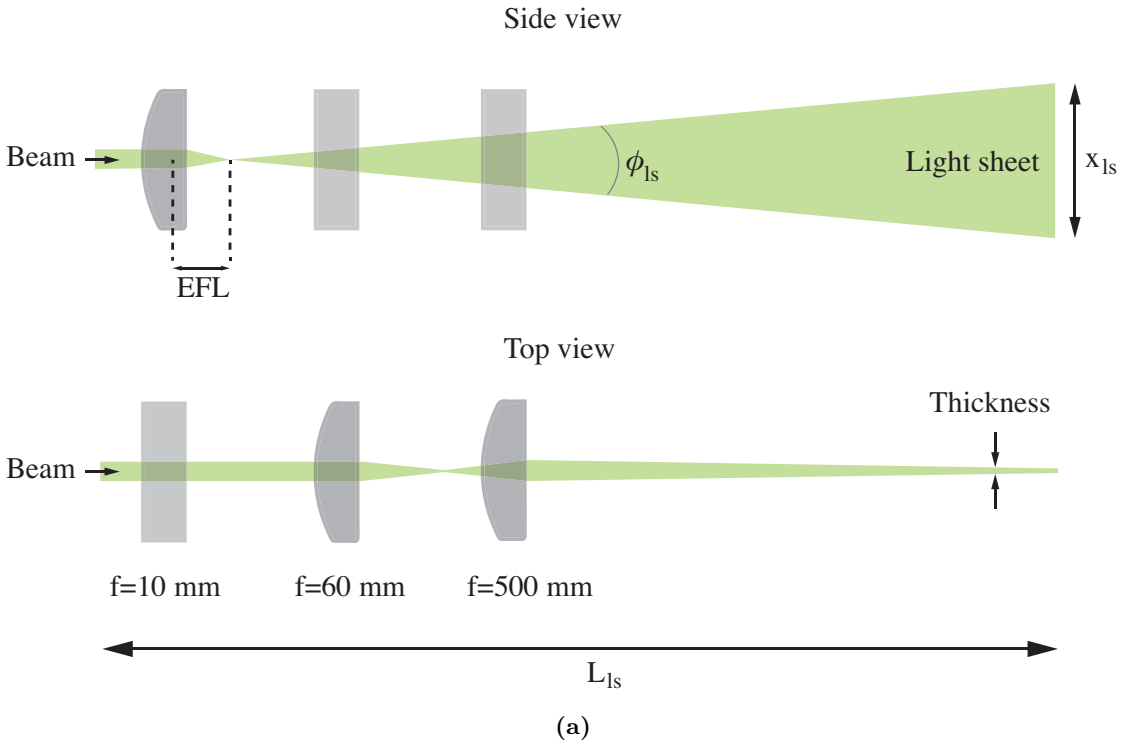

Figure 8.6: System of three cylindrical lenses used to generate the laser sheet. Adapted from [134]

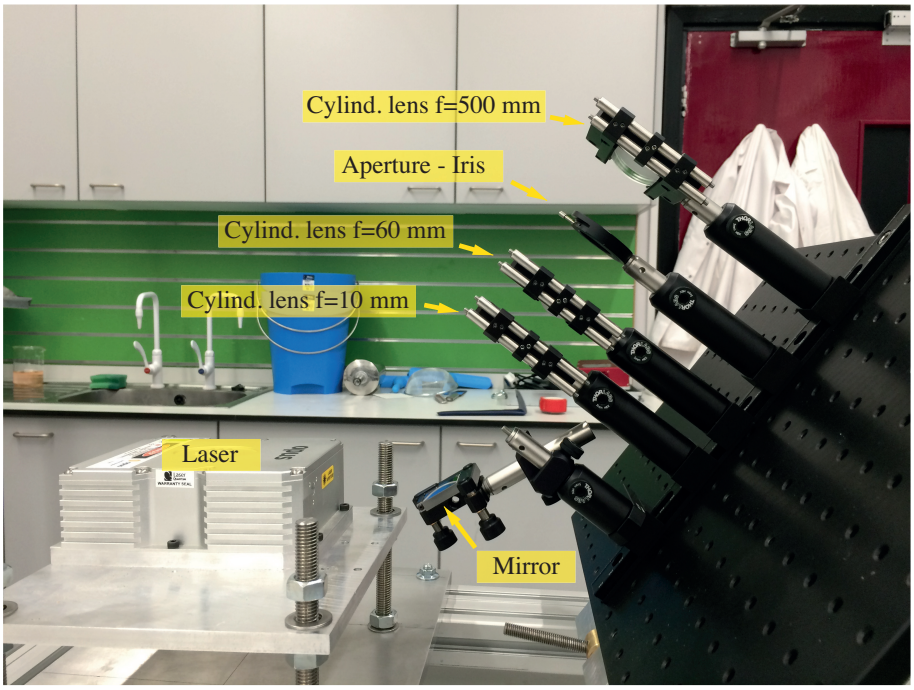

(a)

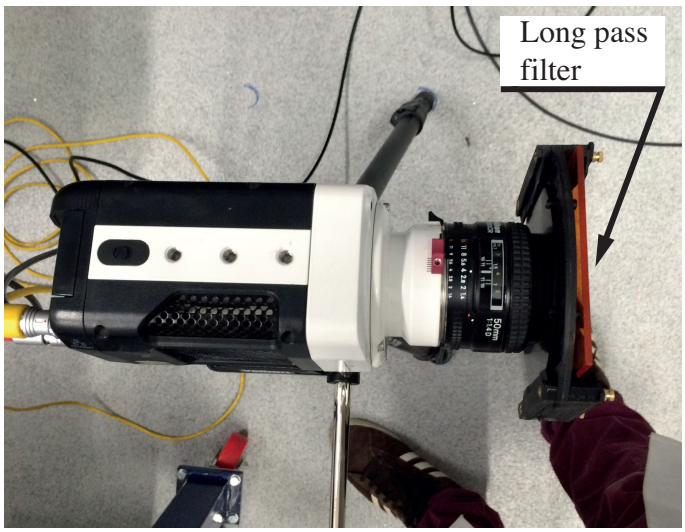

(b)

Figure 8.7: (**a**) Assembled laser sheet generation system and (b) high-speed camera equipped with long-pass filter.

8.5 Test procedure

A first series of tests was conducted with a mixture of fluid and 3 mm glass particles only. The second series of tests was performed with different particle size distributions (PSD) for detailed debris flows model testing. All tests were carried out with the same experimental conditions. The opening height of the gate was kept constant. A total mass of 18 kg for each mixture was loaded inside the hopper and then saturated with 5.9 litre of oil so that the initial sediment volumetric concentration (ν) was 0.57 (i.e. porosity = 0.43). The oil was dyed with Nile Red at a concentration of 2.5 mg/l. Once loaded, the mixtures were stirred to remove air bubbles and ensure a homogeneous test material.
The laser was not moved during testing so that images could be directly compared with one another. To make sure that the laser sheet was 50 mm away from the sidewall throughout, a metallic ruler, wetted with the same dyed oil used in the experiments so that the laser line was clearly visible, was used to measure this distance from the sidewall at different heights from the base. This procedure was performed while keeping the laser power to a minimum.
The camera was positioned and aligned to visualized the side of the chute (Fig. 8.3(c)). A small tank, 1500 mm wide and large enough to cover the camera field of view, was filled with a mixture of oil and 3 mm particles and positioned over the rough base in the correspondence of the observation area, approximately 400 mm before the outlet. The laser was temporarily switch on and the camera focussed on the visible static particles. Then, the camera was slightly defocussed in the attempt to improve the centroid detection (more details on this are given later). The distance from the camera lens to the laser sheet determines the resolution of the images. The flows were recorded at a distance of 130 cm with a 50 mm lens and a resolution of 512x320 pixels, so that for monodisperse flows the image particle diameter was approximately 5 pixels, and a distance of 30 cm with a 85 mm lens and a resolution of 768x576 pixels, so that the particle image diameter was approximately 38 pixels.
The tank containing the static mixture was removed, the laser switched off and a target grid of regular spaced dots 4 mm apart was then firmly fixed and aligned 50 mm away from the sidewall in correspondence to the slit in the rough base. For each test an image of target was captured for the transformation for relating information in pixels to physical lengths. The images obtained from the defocussed camera still allowed an accurate identification of the target grid (Fig. 8.8).
Before running each test, the laser power was set at 1800 mW which guaranteed an initial frame rate of 2000 fps and enough light to reduce the f-number to 4 (Fig. 8.7(b)) for the 50 mm lens and 5.6 for the 85 mm lens, thus increasing the depth of focus and reducing fish-eye and barrelling lens distortions. As in dry conditions, to test the sensitivity of

velocity and granular temperature measurements, the additional frame rates obtained by skipping frames were 1000, 500 and 250 fps.
Over the depositional area a low-speed camera (Canon EOS 1100D) was positioned so that the entire width and enough length of the depositional area could be visualised. The evolution of the material deposition was recorded with a frame rate of 30 fps. This camera allowed long recording (up to minutes) and was triggered in advance. Conversely, the high-speed camera has only a finite amount of memory based on the resolution and frame rate. To record the entire flow evolution from the side of the flume channel, the high-speed camera was connected to the hopper gate via a switch that started the recording only at the opening of the gate.
The tests were conducted in a dark room. Only a LED floodlight was switched on and adjusted over the deposition area to deliver enough light to permit the recording of the material spread but not to disrupt the flowing material crossing the laser light. A barrier installed at one side of the depositional area (Fig. 8.3(d)) limited the amount of light crossing over to the flume channel.

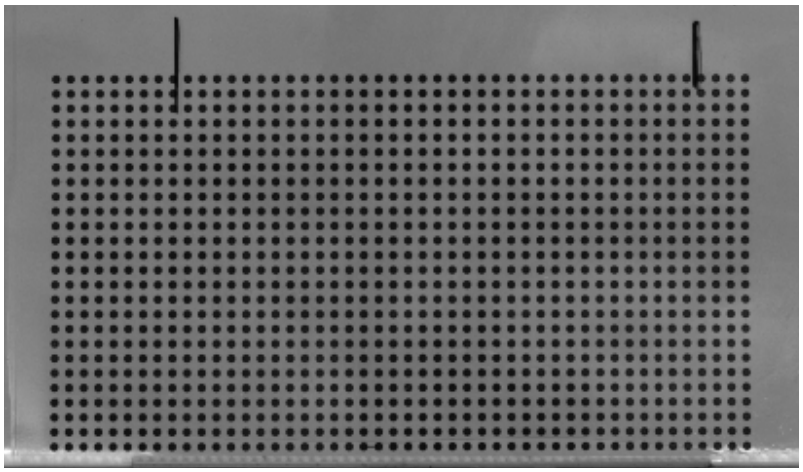

(a)

Figure 8.8: Target used in the investigation of saturated granular flows for the transformation of pixels information to physical lengths

8.6 Data processing

Measurements of monodisperse granular flows were obtained using PTV with the same procedure explained in Sec. 4.4.2 for velocity and granular temperature and Sec. 3.3 for outliers removal. To study the evolution of the depth-averaged velocity over time the PIV algorithm was used instead. For PTV, the main difference between images obtained in dry flows and those captured in saturated conditions is that in the latter case the particle images do not have the same characteristic intensity pattern, i.e., a brightness with a peak near their centroid which progressively decreases one pixel away from this peak. In the attempt to generate this intensity pattern and minimize any spurious pixels in the image (e.g. caused by sporadic air bubbles), the camera was slightly defocussed. However due to the nature of the experiments, the brightness pattern affected the centroid detection, thus particle position errors are more severe than for tests done in dry conditions, affecting in particular the measurements of granular temperature. A comparison between focussed and defocussed images can be seen when comparing the tests of monodisperse granular flows presented later in Fig. 8.10 (focussed camera) and 8.11 (defocused camera). The Gaussian distribution of the laser sheet made difficult the detection of particle centroids at the lateral edges of the images where the light was less. An improvement in image light distribution was made in pre-processing by applying a logarithmic-stretching transformation [66]. This allowed the pixel intensity in the images to be evenly distributed and, along with morphological image adjustments and background subtraction, to detect the majority of the visible particles. A Matlab code illustrating this procedure is given in Appendix F.

Solid concentration profiles were obtained with the method based on images at a greater resolution (Fig. 8.9(c)) described in Sec. 4.4.3. Using this method the results of solid concentration have a 3D value since the images are 2D slices through a 3D flow [104]. The other method to obtain solid concentration profiles based on the roundness of the Voronöi polygons was trialled. However, uncertainties in the magnitude of solid concentration attained by the flows, with maximums of $\nu \approx 0.2$, questioned the applicability of this method when compared to the visual (crystalline) structure observed away from the sidewall (see Sec. 8.7.1.1). Only the results obtained based on images at a greater resolution were used in further computations.

Images lacked information corresponding to the rough base since the plastic base is not visible and information of the first layer of particle cannot be retrieved from the raw images. To facilitate the the binning procedure of PTV, this information was added prior to the centroid detection by manually adding the image of the base visible in the target image and its centroids (Fig. 8.9(b,d)).

The particle tracking algorithm used here is limited to single sized (monodisperse) particle

flow. To study polydisperse flows only PIV was used. This limited the analysis to velocity profiles since the granular temperature measurements are underestimated by PIV (Ch. 6) and the acquisition of solid concentration profiles from images at greater resolution were impeded due to image blurring caused by the 1 mm particles in the flows and the halos created by the big particles (see later, Fig. 8.15). The approach used to estimate solid concentration using images at greater resolution (Sec. 4.4.3) was trialled but the different particle sizes generated a great amount of spurious edges that severely altered the final output. A time consuming manual approach was not undertaken. Finally, analyses of the depositional runouts were limited to the measurement of their spread and surface particle distribution via image analysis once all the material accumulated on the depositional area. Samples and particle size distributions at different deposit locations for the study of particle depositional segregation were not collected.

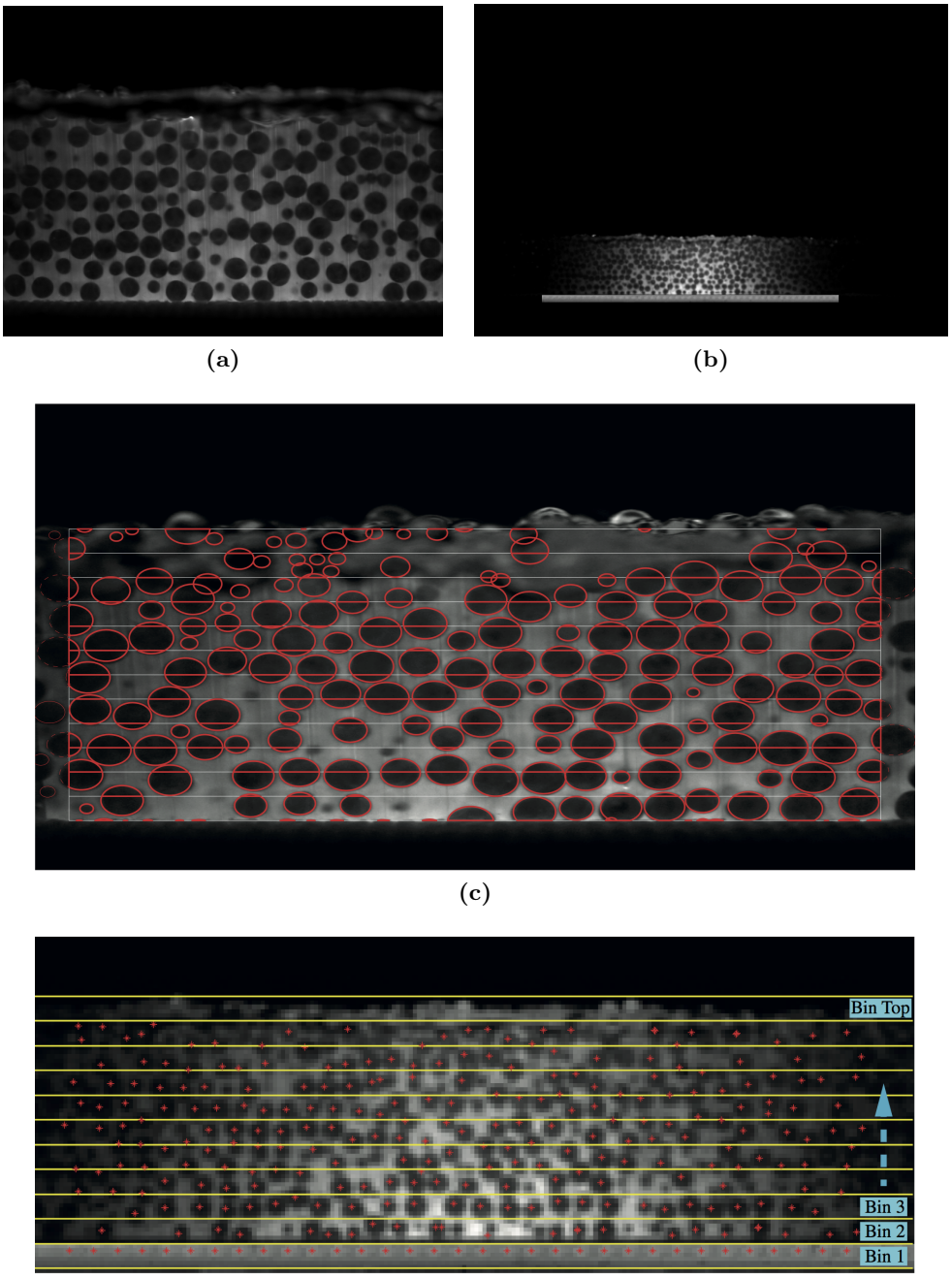

Figure 8.9: (**a**,**b**) Internal monodisperse flow images at different resolutions at 50 mm inside the flow of total width 150 mm. (**c**) Partition of particle edges for the determination of solid concentration by images at greater resolution . (**d**) Binning of the image and particle centroids.

8.7 Saturated granular flows on an inclined channel

The results presented in this section are broken into two parts. The first part presents the physical dynamics of monodisperse granular flows composed of fluid and 3 mm glass beads. Several preliminary tests were used to test the two different flow release mechanisms (aluminium hopper and rectangular tank), to test different methods to remove air entrainment and to visually examine the different monodisperse flow structures over flat and rough bases. Further flows were performed later, after the required flume modifications to obtain the necessary measurements for the comparison with the prediction of kinetic theory.
The second part looks at the flow structure, velocity profiles and physical deposit of saturated polydisperse granular flows that are used to determine their consistency with traditional debris flow behaviour and identify any exception in behaviour.

8.7.1 Monodisperse flows

Monodisperse saturated granular flows were released at two different inclinations, 15° and 20°, respectively. The characteristic particle diameter $d' = 3mm$ is used for the measurement dimensionalization and the same scaling of Sec. 4.3 applies here. The initial measurements were obtained with a sampling interval $\Delta t = 0.22$ (2000 fps) which was then reduced by skipping frames to test the sensibility of velocity and granular temperature to different Δt. The additional sampling intervals Δt are 0.11, 0.05 and 0.02, respectively.

8.7.1.1 Removal of air entrainment and flow structure

One of the problems encountered during the visualization of the free-surface saturated granular flows was the entrainment of air bubbles that formed and were trapped at the commencement of the flow and carried in the bulk of the flow. In the laser image they diffracted the light appearing as dark ovals with darker edges. The first consequence is that these dark spots can be inappropriately picked up during the centroid detection process in PTV or alter the correlation peak detection in PIV thus compromising the quality of the results.
A first series of tests was carried out with the aluminium hopper and a flat flume base. The hopper was fixed on a curved chute element (Fig. 8.2) and the material dropped a few centimetres above it. A sequence of images captured for a monodisperse flow released with this configuration is shown in Fig. 8.10. The flow front is unsaturated and the PLIF technique is not able to illuminate the true interior. The saturation line then rises quickly after this first phase and air bubbles entrained in the front are then transported in the mixture. They remained in the saturated core for some time until they only occasionally appeared

towards at the end of the flow. Considering that the saturated monodisperse flows were set to be analysed for a sufficient period of time in a steady flow as in the dry conditions, another consequence of air bubble entrainment is that the time span for the application of PTV is reduced thus compromising the statistical validity of the measurements.
To avoid the entrapment of the air bubbles, the aluminium hopper was changed with a rectangular tank directly attached to the flume and the 3D-printed rough base was added to cover the entire length of the chute. Additionally, a flexible flap with holes that held a small pocket of liquid (inset of Fig. 8.2(b)) was added to the inner gate. At the opening of the gate this liquid exited first avoiding any entrainment of air bubbles. A sequence of images obtained after these modifications is shown in Fig. 8.11. It can be seen that air bubbles were not entrained allowing the centroid detection right after the flow front once the saturation line was at a constant height above the base.
From the sequences presented here it was also possible to examine the difference in behaviour of these flows over a flat and rough base. In the first case, in the body of the flow (Fig. 8.10(c)), the particles stratify in layers and reach an almost ordered (crystalline) state. This was sometimes less clear during the flow but the ordering was a prominent feature over the flat base. Keeping a simple monodisperse flow, this ordering was partially removed by increasing the basal bumpiness through rough base of 3 mm particles (Fig. 8.11(c)). A particle disordered state was only reach at the flow front and in the shallower tail while the body was still characterized by an order layered structure apart from approximately two particle layers close to the rough bottom.

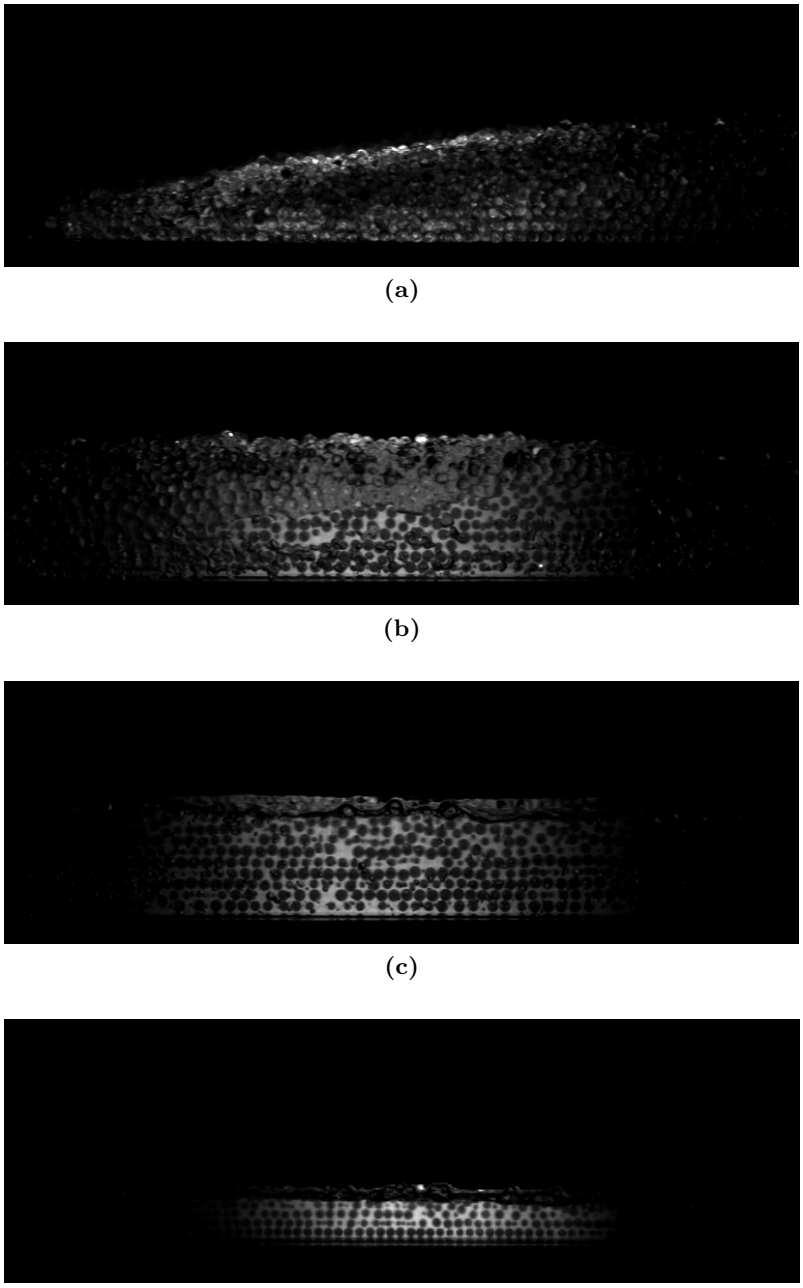

(a)

(b)

(c)

(d)

Figure 8.10: Preliminary test of a monodisperse granular flow released from the aluminium hopper. (**a**) Unsaturated front, (**b**) rise of the saturation line after the flow front, (**c**) body of the flow, (**d**) tail. For this test the camera was not defocussed.

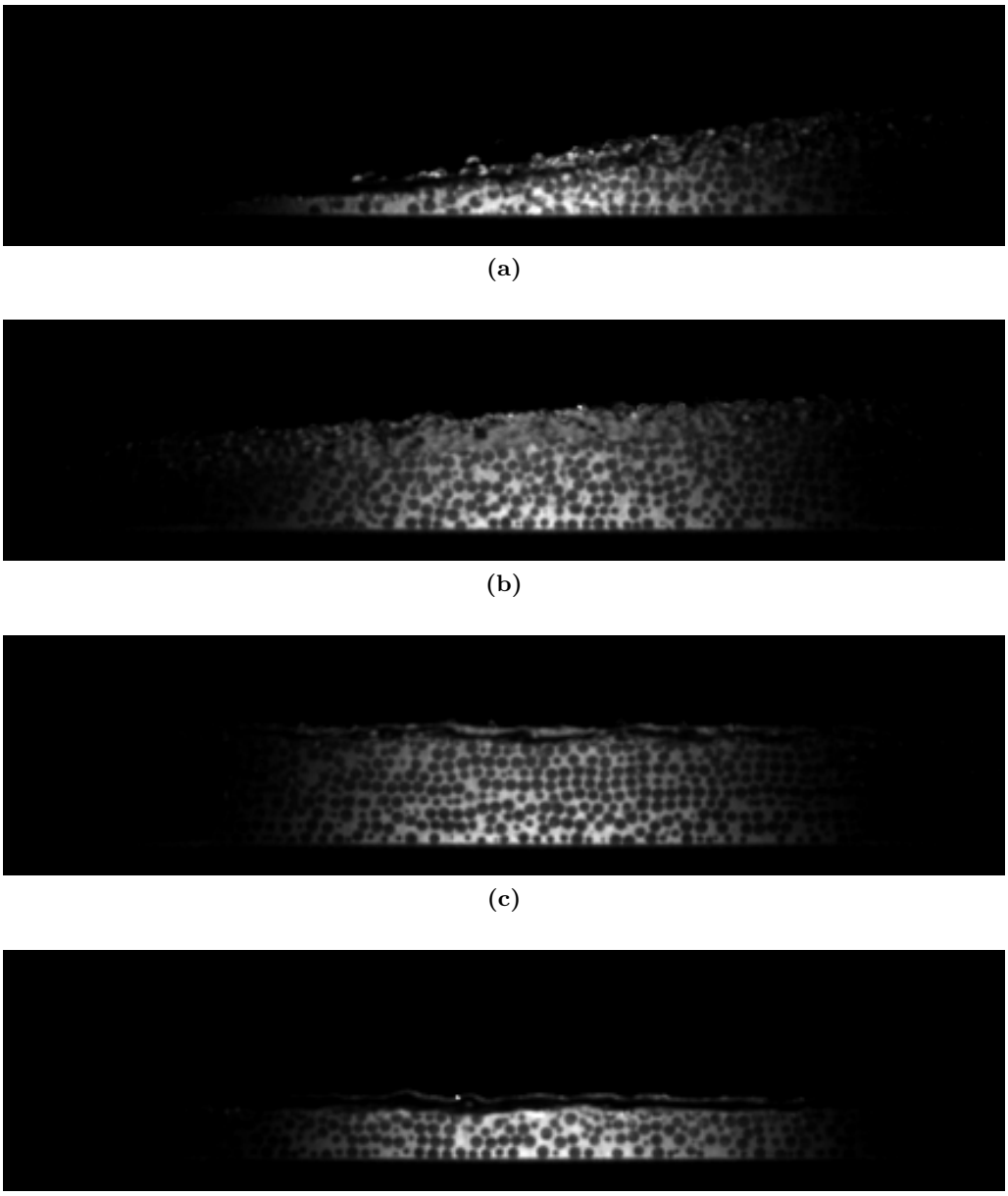

(a)

(b)

(c)

(d)

Figure 8.11: Monodisperse granular flow released from the rectangular tank. (**a**) Saturated front, (**b**) saturation line after the flow front, (**c**) body of the flow, (**d**) tail. For this test the camera was defocussed.

8.7.1.2 Steady states

In Fig. 8.12 an example of depth-averaged velocity over time for the entire duration of one monodisperse saturated flow was obtained using PIV with patch size 24x24 and 12x12, for coarse and refined grids, respectively. At an inclination of 15°, negligible variations of the velocity (thick line) were observed after the flow front when a constant flow height and saturation line were maintained for some time before the flow became shallower and reduced its velocity. This was sufficient to retain a relatively stable and steady flow and set a minimum time $t = 144$ (equivalently 2 s) over which the flows were analysed. Conversely, at 20° the depth-averaged velocity was never maintained for a sufficiently long period of time and decreased rapidly with time as the front passed. Furthermore, with the amount of material used, two characteristic peaks were always visually detected, one after the flow front and one just before the tail. In between, the flows tended to keep depths of about six particle diameters. For these reasons the PTV analyses were restricted to flows at 15° only. For this inclination, as in the dry case, ten tests were conducted to confirm the statistical reliability of the measurements. For a collection of these tests, the system kinetic energy and the expected value for each bin (see Fig. 8.9(d)) were calculated and plotted over time. They are reported in Appendix B for $\Delta t = 0.22$ and confirm the steadiness of the flows.

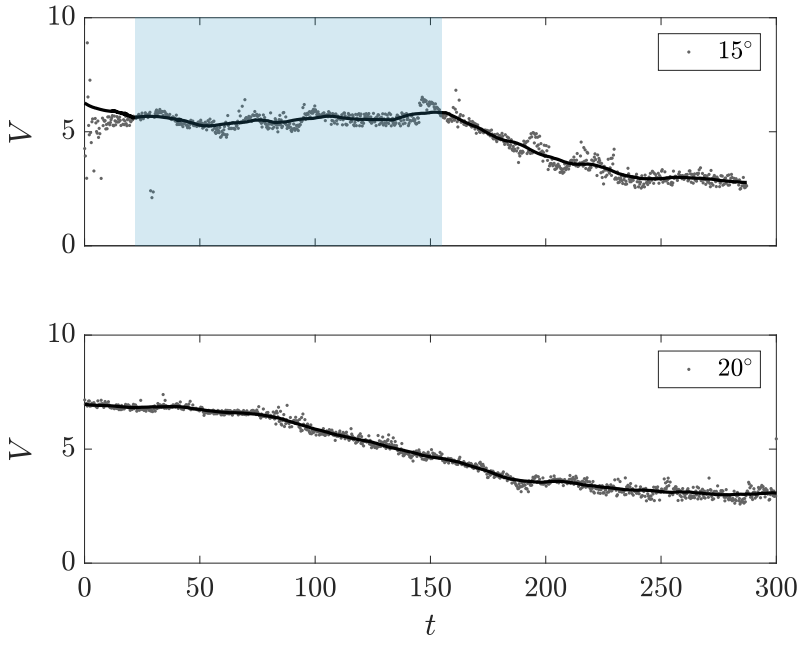

Figure 8.12: Depth-averaged velocity over time for monodisperse saturated granular flows. Thick colour line represents the duration of the steady states.

8.7.1.3 Results

The results reported below are those obtained as the average over ten tests. The PTV measurements start at a height of $1.5d$ above the base, i.e., in the middle of the second bin (see Fig. 8.9(d)) defined in the post-processing procedure of PTV. For clarity, in all the plots reported, the top surface of the static rough base ($z = 1$) is marked by a dashed line.

The stream-wise and slope-normal velocity components shown in Fig. 8.13(a) are insensitive to Δt. While the slope-normal component is negligible, the stream-wise velocity resembles a Bagnold-like profile as was observed in numerical simulations away from the sidewalls. A slip velocity of about 3.2 (0.54 ms^{-1}) develops at the bottom while at the free surface the measurements become corrupted above $z = 8d$ because of the spurious detection of particle centroids above the saturation line.

The gradient in the velocity profile is more apparent from the shear rate curve as shown in Fig 8.13(b). This is shown as one curve since there is negligible variation of the velocity profiles for different Δt. The shear rate is higher at the bottom, where most of the deformation occurs and the slip velocity develops. The value of shear rate then decreases towards the free surface with a convex shape. Similar observations were described in mixtures of angular particles and fluid [146]. Notably, the velocity and shear rate profiles behave differently from the dry flows reported in Sec. 5.7.1 where a linear velocity profile was linked to an almost constant variation of $\dot{\gamma}$ with depth. Here, the velocity resembles a Bagnold-like profile and the shear rate is not linear but has a convex shape.

The granular temperature is sensitive to Δt as depicted in Fig. 8.13(c). The profiles tend to collapse on the same curve for increasing sampling intervals. The previous validation via synthetic images suggested that the largest Δt is likely to yield the best approximated value of granular temperature. Considering this sampling interval and disregarding the measurements above $z = 8d$ the profiles can again be related to the results of numerical simulations away from the sidewall. Higher temperature is generated at the bottom where the bumpy base acts as a source of fluctuational energy but then decays quickly and displays an almost linear profile $2d$ above the base. While the agreement with the numerical simulations can be found at least in terms of profile shape, as already discussed, the accuracy of the measurements may be affected by greater errors in the particle centroid detection. It was not possible to precisely validate these measurements, although this is an aspect that should be addressed for future work in the framework of saturated granular flows and kinetic theory.

Solid concentration profiles are insensitive to Δt and they are shown as one curve in Fig. 8.13(d). The concentration is lower at the base, as expected due the present of the bumpy base, increases at mid depth and then decreases towards the free-surface. Particle edges

entering the laser plane that may contribute to the solid concentration were difficult to detect as it can be seen in Fig. 8.9(c). From the visual observations made in Sec. 8.7.1.1 it was clear as the flow particles stratify in layers. Ordered (crystalline) states are generally associated with solid concentration greater than 0.49 [102]. The measurement may be slightly underestimating the value of solid concentration since 0.49 is the maximum value attained by these flows (approximately $4d$ in Fig. 8.13(d)) while it seems as, apart for a region close to the bumpy base, the flows reached a crystalline state throughout in the steady part of the flow (Fig. 8.11(c)).
While research into causes for the underestimation of the solid concentration should be part of future improvements, the pressure profile of the solid phase can be estimated as:

$$p = (\rho_p - \rho_f)\nu g \cos\theta \tag{8.3}$$

where the prime indicates a derivative with respect to z (the direction normal to bed) and ρ_f is the density of the fluid (Table 8.1). The profile shown in Fig. 8.13(e) and obtained from the integration of Eq. 8.3 displays the characteristic linear (hydrostatic) profiles with values that increase with depth. Similarly to previous chapters, the particle pressure and granular temperature (with $\Delta t = 0.22$) can be used to test the prediction of kinetic theory in terms of the solid phase alone [18]. These results are presented in Fig. 8.13(f) for the few data obtained from the flow at 15°. While the data follow the theoretical curve at least qualitatively, the theory underestimates the data. This may be connected to the estimations of solid concentration (from which pressure was derived) and granular temperature, which the true value is not known. Before claiming that kinetic theory may be also used to describe such flows, it should be ascertained that ν and granular temperature can be accurately measured. Then, it might be possible to obtain a better agreement between experiments and theory.

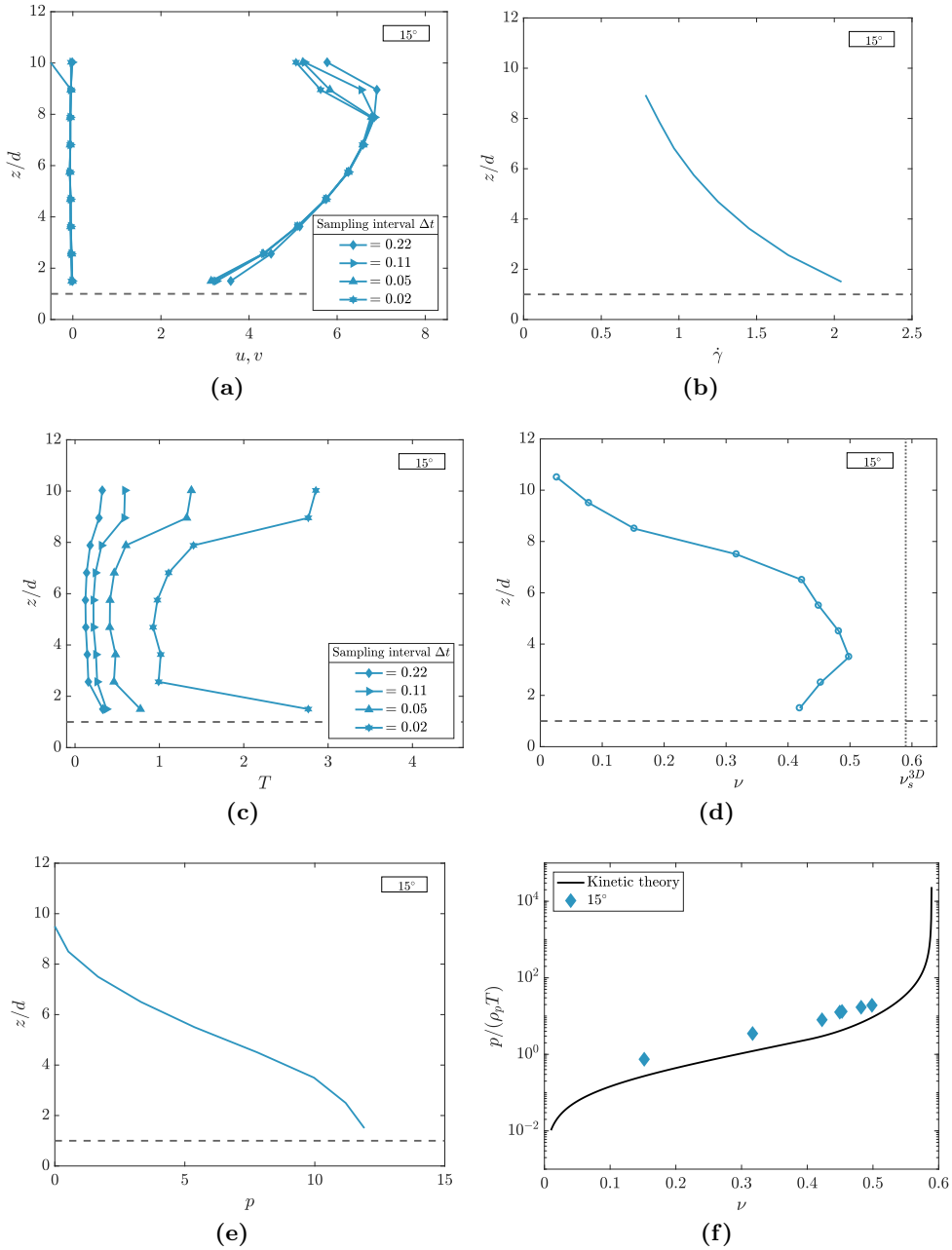

Figure 8.13: (**a**) Velocity, (**b**) shear rate, (**c**) granular temperature, (**d**) solid concentration, (**e**) particle pressure and (**f**) prediction of kinetic theory (Eq. 2.35) in terms of dimensionless pressure against experimental results of monodisperse saturated granular flows. Velocity and granular temperature are given for all the sampling interval Δt tested while the other measurement are given for the $\Delta t = 0.22$.

8.7.2 Polydisperse flows

The polydisperse flows described in the following are characterized by particle size distributions made of few, but distinctly different, particle diameters in the attempt to step away from monodisperse realizations but at the same time, only gradually increase the complexity of the investigations. The velocity results are given in dimensionless form by considering the characteristic median diameter $d_{50} = 7.5$ mm from the particle size distribution (PSD) presented later which can be then used to obtain the different scaling as in Sec. 4.3. Conversely, results relative to the runout distance are given in dimensional form to improve the readability of the plots.
Three chute inclinations were used, respectively, 15°, 20° and 25°. Different sampling intervals were trialled for some flows although negligible changes were observed in the velocity measurements. For this reason, the following results are reported only for $\Delta t = 0.22$ since the fewer frames allowed a quicker analysis of all the data.

8.7.2.1 Particle size distributions

The four particle size distributions (PSD) used in this study are shown in two different ways. They are presented as histograms showing the percentage of mass for each particle size over the total mass in Fig. 8.14(a) while classic gradation curves are depicted in Fig. 8.14(b). The smallest and largest sizes were limited due to practical reasons, however it was possible to approximate those used by Sanvitale and Bowman [144]. For comparison PSD11-up from their work is plotted together with those used here. In Sanvitale and Bowman [144] the particle size of the material was increased by a factor of four in order to account for the different behaviour in terms of particle settlement and drainage/consolidation due to the increase in kinematic viscosity for the substitute fluid, compared with water.
PSD_1, PSD_2 and PSD_3 are composed of spherical particles only. For each of these three the amount of finer materials (1 mm) was progressively increased from 5.53% for PSD_1, 11.2% for PSD_2 and 16.6% for PSD_3, the number of particles in the middle of the distribution (7.5 mm) reduced and the number of larger particles (15.5 mm) increased. The two largest sizes, 20 and 25 mm were kept constant throughout due to the limited number of particles available. PSD_{hyb} is the same as PSD_2 but all 1 mm particles (i.e. 11.2% of the total mass) were substituted by angular particles of 0.6 and 1.18 mm in order enhance expected pore pressure effects caused by addition of fines.

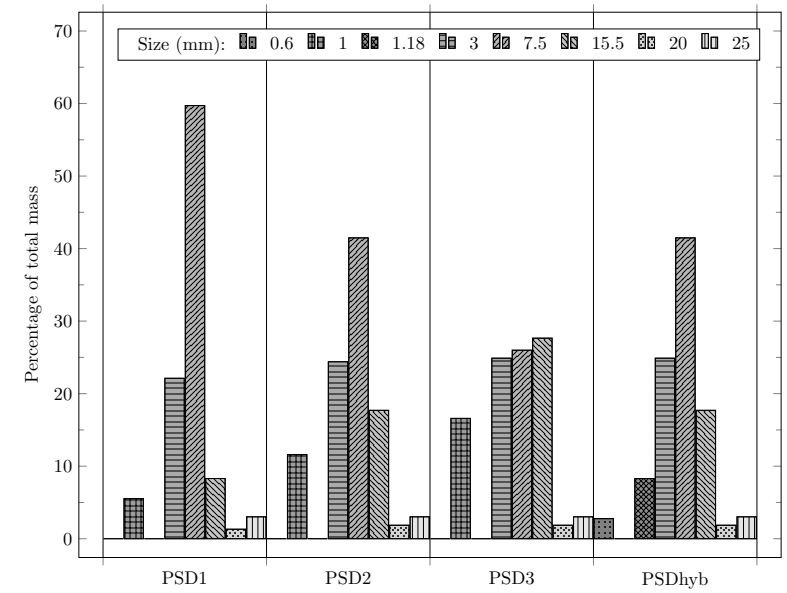

(a)

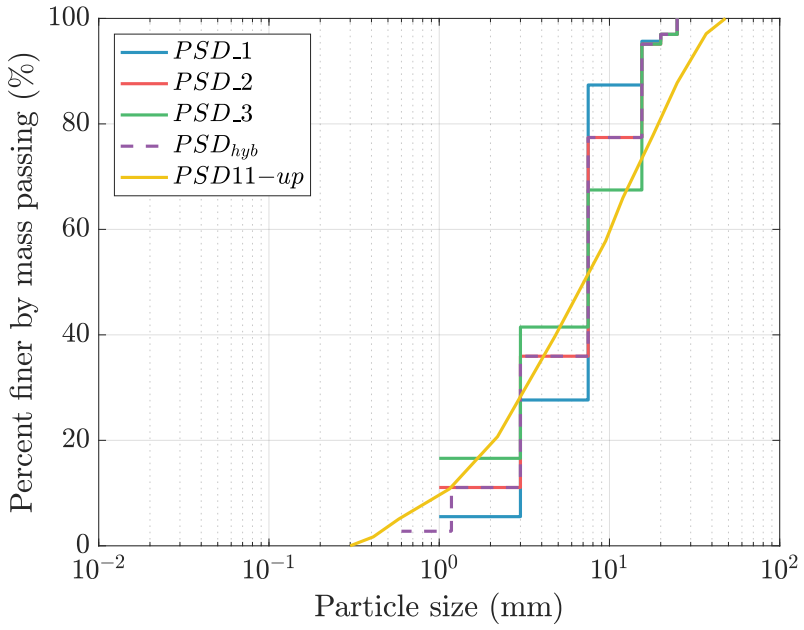

(b)

Figure 8.14: Particle size distributions (PSD) presented as (**a**) histograms of percentage of mass for each particle size over the total mass and (**b**) classic gradation curves. PSD11-up adapted from [142]

8.7.2.2 Internal flow structure and segregation

The controlled flow release adopted to improve the flow visualization increases the saturation of the flow front and appears to eliminate a key aspect of real debris, i.e., the interplay between the less saturated, more resistive friction flow front and the dispersion behind it which shunts the front forward and increases the mobility of such flows. Furthermore, the surge flow rate was controlled by the height of the gate, which is different from what was done previously [142, 144], where a full release of the material occurred for each test. A full release may create a single surge and cause segregation of large particles to the front as previously observed by Sanvitale [142], Sanvitale and Bowman [144]. Conversely, with the controlled release adopted here, trying to achieve a steady flow by releasing only certain amount of material may cause the flow behaviour to be fundamentally different.

For the same flow, the front displayed a particle size distribution similar to that found in the body (the front was not solely dominated by the coarse material but fines were always present) while the tail was in most cases highly fluid and shallow. For this reason, the following analysis focuses only on the body of the surge once the front passed and before the flow height decreased at the tail.

Images of the flows representing the same time after the front passed are shown in Fig. 8.15 for different PSDs and angles of inclination. Producing a good thickness of flow consistently was difficult, however, a different degree of segregation across the flow depth was evident in all tests.

From the analysis of flow images it was revealed that after the saturated front at an inclination of 15° for PSD_1 and PSD_2, the segregation of large particles (20 and 25 mm) was not clearly evident. They were not predominantly carried at the free surface but were able to span the entire depth apart for a close region close to the bottom dominated by fine particles (1 and 3 mm). Some of the 1 mm fines were trapped and slowed by the rough base made of 3 mm semi-spheres. Particles in the range $1 < d < 3$ mm appeared at increasingly higher concentration over time after the front, and the tails were generally characterized by the highest content of these fines. Even when the amount of fine particles was incremented for PSD_3 they were not dispersed throughout the flow but tended to remain close to the rough base, as can be seen from the pockets of clear fluid close to the free-surface for this PSD. The more frictional PSD_{hyb} resulted in a thick layer of material that stopped over the channel, hence this is not shown together with the other flowing materials.

Flows at an inclination of 20° showed similar behaviours to those at 15° but, because the flows were generally shallower, once the fine particle content was incremented for PSD_3 there was an even distribution across the flow. Large particles (> 15 mm) were predominantly carried close to the surface only for PSD_3. PSD_{hyb} behaved similarly to

PDS_2 (its counterpart in the absence of fine angular particles) although the flows was shallower and image quality worsened.
At 25°, flows were the shallowest compared to the same particle size distributions at gentler slope angles. For PSD_1 fine materials ($\leqq$ 3 mm) were not spread across the entire depth but, when compared to flow at 15°, they were characterized by a higher accumulation immediately after the flow front. This was also highlighted by the tail which was less dominated by these fines. The higher flow velocities and grain agitation attained at this inclination allowed a better mixing of the material within the length of the channel leading to a better distribution of fine materials across the entire flows. For PSD_2, PSD_3 and PSD_{hyb}, the large particles (20 and 25 mm) were mainly transported at the surface and appeared to float on the smaller ones. Air bubbles appeared more frequently at this inclination and hardly escaped when the amount of fines was the highest.

8.7.2.3 Deposit morphology

Analysis of experimental deposits included only the measure of the final spread, their shapes and the examination of visible particle segregation via image observations. In Fig. 8.16 the final extent of the runouts and their shapes are shown for the different PSDs and slope angles. While the comparison of the final runouts at each slope angle is discussed in the next section, here the focus is only on segregation patterns and the depositional shape.
The amount of material left along the last meter of the flume varied at different inclinations. At 15° some fines always deposited on this last part. PSD_{hyb} was also able accumulate sediments close to the exit point of the flume although it almost completely stopped on the channel. Less material over this final reach was deposited at the steeper inclinations.
At slope angles of 15° and 20° large particles (20 and 25 mm) were found in all deposits at the free surface and an accumulation of fines was observed predominantly close to the flume outlet although this feature is not so evident and samples taken from different parts of the runout would have clarified this better. When comparing PSD_3 at 15° and 25° it can be seen that at 15° mainly large particles ($\geqq$ 15 mm) are accumulated at the deposit edges with the finer particles behind them while at 25°, diameters of 3 and 7.5 mm were also present at the coarse margin. The less visible segregation in the deposit is also confirmed by what was previously observed in the flowing body at 25°, i.e., the material was better mixed during motion and particles in the range $1 < d < 3$ mm were also present immediately after the flow front. Other PSDs at 25° appeared to have the same depositional segregation.

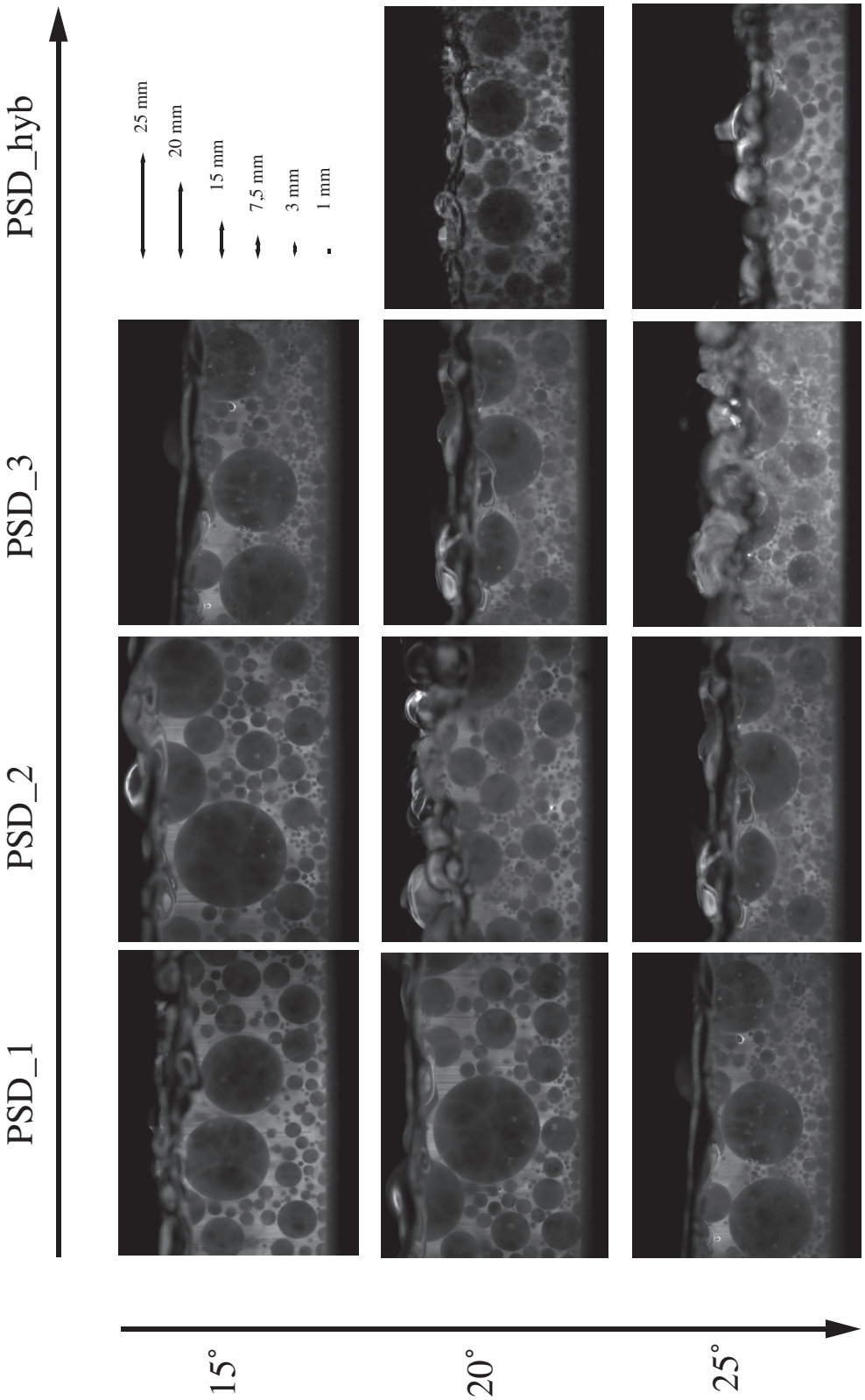

Figure 8.15: Internal flow images representing the same time after the front passed for the four particle size distributions at three slope angles.

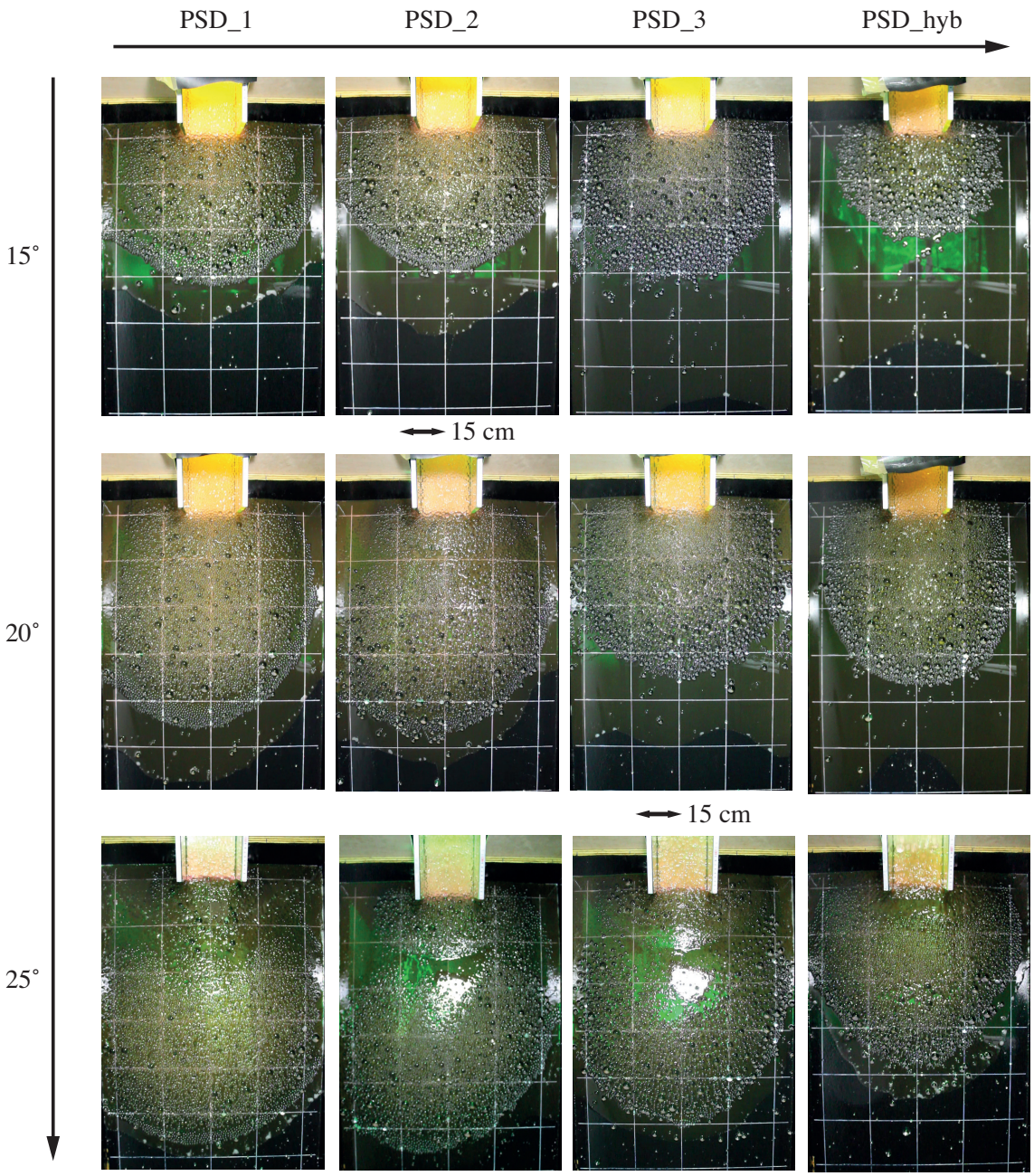

Figure 8.16: Deposit morphology of the polydisperse granular flows for the four particle size distributions at three slope angles.

8.7.2.4 Velocity profiles and runouts

The analyses presented here were obtained using PIV with interrogation areas 24x24 and 12x12, for coarse and refined grids, respectively. Depth-average velocities over time are plotted in Fig. 8.17 where the flows are aligned with respect to the arrival of the flow front ($t = 0$) while the grey lines represent monodisperse flows performed for runout comparisons. Velocity profiles were obtained by averaging over the body of the flows (i.e. avoiding the noisy front and the tail of the surge) for a duration of $t = 36$ (equivalently to ≈ 0.5 s). This time was set for equal comparison although it was difficult to define whether the flows reached a steady state, especially at 25°. The same time span within the almost plateaued values of velocity at different instants after the flow front were trialled but the results changed little.

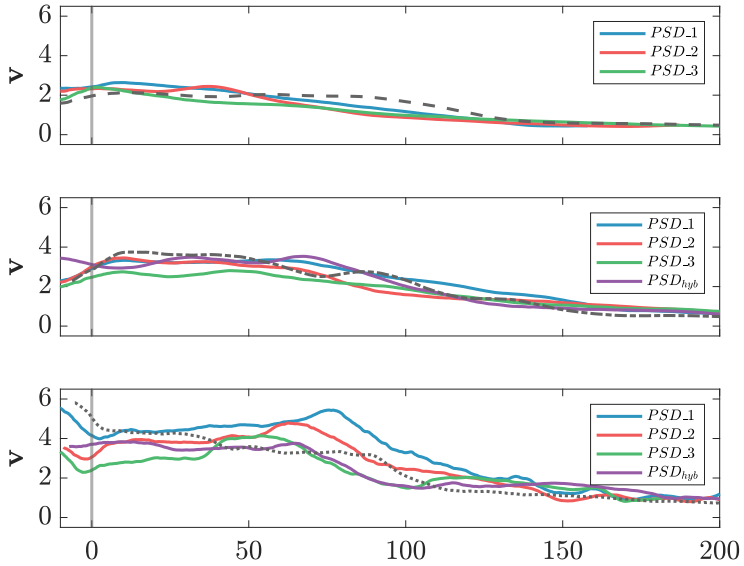

(a)

Figure 8.17: Depth-averaged velocity over time for the four particle size distributions at three slope angles. Monodisperse flows are shown with dashed (▪ ▪ ▪), dash-dotted (▪ · ▪) and dotted (▪ ▪ ▪ ▪) lines, respectively.

For the flows released at an inclination of 15°, velocity profiles are shown in Fig. 8.18(a). In all cases a slip velocity developed at the bottom boundary. PSD_1 and PSD_2 have similar flow heights and velocity magnitudes compared to PSD_3. PDS_{hyb} was not able to develop sufficient momentum which resulted in a thick layer of material being deposited

over the channel. Only a short recording was possible before the material stopped, which did not allow a velocity profile to be determined.
The profiles of the final deposit are shown in Fig 8.18(b). These were similar to each other for PSD_1, PSD_2 and PSD_3. If the velocities are compared to the runout lengths, some changes would be expected for the slower PDS_3. However, the length and shape of the spreads were very similar indicating that not enough inertial energy was induced into the system and that the material was progressively accumulating without showing characteristic depositional behaviour. This was different for PSD_{hyb}, possibly due to the increased frictional resistance provided by the angular fine particles leading to an even shorter runout.
To increase the energy in the system and produce different behaviours, the inclination needed to be increased. At 20° the flows showed intermediate behaviours between 15° and 25°. Velocity profiles reduced with increasing number of fine particles smaller than 1 and 1.18 mm (Fig. 8.18(c)) and similar deposit profiles were produced, i.e., PSD_1 and PSD_2 travel longer but the runout was almost identical as for PSD_3 and PSD_{hyb} (Fig. 8.18(d)). Focusing on flows released at 25°, velocity profiles obtained from the body of the flows are depicted in Fig. 8.18(e). Similarly to the flows at 15°, a distinct slip velocity was generated at the bottom boundary. For PSD_1, PSD_2 and PSD_3 the magnitudes of this quantity decreased progressively with an increasing amount of fines. PDS_{hyb} travelled slower than PSD_3 due to the increased friction. Note that the all profiles tend to reverse back at the free surface (i.e. with slower velocities than the middle part), which is unexpected for these flows, in which we would expect a maximum at the free surface. This was caused by the changing of the saturation line (also the limit for the PLIF technique). For these faster flows, occasional and local reduction of the saturation line is caused by the crossing of large particles transported at the free surface. These are interpreted by PIV as areas with lower velocities. Hence averaging results in an apparent reversing of the velocity profile at the top of the flow. This was also noticed when the average was made over shorter periods of time (e.g. for 30 or 50 frames only). The data reversing back at the top of the flows are depicted with dashed-lines in Fig. 8.18(a,c,e) and should also be considered with care.
The flows analysed at an inclination of 25° produced the depositional profiles shown in Fig. 8.18(f). For PSD_1 a large amount of fines segregated close to the bottom boundary. This resulted in larger particles dominating the mechanics during runout producing a slightly longer spread. Conversely, from the analysis of flow images for PSD_2 and PSD_3 it was clear that fine particles were more evenly distributed throughout the flow height. They have shorter and comparable runouts, with PSD_3 being somewhat longer. Again, PDS_{hyb} produced shortest runout due to the increased frictional resistance of fine angular particles.

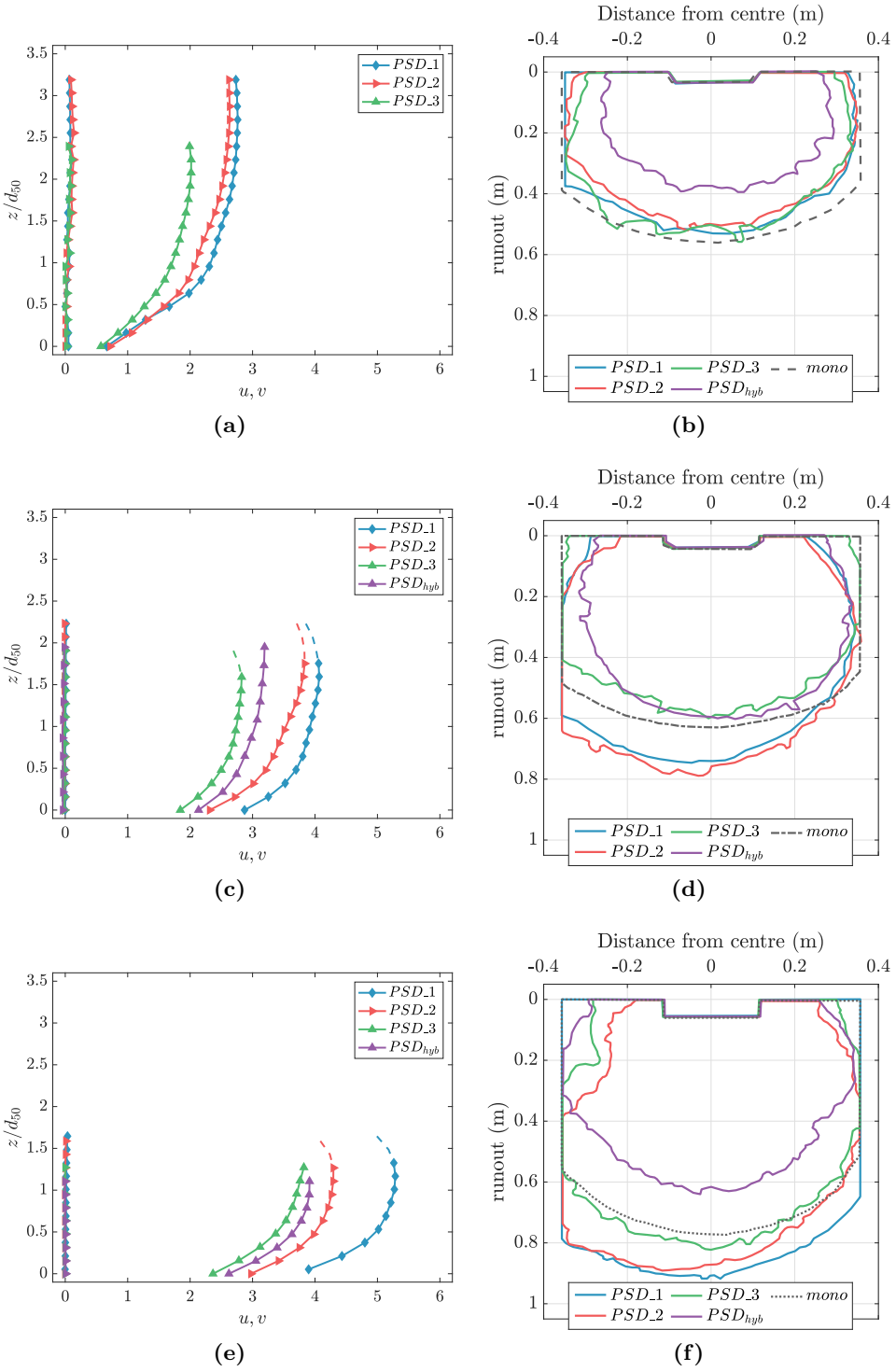

Figure 8.18: (**a**,**c**,**e**) Velocity profiles obtained in the body of the flows for an average time of $t = 36$ and (**b**,**d**,**f**) depositional runouts for the four particle size distributions at three slope angles. The data reversing back a the top of the flows are depicted with dashed-lines.

In the previous works by Bowman and Sanvitale [29], Sanvitale [142] it was found that for mixtures made of angular material at the same mean particle size (d_{50}), different coefficient of uniformity ($C_u = d_{60}/d_{10}$) and constant slope the most well-graded material (with the largest amount of fines and larger particles) had the greater runout distance and overall segregation during flow and deposition and the deposit had an elongated shape. Conversely, for more uniformly graded materials (with lower amount of fines) the runout was less and the deposit became progressively more pear-shaped. In the flows studied here, it has been tried to reproduce these effects with a different particle shape and approximating the particle size distributions with fewer diameters, however, increasing the amount of fine particles (1 mm for these three PSD_1,PSD_2 and PSD_3) considerably slowed the flows. Therefore, the expected changes of runout caused by adding fines to increase pore pressure (i.e. via accumulation of fines in the body and rear) did not occur, instead viscous and particle size segregation effects appeared to dominate.
The fine particles (1 mm) were expected to sustain pore pressure and influence the final deposition behaviour of solid-fluid mixtures. They can still be considered as fine materials, however a better material release mechanism should be considered since the controlled release used here to achieve steady state may have caused the flow behaviour to be fundamentally different from what was done in previous works [142, 144]. Contrary the experiments performed here, in these studies [142, 144] a full release of the material occurred for each test and the interplay between the less saturated, more resistive friction flow front and the dispersion behind it which shunts the front forward was observed.
Perhaps the display of different depositional behaviours could also be achieved by a more careful choice of the PSD compositions. For these tests, the amount of large particles available was limited while considerably increasing the amount of fines. That is, by just increasing the fines content only, additional viscous effects were induced. In addition, large step changes in the specific particle sizes (e.g. beyond Terzaghi's filter limit [157]) may have enabled particle size segregation to spontaneously occur at the commencement of the flows.
Further analyses should be performed based on these experimental flows to further explore the relationship between the square of the front velocity and the runout length [29, 76] and the relationship between the coefficient of uniformity C_u and the the runout length [29]. However, the first relationship (front velocity squared versus runout length) could not be applied to the results of this chapter since it was difficult to reliably obtain a front velocity due to the controlled flow release adopted to improve the flow visualization.

8.8 Conclusion

The results of small scale flume tests consisting of monodisperse and polydisperse granular flows have been presented in this chapter. These were obtained using a non-intrusive technique called planar-laser induce fluorescence (PLIF) that allowed internal imaging of the flows. Modifications in the original apparatus design, a new laser sheet generation system and use of spherical shaped particles were used to improve the quality of internal visualization, however, this came at the cost of altering important characteristics observed in real debris flows.

Mixtures of fluid and monodisperse 3 mm particles were investigate in the framework of kinetic theory. Velocity and granular temperature profiles were in agreement with the results of previous numerical simulations (Ch. 5) in a dry condition and away from the sidewall. The velocity had a Bagnold-like profile and the granular temperature was higher close to the bottom rough base when an appropriate sampling interval Δt was used. Solid concentration was estimated and the profiles of particle pressure calculated. With the information obtained, the experimental results were tested against the prediction of kinetic theory. While the data followed the theoretical curve at least qualitatively, the theory underestimated the data. Granular temperature and solid concentration were affected by the particle image brightness pattern (although this could be minimized with a correct choice of Δt) and undetected small particles entering the laser plane, respectively. Further investigations are required to verify and improve the acquisition of flow properties which may lead to a better agreement with the theory.

Polydisperse granular flows characterized by different particle size distributions and particle shapes were also investigated. While the optical performance of the non-intrusive technique was improved, some of the characteristics commonly seen in these types of granular flows were not observed. Velocity profiles obtained in the body of the flows were similar in shape but with a difference in velocity magnitude depending on the amount of fines and the angularity of the particles in one case. Depositional runouts between flows were similar at low inclinations when little internal energy was supplemented to the system. The results were in contrast with previous works done in small experimental setups with angular materials [29, 142, 144] and full surge behaviour was allowed to develop where the depositional features of real debris flows were successfully recreated. Further investigation needs to be done to find the correct approach for better internal flow visualization without altering the characteristics of real granular flows.

9. Conclusions and outlook

This thesis has focused on the investigation of granular flows down inclined chute geometries, with specific attention to the application related to the modelling of debris flows.

Efforts have been made in the last decades to formulate mathematical models that capture the complex behaviour of granular flows. One of the models that has become increasingly popular is the kinetic theory of granular flows. This theory is part of the current research that focuses on incorporating microscale particle interactions into constitutive modelling. Specifically, the effect induced by particle collisional interactions to the flow dynamics is related in this theory to the concept of granular temperature, a measurable variable upon which the constitutive behaviour of flowing granular material can depend. The research and development into this model is on-going and there is a strong need for experimental and numerical data in order to verify the model and to better understand granular flows, more generally. In this respect, the present thesis has provided new insight into the complex mechanics of dry granular flows and also a variety of measurements that were used to test the predictions of kinetic theory. Ultimately, the work undertaken for this thesis in dry conditions was designed to verify if current approaches based on experiments, numerical simulations and theoretical work could find common agreement.

The same three approaches can be used to study solid-fluid mixtures and gradually increase the complexity of the investigations. However, in this thesis only the experimental part was undertaken, thus adding to the few studies [11, 18, 19, 145] that have experimentally focussed on granular-liquid mixtures in the context of kinetic theory. The investigations presented in this work require further work before claiming that they are sufficiently accurate to be compared to predictions from kinetic theory and discrete numerical simulations, which are in turn challenging to obtain and formulate due to complex solid-fluid interactions. The work started in this thesis does require further improvements but promises to provide a good basis to step away from dry and monodiperse situations and more closely approximate the mechanics of real debris flows, thus leading to new insight into their essential understanding.

The work performed can be categorized into two main sections: the study of simple dry monodisperse granular flows via experimental, numerical and theoretical approaches

and an experimental study of solid-fluid mixtures used to better match the traditional characteristics of debris flows. An overview of the accomplished research work and a brief summary of the major findings are given below.

1. Dry conditions:

   - Experimental results:

     Upon a review of the literature, it was found that PTV lacked an error framework that could be *a priori* applied to remove potential errors affecting measurements of granular flows. For this technique, two main errors were described and analysed, those associated with the particle centroid estimates and those with the particle acceleration. It has been found that the former is reduced for particle image diameters of approximately three pixels or greater (for monodisperse granular flows). The latter requires an appropriate choice of the sampling interval (or frame rate). Indeed, there should be a frequency of acquisition where the aforementioned errors are minimized. A simple simulation of a circular motion was used to help in choosing a most appropriate sampling interval. Notably, high frame rate can greatly worsen velocity errors and compromise the results. The influence of these observations were examined in experiments on dry monodisperse granular flows down an inclined geometry. Measurements of PTV were compared to the result of PIV where also the method proposed by Reynolds et al. [137] to measure granular temperature was used. The results of mean velocity were well matched by the two techniques, which allowed the two algorithms to be cross-validated, at least in terms of this quantity. Conversely, rather different profiles of granular temperature where obtained between the two methods. It has been shown how the choice of the sampling interval, or frame rate, affects both the magnitude of granular temperature and the profile shape determined in the case of PTV. In addition, the determined magnitudes of granular temperature from PIV tends to be considerably lower when directly measured or largely overestimated when theoretically scaled than those of PTV for the same tests, though the shape of the profiles is less sensitive to frame rate.

     To further verify these observations, a validation of PIV and PTV for the measurement of granular temperature was undertaken based on synthetic images created from numerical simulations. It has been shown that, with the appropriate choice of sampling intervals (which do not give the true value but a good approximation of it), PTV is a more reliable technique for the measurement of this quantity, at least for the spherical particle flows investigated in this thesis.

It has been confirmed that very fast sampling intervals (or high frame rate) generate measurements that are indeed dominated by noise. Conversely, PIV results of granular temperature were highly variably and were not able to match the shape and magnitude of the numerical values.

Further dry monodisperse granular flows were investigated with PTV considering the previous findings in terms of error removal. Measurements taken at the sidewall showed that the velocity changed almost linearly with depth and the magnitude increased for steeper slope angles. Solid concentration profiles showed as, near to the bottom the the magnitude of this quantity was close to the random close packing while the flows became more diluted at some distance from the bottom boundary. Granular temperature increased with progressively steeper slope angles and showed a variability from bottom to the free surface that could be related to changes of solid volumetric concentration. With the profiles of particle pressure extracted from the values of solid concentration and granular temperature, it was possible to test the predictions of extended kinetic theory in terms of dimensionless pressure. Good agreement was found in the limit of validity of the solid concentration estimation, supporting the fact that kinetic energy can be used to model such flows.

- Numerical results:

  Discrete element method (DEM) simulations of steady and fully-developed, inclined flows of inelastic, monosized spheres were performed over bumpy bases in the absence (i.e., in a small cells with periodic boundaries everywhere but at the direction normal to the bed) and in the presence of flat, frictional sidewalls (i.e. chute flows). The findings of similar works found in the literature were confirmed by the simulations performed in a periodic cell. Conversely, only few studies [70, 172] have focused on chute flows over a bumpy base. The chute flow configuration used in the simulation was designed to represent the experiments setup. In the middle of the channel the behaviour was similar to that observed in absence of sidewalls. Disregarding the measurements two diameters away from flat, rigid boundaries due to the erroneous interpretation of the coarse-graining procedure, close to the sidewalls velocity profiles were linear and granular temperature was less and varied almost linearly with depth compared to the middle cross section. For one flow, the matching of the numerical data with the experimental results were obtained by introducing rolling resistance which led to a good agreement of the different calculated flow properties between the two approaches.

  The results of DEM simulations were coarse-grained and it was confirmed that

there is a scale-dependency of the stresses that can be removed if the smoothing length in the coarse-graining is taken to be one tenth of the particle diameter (other suggestions from the literature to remove the scale-dependency did not work). After the removal of the scale-dependency from the simulations, the constitutive relation for the pressure of kinetic theory was in excellent agreement with the numerical results, but for a region of a few diameters close to the bumpy base where the particle-boundary collisions affect the radial distribution function at contact g_0. This specific function, as is yet not known in proximity of a solid boundary and future works devoted to address, this aspect of the research may be used to improve the prediction and obtain a better agreement.

- Theoretical results:

  Using the results of DEM simulations, and experiments of bead flows, comparisons were made with the predictions of extended kinetic theory (EKT).

  In the case of numerical simulations, the constitutive relations of EKT and momentum and energy balances were transformed into a set of differential equations that were then solved numerically to find distributions of stresses, velocity, solid volume fraction and granular temperature. Analytical solutions were also obtained for the assumptions of incompressibility and algebraic balance between the work of the shear stress and the energy dissipated in collisions. From this work, it is suggested that the most crucial consequence of an incorrect choice of g_0 in the proximity of the boundary is a substantial underestimation by EKT of the range of angles of inclination of the base for which steady and fully-developed flows are possible. It has also been found that the current state of the art of the boundary conditions for kinetic theory applied at a bumpy bottom underestimates the energy dissipation there. Besides the above mentioned limitations that need to be addressed in future works, extended kinetic theory (even its incompressible, algebraic approximation) agreed well with the DEM results in the absence of sidewalls (i.e. one-dimensional flow).

  It has been demonstrated though, as previously suggested, that the spanwise averaged ratio of shear stress to pressure linearly decreases with the distance from the free surface, in accordance with the approximation of considering the sidewalls as providing a Coulomb-like resistance to the flow. The effective Coulomb friction coefficient was found to be less than half the actual value of the friction coefficient of the particles with the flat wall. Using this effective friction coefficient allowed extended kinetic theory to agree with the DEM results, even in the presence of the sidewalls.

  While a good agreement with the simulations was shown, the disagreement

found when the theory was compared to an experimental flow, which was successfully matched by the DEM simulation by introducing an additional rolling resistance, demonstrates that kinetic theory is still not able to reproduce some fundamental physics involved in simple and real experimental granular flows.

2. Saturated conditions:

- Experimental results:

  Only the experimental approach was used for solid-fluid mixtures. Flows visualization via plane-laser induced florescence (PLIF) required specific modifications to improve the image quality and allow the tracking of the particles in case of monodisperse saturated systems. The specific goal set to test the prediction of the kinetic theory showed that only some results were in agreement with previous findings of this thesis under dry conditions. Velocities had a Bagnold-like profile and granular temperatures were higher close to the bottom rough base before attaining an almost linear profile over depth. Solid concentration profiles were estimated and the granular pressure calculated. With the information obtained, it was possible to test the prediction of kinetic theory in terms of dimensionless pressure. The experimental results followed the theory at least qualitatively, however the theory underestimated the data. Better accuracy in the measurements of solid concentration and granular temperature should be considered. Extracting accurate particle properties from solid-liquid mixtures were more challenging than the flows performed in dry conditions. Data processing can be improved and future work specifically focussed on such flows might generate better results and find agreement with such theory.

  Polydisperse granular flows made of few, but distinctly different, particle diameters were performed in order to increase a step further the complexity of the investigations. The results of depositional runout were unexpected although these were connected to the choice made to achieve a better visualization of the flows. Particle size distributions (PSD) made of spherical particles only or a combinations of spherical and angular fine particles were used. Perhaps the display of different depositional behaviours could be achieved by a more careful choice of the PSD compositions, especially in the upper part of the distributions (i.e., particle $\gtrapprox$ 20 mm). In addition, in previous works [142, 144], which were able to reproduce characteristic debris flow behaviours (e.g. the segregation of particle at the front), a full release of the material from the hopper was performed. Conversely, the controlled released used here to achieve steady state may have caused the flow behaviour to be fundamentally different. More work

needs to be done to find a balance between flow visualization, experimental apparatus and the generation of appropriate mechanics characteristic of real debris flows.

9.1 Recommendations for future work

The following topics for potential future work were established:

- Steady dry granular flows over long period of time were limited due the small size of the apparatus. Longer flow duration can be achieved using a conveyor-like system that recirculates the material. The advantages are: experiments can be better represented by DEM simulations with steam-wise period boundaries and methods for *a posteriori* correction of granular temperature (e.g., [10]) can be used in addition to the error framework for PTV developed in this thesis.

- There are methods, e.g. [55, 67, 108, 118], that can be used to obtain better estimation of ceramic bead properties, such as coefficient of restitution, inter-particle friction, particle-wall friction and also alternative methods, e.g. [38], for an estimation of the particle shape anisotropicity. This will provide better parameters to be used in numerical simulations.

- When PTV is used for the analyses, a further minimization of the errors could be achieved by dividing the flow in different regions. In each of these, a different frame rate can be used (by isolating and skipping frame only in that specific region), which will results in a reduction of the error caused by the linear approximation of the particle trajectory.

- The validation of PIV and PTV was based on synthetic images without adding noise. Different levels of Gaussian white noise can be added after the images have been generated using the Matlab function "imnoise". More realistic illumination conditions can be recreated and the ability of centroid estimation method for PTV further tested. In addition, for dry flows of ceramic beads and PTV, the same synthetic images can be used to test the limits and verify the calibration parameters for the solid concentration estimations based on the method of Capart et al. [36].

- The study of the radial distribution function at the boundaries could be investigated experimentally rather than using the convectional numerical simulation approach. To overcome the opacity of the flow, transparent mixture of oil and glass bead can be used a first approach to study simple flows in enclosed configurations (shear box

or shear cell, e.g. [125] in fully saturation), thus avoiding the entrainment of air and any interference of the saturation line.

- In the simulation of dry granular flows, rolling friction was used to match the experimental results. The use of only one representative value of rolling friction for all particles lends a relatively high degree of artificiality. However, in reality some contacts will be flat-convex, others convex-convex etc., thus having different resistance to rolling. For more realistic simulations, using the DEM code employed in this thesis, particles can be grouped into "species" with different rolling friction angle. Comparison can then again be made with the experimental results to verify the realism of this numerical approach.

- The series of experiments carried out with spherical glass beads and fluid represent the early stages of debris flow testing with an improved image visualization. However, the results of deposition runouts were unexpected and the consequence of using spherical particle should be an important lesson for future applications in small scale flume modelling. The use of spherical particles requires further attention, testing should be undertaken with more well-graded particle size distributions and the influence of less volume released should also be verified.

Appendices

A Kinetic energy and expected value for bead flows

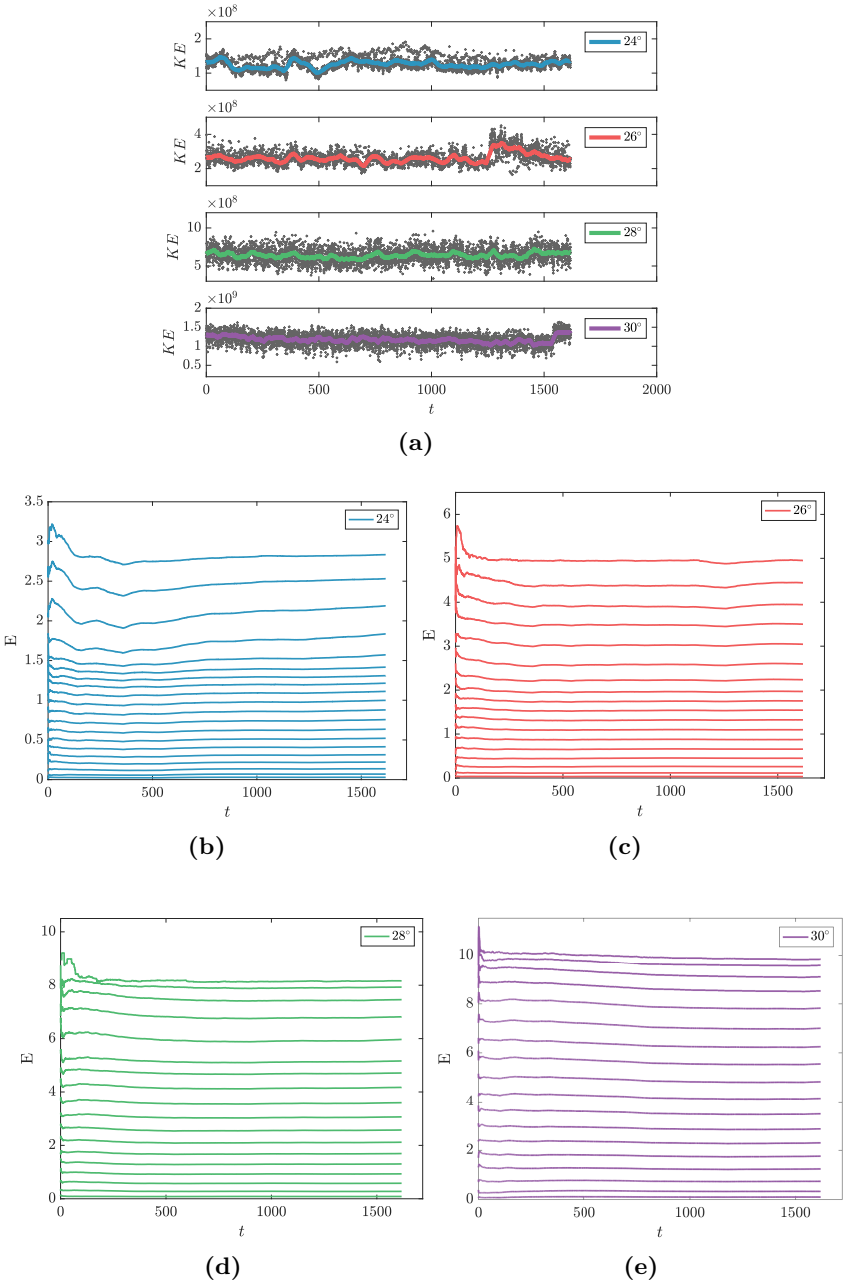

Figure A.1: (**a**) Kinetic energy of all velocity data at each time step and the expected value (i.e. the long time average velocity) for each bin (e.g., see Fig. 4.4) over time. Measurements refer to a collections of 10 bead flow tests (i.e., $0 < t < 162x10$) at each inclination with $\Delta t = 0.32$ for 24° (**b**), 26° (**c**), 28° (**d**) and $\Delta t = 0.24$ for 30° (**e**), respectively.

B Kinetic energy and expected value for monodisperse saturated flows

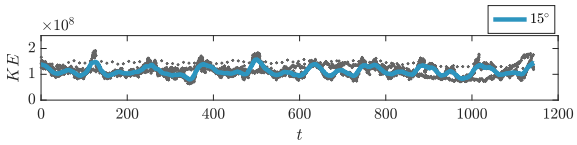

(a)

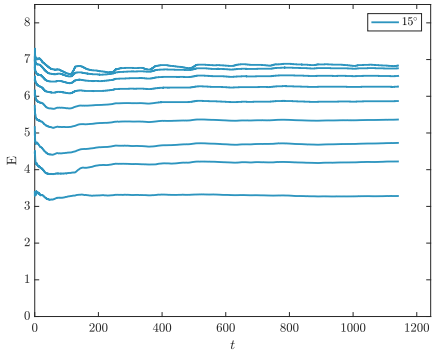

(b)

Figure B.1: (**a**) Kinetic energy of all velocity data at each time step and the expected value (i.e. the long time average velocity) for each bin over time. Measurements refer to a collection of 10 monodisperse saturated flow tests (i.e., $0 < t < 114x10$) at an inclination of 15° (**b**) with $\Delta t = 0.22$

C Comparison of chute flows results between simulations and experiments for all angles of inclination

C.1 Angle of inclination: 24°

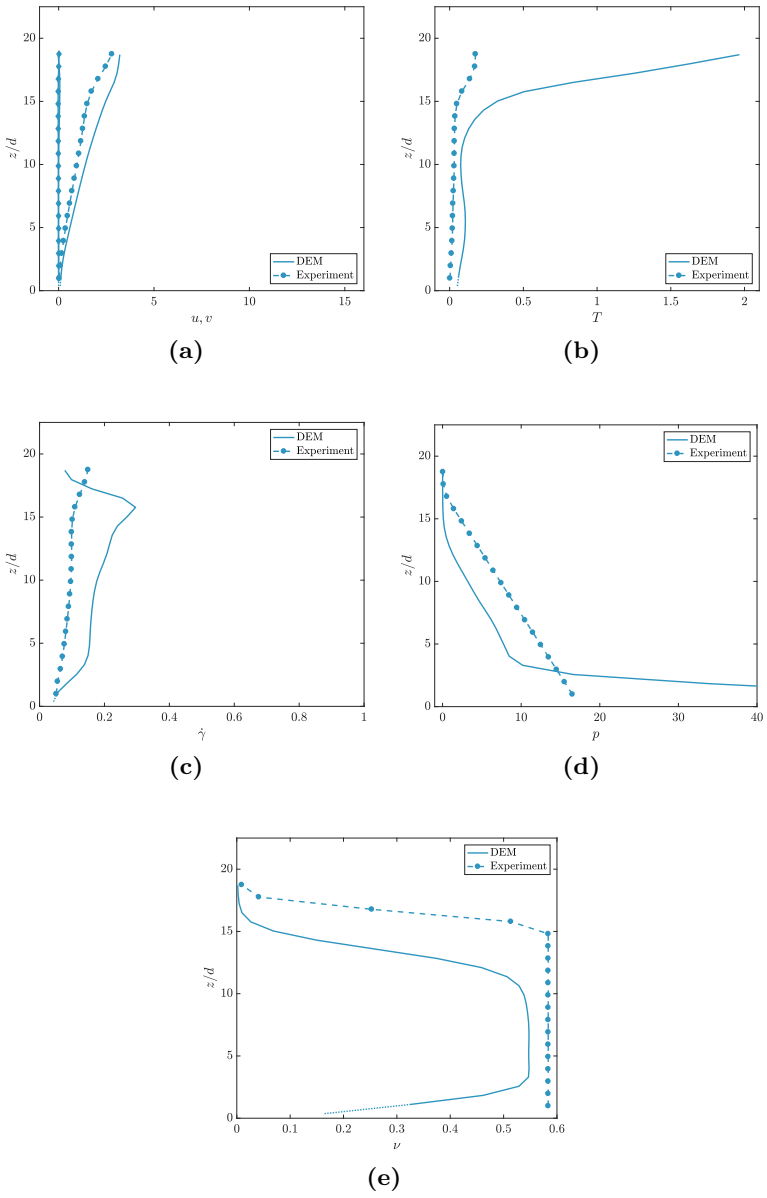

Figure C.1: Comparison between experimental measurements (dashed-line with symbols) and numerical results (solid lines) with rolling friction ($\mu_r = 0.2$) for the flow at 24°: velocity (**a**), granular temperature (**b**), shear rate (**c**), pressure (**d**), solid concentration (**e**).

C.2 Angle of inclination: 28°

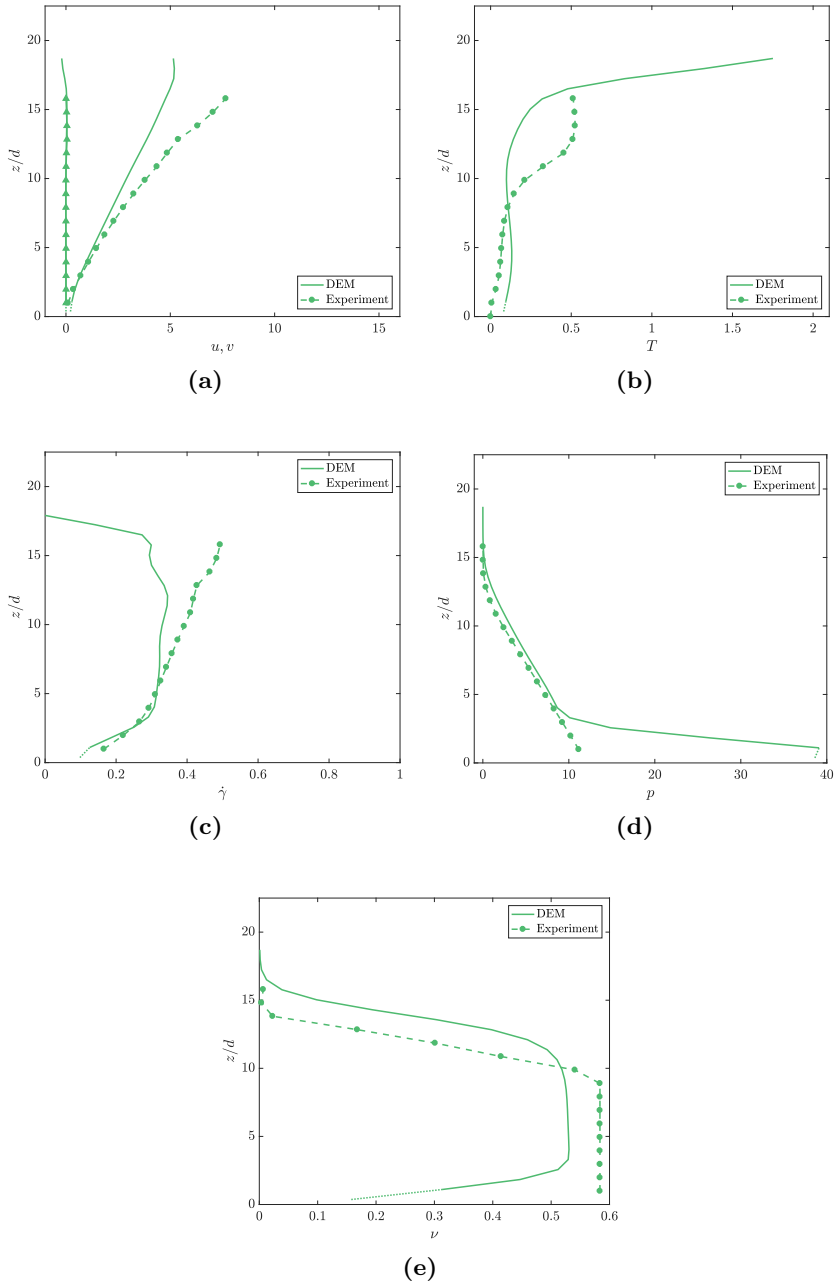

Figure C.2: Comparison between experimental measurements (dashed-line with symbols) and numerical results (solid lines) with rolling friction ($\mu_r = 0.2$) for the flow at 28°: velocity (**a**), granular temperature (**b**), shear rate (**c**), pressure (**d**), solid concentration (**e**).

C.3 Angle of inclination: 30°

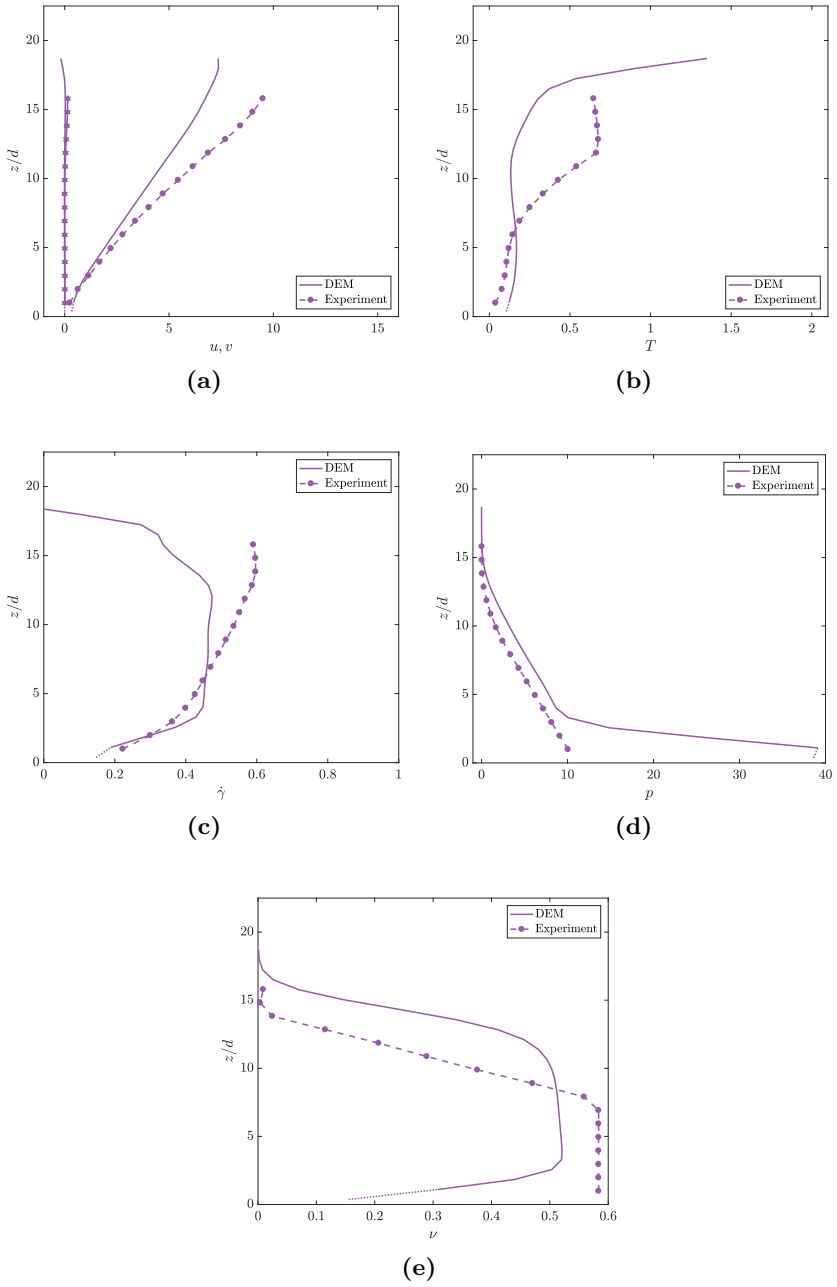

Figure C.3: Comparison between experimental measurements (dashed-line with symbols) and numerical results (solid lines) with rolling friction ($\mu_r = 0.2$) for the flow at 30°: velocity (**a**), granular temperature (**b**), shear rate (**c**), pressure (**d**), solid concentration (**e**).

D Testing the prediction of extended kinetic theory in the absence of sidewalls

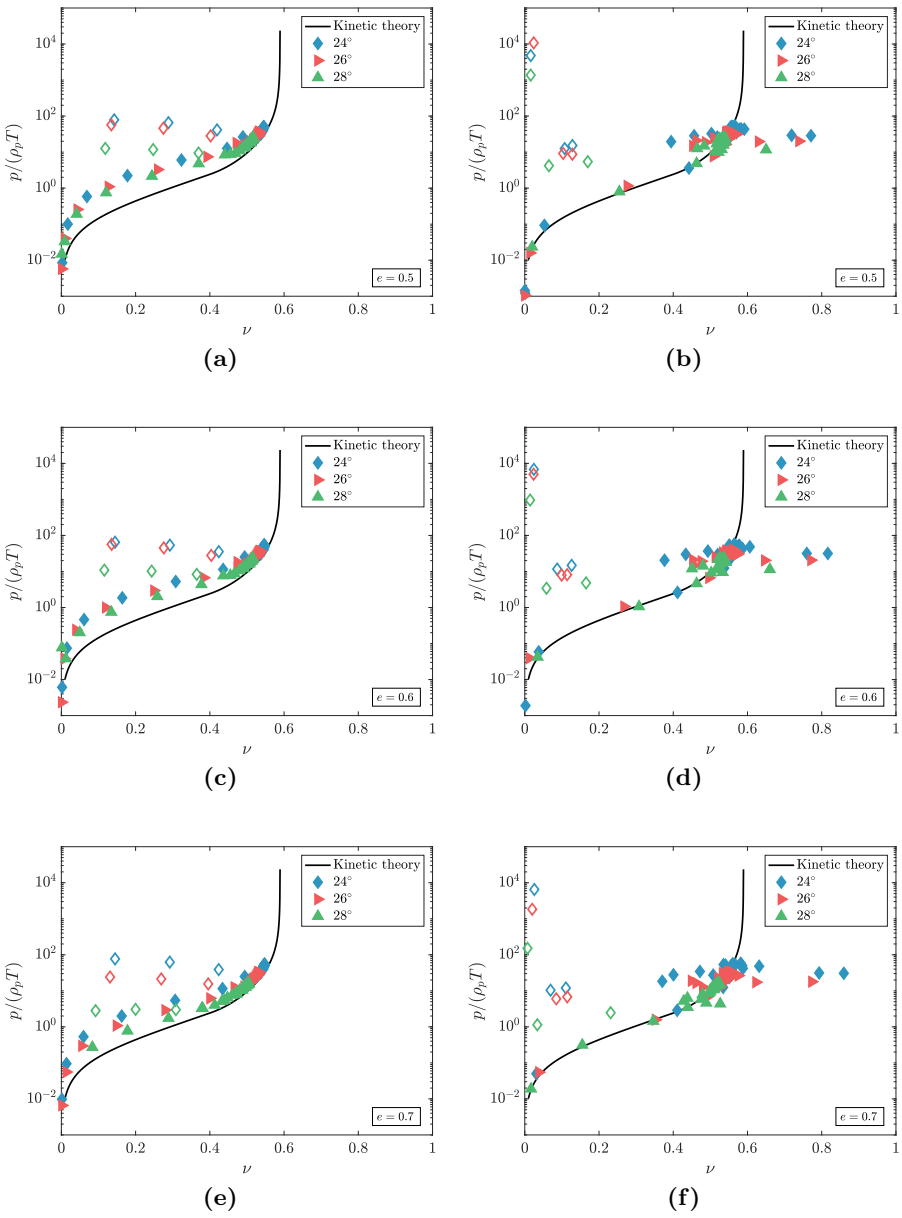

Figure D.1: Dimensionless pressure $p/(\rho_p T)$ against the solid volume fraction measured in the DEM simulations in the absence of sidewalls with smoothing lengths of $w = 1$ (**a**,**c**,**e**) and $w = 0.1$ (**b**,**d**,**f**), respectively. Empty symbols indicate DEM results referring to a region within three particle diameters from the base. Theoretical predictions of kinetic theory (solid line) obtained from Eq. 2.35.

E Comparison of EKT predictions and DEM results obtained with coarse-graining width $w = 0.1$

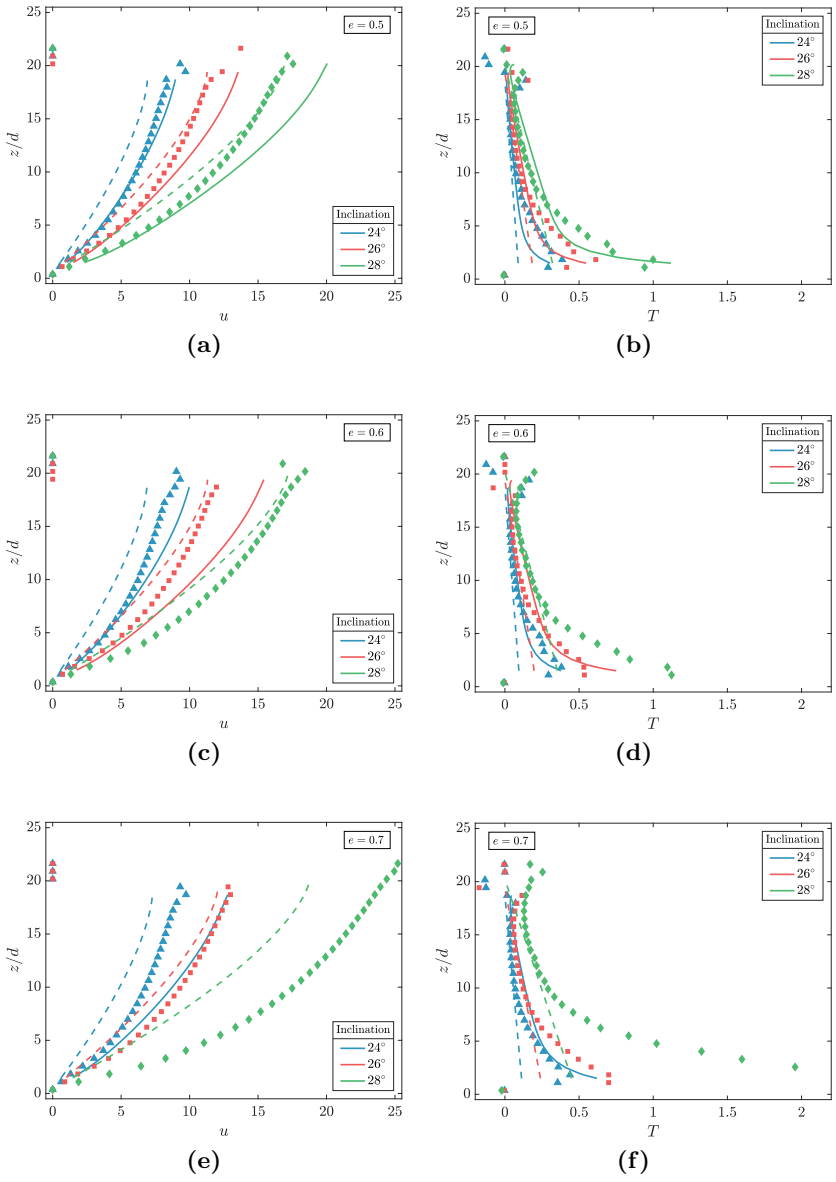

Figure E.1: Numerical (symbols) profiles of (**a**,**c**,**e**) dimensionless particle velocity and (**b**,**d**,**f**) dimensionless granular temperature obtained from DEM simulations of inclined flows in the absence of sidewalls for different value of e, $\mu = 0.45$ and $\theta = 24°$ (triangles), $\theta = 26°$ (squares) and $\theta = 28°$ (diamonds). Coarse-graining width $w = 0.1$. Solid and dashed lines represent the results of the numerical integration of the full system of differential equations of EKT and its incompressible, algebraic approximation, respectively.

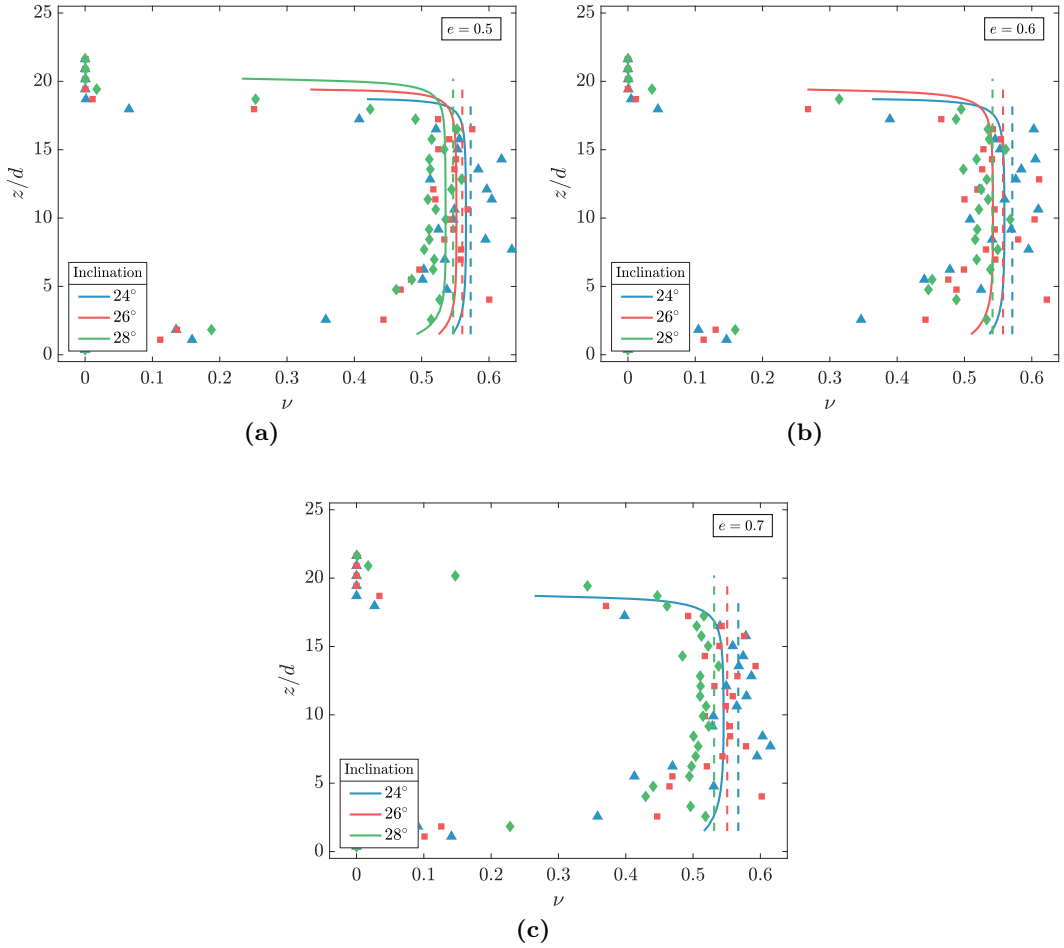

Figure E.2: Numerical (symbols) profiles of solid concentration obtained from DEM simulations of inclined flows in the absence of sidewalls for different value of e, $\mu = 0.45$ and $\theta = 24°$ (triangles), $\theta = 26°$ (squares) and $\theta = 28°$ (diamonds). Coarse-graining width $w = 0.1$. Solid and dashed lines represent the results of the numerical integration of the full system of differential equations of EKT and its incompressible, algebraic approximation, respectively.

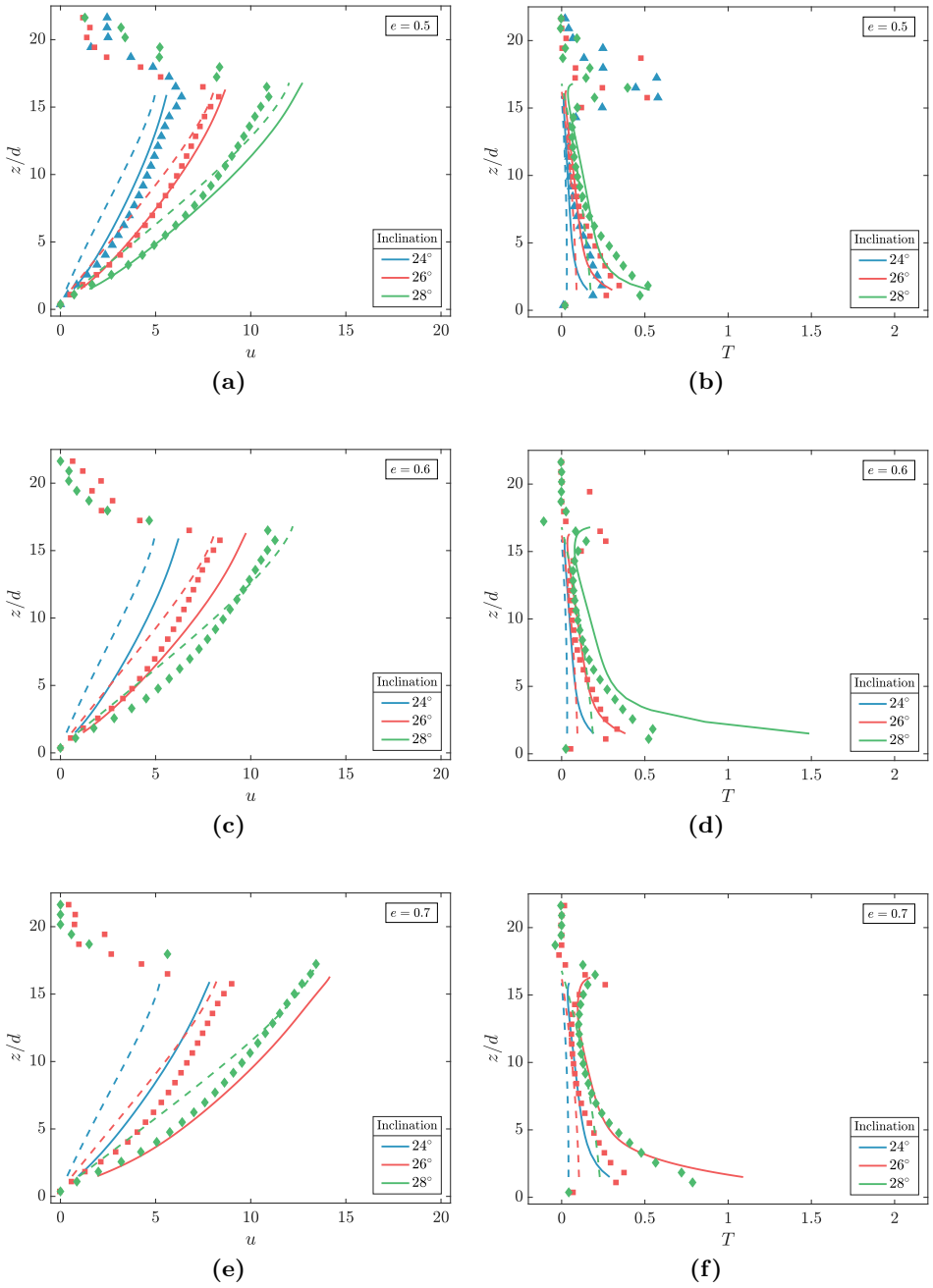

Figure E.3: Numerical (symbols) profiles of (**a**,**c**,**e**) dimensionless particle velocity and (**b**,**d**,**f**) dimensionless granular temperature obtained from DEM simulations of inclined flows in the presence of sidewalls for different value of e, $\mu = 0.45$ and $\theta = 24°$ (triangles), $\theta = 26°$ (squares) and $\theta = 28°$ (diamonds). Coarse-graining width $w = 0.1$. Solid and dashed lines represent the results of the numerical integration of the full system of differential equations of EKT and its incompressible, algebraic approximation, respectively.

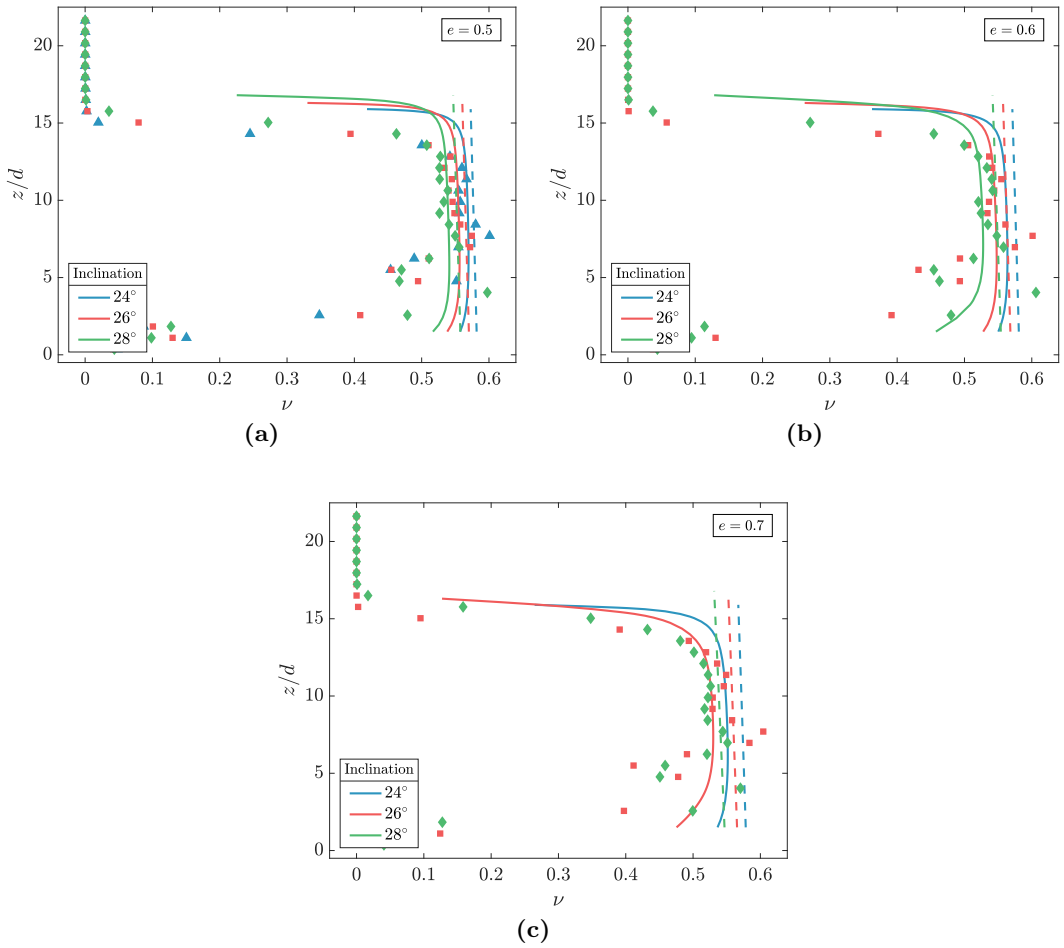

Figure E.4: Numerical (symbols) profiles of solid concentration obtained from DEM simulations of inclined flows in the presence of sidewalls for different value of e, $\mu = 0.45$ and $\theta = 24°$ (triangles), $\theta = 26°$ (squares) and $\theta = 28°$ (diamonds). Coarse-graining width $w = 0.1$. Solid and dashed lines represent the results of the numerical integration of the full system of differential equations of EKT and its incompressible, algebraic approximation, respectively.

F Pre-processing of saturated granular flow images in Matlab

This code is a simple pre-processing step used to improve the image quality of the saturated monodisperse granular flows studied in this thesis. The code requires to input the path of the image. Once the image is read and stored, the pixel intensity is evenly distributed with a logarithmic-stretching transformation followed by morphological image adjustments ("imcomplement" should be applied only if necessary) and background subtraction.

```
% User input
filepath = 'User input';

% Read image
I = imread(filepath);
% Logarithmic-stretching transformation
I = mat2gray(log(1+double(I)));
% Invert the gray scale (if necessary)
I = imcomplement(I);
% Image opening
se = strel('disk',1);
I = imopen(I,se);
% Background subtraction
background = imopen(I,strel('disk',10));
I = imsubtract(I,background);
```

Bibliography

[1] Adrian, R. (1991). Particle-imaging techniques for experimental fluid mechanics. *Annual Review of Fluid Mechanics*, 23(1):261–304.

[2] Adrian, R. and Westerweel, J. (2011). *Particle Image Velocimetry*. Cambridge Aerospace Series. Cambridge University Press.

[3] Ahn, H., Brennen, C. E., and Sabersky, R. H. (1991). Measurements of velocity, velocity fluctuation, density, and stresses in chute flows of granular materials. *Journal of Applied Mechanics*, 58:792–803.

[4] Ai, J., Chen, J.-F., Rotter, J. M., and Ooi, J. Y. (2011). Assessment of rolling resistance models in discrete element simulations. *Powder Technology*, 206(3):269 – 282.

[5] Ancey, C. (2002). Dry granular flows down an inclined channel: experimental investigations on the frictional-collisional regime. *Physical Review E*, 65(1):011304.

[6] Ancey, C., Andreini, N., and Epely-Chauvin, G. (2013). Granular suspension avalanches. I. macro-viscous behavior. *Physics of Fluids*, 25(3):033301.

[7] Ancey, C., Coussot, P., and Evesque, P. (1999). A theoretical framework for granular suspensions in a steady simple shear flow. *Journal of Rheology*, 43(6):1673–1699.

[8] Andreotti, B., Forterre, Y., and Pouliquen, O. (2012). *Granular Media: Between Fluid and Solid*. Cambridge University Press, Cambridge.

[9] Aranson, I. S. and Tsimring, L. S. (2006). Patterns and collective behavior in granular media: Theoretical concepts. *Rev. Mod. Phys.*, 78:641–692.

[10] Armanini, A., Capart, H., Fraccarollo, L., and Larcher, M. (2005). Rheological stratification in experimental free-surface flows of granularliquid mixtures. *Journal of Fluid Mechanics*, 532:269–319.

[11] Armanini, A., Larcher, M., Nucci, E., and Dumbser, M. (2014). Submerged granular channel flows driven by gravity. *Advances in Water Resources*, 63:1–10.

[12] Artoni, R. and Richard, P. (2015). Average balance equations, scale dependence, and energy cascade for granular materials. *Phys. Rev. E*, 91:032202.

[13] Aussillous, P., Chauchat, J., Pailha, M., Mdale, M., and Guazzelli, . (2013). Investigation of the mobile granular layer in bedload transport by laminar shearing flows. *Journal of Fluid Mechanics*, 736:594615.

[14] Azanza, E., Chevoir, F., and Moucheront, P. (1999). Experimental study of collisional granular flows down an inclined plane. *Journal of Fluid Mechanics*, 400:199–227.

[15] Bagnold, R. A. (1954). Experiments on a gravity-free dispersion of large solid spheres in a newtonian fluid under shear. *Proceedings of the Royal Society of London A: Mathematical, Physical and Engineering Sciences*, 225(1160):49–63.

[16] Ballard, D. H. and Brown, C. M. (1982). *Computer Vision*. Prentice Hall Professional Technical Reference, 1st edition.

[17] Berzi, D. (2014). Extended kinetic theory applied to dense, granular, simple shear flows. *Acta Mechanica*, 225(8):2191–2198.

[18] Berzi, D. and Fraccarollo, L. (2015). Turbulence locality and granular-like fluid shear viscosity in collisional suspensions. *Phys. Rev. Lett.*, 115:194501.

[19] Berzi, D. and Jenkins, J. T. (2008). A theoretical analysis of free-surface flows of saturated granular-liquid mixtures. *Journal of Fluid Mechanics*, 608:393–410.

[20] Berzi, D. and Jenkins, J. T. (2011). Surface flows of inelastic spheres. *Physics of Fluids*, 23(1):013303.

[21] Berzi, D. and Jenkins, J. T. (2015). Steady shearing flows of deformable, inelastic spheres. *Soft Matter*, 11:4799–4808.

[22] Berzi, D., Jenkins, J. T., Di Prisco, C., Magnanimo, V., and Luding, S. (2015). Lecture notes distributed in the doctoral course: Granular matter - from packing to flow.

[23] Berzi, D., Jenkins, J. T., and Larcher, M. (2010). Debris flows: Recent advances in experiments and modeling. In Dmowska, R., editor, *Advances in Geophysics*, volume 52 of *Advances in Geophysics*, pages 103–138. Elsevier.

[24] Berzi, D. and Vescovi, D. (2015). Different singularities in the functions of extended kinetic theory at the origin of the yield stress in granular flows. *Physics of Fluids*, 27(1):013302.

[25] Berzi, D. and Vescovi, D. (2016). Shearing flows of frictionless spheres over bumpy planes: slip velocity. *Computational Particle Mechanics*, pages 1–5.

[26] Bi, W., Delannay, R., Richard, P., Taberlet, N., and Valance, A. (2005). Two-and three-dimensional confined granular chute flows: experimental and numerical results. *Journal of Physics: Condensed Matter*, 17(24):S2457.

[27] Bi, W., Delannay, R., Richard, P., and Valance, A. (2006). Experimental study of two-dimensional, monodisperse, frictional-collisional granular flows down an inclined chute. *Physics of Fluids*, 18(12):123302.

[28] Boltzmann, L. (1872). Weitere studien über das wärmegleichgewicht unter gasmolekülen. *Wiener Berichte*, 66:275–370.

[29] Bowman, E. and Sanvitale, N. (2009). The role of particle size in the flow behaviour of saturated granular materials. 17th International Conference on Soil Mechanics and Geotechnical Engineering.

[30] Bowman, E. T., Laue, J., Imre, B., and Springman, S. M. (2010). Experimental modelling of debris flow behaviour using a geotechnical centrifuge. *Canadian Geotechnical Journal*, 47(7):742–762.

[31] Brevis, W. and García-Villalba, M. (2011). Shallow-flow visualization analysis by proper orthogonal decomposition. *Journal of Hydraulic Research*, 49(5):586–594.

[32] Brevis, W., Niño, Y., and Jirka, G. H. (2011). Integrating cross-correlation and relaxation algorithms for particle tracking velocimetry. *Experiments in Fluids*, 50(1):135–147.

[33] Brodu, N., Delannay, R., Valance, A., and Richard, P. (2015). New patterns in high-speed granular flows. *Journal of Fluid Mechanics*, 769:218228.

[34] Brodu, N., Richard, P., and Delannay, R. (2013). Shallow granular flows down flat frictional channels: Steady flows and longitudinal vortices. *Phys. Rev. E*, 87:022202.

[35] Campbell, C. S. (2006). Granular material flows - An overview. *Powder Technology*, 162(3):208 – 229.

[36] Capart, H., Young, D. L., and Zech, Y. (2002). Voronoï imaging methods for the measurement of granular flows. *Experiments in Fluids*, 32(1):121–135.

[37] Carnahan, N. F. and Starling, K. E. (1969). Equation of state for non-attracting rigid spheres. *The Journal of Chemical Physics*, 51(2):635–636.

[38] Cavarretta, I., O. C. and Coop, M. (2009). Applying 2D shape analysis techniques to granular materials with 3D particle geometries. *6th International Conference on the Micromechanics of Granular Media, 2009-07-13 - 2009-07-17, Golden, CO.*

[39] Chapman, S. (1916a). The kinetic theory of simple and composite monatomic gases: Viscosity, thermal conduction, and diffusion. *Proceedings of the Royal Society of London A: Mathematical, Physical and Engineering Sciences*, 93(646):1–20.

[40] Chapman, S. (1916b). On the law of distribution of molecular velocities, and on the theory of viscosity and thermal conduction, in a non-uniform simple monatomic gas. *Philosophical Transactions of the Royal Society of London A: Mathematical, Physical and Engineering Sciences*, 216(538-548):279–348.

[41] Chapman, S., Cowling, T. G., and Burnett, D. (1970). *The mathematical theory of non-uniform gases.* Cambridge University Press, Cambridge, U.K.

[42] Chialvo, S., Sun, J., and Sundaresan, S. (2012). Bridging the rheology of granular flows in three regimes. *Phys. Rev. E*, 85:021305.

[43] Chialvo, S. and Sundaresan, S. (2013). A modified kinetic theory for frictional granular flows in dense and dilute regimes. *Physics of Fluids*, 25(7):070603.

[44] Coussot, P. and Meunier, M. (1996). Recognition, classification and mechanical description of debris flows. *Earth-Science Reviews*, 40(3):209 – 227.

[45] Coussot, P. and Piau, J. (1995). A largescale field coaxial cylinder rheometer for the study of the rheology of natural coarse suspensions. *Journal of Rheology*, 39(1):105–124.

[46] Cowen, E. A., Monismith, S. G., Cowen, E. A., and Monismith, S. G. (1997). A hybrid digital particle tracking velocimetry technique. *Experiments in Fluids*, 22(3):199–211.

[47] da Cruz, F., Emam, S., Prochnow, M., Roux, J.-N., and Chevoir, F. m. c. (2005). Rheophysics of dense granular materials: Discrete simulation of plane shear flows. *Phys. Rev. E*, 72:021309.

[48] Delannay, R., Louge, M., Richard, P., Taberlet, N., and Valance, A. (2007). Towards a theoretical picture of dense granular flows down inclines. *Nature Materials*, 6:99108.

[49] Dijksman, J. A., Rietz, F., Lrincz, K. A., van Hecke, M., and Losert, W. (2012). Refractive index matched scanning of dense granular materials. *Review of Scientific Instruments*, 83(1):011301.

[50] Duncan, J., Dabiri, D., Hove, J., and Gharib, M. (2010). Universal outlier detection for particle image velocimetry (PIV) and particle tracking velocimetry (PTV) data. *Measurement Science and Technology*, 21(5):057002.

[51] Enskog, D. (1921). Kinetische theorie. *K. Svensk. Vet.-Akad. Handl.,*, 63(4).

[52] Estrada, N., Taboada, A., and Radjaï, F. (2008). Shear strength and force transmission in granular media with rolling resistance. *Phys. Rev. E*, 78:021301.

[53] Fei, M., Sun, Q., Zhong, D., and Zhou, G. G. (2012). Simulations of granular flow along an inclined plane using the Savage-Hutter model. *Particuology*, 10(2):236 – 241. Advances in Characterization and Modeling of Particulate Processes.

[54] Feng, Y., Goree, J., and Liu, B. (2011). Errors in particle tracking velocimetry with high-speed cameras. *Review of Scientific Instruments*, 82(5):053707.

[55] Foerster, S. F., Louge, M. Y., Chang, H., and Allia, K. (1994). Measurements of the collision properties of small spheres. *Physics of Fluids*, 6(3):1108–1115.

[56] Forterre, Y. and Pouliquen, O. (2008). Flows of dense granular media. *Annual Review of Fluid Mechanics*, 40(1):1–24.

[57] Frankowski, P. and Morgeneyer, M. (2013). Calibration and validation of DEM rolling and sliding friction coefficients in angle of repose and shear measurements. *AIP Conference Proceedings*, 1542(1):851–854.

[58] Fuchs, R., Weinhart, T., Meyer, J., Zhuang, H., Staedler, T., Jiang, X., and Luding, S. (2014). Rolling, sliding and torsion of micron-sized silica particles: experimental, numerical and theoretical analysis. *Granular Matter*, 16(3):281–297.

[59] Garzó, V. and Dufty, J. W. (1999). Dense fluid transport for inelastic hard spheres. *Phys. Rev. E*, 59:5895–5911.

[60] Garzó, V., Hrenya, C. M., and Dufty, J. W. (2007). Enskog theory for polydisperse granular mixtures. ii. sonine polynomial approximation. *Phys. Rev. E*, 76:031304.

[61] GDR, M. (2004). On dense granular flows. *The European Physical Journal E*, 14(4):341–65.

[62] George, D. L. and Iverson, R. M. (2014). A depth-averaged debris-flow model that includes the effects of evolving dilatancy. ii. numerical predictions and experimental tests. *Proceedings of the Royal Society of London A: Mathematical, Physical and Engineering Sciences*, 470(2170).

[63] Goldhirsch, I. (2003). Rapid granular flows. *Annual Review of Fluid Mechanics*, 35(1):267–293.

[64] Goldhirsch, I. (2008). Introduction to granular temperature. *Powder Technology*, 182(2):130 – 136. Granular Temperature.

[65] Goldhirsch, I. (2010). Stress, stress asymmetry and couple stress: from discrete particles to continuous fields. *Granular Matter*, 12(3):239–252.

[66] Gonzalez, R. C., Woods, R. E., and Eddins, S. L. (2003). *Digital Image Processing Using MATLAB*. Prentice-Hall, Inc., Upper Saddle River, NJ, USA.

[67] Gorham, D. and Kharaz, A. (2000). The measurement of particle rebound characteristics. *Powder Technology*, 112(3):193 – 202.

[68] Gray, J. M. N. T. and Ancey, C. (2011). Multi-component particle-size segregation in shallow granular avalanches. *Journal of Fluid Mechanics*, 678:535–588.

[69] Gray, J. M. N. T. and Kokelaar, B. P. (2010). Large particle segregation, transport and accumulation in granular free-surface flows. *Journal of Fluid Mechanics*, 652:105–137.

[70] Hanes, D. M. and Walton, O. R. (2000). Simulations and physical measurements of glass spheres flowing down a bumpy incline. *Powder Technology*, 109(13):133 – 144.

[71] Hart, D. P. (2000). Piv error correction. *Experiments in Fluids*, 29(1):13–22.

[72] Hassan, Y., Blanchat, T. K., and Seeley, C. H. (1992). IV flow visualisation using particle tracking techniques. *Measurement Science and Technology*, 3(7):633.

[73] Holyoake, A. J. and McElwaine, J. N. (2012). High-speed granular chute flows. *Journal of Fluid Mechanics*, 710:35–71.

[74] Hsu, L., Dietrich, W. E., and Sklar, L. S. (2008). Experimental study of bedrock erosion by granular flows. *Journal of Geophysical Research: Earth Surface*, 113(F2). F02001.

[75] Hübl, J. and Steinwendtner, H. (2000). Estimation of rheological properties of viscous debris flow using a belt conveyor. *Physics and Chemistry of the Earth, Part B: Hydrology, Oceans and Atmosphere*, 25(9):751 – 755.

[76] Hunger, O. and Morgenstern, N. R. (1984). Experiments on the flow behaviour of granular materials at high velocity in an open channel. *Géotechnique*, 34(3):405–413.

[77] Hunter, R. P. (2012). Development of transparent soil testing using planar laser induced fluorescence in the study of internal erosion of filters in embankment dams. *Ph.D dissertation, University of Canterbury.*

[78] Iverson, R. M. (1997). The physics of debris flows. *Reviews of Geophysics*, 35(3):245–296.

[79] Iverson, R. M. and Denlinger, R. P. (1987). The physics of debris flows: a conceptual assessment. *International Association of Hydrological Sciences Publication*, 165:155–165.

[80] Iverson, R. M. and Denlinger, R. P. (2001). Flow of variably fluidized granular masses across three-dimensional terrain 1. coulomb mixture theory. *Journal of Geophysical Research-Solid Earth*, 106(B1):537–552.

[81] Iverson, R. M., Reid, M. E., and LaHusen, R. G. (1997). Debris-flow mobilization from landslides. *Annual Review of Earth and Planetary Sciences*, 25(1):85–138.

[82] J. Shäfer, S. Dippel, and D. E. Wolf (1996). Force schemes in simulations of granular materials. *J. Phys. I France*, 6(1):5–20.

[83] Jenkins, J. T. (2006). Dense shearing flows of inelastic disks. *Physics of Fluids*, 18(10):103307.

[84] Jenkins, J. T. (2007). Dense inclined flows of inelastic spheres. *Granular Matter*, 10(1):47–52.

[85] Jenkins, J. T. and Berzi, D. (2010). Dense inclined flows of inelastic spheres: tests of an extension of kinetic theory. *Granular Matter*, 12(2):151–158.

[86] Jenkins, J. T. and Berzi, D. (2012). Kinetic theory applied to inclined flows. *Granular Matter*, 14(2):79–84.

[87] Jenkins, J. T. and Berzi, D. (2016). Erosion and deposition in depth-averaged models of dense, dry, inclined, granular flows. *Phys. Rev. E*, 94:052904.

[88] Jenkins, J. T. and Hanes, D. M. (1993). The balance of momentum and energy at an interface between colliding and freely flying grains in a rapid granular flow. *Physics of Fluids A: Fluid Dynamics*, 5(3):781–783.

[89] Jenkins, J. T. and Zhang, C. (2002). Kinetic theory for identical, frictional, nearly elastic spheres. *Physics of Fluids*, 14(3):1228–1235.

[90] Jiang, M., Shen, Z., and Wang, J. (2015). A novel three-dimensional contact model for granulates incorporating rolling and twisting resistances. *Computers and Geotechnics*, 65:147 – 163.

[91] Johnson, A. M. (1965). A model for debris flow. *Ph.D dissertation. The Pennsylvania State University.*

[92] Johnson, A. M. (1984). Debris flow. *Slope Instability*, Edited by D. Brunsden and D. B. Prior:pages 257–361.

[93] Jop, P., Forterre, Y., and Pouliquen, O. (2005). Crucial role of sidewalls in granular surface flows: consequences for the rheology. *Journal of Fluid Mechanics*, 541(-1):167–192.

[94] Jop, P., Forterre, Y., and Pouliquen, O. (2006). A constitutive law for dense granular flows. *Nature*, 441(7094):727–30.

[95] Kailey, P. (2013). Debris flows in New Zealand alpine catchments. *Ph.D dissertation, University of Canterbury.*

[96] Kaitna, R., Dietrich, W. E., and Hsu, L. (2014). Surface slopes, velocity profiles and fluid pressure in coarse-grained debris flows saturated with water and mud. *Journal of Fluid Mechanics*, 741:377–403.

[97] Kaitna, R., Palucis, M. C., Yohannes, B., Hill, K. M., and Dietrich, W. E. (2016). Effects of coarse grain size distribution and fine particle content on pore fluid pressure and shear behavior in experimental debris flows. *Journal of Geophysical Research: Earth Surface*, 121(2):415–441.

[98] Kamrin, K. and Koval, G. (2012). Nonlocal constitutive relation for steady granular flow. *Phys. Rev. Lett.*, 108:178301.

[99] Keane, R. D. and Adrian, R. J. (1992). Theory of cross-correlation analysis of PIV images. *Applied Scientific Research*, 49(3):191–215.

[100] Klaus, S., Barbara, T., Brian, M., Christoph, G., Oldrich, H., and Roland, K. (2015). *Modeling Debris-Flow Runout Pattern on a Forested Alpine Fan with Different Dynamic Simulation Models*, pages 1673–1676. Springer International Publishing, Cham.

[101] Kumaran, V. (2008). Dense granular flow down an inclined plane: from kinetic theory to granular dynamics. *Journal of Fluid Mechanics*, 599:121168.

[102] Kumaran, V. (2009a). Dynamics of dense sheared granular flows. part 1. structure and diffusion. *Journal of Fluid Mechanics*, 632:109–144.

[103] Kumaran, V. (2009b). Dynamics of dense sheared granular flows. part ii. the relative velocity distributions. *Journal of Fluid Mechanics*, 632:145198.

[104] Kuo, C. Y., Frost, J. D., and Chameau, J. L. A. (1998). Image analysis determination of stereology based fabric tensors. *Géotechnique*, 48(4):515–525.

[105] Larcher, M. (2004). Vertical structure of high concentration liquid-granular flows. *Ph.D dissertation, University of Trento.*

[106] Leornardi, A. (2015). Numerical simulation of debris flow and interaction between flow and obstacle via dem. *Ph.D dissertation, ETH Swiss Federal Institute of Technology.*

[107] Lo, C. Y., Bolton, M. D., and Cheng, Y. P. (2010). Velocity fields of granular flows down a rough incline: a DEM investigation. *Granular Matter*, 12(5):477–482.

[108] Lorenz, A., Tuozzolo, C., and Louge, M. Y. (1997). Measurements of impact properties of small, nearly spherical particles. *Experimental Mechanics*, 37(3):292–298.

[109] Louge, M. Y. (2003). Model for dense granular flows down bumpy inclines. *Phys. Rev. E*, 67:061303.

[110] Louge, M. Y. and Keast, S. C. (2001). On dense granular flows down flat frictional inclines. *Physics of Fluids*, 13(5):1213–1233.

[111] Luding, S. (1998). *Collisions & Contacts between Two Particles*, pages 285–304. Springer Netherlands, Dordrecht.

[112] Luding, S. (2008). Introduction to discrete element methods: Basics of contact force models and how to perform the micro-macro transition to continuum theory, EJECE (Alert Course Lecture, Aussois).

[113] Luding, S. (2010). *From Molecular Dynamics and Particle Simulations towards Constitutive Relations for Continuum Theory*, pages 453–492. Springer Berlin Heidelberg, Berlin, Heidelberg.

[114] Maheshwari, S. and Kumaran, V. (2012). Effect of base dissipation on the granular flow down an inclined plane. *Granular Matter*, 14(2):209–213.

[115] Major, J. J. (2000). Gravity-driven consolidation of granular slurries - implications for debris-flow deposition and deposit characteristics. *Journal of Sedimentary Research*, 70(1):64–83.

[116] Major, J. J. and Iverson, R. M. (1999). Debris-flow deposition: Effects of pore-fluid pressure and friction concentrated at flow margins. *Geological Society of America Bulletin*, 111(10):1424–1434.

[117] McArdell, B. W., Bartelt, P., and Kowalski, J. (2007). Field observations of basal forces and fluid pore pressure in a debris flow. *Geophysical Research Letters*, 34(7). L07406.

[118] Meninno, S. (2015). Mechanics of dry granular flows driven by gravity. *Ph.D dissertation, University of Trento.*

[119] Mitarai, N. and Nakanishi, H. (2005). Bagnold scaling, density plateau, and kinetic theory analysis of dense granular flow. *Phys. Rev. Lett.*, 94:128001.

[120] Mitarai, N. and Nakanishi, H. (2007). Velocity correlations in dense granular shear flows: Effects on energy dissipation and normal stress. *Phys. Rev. E*, 75:031305.

[121] Ni, W.-J. and Capart, H. (2015). Cross-sectional imaging of refractive-index-matched liquid-granular flows. *Experiments in Fluids*, 56(8):163.

[122] Ohmi, K. and Li, H.-Y. (2000). Particle-tracking velocimetry with new algorithms. *Measurement Science and Technology*, 11(6):603.

[123] Okabe, A., Boots, B., and Sugihara, K. (1992). *Spatial Tessellations: Concepts and Applications of Voronoi Diagrams.* John Wiley & Sons, Inc., New York, NY, USA.

[124] Owaga, S. (1978). Multitemperature theory of granular materials. *in: S.C. Cowin, M. Satake (Eds.), Proc. U. S.-Japan Symp. on Continuum Mechanics and Statistical Approaches in the Mechanics of Granular Materials, Gakujutsu Bunken Fukyu-kai,*, pages 208–217.

[125] Panaitescu, A. and Kudrolli, A. (2010). Spatial distribution functions of random packed granular spheres obtained by direct particle imaging. *Phys. Rev. E*, 81:060301.

[126] Papa, M., Egashira, S., and Itoh, T. (2004). Critical conditions of bed sediment entrainment due to debris flow. *Natural Hazards and Earth System Sciences*, 4(3):469–474.

[127] Pasini, J. M. and Jenkins, J. T. (2005). Aeolian transport with collisional suspension. *Philosophical Transactions of the Royal Society of London A: Mathematical, Physical and Engineering Sciences*, 363(1832):1625–1646.

[128] Pitman, E. B. and Le, L. (2005). A two-fluid model for avalanche and debris flows. *Philosophical Transactions of the Royal Society of London A: Mathematical, Physical and Engineering Sciences*, 363(1832):1573–1601.

[129] Pouliquen, O. (1999). Scaling laws in granular flows down rough inclined planes. *Physics of Fluids*, 11(3):542–548.

[130] Pouliquen, O. and Forterre, Y. (2002). Friction law for dense granular flows: application to the motion of a mass down a rough inclined plane. *Journal of Fluid Mechanics*, 453:133–151.

[131] Prasad, A. K., Adrian, R. J., Landreth, C. C., and Offutt, P. W. (1992). Effect of resolution on the speed and accuracy of particle image velocimetry interrogation. *Experiments in Fluids*, 13(2):105–116.

[132] Pudasaini, S. and Hutter, K. (2007). *Avalanche Dynamics: Dynamics of Rapid Flows of Dense Granular Avalanches*. Springer.

[133] Pudasaini, S. P., Wang, Y., and Hutter, K. (2005). Rapid motions of free-surface avalanches down curved and twisted channels and their numerical simulation. *Philosophical Transactions of the Royal Society of London A: Mathematical, Physical and Engineering Sciences*, 363(1832):1551–1571.

[134] Raffel, M., Willert, E. C., Wereley, S., and Jürgen, K. (2007). *Particle Image Velocimetry*. Springer-Verlag Berlin Heidelberg, 2nd edition.

[135] Rajchenbach, J. (2003). Dense, rapid flows of inelastic grains under gravity. *Phys. Rev. Lett.*, 90:144302.

[136] Rauter, M., Fischer, J.-T., Fellin, W., and Kofler, A. (2016). Snow avalanche friction relation based on extended kinetic theory. *Natural Hazards and Earth System Sciences*, 16(11):2325–2345.

[137] Reynolds, G. K., Nilpawar, A. M., Salman, A. D., and Hounslow, M. J. (2008). Direct measurement of surface granular temperature in a high shear granulator. *Powder Technology*, 182(2):211 – 217.

[138] Richman, M. W. (1988). Boundary conditions based upon a modified maxwellian velocity distribution for flows of identical, smooth, nearly elastic spheres. *Acta Mechanica*, 75(1):227–240.

[139] Ries, A., Brendel, L., and Wolf, D. E. (2014). Coarse graining strategies at walls. *Computational Particle Mechanics*, 1(2):177–190.

[140] Rognon, G. P., Roux, J., Naaïm, M., and Chevoir, F. (2008). Dense flows of cohesive granular materials. *Journal of Fluid Mechanics*, 596:2147.

[141] Saha, S. and Alam, M. (2016). Normal stress differences, their origin and constitutive relations for a sheared granular fluid. *Journal of Fluid Mechanics*, 795:549580.

[142] Sanvitale, N. (2010). An experimental study on saturated granular flows and its application to the physical modelling of debris flows. *Ph.D dissertation, Università degli Studi di Padova.*

[143] Sanvitale, N., Bowman, E., and Genevois, R. (2009). Experimental measurements of velocity through granular-liquid flows. 5th International Conference on Debris-Flow Hazards Mitigation: Mechanics, Prediction and Assessment.

[144] Sanvitale, N. and Bowman, E. T. (2012). Internal imaging of saturated granular free-surface flows. *International Journal of Physical Modelling in Geotechnics*, 12(4):129–142.

[145] Sanvitale, N. and Bowman, E. T. (2016). Using PIV to measure granular temperature in saturated unsteady polydisperse granular flows. *Granular Matter*, 18(3):57.

[146] Sanvitale, N. and Bowman, E. T. (2017). Visualization of dominant stress-transfer mechanisms in experimental debris flows of different particle-size distribution. *Canadian Geotechnical Journal*, 54(2):258–269.

[147] Sassa, K. (2007). *Landslide Science as a New Scientific Discipline*, pages 3–11. Springer Berlin Heidelberg, Berlin, Heidelberg.

[148] Savage, S. B. (1979). Gravity flow of cohesionless granular materials in chutes and channels. *Journal of Fluid Mechanics*, 92(1):5396.

[149] Savage, S. B. and Hutter, K. (1989). The motion of a finite mass of granular material down a rough incline. *Journal of Fluid Mechanics*, 199:177–215.

[150] Scarano, F. (2002). Iterative image deformation methods in PIV. *Measurement Science and Technology*, 13(1):R1.

[151] Scarano, F. and Riethmuller, M. L. (2000). Advances in iterative multigrid PIV image processing. *Experiments in Fluids*, 29(1):S051–S060.

[152] Schatzmann, M. (2005). Rheometry for large particle fluids and debris flows. *Ph.D dissertation, Swiss Federal Institute of Technology.*

[153] Silbert, L. E. (2010). Jamming of frictional spheres and random loose packing. *Soft Matter*, 6:2918–2924.

[154] Silbert, L. E., Ertas, D., Grest, G. S., Halsey, T. C., Levine, D., and Plimpton, S. J. (2001). Granular flow down an inclined plane: Bagnold scaling and rheology. *Phys. Rev. E*, 64:051302.

[155] Silbert, L. E., Grest, G. S., Plimpton, S. J., and Levine, D. (2002). Boundary effects and self-organization in dense granular flows. *Physics of Fluids*, 14(8):2637–2646.

[156] Silbert, L. E., Landry, J. W., and Grest, G. S. (2003). Granular flow down a rough inclined plane: Transition between thin and thick piles. *Physics of Fluids*, 15(1):1–10.

[157] Skempton, A. W. and Brogan, J. M. (1994). Experiments on piping in sandy gravels. *Géotechnique*, 44(3):449–460.

[158] Skermer, N. A. and VanDine, D. F. (2005). *Debris flows in history*, pages 25–51. Springer Berlin Heidelberg, Berlin, Heidelberg.

[159] Taberlet, N., Richard, P., Henry, E., and Delannay, R. (2004). The growth of a super stable heap: An experimental and numerical study. *EPL (Europhysics Letters)*, 68(4):515.

[160] Taberlet, N., Richard, P., Valance, A., Losert, W., Pasini, J. M., Jenkins, J. T., and Delannay, R. (2003). Superstable granular heap in a thin channel. *Phys. Rev. Lett.*, 91:264301.

[161] Takagi, D., McElwaine, J. N., and Huppert, H. E. (2011). Shallow granular flows. *Phys. Rev. E*, 83:031306.

[162] Takahashi, T. (1978). Mechanical characteristics of debris flow. *Journal of the Hydraulics Division ASCE*, 104(8):1153–1169.

[163] Takahashi, T. (1991). *Debris flows*. Balkema Rotterdam Netherlands, Rotterdam, Netherland.

[164] Takehara, K. and Etoh, T. (1999). A study on particle identification in PTV particle mask correlation method. *Journal of Visualization*, 1(3):313–323.

[165] Thielicke, W. and Stamhuis, E. (2014). Pivlab - towards user-friendly, affordable and accurate digital particle image velocimetry in matlab. *Journal of Open Research Software*, 2(1):355–364.

[166] Thornton, A. R., Weinhart, T., Luding, S., and Bokhove, O. (2012). Frictional dependence of shallow-granular flows from discrete particle simulations. *The European Physical Journal E*, 35(12):127.

[167] Torquato, S. (1995). Nearest-neighbor statistics for packings of hard spheres and disks. *Phys. Rev. E*, 51:3170–3182.

[168] Tunuguntla, D. R., Thornton, A. R., and Weinhart, T. (2016). From discrete elements to continuum fields: Extension to bidisperse systems. *Computational Particle Mechanics*, 3(3):349–365.

[169] Vescovi, D. (2014). Granular shear flows: constitutive modelling and numerical simulations. *Ph.D dissertation, Politecnico di Milano*.

[170] Vescovi, D., Berzi, D., Richard, P., and Brodu, N. (2014). Plane shear flows of frictionless spheres: Kinetic theory and 3d soft-sphere discrete element method simulations. *Physics of Fluids*, 26(5):053305.

[171] Voellmy, A. (1955). Über die zerstörungskraft von lawinen. *Schweizerische Bauzeitung*, 73:212–217.

[172] Walton, O. R. (1993). Numerical simulation of inclined chute flows of monodisperse, inelastic, frictional spheres. *Mechanics of Materials*, 16(1):239 – 247.

[173] Weinhart, T., Hartkamp, R., Thornton, A. R., and Luding, S. (2013). Coarse-grained local and objective continuum description of three-dimensional granular flows down an inclined surface. *Physics of Fluids*, 25(7):070605.

[174] Weinhart, T., Thornton, A. R., Luding, S., and Bokhove, O. (2012). Closure relations for shallow granular flows from particle simulations. *Granular Matter*, 14(4):531–552.

[175] Wensrich, C. and Katterfeld, A. (2012). Rolling friction as a technique for modelling particle shape in {DEM}. *Powder Technology*, 217:409 – 417.

[176] Westerweel, J. (1994). Efficient detection of spurious vectors in particle image velocimetry data. *Experiments in Fluids*, 16(3):236–247.

[177] Westerweel, J. and Scarano, F. (2005). Universal outlier detection for PIV data. *Experiments in Fluids*, 39(6):1096–1100.

[178] White, D. J., Take, W. A., and Bolton, M. D. (2003). Soil deformation measurement using particle image velocimetry (PIV) and photogrammetry. *Géotechnique*, 53(7):619–631.

[179] Windows-Yule, C. R. K., Tunuguntla, D. R., and Parker, D. J. (2016). Numerical modelling of granular flows: a reality check. *Computational Particle Mechanics*, 3(3):311–332.

[180] Xu, H., Louge, M., and Reeves, A. (2003). Solutions of the kinetic theory for bounded collisional granular flows. *Continuum Mechanics and Thermodynamics*, 15(4):321–349.

[181] Yano, K. and Daido, A. (1965). Fundamental study on mud-flow. *Bulletin of the Disaster Prevention Research Institute, Kyoto University*, 14(2):69–83.

[182] Zanuttigh, B. and Lamberti, A. (2007). Instability and surge development in debris flows. *Reviews of Geophysics*, 45(3):RG3006.

[183] Zhou, Y., Xu, B., Yu, A., and Zulli, P. (2002). An experimental and numerical study of the angle of repose of coarse spheres. *Powder Technology*, 125(1):45 – 54.